Evaluation of radiolabelled hynic-salmon calcitonin analogues as imaging agents for multiple myeloma and characterisation of novel hynic derivatives as chelators for technetium

Meszaros, Levente

Awarding institution:
King's College London

Title: Evaluation of radiolabelled hynic-salmon calcitonin analogues as imaging agents for multiple myeloma and characterisation of novel hynic derivatives as chelators for technetium

Author: Levente Meszaros

Evaluation of radiolabelled hynic-salmon calcitonin analogues as imaging agents for multiple myeloma and characterisation of novel hynic derivatives as chelators for technetium

A thesis submitted to King's College London for the degree of Doctor of Philosophy in Imaging Sciences and Radiation Biology

Levente Kornel Meszaros

Division of Imaging Sciences and Biomedical Engineering

King's College London

September 2012

Abstract

Calcitonin is a peptide hormone produced by the C-cells of the thyroids. Calcitonin receptors (CTR) are expressed by osteoclasts in the normal bone and in many cancers such as multiple myeloma (MM), breast and prostate cancer.

In this thesis we report on the synthesis and evaluation of Tc-99m labelled salmon calcitonin (sCT) derivatives, sCTLys^{18}-hynic-TFA and sCT(8-32)Lys^{18}-hynic-TFA as potential imaging agents for MM and other CTR+ malignancies and the characterisation of novel hydrazinonicotinate (hynic) chelators. Following chemical characterisation *in vitro* stabilities of the radiopeptides were assessed on incubation in human serum. *In vitro* uptake studies in CTR+ MCF-7 cells confirmed that the Tc-99m labelled sCTLys^{18}-hynic-TFA and sCT(8-32)Lys^{18}-hynic-TFA were both ligands for CTR with nanomolar affinity. These findings also confirmed that the evolutionarily conserved disulfide loop in calcitonin peptides is not vital for receptor binding. We evaluated the radiopeptides *in vivo* in the 5T33 murine MM model. By using In-111-oxine labelled enhanced green fluorescence protein transfected 5T33 cells (eGFP-5T33) we confirmed that MM cells have a very high affinity to haemopoietic organs *i.e.* the liver, spleen and bone marrow. When imaging eGFP-5T33 myeloma bearing mice with Tc-99m labelled sCTLys^{18}-hynic-TFA and sCT(8-32)Lys^{18}-hynic-TFA we found increased radiopeptide uptake in the liver, spleen and femora when compared to healthy controls. We could not establish correlation between radiopeptide uptake and the size of eGFP+ or CTR+ cell population in target organs.

Our results suggest that the Tc-99m labelled hynic-sCT peptides may be capable of detecting changes caused by MM in the biology of the liver, spleen and bone marrow.

Studies with novel hynic derivatives confirmed that hynic was most likely a bidentate chelator rather than a monodentate ligand in technetium complexes. Some of the novel derivatives could be trifunctionalised and used for multimodality imaging.

Acknowledgments

First and foremost my thanks go to my supervisors Phil Blower and Yolanda Calle for their continuous support over the past four years. I am deeply grateful to Phil for giving me the opportunity to spend some time and learn some new techniques at the Memorial Sloan-Kettering Cancer Center in New York. I am grateful to Rafa Torres for helping with the synthetic work in my first year and all his support over the years. A massive thank you goes to David Thakor for running the imaging labs so efficiently, Jim Ballinger and Greg Mullen for all their advice, Kevin Howland from the University of Kent for the help in peptide synthesis, Istvan Szanda for helping with the NanoSPECT/CT system and Sheila Foolheea for the administrative support. Thanks to Max Handley for being a great desk buddy for more than three years, Jen Williams and Alex O'neill for all the fun in the lab, in the pub, in Florida and in New York. Puth Charoenphun, Julia Blower, Maite Jauregui, Fiona Shaughnessy and the rest of the Blower group who have made this a very enjoyable four years. Thanks to Jason Lewis and his group for making my stay in New York a very pleasant experience. The very generous funding from Cancer Research UK is also gratefully acknowledged.

A big thank you goes to my family and my partner for all their support and for coping with my hectic schedule over the years.

Contents

Abbreviations

AIDS	acquired immune deficiency syndrome
APC	allophycocyanin
ATP	adenosinetriphosphate
AUC	area under the curve
BLC	B lymphocyte chemoattractant
BM	bone marrow
Boc	tertbutyloxy-carbonyl
BSA	bovine serum albumin
BSU	biological services unit
cAMP	cyclic adenosinemonophosphate
CGRP	calcitonin gene related peptide
CNS	central nervous system
CRLR	calcitonin receptor-like receptor
CRSP	calcitonin receptor stimulating peptide
CT	computed tomography
CTR	calcitonin receptor
dH_2O	distilled water
DIEA	N,N-diisopropylethylamine
DMF	N,N-dimethyl formamide
DMSA	dimercaptosuccinic acid
DMSO	dimethylsulfoxide
DNA	desoxyribonucleic acid
DTPA	diethylenetriamine-pentaacetic acid
EDDA	ethylenediaminediacetic acid

EDTMP	ethylenediamine tetramethylene phosphonate
eGFP	enhanced green fluorescent protein
ESI	electrospray ionisation
F-18-FDG	2-deoxy-2-[F-18]-fluoro-D-glucose
FA	formic acid
FACS	fluorescence-activated cell sorting
FLT	[F-18]-3'-fluoro-3'-deoxy-L-thymidine
Fmoc	9-fluorenylmethyl carbamate
HBS	Hanks' balanced salt solution
HBTU	(benzotriazol-1-yl)-*N,N,N′,N′*-tetramethyluronium hexafluorophosphate
hCT	human calcitonin
hCTR	human calcitonin receptor
HHV	human herpes virus
HIV	human immunodeficiency virus
HOBT	1-hydroxy-benzotriazole
HPLC	(high performance) liquid chromatography
hynic	6-hydrazinonicotinic acid
Ig	immunoglobulin
IL	interleukin
ISH	*in situ* hybridisation
ITLC	instant thin layer chromatography
i.v.	intravenous
λ_{Ex}	excitation wavelength
λ_{Em}	emission wavelength

LC-MS	liquid chromatography-mass spectrometry
LRP	lung resistance protein
M-CSF	macrophage colony stimulating factor
MDP	methylene diphosphonate
MFE	molecular feature extraction
MFI	mean fluorescent intensity
MGUS	monoclonal gammopathy of undetermined significance
MIP	maximum intensity projection
MM	multiple myeloma
M-protein	monoclonal protein
MRI	magnetic resonance imaging
mRNA	messenger ribonucleic acid
MS	mass spectrometry
NA	nicotinic acid
NHS	N-hydroxy-succinimid(il)
NIS	sodium iodide symporter
NK cell	natural killer cell
PBMC	peripheral blood mononuclear cell
PBS	phosphate buffered saline
PCR	polimerase chain reaction
pCT	porcine calcitonin
PET	positron emission tomography
PET/CT	positron emission tomography/computed tomography
Pgp	plasma glycoprotein pump
PIL	personal investigator licence

PPL	personal project licence
PTH	parathyroid hormone
RAMP	receptor activity modifying protein
RANK	receptor activator of nuclear factor kappa-B
RANKL	receptor activator of nuclear factor kappa-B ligand
RCP	radiochemical purity
R_f	retention factor
RNA	ribonucleic acid
RPE	R-phycoerythrin
RT-PCR	reverse transcriptase polimerase chain reaction
sCT	salmon calcitonin
SDF	stromal cell derived factor
SEC	size exclusion chromatography
SEM	standard error of the mean
SN	supernatant
SPECT	single photon emission computed tomography
STD	sexually transmitted disease
SUV	standardised uptake value
TEM	transmission electron microscopy
TFA	trifluoroacetic acid
TIS	triisopropylsilane
TRAP	tartarate resistant acidic phosphatase
tricine	N-(Tri(hydroxymethyl)methyl)glycine
UV	ultraviolet
vIL-6	viral interleukin-6

Chapter 1: Imaging multiple myeloma and osteoclastic lesions: the role of calcitonin receptor and salmon calcitonin

1.1 Aims

In this chapter we aimed to give a brief summary on multiple myeloma (MM) focussing on the role of different imaging modalities in the diagnosis and management of the disease. In the second part of the chapter we give a summary on osteoclasts, calcitonin, calcitonin binding sites and their role in cancer especially bone-related malignancies such as MM.

1.2 Multiple Myeloma

1.2.1 The origin and differentiation of B cells

MM is "a hematologic malignancy characterized by the development of a progressive and destructive osteolytic bone disease" [1]. It is usually a disease of the elderly population *i.e.* rarely occurs in people below the age of 50 [2]. Although MM has been described in 1844 (surprisingly in a 39 year-old woman), it still remains incurable – despite the fact that a large number of therapeutic regimens have been tried in the past half century [3]. The average survival of MM patients is only 2-3 years in Europe [3, 4]. In some exceptional cases, the survival can reach 10 years (relapse can occur even after 9 disease-free years), but the 5 year survival is still only 30% [5].

Before moving on to MM, it is worth summarising the normal (*i.e.* physiological) B-cell maturation. Changes or mutations in some points of this process lead to MM. Stevenson and Sahota's and Van Riet's reviews give a good and illustrated summary of this [6, 7]; understandable for people who do not have

too much background in haematology. The maturation process is summarised in Figure 1.1.

Plasma cells (Figure 1.1) are mature immune cells (B-cells) whose main function is to produce immunoglobulins (Igs). MM is a disease characterised by the endless division of an abnormal plasma cell clone. Thus MM is a B-cell malignancy, the figure below shows the normal B-cell differentiation process. B-cells are the basis of the so-called humoral immune response: they are able to produce antibodies with high specificity against antigens.

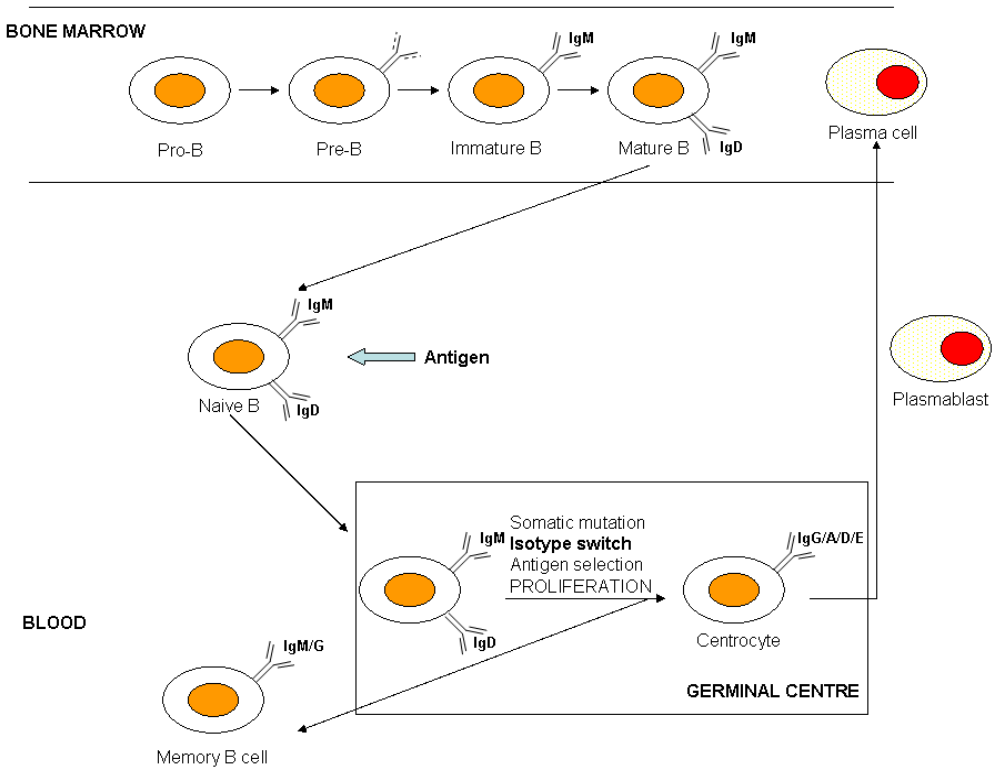

Figure 1.1: The maturation of B cells. Figure reproduced from [6, 7].

These antibodies serve as tracers: once they have been conjugated with the appropriate antigen they attract the cellular immune system, *i.e.* T-cells and natural killer cells (NK cells) which then phagocytose the antigen. Like blood cells in general, B-cells originate from the bone marrow (BM). It is noteworthy that the first

stage of B-cell differentiation, which happens in the BM is always antigen and T-cell independent [7], whereas the differentiation phase outside the BM is antigen and T-cell dependent.

In the marrow, pro-B cells (Figure 1.1) are the first precursors which are obviously and exclusively related to the B-cell lineage. Pro-B cells themselves originate from stem cells. Once the rearrangement of Ig heavy chain genes of pro-B cells has happened, they turn into a new cell type (pre-B cells). Pre-B cells express Ig μ heavy chains in their cytoplasm. Further rearrangement of the Ig genes gives cells the possibility to express cell surface IgM antibodies (Immature B cells) and later IgD antibodies (Mature B cells). At this stage B cells leave the BM by entering the sinusoid capillaries and become naïve B cells (Figure 1.1) [7]. Naïve B cells then enter the secondary lymphoid organs *i.e.* germinal centres in lymph nodes. If they do not meet antigens on their way, they will re-enter circulation without undergoing any changes. If they meet an antigen and become activated before entering a secondary lymphoid organ, important changes will take place in the lymph node. First and foremost activated B cells begin to proliferate in the lymphoid tissue. Due to somatic mutations the clones begin to express highly antigen-specific antibodies. Isotype switching also occurs (see Figure 1.1). A minority of B-cell clones differentiate to centroblasts in the follicles. These cells do not express surface antibodies and are extremely proliferative. Centroblasts then differentiate to centrocytes and express (the now highly specific) surface antibodies. Centrocytes with high affinity surface Igs then differentiate into memory B cells: these cells are capable of starting clonal proliferation in the germinal centre, establishing a quicker immune response when the immune system meets the same antigen later. Another part of centrocytes

develops plasmablasts – these cells then head for the BM where they differentiate into plasma cells (the final stage of B-cell differentiation).

To summarise, the normal maturation process of B cells is a consecutive chain of mutations. As a result, “at any stage of its differentiation, a B cell can become target for an oncogenic transformation…” [7]. It has been proven that B cell malignancies reflect the characteristics of normal B cells, “frozen at a particular differentiation phase” [7]. Most of the MM patients are IgG or IgA secretors; a rare minority with IgD secretion also occurs. The antigen whose plasma cells cause MM may differ inter-individually; in some cases, MM antibodies have been proven to be autoantibodies [6]. Some studies also hypothesised viral origin for MM (*vide infra*).

MM can be defined as a B cell neoplasia “characterised by a monoclonal proliferation of end stage B cells in the bone marrow” [7]. It is noteworthy that the variable region of Ig heavy chains in MM cells remains “stable”, in other words, intraclonal variability does not occur in MM lineages [6]. Hence it seems that somehow mutation mechanisms are “silenced” in MM cells.

1.2.2 Regulatory factors and the role of the BM microenvironment

It had been generally accepted that until the very final (*i.e.* terminal) stage of MM, MM cells can be found in the BM only and are highly dependent on their microenvironment in the marrow [7-9]. However, it may be better to say that MM cells are only detected in the BM until the very final stages. Quite a few publications (most of them are recent case studies but some were published more than 20 years ago) report on soft tissue, mostly liver involvement in MM patients (*vide infra*).

The tight relationship with the BM helps MM cells to survive and also triggers their drug resistance [10]. The observation that cells are strictly retained in a particular tissue is due to the phenomenon called cell homing. According to Van

Riet, two factors contribute to the homing mechanism of MM cells: adhesion and chemotactic factors. Adhesion molecules might be of very different types, such as Igs, integrins, proteoglycans *etc*. During its differentiation, the B cell will express different adhesion factors depending on its actual cellular environment and needs. On the other hand BM stromal cells express regulating factors that affect B-cell differentiation and maturation. The nature of such regulating mechanisms has not yet been described completely. Chemotactic factors also have an important role in B-cells development: they “bind” immature B-cells to the BM: stromal cell derived factor-1 (SDF-1) is a potential chemoattractant for pre- and pro-B cells but not for more mature B cells. Another example is B lymphocyte chemoattractant (BLC), a factor that has an important role in regulating the migration of B cells to lymph node follicles.

MM cells may be present in the circulation of patients at any stage of the disease, but are unable to proliferate and form lesions outside the BM until the latest phase of MM. Interestingly, quite sharp differences have been observed between the adhesion factor expression of medullary (*i.e.* in the BM) and extramedullary (*i.e.* outside the BM) MM cells [7]. In the BM, the most important tumour stimulating factor is interleukin-6 (IL-6): *in vitro* experiments show that this molecule stimulates the proliferation of malignant plasma cells, and studies have found correlation between IL-6 levels and *in vitro* and *in vivo* proliferation of MM cells [7, 9]. IL-6 is mainly produced by BM stromal cells however in some cases MM cells themselves express it hence in such cases it acts as an autocrine stimulator [9]. According to Van Riet, IL-6 is not the only MM stimulating factor in the BM but it is certainly the most important one [7]. In addition to its stimulating effect IL-6 inhibits apoptosis in MM cells and can enhance their drug resistance as well [9, 11]. A study by

Lichtenstein *et al.* clearly demonstrates the effectiveness of IL-6 in inhibiting apoptosis [11]: after evoking apoptosis by serum starvation or drugs in four MM cell lines (three of them IL-6 dependent) the addition of IL-6 inhibited programmed cell death in a dose-dependent manner in some of the serum-starved and drug treated cultures. However no inhibitory effect occurred when cell cultures were treated with certain chemotherapeutics (doxorubicin and etoposide, respectively).

The fact that extramedullary MM lesions occur at the terminal stage of the disease means that in terminal stage of MM, MM cells lose their stroma dependency. This finding suggests that MM cells at this stage are able to develop molecular mechanisms to avoid apoptosis and they probably become capable of expressing autocrine growth stimulating factors. According to Van Riet [7], it is also possible that MM cells at this stage produce extracellular matrix proteins so that they are able to mimic their BM microenvironment.

1.2.3 Extraosseous MM lesions

Extramedullary (extraosseous) myeloma can occur in soft tissues surrounding affected bones when MM cells infiltrate the bone matrix and enter other tissues. Another type of soft tissue involvement occurs in organs not neighbouring to primary lesions. This type of disease can affect virtually any organ. A consecutive set of autopsies in 52 MM patients revealed kidney involvement in 31%, spleen involvement in 31%, liver involvement in 29% and lymph node infiltration in 23% of cases; in 10% of the cases tumour involvement was detected in the heart and digestive tract. It is noteworthy that 33 of the 52 patients had at least 1 extraosseous lesion [12]. This finding suggests that thorough whole-body *post-mortem* examination would probably reveal extramedullary lesions in a high number of MM patients. In some exceptional cases MM cells invading the pericardium can even

cause cardiac tamponade (*i.e.* collapsed ventricles and decreased stroke volume due to increased pericardial pressure) [13]. Hall *et al.* compiled a set of computed tomography (CT), 2-deoxy-2-(^{18}F)fluoro-D-glucose positron emission tomography/computed tomography (F-18-FDG-PET/CT), magnetic resonance imaging (MRI) and ultrasound imaging images of extramedullary myeloma. In one of the patients ultrasound imaging revealed that MM completely replaced testicular tissues in one of the testicles [14].

Even early studies highlighted that - at least in some MM patients – liver involvement can cause clinical symptoms. However, as Perez-Soler and colleagues wrote in 1985 liver biopsies are rarely carried out even when liver involvement is suspected as "liver involvement in multiple myeloma has not been proved to be a prognostic characteristic…" [15]. Reviewing more than a hundred MM patient records they found that liver biopsy was only carried out in 5 patients and 2 of them were found to have diffuse plasma cell infiltration in the liver. Only *post-mortem* histology data was available from a further 16 patients and 8 of them turned out to have diffuse liver infiltration (*N.B.* 3 of the above patients were diagnosed with hepatomegaly when alive). Nineteen of the patients with liver problem (hepatomegaly or elevated serum transaminase or bilirubin levels) were not evaluated by clinicans at all (no biopsy performed) even though MM therapy treated hepatomegaly in 3 patients. This article perfectly demonstrates that in the early days clinicians did not pay enough attention to liver involvement in MM patients. This approach has started to change recently when it turned out that more and more MM patients present with soft tissue involvement. Varettoni *et al.* reviewed 1003 patient records obtained in the same centre between 1971 and 2007 [16]. In total 7% of patients had extramedullary disease at diagnosis (diagnosed by imaging) and 6%

developed extraosseous lesions during follow-up. *N.B.* three quarter of patients with extramedullary lesions had the disease affecting soft tissues near skeletal sites. They divided patients into 3 groups based on the therapy that was used to treat them: 1971-1993 (group 1), 1994-1999 (group 2) and 2000-2007 (group 3). At diagnosis, 4% of patients in group 1, 6% in group 2 and 12% in group 3 presented with extramedullary myeloma. Due to improved chemotherapeutics the onset of extramedullary disease in patients during follow up was much later in patients in group 3 than the other two groups: 34.6 *vs.* 18.9 months. In a study on 174 patients with relapsed refractory myeloma (hence heavily pre-treated patients) Detweiler Short and co-workers found that extramedullary lesions developing after diagnosis can be associated with a bad outcome. They also found that the majority of extraosseous lesions emerged in tissues surrounding skeletal sites [17]. When citing the above work of Varettoni *et al.* with two other publications Detweiler Short and co-workers conclude that novel therapeutics may increase the incidence of extramedullary myeloma. However we should point out that the high incidence at diagnosis cannot be associated with the latter treatment. It is true that Varettoni and colleagues found significantly higher incidence of extramedullary lesions during follow up in group 3; their explanation to this finding seems reasonable *i.e.* the increase in extramedullary involvement is likely to reflect the "prolongation of patients' survival" [16]. In addition Detweiler Short *et al.* made a very reasonable point: although the incidence of extramedullary lesions significantly increased in the past decade the true incidence might not have changed; it may only reflect the improvement in imaging techniques, namely the wider availability of CT and PET [17].

A recent case report entitled “Liver failure as the only clinical manifestation of multiple myeloma” described a very unique case of MM [18]. The patient had hepatomegaly, and 24-hour urine analysis suggested that he was suffering from MM (presence of Ig free light chains). Liver biopsy confirmed that his liver was infiltrated by plasma cells. CT and MRI did not reveal bone lesions and BM biopsy specimens only contained 7% plasma cells (*N.B.* below the 10% lower limit for MM, *vide infra*). Although this publication reported a unique finding it suggests that MM cells may not be as dependent on the BM microenvironment as previously thought and that – at least in some cases – extramedullary lesions can play an important role in disease progress.

The cited studies, especially the one published by Oshima and co-workers [12], demonstrate that extraosseous MM lesions may be much more common that one would think. It is likely that MM specific imaging agents could visualise such lesions better than the currently used (non-specific) imaging modalities.

1.2.4 Human herpes virus-8 and MM

Human herpes virus-8 (HHV-8) or Kaposi’s sarcoma associated herpesvirus has recently been described by Moore and co-workers as a member of the gamma-herpesvirus family [19]. The virus encodes a protein of 204 amino acids which shows 24.8% amino acid identity and 62.2% overall similarity to human IL-6. The sequence of this protein (called viral IL-6 (vIL-6)) also contains an amino acid sequence characteristic of “IL-6-like interleukins” [19]. Biological assays suggested that vIL-6 acts like IL-6 in a dose-dependent manner: it had the same anti-apoptotic effect as the human protein in a cell-assay thus, as authors report “vIL-6 can substitute for cellular IL-6 in preventing B9 [the cell line used for the study] apoptosis.” Not surprisingly, only a year after Moore’s observations vIL-6 was

described to stimulate the growth of human MM cells. Burger and co-workers studied the effect of vIL-6 on a human MM cell line (INA-6) [20]. Similarly to B9 this cell line is also IL-6 dependent, both for survival and proliferation. Burger *et al.* found that vIL-6 had the same effect on INA-6 cells as its human analogue however, in much larger concentrations only (4000-fold, respectively) hence the biological activity of vIL-6 was lower than that of the human IL-6.

One may ask whether HHV-8 can have a crucial effect in MM. Several studies attempted to answer the question. Said and co-workers screened MM patients (and controls) for HHV-8. They found that HHV-8 was present in BM biopsies in 17 of 20 MM patients whilst the virus was not detected in BM biopsies of 4 healthy volunteers and 21 patients with lymphoma or leukaemia [21]. An interesting finding was that in a MM patient with BM transplantation (not mentioned whether it had been syngeneic or heterologous), the virus had been present before the operation but could not be detected after transplantation. Two other MM patients who had previously undergone BM transplantation were also negative (no sample was obtained from them before transplantation). Based on their own and other groups' results Said and co-workers suggested a causative role of HHV-8 in MM. The same group later confirmed the presence of HHV-8 in BM stromal cells of MM patients (15 of 15) but the complete lack of HHV-8 in MM cells by polymerase chain reaction (PCR) and *in situ* hybridisation (ISH) [22]. Ismail and co-workers found 7 HHV-8 positive BM samples in a group of 17 MM patients and no positive samples in healthy controls by PCR [23]. On the other hand the role of the virus in MM still remains to be determined as there are a couple of conflicting research papers on the field. For example in a recent report Sadeghian *et al.* found that only 4 out of 30 BM

samples obtained from MM patients were HHV-8 positive and all the 30 control samples were negative by immunohistochemistry [24].

Since HHV-8 seems to play an important role in MM it may be worth having a closer look at how the virus spreads. In their brief review, Berenson and Vescio [25] highlighted that the virus is present in “sexual and other body secretions”. With a 10-year long study focussing on human immunodeficiency virus (HIV) and acquired immunodeficiency syndrome (AIDS) in homo- and bisexual men, Martin and co-workers elegantly proved that HHV-8 is sexually transmitted [26]: HHV-8 positivity showed correlation with the number of previous sexually transmitted diseases (STDs) and linear correlation was established between the number of homosexual intercourses and the probability of being HHV-8 positive. Berenson and Vescio [25] studied 37 MM patients, 80% of them were HHV-8 positive (peripheral blood mononuclear cells were examined only). However, none of their studied sexual partners were positive based on peripheral blood mononuclear cell (PBMC) screening. Berenson and Vescio mention that this finding does not necessarily mean that each subject was HHV-8 negative: it is also possible that their HHV-8 levels were below the sensitivity of the assay (or refer to Said and Rettig *et al.* [21, 22]).

1.2.5 Clinical symptoms of MM and related disorders

A thorough review on the symptoms and clinical manifestation of MM was published by Kyle [27]. According to this review 98% of MM patients have a high level of monoclonal protein (M-protein) in their blood or urine secreted by MM lesions and among these patients 92% have the M-protein present in their sera. Thus at first glance proteinaemia or proteinuria can be reliable markers of the disease.

Ninety percent of patients present with a BM plasma cell count (that is the percentage of plasma cells in a BM sample) higher than 10%. Bone pain, generalised

osteoporosis and anaemia are present in approximately 2/3 of patients [28, 29]. Although none of these symptoms are fully specific to MM, high plasma cell count in the BM is considered as a very reliable marker. Thus (minimum) criteria for the diagnosis of MM, established and accepted by the International Myeloma Working Group are: BM aspirate with more than 10% plasma cells **or** a plasmacytoma (malignant focal plasma cell tumour) **and** monoclonal protein in the serum (>3 g/dl) *and/or* urine **and** lytic bone lesions or other end-organ(tissue) damage (*e.g.* kidney damage) [27, 29]. In some (rare cases) MM can be diagnosed upon morphological and cytologic features only even if BM plasma cell count is normal (*i.e.* below 5% in atypical cases) [28]. The most recent diagnostic criteria of *active myeloma*[1], approved by the International Myeloma Working Group are slightly different to the above criteria [10] (refer to Table 1.1). *N.B.* some forms of MM such as smouldering MM (*vide infra*) may not require treatment at time of diagnosis.

C: hypercalcaemia calcium levels 0.25mM above normal range or above 2.75 mM
R: renal insufficiency creatinine concentration >173 mM
A: anaemia haemoglobin concentration 20 g/L below normal range or <100 g/L
B: bone lesions lytic bone lesions of osteoporosis with compression fractures

Table 1.1: CRAB criteria for the diagnosis of active MM. Table was reproduced from [10].

Bastard briefly summarised the genetics of MM [30]. Based on genetic analysis, important prognostic information can be assessed. In the future when PCR becomes a routine clinical laboratory tool genetic analysis can give the opportunity

[1] Active MM is, by definition MM that needs immediate treatment.

of more specific treatment: if the place of mutation can be identified (*i.e.* which chromosome is affected) maybe not only prognostic information but “personalised” therapeutic strategies can also be achieved.

1.2.6 Monoclonal gammopathy of undetermined significance: the pre-malignant state of MM

Monoclonal gammopathy of undetermined significance (MGUS) is a benign disease considered as the pre-malignant state of MM [29, 31, 32]: patients with MGUS are likely to develop MM on a longer term; long-term follow-up studies suggest that 16-20% of MGUS patients will develop MM within 10 years of diagnosis and 30% of them will be diagnosed with MM within 20 years. The disease is quite common, 1.0-3.4% of the population over 50 and more than 3% of the population over 70 years of age are affected [9, 29]. In the US 10% of the population over the age of 80 suffer from MGUS [22]. As a pre-malignant state of MM, MGUS is characterised by the same parameters as MM apart from osteolytic bone lesions/end-organ damage. In other words if bone lesions (end-organ damage) are present the disease will be classified as malignant [9, 29, 31, 32].

A usual clinical definition of MGUS is the presence of less than 3 g/dl of M-protein in the serum, only light or no proteinuria and less than 10% plasma cells in the BM with no bone/tissue lesions present [31, 32]. The above mentioned criteria are widely accepted and have been approved by the International Myeloma Working Group. These criteria are quite straightforward but excluding the presence of end-organ damage can sometimes be quite challenging.

1.2.7 Asymptomatic forms of MM

Relatively rare (1-5% of diagnosed cases) asymptomatic forms of MM, such as smouldering and non-secretory myeloma, plasma cell leukaemia, osteosclerotic myeloma and plasmacytomas have been described in the past couple of decades [27-29].

Patients with smouldering myeloma present with elevated levels (>3 g/dl) of M-protein and/or >10% BM plasma cells (usually mature plasma cells) but no end-organ damage (bone lesion or renal problems) [27-29].

Patients with non-secretory MM do not develop proteinaemia and proteinuria but still fulfil the remaining diagnostic criteria such as >10% BM plasma cell count and end-organ damage [27, 29].

Plasma cell leukaemia is characterised by presence of >20% plasma cell count in peripheral blood and an absolute plasma cell number of $>2x10^9$/l [27, 29].

Osteosclerotic myeloma is a disease with a very complex set of symptoms such as polyneuropathy, organomegaly, endocrinopathy, M-protein and skin changes (POEMS-syndrome) with imbalanced osteoblast activation [27, 28].

Plasmacytomas (either solitary bone (1) or extramedullary plasmacytomas (2)) are characterised by the lack of serum and/or urine M-protein and the presence of a destructive bone lesion due to plasma cell proliferation (1) or extramedullary tumours of clonal plasma cells with normal BM (2) [27, 29].

1.2.8 The role of BM biopsies in MM

BM biopsies have a very important role in the diagnosis and follow-up of MM. The iliac bone is the most ideal bone for this purpose as it is easily accessible and usually provides pathologists with representative samples [28]. According to the International Myeloma Working Group only 5% of BM biopsies obtained from MM

patients contain <10% of plasma cells and even this low ratio of low plasma cell counts is usually caused by inadequate specimen collection or uneven plasma cell distribution [29]. In healthy subjects the biopsy specimen contains only a few plasma cells (around ~1%, between 0.5-4%). Marrow plasma cell count in MM patients can go up to 30% [28]. *N.B.* not only the quantity of BM cells matters; their characteristics may also be of important diagnostic value.

1.2.9 Most common therapies of MM

1.2.9.1 Chemotherapy

MM is an incurable disease. However, therapeutic strategies that prolong survival and provide patients with relief of symptoms have been in clinical use for many years. At the moment, chemotherapy is the usual treatment of MM. The following section is a brief summary on the most widely used therapeutic approaches, based on a review by Blade [33].

Normally patients do need treatment at time of diagnosis. However, it is crucial to differentiate patients with MM from those with "similar" diseases, such as MGUS and smouldering myeloma; in Blade's words "asymptomatic patients" must not receive treatment till they present with MM.

For a few decades combined melphalan and prednisone have been the most widely used regimen to treat MM (although nowadays the combination of melphalan with novel agents such as bortezomib is becoming widely available too). Melphalan is an alkylating agent and prednisone is a very effective steroid-anti-inflammatory drug. Although the melphalan-prednisone therapy is quite harsh, it usually takes 2 to 6 months to achieve any response. This combination is effective in 50-60% of patients and increases median survival from 1 year to 2-3 years. To improve effectiveness combination of 5-6 different chemotherapeutics (including melphalan

and prednisone) was tested. Such combinations resulted in slightly higher median survivals (*i.e.* up to 38 months) and response rates. After several months of therapy, a plateau phase will develop in clinical parameters and it will not be possible to achieve further improvement. Therapy should then be re-started when patients relapse.

As in many cancers, multi drug resistance can occur in MM too [34]. This phenomenon is mainly associated with expression of the plasma glycoprotein pump (Pgp). Other membrane efflux proteins in multidrug resistant MM cells (such as lung resistance protein, LRP) have also been identified. Drugs that can switch-off Pgp, such as cyclosporin A and quinine have been successfully tested in terminal-stage patients. However, their side-effects can be harsh hence even in end-stage patients such agents are not yet used routinely (as of 1999) [34].

Two recent reviews summarise the role of novel chemotherapeutics in MM [10, 35]. Maybe the most interesting novel agents are the infamous thalidomide and its analogues. The agent is a potent anti-angiogenic compound that also stimulates the immune system thus it could successfully be used in cancer treatment. However, thalidomide is neurotoxic and its use evokes the formation of (mainly deep vein) thrombi. As a result thalidomide is usually co-administered with aspirin, warfarin or heparin. The combined use of thalidomide with dexamethasone or other novel agents (*vide infra*) is definitely superior to single-agent therapies. Other novel agents are lenalidomide and bortezomib. Lenalidomide, a thalidomide analogue, can also stimulate the immune system but its side effects are more tolerable. Bortezomib is a dipeptide that inhibits proteasome, the cell organelle responsible for protein degradation. Although these compounds can be effective on their own, when combined with each other or with other chemotherapeutics such as dexamethasone

response rates will significantly increase. In combination they can successfully treat patients in relapse (on the other hand bortezomib has also been shown to be effective as a single agent in such patients [10]). Laubach and co-workers highlight the advantages of combined thalidomide, dexamethasone and liposomal doxorubicin [35].

1.2.9.2 Stem cell transplantation in MM

According to Fermand and Brechignac [36] high(er) doses of melphalan could result in high(er) response rates. However such alkylating agents in high doses have serious myelotoxic effect. External beam irradiation of osseous lesions, especially when combined with high-dose chemotherapy, is also proven to be effective but its myelotoxicity is an important issue. If BM transplantion is feasible and the patient is fit enough the above therapies can safely be carried out as normal BM function can be restored by transplantation. On the other hand graft-versus-host and host-versus-graft effects may result in serious problems. Syngeneic blood stem cell transplantation is an important alternative: before therapy, a blood sample is collected and “stem cells” (mononuclear cells) are separated. These cells are then stored and re-injected after chemotherapy and provide recovery within 2 weeks. Using appropriate laboratory techniques, the risk of re-injecting MM cells is very low (usually <1 plasma cell/1,000 mononuclear cells) [36].

Gahrton also highlighted the advantages of combined radio- and (high-dose) chemotherapy in combination with allogeneic BM transplantation (not stem cells). Compared to syngeneic BM transplantation relapse rates are lower however 10% of patients die due to graft-versus host and host-versus-graft diseases [5].

1.2.9.3 Bisphosphonates in MM

Since bisphosphonates are known to have inhibitory effects on osteoclasts, the bone cells responsible for the digestion of organic and inorganic bone matrices they might be of use in the treatment of MM. More than 50% of MM patients have vertebral and 30% non-vertebral fractures and 20-30% are hypercalcaemic therefore the treatment of general bone-related symptoms (myeloma bone disease) has a particular importance. Moreover, increased bone resorption (osteoclast activation) occurs at very early stages of the disease [37]. After reviewing a number of clinical studies Apperley and Croucher concluded that data on the role of bisphosphonates in MM are conflicting [37]. For example a study on 13 patients found that oral administration of clodronate reduced bone pain and progression of skeletal lesions. Other (larger) studies on clodronate with placebo control groups found "beneficial effects on bone disease" and lower occurrence of hypercalcaemia. On the other hand oral administration of pamidronate, a bisphosphonate that is 10-times more effective than clodronate was not beneficial whilst in another study intravenous administration of the compound significantly reduced bone pain and incidence of skeletal events in patients [37]. In a clinical paper Bartl and Frisch mention how they apply bisphosphonates from diagnosis of MM [28] to treat hypercalcaemia and prevent further bone destruction. Vogel and co-workers also mention the importance of bisphosphonates in reducing the risk of fractures in patients with MM [38]. Vogel *et al.* treated MM patients with pamidronate and found that only 36 of 191 patients (19%) experienced fractures (median follow-up: 23 months). Normally 45% of patients with MM have a fracture in the first year of disease [38].

In a large multi-centre study involving 392 patients (196 receiving pamidronate and 181 being administered with placebo) with stage III MM Berenson

and co-workers found that i.v. administration of 90 mg pamidronate (once a month) can significantly reduce the number of "skeletal events" *i.e.* fractures, from 41 to 24% [39]. Although there were no differences in serum or urine M-protein levels markers of bone resorption and formation were significantly lower in patients receiving pamidronate (markers were ratio of urinary calcium to urinary creatinine and ratio of urinary hydroxyproline to urinary creatinine).

1.2.10 Imaging MM and osteolytic bone lesions

1.2.10.1 Introduction

Radionuclide, radiological and magnetic imaging have all been applied to image MM lesions in the past decades. Due to its "exceptional" behaviour (*i.e.* unlike many bone tumours and metastases MM is an osteolytic disease) imaging of MM lesions still remains challenging.

In the early days imaging was inferior to clinical parameters when staging patients with MM. The Salmon-Durie staging system, published in 1975, was based on parameters such as BM MM cell count, serum calcium and M-protein levels [40]. A recent, updated version of the staging system (Durie/Salmon Plus) that mainly relies on imaging highlights the emerging role of molecular imaging techniques in MM. The staging system is reported in Table 1.2.

Classification	MRI and/or F-18-FDG-PET
MGUS	All negative
Stage 1A (smouldering)	single plasmacytoma and/or limited disease
Stage 1B	<5 focal lesions, mild diffuse disease
Stage 2A/B	5-20 focal lesions, moderate diffuse disease
Stage 3A/B	>20 focal lesions, severe diffuse disease

A: serum creatinine <2 mg/dl, no extramedullary disease

B: serum creatinine >2 mg/dl, extramedullary disease

Table 1.2: The Durie/Salmon Plus staging system for MM. Table reproduced from [40].

1.2.10.2 Conventional X-ray, CT and MR imaging

X-ray imaging is the cheapest, easiest and most widely available imaging modality; especially in the early days it was quite widely used in imaging MM. Winterbottom and Shaw highlight that its specificity is sometimes very low especially in early stages of the disease. X-ray imaging will only visualise the consequences of MM *i.e.* the resulting bone tissue loss and fractures thus will not be able to detect small lesions [40]. Dimopoulos and co-workers also list several downsides of planar X-ray imaging such as observer dependency, limited sensitivity and length of examination (20 exposures for a whole body radiography) however they also note that this technique still remains the gold standard in the evaluation of MM [41]. CT is much better in imaging very small lesions than planar radiography but a whole body CT scan gives an effective radiation dose of 8mSv to the patient. Nonetheless CT is very useful in imaging MM, it is widely available and relatively cheap nowadays [40]. It has a higher sensitivity and specificity and the examination is quicker and more comfortable for the patient than whole body radiography [41].

MRI is a novel and useful tool in imaging bone diseases as it can image “the bone marrow directly” and not only the consequences of MM. Many false negative (by X-ray) patients turn out to be positive by MRI: a study found that 19% of X-ray negative patients were positive with MRI. The presence or lack of bone lesions is an important factor in differential diagnosis of MGUS and MM [31, 32] hence accurate detection of such lesions is very important as either false positivity or false negativity can have serious consequences. Dimopoulos *et al.* also highlights the high sensitivity and selectivity of MRI, moreover this imaging technique does not require the use of ionising radiation.

1.2.10.3 FDG-PET and SPECT imaging

Winterbottom and Shaw describe the role of “bone scintigraphy” (imaging agent not specified, probably Tc-99m-labelled methylene diphosphonate, MDP) in MM very briefly: as this imaging modality is osteoblast-specific, its sensitivity in imaging MM is very low hence it is not routinely used in patients with MM. According to this review Tc-99m-sestamibi (MIBI) scans are not too reliable in some regions due to the physiological liver uptake of the imaging agent [40]. *N.B.* Tc-99m-MIBI is not a bone imaging agent, it was originally developed as a myocardial perfusion imaging agent. However it was found that (at least some) MM lesions appear as hot spots on Tc-99m-MIBI scans, *vide infra*.

According to Mulligan and Badros MIBI scans are used for the initial staging of MM in some centres [42]. A number of authors reported on the use of MIBI scans in MM (*e.g.* [43-45]) but none of them compared findings directly to MRI or PET-CT scans; this is what Winterbottom and Shaw pointed out.

In a case study Adams and co-workers found MIBI uptake in MM lesions (confirmed by biopsy) in a patient with wide-spread MM. Interestingly the original

aim of the scan was to image parathyroidal abnormality [43]. In a larger study on 46 patients Balleari *et al.* aimed to determine the sensitivity and accuracy of Tc-99m-MIBI scans in evaluating MM and MGUS [44]. Before the scans patients were staged based on the standard Salmon-Durie criteria. Tc-99m-MIBI scans were acquired 20 minutes post-injection to avoid problems that normal hepatobiliary and bladder uptake could have caused. All patients with MGUS were MIBI negative and an overall sensitivity of 90% and specificity of 88% were found. Moreover the so-called MIBI scores[2] showed good correlation with disease stage and prognosis. This study therefore suggests that Tc-99m-MIBI imaging is a useful tool in management and follow-up of MM. A similar study by Giovanella and co-workers on 30 patients confirmed the above findings: MIBI scans are quite accurate in imaging MM and there is a strong correlation between MIBI scores and prognosis: the higher the MIBI score the poorer the prognosis. They also found that for stage II patients, MIBI score could differentiate (better than the classical staging) patients with good outcome from those with poor prognoses [45].

In a series of papers from the early 2000's Pace and co-workers give a thorough description on the role of MIBI scans and scores in the initial and follow-up imaging of MM [46-48]. In accordance with Koutsikos *et al.* (*vide infra*) they suggest that MIBI positivity is mainly specific to active lesions *i.e.* foci with continuously proliferating MM cells. In their first study 100% of patients with active and relapsed disease presented MIBI positivity (mainly diffuse or focal+diffuse) whereas 70% of the patients with remissive disease were MIBI negative (n_{tot}=39) [46]. In another study the same group carried out *in vitro* uptake experiments on mononuclear cells isolated from the BM of MM patients (n=29) and found a

[2] Scans are scored based on the extension of lesions and the intentsity of uptake. The two scores are then summed to give a MIBI score of 0-7 where 0 means no lesions detected and 7 is the worse prognosis *i.e.* high number of lesions with high Tc-99m-MIBI uptake.

significant positive correlation between *in vitro* uptake of Tc-99m-MIBI and scintigraphic findings [47]. Pace *et al.* also confirm that MIBI positivity/negativity and uptake patterns predict disease stage and prognosis [48] with focal or focal/diffuse pattern suggesting the worst prognosis, diffuse uptake suggesting stable disease and negative scans clearly indicating remission.

Koutsikos and co-workers recently reported on the combined use of MIBI and pentavalent Tc-99m labelled dimercaptosuccinic acid (DMSA) in imaging MM [49]. They identified a large number of MIBI positive (quoted as active, referring to MM cell proliferation and activity) lesions in patients with active disease and a large number of pentavalent DMSA positive (but not MIBI positive) lesions in patients in remission ("inactive lesions", referring to "resting" lesions that are not growing and possibly undergoing apoptosis). In the group of patients with active MM the total number of positive (either DMSA or MIBI positive or both) lesions was 58; 16 of these were uniquely DMSA positive. In the patient cohort with remissive disease the total number of positive lesions was 27 and 22 of these were DMSA positive only. Koutsikos and co-workers also reported that in patients treated with high-dose chemotherapy MIBI positive lesions disappear and become DMSA positive. As confirmed by MRI DMSA positive lesions are not necessarily viable: some of them are partially necrotic but still take up DMSA. Therefore pentavalent DMSA is taken up by active and non-active MM lesions whilst MIBI preferably accumulates in active lesions only. *N.B.* El-Shirbiny and co-workers recently reported on MIBI accumulation in both active and inactive MM lesions in a patient whilst FDG was taken up in active sites only [50].

In their recent review Dimopoulos and co-workers from the International Myeloma Working Group confirmed the high sensitivity and specificity of MIBI

scans in MM (~92 and 96% respectively) [41]. More importantly they mention that MIBI scans are *always* negative in MGUS patients. Based on the studies cited above we can conclude that MIBI uptake is a reliable marker of MM. However as Dimopoulos *et al.* pointed out the reliability of MIBI scans is compromised in detecting spinal and pelvic lesions [41].

In a recent study, mice bearing myeloma xenografts were infected intravenously or intratumorally with virus vectors encoding the sodium iodide symporter (NIS) gene and imaged with I-123 [51]. Interestingly even the infection itself (using an oncolytic virus) could significantly increase the survival of the animals and decrease tumour volumes by ~60%. When I-131 (suitable for imaging and therapy) was administered 90% decrease in tumour volumes was observed. Route of viral infection did not make major differences in survival times.

PET/CT imaging using F-18-FDG has been shown to be the most sensitive method in detecting MM lesions with a sensitivity of around 90% (85% for F-18-FDG-PET, 83% for MRI, 70% for CT and only 45-50% for X-ray). On the other hand this imaging modality is currently not widely-available, expensive and a combined PET/CT scan results in an effective radiation dose of 15-20 mSv [40, 41]. Mulligan and Badros also suggest that PET-CT imaging is superior to MRI in imaging MM, but due to its very high cost they do not recommend its routine use in initial imaging of patients with MM [42].

In a recent report Durie and colleagues summarised their findings in 66 MM patients examined by F-18-FDG-PET [52]. All the patients with stable MGUS had negative PET scans and no false negative results were found. Thus, F-18-FDG-PET could be useful in differentiating patients with MGUS from those with active MM. F-18-FDG-PET can also help in staging or restaging patients.

Schirrmeister and co-workers suggest that F-18-FDG-PET (without CT!) has a very high (>90%) sensitivity in imaging both focal and diffuse lesions (can be lower in patients with remissive disease) and that the only disadvantage of F-18-FDG-PET is that it is unable to detect or predict fracture risk [53] (combined F-18-FDG-PET/CT can do so).

Comparing F-18-FDG-PET/CT, Tc-99m-MIBI and MRI (spinal and pelvic regions only) Fonti *et al.* found MRI to be inferior to the radionuclide imaging techniques [54]. F-18-FDG-PET/CT was more efficient even in the spinal and pelvic regions, identifying 50% more focal lesions than MRI. Unlike many other clinical studies this paper only evaluated previously untreated patients (n=30). Therefore findings represent the efficiency of the above techniques in the primary detection of MM. The cited study reminds us that there is no “magic tool” to reliably image MM, as F-18-FDG-PET/CT was only superior to the other two techniques (MRI and MIBI scans) in imaging focal lesions and was found to be inferior in imaging diffuse MM.

Conflicting with the results of Fonti and colleagues, Nanni and co-workers recently demonstrated that MRI was more sensitive in detecting spinal lesions (especially small lesions) than F-18-FDG-PET/CT [55].

1.2.10.4 Novel PET imaging agents

F-18-3'-fluoro-3'-deoxy-L-thymidine (FLT), a novel PET imaging agent that is putatively more cancer specific (than F-18-FDG) was evaluated in a small group of patients with haematological diseases in a recent study [56]. Although only two of the 18 patients suffered from MM and therefore findings are far from being representative, it is worth mentioning that Agool and colleagues found lower BM uptake in MM patients than in healthy controls. They explain this phenomenon by the cyclic behaviour of MM. Unfortunately Ki-67 staining was only carried out on a

subgroup of samples, excluding those obtained from patients with MM. Also no clinical data were provided regarding the status of patients. On the other hand according to a recent review, due to the higher proliferative activity, F-18-FLT-PET may be useful in assessing BM activity after transplantation [57].

In the past 1-2 years several groups published studies and case reports on the use of C-11 based imaging agents in imaging MM bone lesions. Only a small number of (preliminary) studies have been published so far but we should not forget that C-11 based amino acids and small molecules are just about to become routinely used in clinical centres and may be the next generation of PET radiopharmaceuticals.

Nanni *et al.* compared C-11-choline to F-18-FDG-PET/CT in assessing myeloma bone disease (n=10) [58]. C-11-choline scans detected 37 lesions while F-18-FDG scans could identify only 22. In two of the patients C-11-choline detected many more (8 *vs*. 1 and 10 *vs.* 2) lesions than F-18-FDG (no explanation for this finding). The mean maximal standardised uptake value (SUV) was significantly higher for C-11 choline than F-18-FDG (5 *vs.* 3.8). Although this study suggests a higher sensitivity for C-11-choline its physiological liver uptake hinders the detection of liver and possibly vertebral lesions.

Dankerl *et al.* assessed the tumour targeting properties of C-11-methionine in MM patients (n=19) [59]. The radiotracer identified 45 lesions that were negative by CT. Only 66% of the CT positive lesions turned out to be C-11-methionine positive and this ratio was only 34% in patients who had been treated before imaging. These findings suggest that the C-11 labelled amino acid is highly specific to active MM lesions. A case study by Nishizawa and co-workers confirm the above findings *i.e.* newly formed MM lesions in a heavily pre-treated patient that had been missed by BM aspiration and F-18-FDG-PET were highly C-11-methionine positive [60].

Lee and colleagues report on the potential usefulness of C-11-acetate in the "first report describing the C-11-acetate PET findings of multiple myeloma" (*N.B.* in prostate cancer fatty acid synthesis is responsible for the increased acetate uptake, this may be the case in other malignancies too) [61]. C-11-acetate and F-18-FDG-PET scans were almost identical (see Figure 1.2). C-11 acetate scans were acquired 20 minutes post-injection with no restrictions to the patient whilst F-18-FDG-PET scans were obtained 4 hours post-injection with the usual restrictions *i.e.* fasting is required before the scan and even minimal physical activities are forbidden (that includes chewing) to avoid tracer accumulation in the muscles.

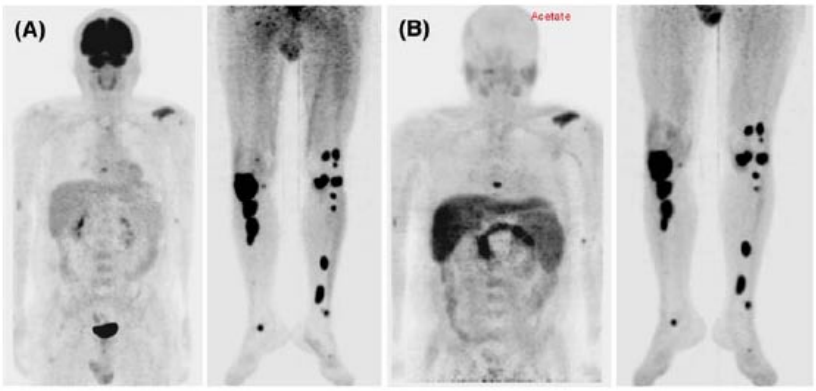

Figure 1.2: F-18-FDG-PET (A) and C-11-acetate-PET scans (B) of a patient with MM. Picture reproduced from [61].

Wadas and co-workers tested a Cu-64-labelled RGD conjugate to image osteolytic bone lesions in a mouse model of spontaneously developing osteolytic tumours [62]. They exploited the finding that osteoclasts express large numbers of the $\alpha_v\beta_3$ integrin. Wadas *et al.* found that this agent is a good and specific marker of increased osteoclastic activity. Response to zoledronic acid (bisphosphonate) therapy was also imaged successfully, resulting in a very significant (~70%) decrease in SUVs. Difference between SUVs in ill and control mice was 2-fold and significant therefore at least in this mouse model the Cu-64-labelled RGD peptide looks to be a reliable marker of osteoclastic bone lesions.

1.2.10.5 Exotic SPECT radionuclides

In the late 1990's Watanabe reported the results of a study comparing Tl-201 and Tc-99m bisphosphonate scintigraphy in imaging myeloma bone disease (n=19) [63]. Although 14 of 19 patients were Tl-201 positive, thallium scintigraphy was "less useful" in 6 of 17 patients and was completely negative in 5 of the 19 patients (only 2 of 19 with MDP). Based on this study Tl-201 scintigraphy should be considered as inferior to Tc-99m-bisphosphonate scans, especially if we take into account its 73h half-life. In 5 patients with diffuse disease Tc-99m-MDP scans failed to image the pattern of the disease (*i.e.* diffuse) whereas Tl-201 scans clearly visualised diffuse lesions. Therefore Tl-201 scintigraphy could be useful in imaging diffuse osteolytic lesions. Ishibashi and co-workers confirm the above conclusion when they report on using Tl-201 scintigraphy to image therapeutic response in a patient with diffuse bone involvement [64].

Edwards and colleagues reported on the use of Sr-89 to treat osteoblastic lesions in MM [65]. Their idea was based on the fact that Sr-89 predominantly accumulates in Tc-99m-MDP positive lesions. A previous Tc-99m-MDP scan revealed a number of positive foci thus they decided to administer the therapeutic radionuclide. Sr-89 therapy resulted in significant improvement in the patient's quality of life.

A phase II study comparing the therapeutic efficacy of high dose melphalan therapy and subsequent syngeneic stem cell transplantation with or without Sm-153-ethylenediamine tetramethylene phosphonate (EDTMP) therapy was recently conducted by Dispenzieri *et al.* [66]. Sm-153-EDTMP is a bone seeking therapeutic radiopharmaceutical that is in clinical use for the palliation of bone pain caused by bone metastases of primary soft tissue tumours. They found that the use of Sm-153-

EDTMP improved the median survival of patients from 4.8 to 6.2 years and that side-effects caused by the radiopharmaceutical were tolerable.

1.2.10.6 Summary

To date a number of imaging modalities and imaging agents have been used to image patients with MM. Despite the rapidly increasing availability of molecular imaging techniques X-ray imaging remains the gold standard in imaging patients with MM. As we reported in sections 1.2.10.2-1.2.10.5 the use of molecular imaging modalities widely varies among centres, but none of the techniques are considered as "standard" imaging techniques for imaging MM (the Durie/Salmon Plus staging system, introduced by the International Myeloma Working Group relies on MRI and F-18-FDG-PET hence one of these techniques might become the new gold standard in the future). In Table 1.3 we summarise the advantages and disadvantages of the most widely used imaging agents and modalities in clinical use to image MM.

Imaging modality	Advantages	Disadvantages
X-ray radiography (whole-body)	low cost high availability "gold standard"	high radiation dose to the patient low spatial resolution medium sensitivity and specificity
CT	low cost high availability whole-body imaging technique high(er) sensitivity and specificity high spatial resolution	radiation dose to the patient anatomical information only
MRI	very high sensitivity and specificity high resolution and soft tissue contrast whole-body imaging available no radiation dose to the patient	high cost low availability individual problems (metal implants, claustrophobia)
F-18-FDG-PET/CT	very high sensitivity and specificity combined anatomical and molecular imaging whole-body imaging technique reliable at imaging focal and diffuse lesions	high cost low availability high radiation dose to the patient special requirements (fasting, no physical activity after injection)
Tc-99m-MIBI (SPECT/CT)	medium cost medium availability high sensitivity and specificity combined anatomical and molecular imaging reliable at diagnosing and staging (MIBI scores)	radiation dose to the patient possible problems in pelvic region (liver uptake)

Table 1.3: Advantages and disadvantages of the most widely used imaging agents and modalities in imaging MM [40, 46-49, 52-55].

1.2.11 Conclusions

MM is an incurable haematological malignancy characterised by the uncontrolled proliferation of malignant plasma cells in the BM resulting in focal or diffuse destruction of the marrow and the bone matrix. Plasma cells secrete an M-protein therefore patients present with elevated serum and/or urine M-protein levels. BM plasma cell counts above 10% and elevated serum M-protein levels together with the usually image based evidence for end-organ damage (usually bone lesions) fulfil the diagnostic criteria for MM.

X-ray imaging still remains the gold standard in diagnosing MM however the role of MRI and radionuclide imaging techniques, especially F-18-FDG-PET/CT recently started to emerge in staging patients with MM. The role of molecular imaging in MM has been recognised by introduction of the Durie/Salmon Plus staging system. Molecular imaging techniques are becoming more widely available and cost-effective thus their role in the diagnosis and follow-up of MM is likely to increase significantly in the next couple of years. For example the fact that MM cells express integrins could make them suitable for imaging with radiolabelled RGD peptides. Some of the currently used imaging agents and modalities, especially F-18-FDG-PET/CT are highly sensitive in most cases however none of them are MM-specific and most of them are not even cancer specific. Therefore developing an imaging agent that is (more) MM specific would be desirable.

1.3 Calcitonin gene peptides, calcitonin receptor and their role in the regulation of osteoclasts

1.3.1 Calcitonin

Calcitonin is a 32 amino-acid peptide hormone. Its structure is shown in Figure 1.3. The sequence between amino acids 1-7 and the disulfide bond is very highly conserved evolutionarily [67]. Calcitonin was discovered by Copp *et al.* in 1962, as a hypocalcaemic hormone of the parathyroid gland in the dog [68]. A few years later its thyroidal origin was reported and confirmed by several independent experiments [69] (a goat model was used as it is possible to isolate the parathyroid from the thyroid in this species). It is now known that (in mammals) calcitonin is the product of the C-cells[3] of the thyroid and the hormone is the main inhibitor of osteoclasts, the cells responsible for the digestion of the bone matrix. A detailed description on the physiological role of calcitonin will be given in sections 1.3.6-8 and 1.4. Evolutionarily, C-cells have ultimobranchial origin; although this had been hypothesised early was only confirmed in 1967 [70].

Normal serum calcitonin levels are in the range of several picograms per millilitre. The hormone is also produced in the central nervous system (CNS), lungs and prostate gland: calcitonin levels in the semen are 10-40-times higher than in the blood [71, 72]. Interestingly, human breast milk also contains high levels of calcitonin even in thyroidectomised subjects suggesting that breast tissue can express calcitonin [73]. Whitehead and co-workers proved that pregnant women have increased levels of plasma calcitonin during the whole period of pregnancy. They

[3] C-cell=”clear cell” referring to the appearance of these cells under the microscope. Others call the cells “light cells” upon their characteristics and say “C” refers to calcitonin secretion.

assumed that the role of elevated levels of the hormone is to counteract the elevated levels of 1,25-diOH-D3 [74].

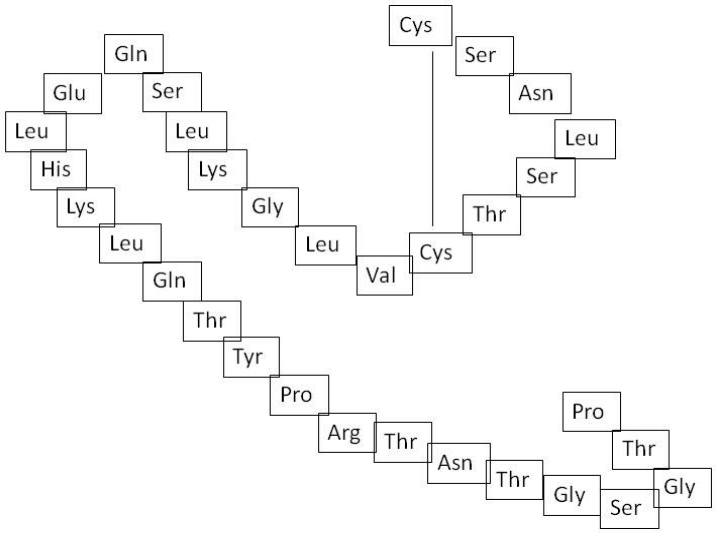

Figure 1.3: Structure of oxidised salmon calcitonin with a disulfide bond between Cys[1] and Cys[7].

1.3.2 Pharmacology and pharmacokinetics of calcitonin

It is important to highlight that salmon calcitonin (sCT) has higher plasma stability than human calcitonin (hCT) and it has much higher affinity to human calcitonin receptor (CTR) than the human peptide [67, 75, 76]. However, at least on human receptors, sCT and hCT stimulate cyclic adenosine monophosphate (cAMP) production with the same potency [76]. Because of the above factors sCT is more widely (if not uniquely) used in *in vivo* and *in vitro* experiments.

In the early 1970's Marx and co-workers confirmed that biological activities of sCT and I-125-iodo-Tyr^{22}-sCT are identical [77] thus the iodinated hormone is a perfect and easily detectable model compound of calcitonin. The pharmacokinetics of calcitonin and its radioiodinated analogue were also published in the 1970's. Human studies suggest high arteriovenous difference for both hCT and sCT hence it can be concluded that kidneys have a key role in the extraction of calcitonin from the blood [78]. Marx and co-workers confirmed this assumption: incubating I-125-iodo-

Tyr^{22}-sCT with renal membrane preparates resulted in degradation and inactivation of the hormone [77]. A set of *in vitro* experiments with rat kidney homogenates confirmed the former findings *i.e.* kidneys are the main place of the metabolism of I-125-iodo-Tyr^{22}-sCT and I-125-iodo-Tyr^{12}-hCT, while I-125-iodo-Tyr^{12}-porcine calcitonin (pCT) seems to be metabolized in the liver [75]. The escape phenomenon (*vide infra*) in the kidneys was also reported by Marx *et al.* as they found that incubating kidney membranes with I-125-iodo-Tyr^{22}-sCT resulted in loss of binding sites.

In the early 80's Epand and co-workers evaluated the secondary structure of calcitonin peptides isolated from different species. They found that hCT is less helical in presence of lipids (and organic solvents) than sCT or pCT and this feature may determine its lower *in vivo* stability [79]. Importantly calcitonin peptides do not have detectable secondary structure in aqueous media as confirmed by circular dichroism [79, 80]. However they do form a helix (roughly between amino acids 8-22) in methanol and more importantly in presence of acidic phospholipids. As a result of the structural change a peptide-phospholipid complex is formed (proven by electron microscopy), where species are bound by ionic interactions. Due to its higher overall charge (+3 at physiological pH) sCT forms more intensive helices than its human counterpart hence it is not surprising that the salmon peptide interacts better with acidic phospholipids. Taking into account that CTRs are membrane receptors the above findings may explain why sCT has much stronger affinity to even human receptors than hCT.

In the 1990's Blower and co-workers evaluated a radioiodinated sCT derivative *i.e.* (I-123-diiodo-Tyr^{22})-sCT in normal mice and patients with Paget's disease [81]. In the mouse 10 minutes post injection 60% of the injected dose

accumulated in the kidneys with moderate uptake in the liver and lungs. Analysis of the urine suggested quick *in vivo* degradation (in agreement with Marx and colleagues [77]) to iodide and diiodotyrosine. Human studies on patients with Paget's disease gave similar results *i.e.* very high kidney and liver uptake with moderate uptake in bones affected by the disease (as confirmed by Tc-99m-MDP scans). Due to the quick *in vivo* breakdown of the iodinated peptide images were very noisy.

1.3.3 Special and unexpected results with calcitonin

Numerous papers have confirmed the inhibitory effect of calcitonin on osteoclasts in the past four decades. However, in the 2000's, quite a few articles reported conflicting data, and some of them were published in journals with very high impact factors.

In 2002, Hoff and co-workers found that deletion of the calcitonin gene in mice resulted in significantly higher bone volume and 1.5-2-fold increase in neonatal bone formation [82]. Moreover, no significant differences in plasma calcium or phosphate levels were detected between the control group and knockout animals. Other aspects of bone metabolism were normal in knockout mice: injection of human parathyroid hormone (PTH) resulted in significant increase of serum calcium levels. The average number of osteoclasts was the same in both groups and osteoclasts remained fully functional in calcitonin gene-deleted mice. As Hoff *et al.* write, unlike thyroidectomy, the gene deletion technique can give unquestionable results as not only the thyroids produce calcitonin in the body. By deleting the calcitonin gene no calcitonin secretion will occur in the subject [82].

By using gene deletion techniques Dacquin *et al.* showed that amylin, another product of the calcitonin gene is the main regulating factor (*i.e.* inhibitor) of

bone resorption and CTRs only control bone formation (but not resorption) [83]: they demonstrated that amylin-deficient mice have a low bone mass phenotype *i.e.* they become osteoporotic in the age of 24 weeks. Dacquin and co-workers also described how amylin affects osteoclasts *i.e.* the peptide inhibits the differentiation and fusion of osteoclasts. Once cells have become fully functional (*i.e.* multinuclear) amylin no longer can influence them in any way.

A recent clinical study highlighted how a single high dose of calcitonin had caused extreme hypercalcemia in a woman with breast cancer [84]. The report also refers to studies from the 1980's that described the hypercalcemic effect of calcitonin in fish and frogs [85, 86]. Other papers from the early 1990's reported on the cell-cycle dependent effect of calcitonin on ion transporters (Na^+/K^+ ATPase and Na^+/H^+ exchanger) [87, 88]: the strong natriuretic effect of calcitonin could only be detected when kidney tubule cells were in S phase: calcitonin could inhibit Na^+ reabsorption by 80% in cells in S phase, whilst no inhibition was found when cells were in G2 phase. Interestingly, these papers have remained forgotten in the past two decades.

To deepen the scientific "conflict", there is a third point of view to mention: some scientists say that calcitonin has no physiological role in the bone. Those who support this point of view argue mainly by the fact that after subtotal or total thyroidectomy the lack of calcitonin does not cause any symptom either in humans or in the rat [67, 89]. On the other hand, as it has been pointed out by *e.g.* Hoff *et al.* [82] not only the thyroids can produce calcitonin hence referring to thyroidectomy as a method for eliminating calcitonin from the body is not very elegant. One should also take into account that total thyroidectomy removes the parathyroids too thus the lack of PTH can counterbalance the putative lack of calcitonin in thyroidectomised subjects.

1.3.4 Calcitonin expression in cancers: abnormal hormone levels

Recent papers have described very rare types of pancreatic and other intestinal tumours that express calcitonin [90-94]. *N.B.* even pancreatic endocrine tumours are quite rare with incidences of around 1-5/1,000,000 [90]. Delis and co-workers described a patient with metastatic pancreatic tumour who, despite not having thyroidal or parathyroidal problems had been diagnosed with a serum calcitonin level of 129 pg/ml (normal range: 0-19 pg/ml) [90]. The study of Wuilmet and co-workers described 32 patients with endocrine tumours of the foregut [91]. Among them, 5 had calcitonin-secreting tumours with serum calcitonin levels as high as 7460 pg/ml. In two of the patients the primary site was the pancreas, in other two the primary site was the stomach whilst the primary site was unknown in one subject. It is also noteworthy that very high serum calcitonin levels cause severe symptoms in patients [91, 92] such as dehydration and hypokalaemia (due to severe diarrhoea) accompanied by hypercalcaemia and hyperphosphataemia.

1.3.5 Products of the calcitonin gene

Zaidi *et al.* [67] and Wimalawansa [95] published very detailed reviews on the chemistry and biology of the calcitonin gene peptide family. This section will summarise their findings.

Calcitonin gene related peptide (CGRP), a 37 amino-acid neuropeptide is an effective vasodilator and neurotransmitter, secreted by perivascular and cardiac nerve termini. It has the same effect in the bone as calcitonin, but only in several hundred times higher concentrations. Therefore it is not considered as a physiological ligand of CTR. A small amount of the peptide is co-secreted with calcitonin by C-cells. The highest density of CGRP receptors can be found in the

cerebellum; CGRP binding sites are also present in the exocrine pancreas, kidneys, bone and adrenal gland.

Amylin is a 37 amino-acid peptide (with human amylin showing only ~15% homology with hCT [95]), secreted by pancreatic cells in the normal pancreas. Amylin has an "anti-insulin" effect and might mimic the vasodilator effect of CGRP. It strongly stimulates glycogen breakdown in skeletal muscles. The peptide and its amide derivative are strong and potent osteoclast inhibitors, amylin amide is only 30-40 times less potent in lowering plasma calcium levels than calcitonin. The effect of amylin and CGRP on osteoclasts cannot completely mimic that of calcitonin though: these peptides only evoke the Q effect (*vide infra*) [96].

In the early 90's Zaidi suggested that the main physiological role of amylin amide is to regulate calcium metabolism (and not carbohydrate metabolism) as, again, the peptide is a very potent osteoclast inhibitor and hypocalcaemic agent [97]: Zaidi's group found that in rats human amylin amide is 44-times less potent in lowering serum calcium levels than hCT. *In vitro* experiments on rat osteoclasts showed that amylin amide is ~75-times less potent in inhibiting osteoclasts than hCT. In a study on patients with Paget's disease (n=8), Wimalawansa and co-workers demonstrated that the hypocalcaemic effect evoked by amylin amide lasted much longer than that caused by hCT [98]. Based on these results it seems that the escape phenomenon (*i.e.* cells becoming refractory to calcitonin, refer to section 1.3.6) does not occur with amylin amide. On the other hand, they also found that patients refractory to hCT (n=4) (those who had been treated for years with calcitonin before) did not respond to hCT (*N.B.* escape phenomenon) or amylin amide either [98].

Adrenomedullin is a 52 amino-acid peptide. It acts as a vasodilator of the pulmonary blood vessels. Although it is a more potent vasodilator than CGRP its effect has a shorter half-life. Since it reduces peripheral vascular resistance, adrenomedullin evokes decrease in peripheral blood pressure.

In 2003 a new peptide, calcitonin receptor stimulating peptide (CRSP) was isolated from porcine brain [99]. The sequence of this peptide (38 amino acid long) has ~60% identity with that of CGRP. Binding of CRSP to CTR results in a 350 times higher stimulus than the binding of sCT. The cited study concluded that CRSP is the physiological ligand for CTRs located in the CNS. Although CRSP is "abundantly" expressed in the CNS and the thyroids CRSP RNA expression has also been detected in the lungs, spleen, liver, small intestine and ovaries [99, 100]. The same year the above group also identified a second and third CRSP subtype in porcine brain (CRSP-2, CRSP-3) [100]. Subtypes show very high similarity with one another: 31 amino acids in the 38 amino acid-long sequence are conserved in every subtype. In addition amino acid sequences around the disulfide bond are highly conserved in the three CRSP subtypes and CGRP as well. Apart from the CNS CRSP-2 was detected in the thyroids whilst CRSP-3 is also present in the lungs and ovaries [100]. The same group identified CRSPs in bovine and canine thyroidal glands and characterised these peptides as well [101].

1.3.6 Calcitonin receptors

By definition calcitonin is the ligand for CTR. CTRs are present on the membrane of osteoclasts in very high densities (~10^6/cell) [67]. The number of CTRs per osteoclast is almost uniquely high: only the number of epidermal growth factor receptors on epidermal carcinoma cells is comparable to that [67]. Osteoclasts are multinuclear bone cells with a haemopoietic origin, they are responsible for the

digestion of organic and inorganic bone matrices (*vide infra*). In certain bone malignancies such as MM the number of osteoclasts can focally increase around the malignant lesion. As a result, CTRs on osteoclasts are potential targets for radionuclide imaging and therapy of osteolytic bone diseases.

However, it seems that the hormone also influences osteoblasts[4], although calcitonin binding sites have not yet been shown to be present on their cell membrane [102]. Beyond the bone, CTRs are present in the kidneys, testicles and CNS. CTRs were also found on the surface of sperm cells and epithelial cells in the prostate [71, 72].

Renal CTRs were first characterised by Marx and co-workers in 1973 [77]. They identified the receptor on luminal and antiluminal membranes as well. Although the number of calcitonin binding sites in the kidneys and organs other than the bone is much lower than in the skeletal matrix (only 5-30000 CTRs/cell), calcitonin (and thus CTR) does have an important role in these tissues too. For example when renal CTRs bind calcitonin the production of 1,25-dihydroxy-cholecalciferol is enhanced [67] which then affects calcium homoeostasis. Renal CTRs also evoke increased sodium-, phosphate- and calcium clearance as calcitonin acts as a regulator of several ion pumps in the tubular membrane.

In a recent study Cafforio *et al.* demonstrated the presence of CTR in (on) human T and B cells [103]. They found that receptors were functional *i.e.* calcitonin had a dose-dependent proliferative effect on these blood cells probably due to the increase of intracellular calcium concentration. Cells were obtained from both healthy volunteers and leukaemia patients. In healthy patients tonsil T and B cells contained higher levels (~7-fold) of CTR messenger RNA (mRNA) than peripherial

[4] Osteoblasts: the cells responsible for bone formation.

T and B cells. Eleven times higher levels of CTR mRNA were detected in B cells from leukaemia patients than in cells isolated from healthy volunteers. Marx and co-workers also reported on the presence of CTRs on cultured T and B cells much earlier (1974) [104].

Intravenously administered calcitonin has been successfully used for pain palliation [67]. Testicular CTRs seem to have a role in spermatogenesis, while calcitonin is also important in the capacitation of sperm cells in the semen [71]. Despite its effectiveness in some cell types it is important to note that calcitonin cannot be used in pharmacological doses for longer periods due to the so-called escape phenomenon: once a high dose of calcitonin has been administered CTRs become reversibly internalized. High calcitonin levels also evoke the down regulation of CTR gene-expression [71, 105]. The number of CTRs on osteoclasts starts to decrease 12-24 hours post-injection of a therapeutic dose of the hormone (100 IU, approximately 20-25 μg) and remains significantly low until higher amounts of calcitonin are present in the circulation [105].

1.3.7 CTR subtypes and receptor activity modifying proteins

Recently a number of groups have started working on the identification of CTR subtypes. Four practically important subtypes (genotypes) of the human calcitonin receptor (hCTR) exist: hCTR1-4; with only a single nucleotide (hence single amino acid) difference between hCTR2 and hCTR3 [106, 107]. A more “significant” difference has been established between hCTR1 and hCTR2: these phenotypes differ in having (hCTR1) or lacking (hCTR2) a 16 amino acid insert in the first intracellular domain of the receptor. Gorn and co-workers found a 10-fold difference between the sCT binding affintity of these subtypes (higher for hCTR1). However sCT evokes a more intensive cAMP response when it binds to hCTR2

[107]. After studying 20 healthy prostate specimens by reverse transciptase PCR (RT-PCR) Wu *et al.* concluded that only the hCTR2 subtype is present in the (healthy) human prostate; this finding may be important in differential diagnosis of normal and malignant tissue samples [72].

The fourth subtype was described and characterised by Albrandt *et al.*; they isolated this isoform from MCF-7 breast cancer cells and also proved its presence in the T47D breast cancer cell line [108]. This isoform lacks the first 47 amino acids of the last (*i.e.* N-terminal) extracellular domain and also lacks the 16 amino acid insert in its first intracellular domain. Tissue distribution studies showed that hCTR4 is present in skeletal muscles, the brain, lungs and kidneys and has the same affinity to sCT as hCTR2 (on the other hand its affinity to amylin is 9-times lower than that of hCTR2).

Recently Beaudreuil and co-workers isolated two new truncated CTR isoforms from T47D cells [109]. These alternative splicing products are truncated from the fourth intracellular domain and one of them is unable to bind sCT either because it has no affinity to the peptide or simply it is not present on the cell membrane. The importance of these isoforms has not yet been fully established however they are not expressed by cultured human osteoclasts and only one of them is proven to be present in the kidneys.

In a study carried out on 152 women Nakamura and co-workers tried to correlate CTR genotypes with physical parameters such as body height, weight and bone mineral density [110]. They established a statistically significant correlation between body weight (normalised to height) and CTR genotype. Reviewing several studies Purdue *et al.* found that even the single amino acid difference in the CTR phenotype may significantly affect bone mineral densities of women [76].

A high amino acid analogy has been found between human and rodent (78%) and human and porcine (67%) receptors [76]. Two isoforms of the rodent receptor (C1a and C1b) have been described, these isoforms differ in the presence of a 37 amino acid insert [76]. According to Nakamura *et al.* the affinity of C1b to its ligand is 6-fold lower than that of C1a (refer to hCTR1 *vs.* hCTR2) [111]. Also, the affinity of hCTR2 and hCTR4 to sCT is the same as that of rat C1a receptors [108].

Receptor activity modifying proteins (RAMP) were discovered in 1998. RAMP subtypes share a 30% homology with each other [112]. These proteins seem to have crucial role in the regulation of CTRs and calcitonin receptor-like receptor (CRLR) [113]. CRLR presents 55% amino acid homology with CTR in humans [76]. As of 2010 three types of RAMPs have been described, all of them modify the basic ligand binding properties of CRLR and CTR. For example, CRLR co-expressed with RAMP1 is a potent receptor for CGRP, while CTR co-expressed with RAMP1 form a potential binding site for amylin [89, 113]. RAMP2 and RAMP3, in conjugation with CTR form other subtypes of amylin and adrenomedullin receptors. The biodistribution of these receptors and receptor-RAMP complexes is not fully characterised yet. According to Granholm and co-workers RAMPs are expressed in a high number of tissues and more importantly their expression is not necessarily accompanied by CTR or CRLR expression [112]. Based on these novel results screening samples for CTR and RAMPs could lead to find more efficient imaging and therapeutic targets *e.g.* in some cases using amylin instead of sCT could potentially improve treatment.

1.3.8 CTR expression in cancers

Some non-bone cancer cell lines express CTRs, for example the MCF-7 and T47D breast cancer cell lines [73, 114, 115]. CTRs in the above cell lines are

functional: calcitonin is a potent inhibitor of cell growth in MCF-7 cells [116]. Greenland found 20-30,000 CTR/cell on MCF-7 cells [114]. Recent studies provided evidence for the presence of CTRs in primary cancer cells too (*vide infra*). The presence of CTR in tumours may give us the opportunity to image and treat non-bone tumour lesions with radiolabelled sCT.

Gillespie and co-workers were the first to describe the presence of CTR in primary breast cancer cells [116]. They studied 18 samples by RT-PCR and amplified CTR mRNA in all of them. Surrounding healthy tissues were CTR negative in every patient. Receptor functionality was not assessed. Wang *et al.* could partially confute the results of Gillespie *et al.* Although they confirm the presence of CTR in primary breast cancer cells (60 samples) Wang and colleagues also give experimental proof for CTR expression in normal breast (ductal) cells [73]. Interestingly they found significant (more than 2-fold) decrease in CTR expression in 44 of 60 malignant samples when compared to levels in healthy controls. They also established correlation between reduced CTR expression and disease outcome: samples with low CTR levels presented higher number and/or more infiltrative metastases than the minority with elevated or unchanged CTR levels. This finding confirms that calcitonin can be a potent inhibitor of cell proliferation. Nakamura and co-workers evaluated the presence of three CTR isoforms in Japanese women (46 breast cancer patients and 50 healthy controls) [117], their results suggest that none of the CTR subtypes predispose to breast cancer.

Several studies suggest that calcitonin and CTR have a great importance in prostate cancer. Regarding the tissue distribution of CTR in the prostate it is noteworthy that both calcitonin and CTR are expressed in the basal epithelium of normal prostate but both ligand and receptor are present in the whole epithelium in

malignant loci. In general, CTR+ prostate cancer cells are more malignant than others *i.e.* they proliferate more rapidly and are more invasive than CTR- ones [118-120]. Sabbisetti and co-workers found that exogenous calcitonin stimulates proliferation and growth of CTR+ prostate cancer cells in nanomolar concentrations. Above 50 nM the stimulatory effect disappears and calcitonin levels above 1 μM significantly inhibit cell growth [118].

Some prostate cancers express both calcitonin and its receptor resulting in a highly effective autocrine stimulatory system [119, 120]. Thomas and co-workers carried out *in vivo* studies to demonstrate the effectiveness of the above phenomenon. Five weeks after inoculation the average tumour mass in mice bearing CTR+/calcitonin+ prostate carcinoma xenografts was 1 g whereas it was only 0.01 g in CTR-/calcitonin+ prostate cancer bearing subjects [120].

1.3.9 Osteoclasts and their role in bone homoeostasis

Osteoclasts are multinuclear bone cells with a haemopoietic origin. They were first described and characterised in the 1800's. Even in those early days it was suggested that osteoclasts are responsible for the resorption of organic and inorganic bone matrices [96]. Osteoclasts (when active) have a characteristic ruffled border surrounded by an organelle-free zone (clear zone) that contains actin-like filaments only. Osteoclast regulators can evoke rapid changes in the form and size of the ruffled border and clear zone. Cells can only become activated if they are in direct contact with the inorganic bone matrix [96].

Only multinuclear (fully differentiated) osteoclasts will be fully functional [96, 121, 122]: if osteoclast precursors are unable to fuse (*i.e.* combination of mononuclear cells to form one multinuclear cell), usually due to congenital lack of crucial molecules such as integrins serious osteopetrosis will occur. According to *in*

vitro studies, cell fusion is not essential for bone resorption, but mononuclear cells are much less capable of resorbing the bone simply due to their physical parameters: a spherical cell model by Ishii and Saeki suggests that the fusion of “n” cells results in √n-fold increase in overall cell surface [122].

Their basolateral membrane is rich in Na^+/H^+ and HCO_3^-/Cl^- exchangers as well as Na^+/K^+ pumps. Intensive proton secretion makes osteoclasts capable of digesting the inorganic bone matrix. An ion channel (the so-called ClC-7 chloride channel) has a particular physiological importance as this pump helps to prevent quick cellular hyperpolarisation that could be caused by intensive proton efflux that is accompanied by chloride influx. A schematic representation of the osteoclast is shown in Figure 1.4.

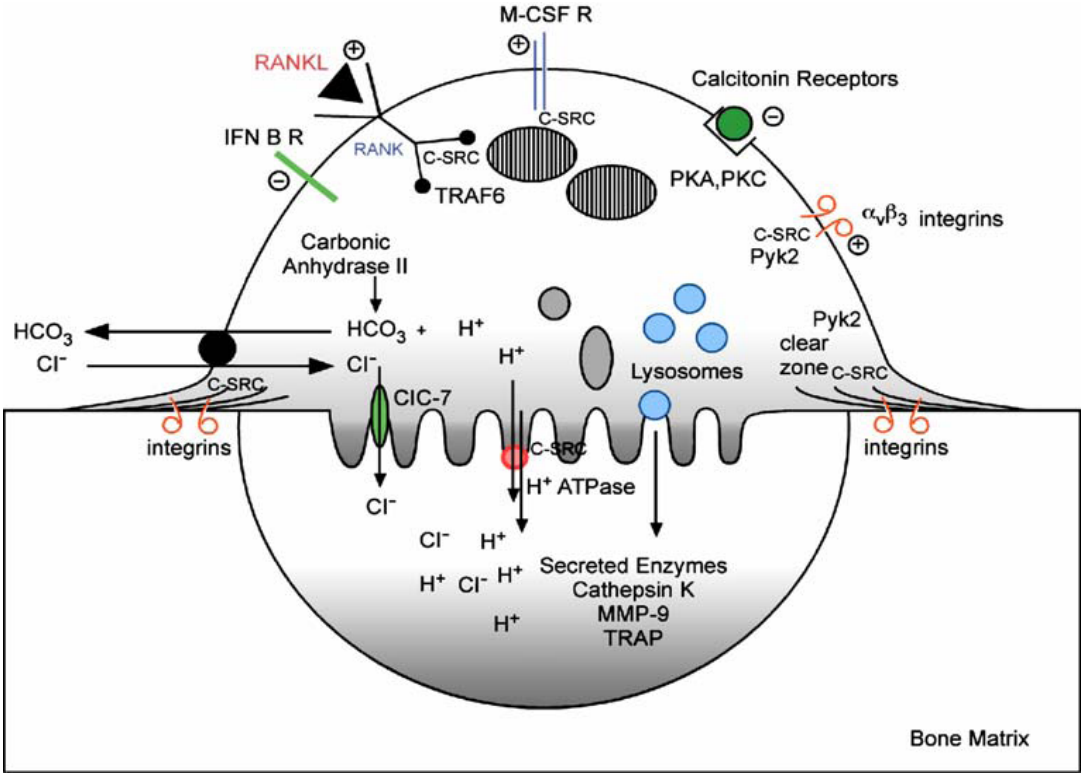

Figure 1.4: A schematic representation of the osteoclast. Figure reproduced from [121].

Proton secretion follows a mechanism similar to what had been described in lysosomal and gastrointestinal membranes. Protons are produced by intracellular carbonic anhydrase hence the bone resorption process strongly depends upon CO_2 concentration. The presence of carbonic anhydrase is crucial for physiological bone homoeostasis; its absence is associated with osteopetrosis. Experimental inhibition of carbonic anhydrase also results in inhibited bone resorptive activity.

The organic (*i.e.* collagenic) bone matrix will not hydrolyse at the acidic pH generated by proton efflux from osteoclasts. Lysosomal enzymes, secreted into the so-called resorptive hemivacuole will digest the collagenic core (a representative member of this enzyme subset is the tartrate resistant acid phosphatase, TRAP). These enzymes “cleave the non-helical extensions of the collagen molecule on the helical side of intermolecular cross-links” [96], resulting in collagen denaturation.

Some leukocytes endocytose other cells or objects for lysis but not the osteoclast: bone resorption mainly happens extracellularly. Some components are taken up for further (intracellular) degradation, whilst others are taken up through the basolateral membrane and secreted via the basal membrane; this phenomenon is called transcytosis. Components left behind by the osteoclast are important precursors in the dynamic equilibrium of bone remodelling [121].

Due to its unique role in bone resorption mutations affecting the osteoclast usually result in serious symptoms. In many (congenital) diseases the osteoclast as well as its BM microenvironment become abnormal hence qualitative evaluation of a BM biopsy specimen can give important diagnostic information in diseases causing osteoclast malfunction [123].

In 1993 Zaidi and co-workers described the morphology and dimensions of osteoclastic excavations on bone slices (rat osteoclasts and bovine bone slices) and used these parameters to develop a potential calcitonin probe [124]. First, a good linear correlation was established between the $(\text{Volume})^{2/3}$ of excavations and the surface area of excavations. A significant (4-10-fold) difference was established between the total mean resorbed area when osteoclasts were cultured on bone slices in absence or presence of hCT suggesting that hCT strongly inhibited their bone resorptive activity in the experimental system.

1.3.10 Regulation of osteoclasts by calcitonin

The basolateral membrane of osteoclasts is enriched in CTRs (refer to Figure 1.4). Calcitonin has a very strong effect on osteoclasts: when normal or PTH-treated cells are treated with calcitonin they quickly lose their ruffled border and clear zone resulting in the osteoclast becoming physically separated from the bone matrix [121].

To summarise, the effect of calcitonin on the osteoclast consists of two components. The first, called Q-effect[5] with a half-life of 15 minutes slows down osteoclast-motility processes. The effect is mediated via a cholera toxin-sensitive G protein [67, 96]. During the second part (R-effect[6], 27 minutes half-life), significant pseudopodial retraction and extreme cell surface reduction can be observed [67]. The R-effect is mediated via a pertussis toxin-sensitive G protein [67, 96]. The physiological-morphological changes are accompanied by biochemical changes as well: acid hydrolase release, Na^+-K^+ ATPase and carbonic anhydrase activities all become decreased (*i.e.* resorption inhibition) [67, 96, 105]. Yumita and co-workers qualitatively demonstrated how (salmon) calcitonin, even in low concentrations influences TRAP activity in rat osteoclasts [125]. In the first step (first 2 hours) enzyme activity elevated intracellularly and only began to decrease thereafter. Dose-response curves suggested that the effect of sCT was detectable from as low as 10^{-16} M *in vitro* (EC50=8×10^{-14} M). The above results of Yumita and co-workers therefore suggest that calcitonin has a dual effect on osteoclastic TRAP: first, it promptly inhibits TRAP release from cells (probably due to the peptide affecting cytoskeletal activities). Then, on a longer term, it also inhibits enzyme expression.

Calcitonin is capable of inhibiting osteoclasts in *in vitro* cultures suggesting that the hormone has a direct effect on these cells (even femtomolar concentrations of calcitonin influence cells *in vitro, vide supra*) [96]. It might be important to note that in the 1980's some studies found that calcitonin did not have any effect on avian osteoclasts as those cells do not express CTR; others however found the opposite [96].

[5] The name Q-effect refers to "quiescene"
[6] R-effect refers to "retraction".

Calcitonin can delay apoptosis in (rat) osteoclasts [126]. Selander and co-workers cultured rat osteoclasts on bone slices and glass coverslips [126]. Apoptotic index (defined as percentage of morphologically apoptotic cells) on glass coverslips was much higher than on bone slices (21 *vs.* 3%). However when 10 nM eel calcitonin were added to the culture media a siginificant (up to 80%) decrease was observed in apoptotic indexes in both types of cultures. On the other hand, when cells were treated with clodronate, the addition of calcitonin to the medium did not change apoptotic indexes. The above observation suggests that calcitonin can delay the physiological (natural) but not the pharmacologically induced apoptosis of osteoclasts. Based on these results the existence of different apoptotic pathways can also be assumed [126]. While characterising the apoptotic pathway that osteoclasts undergo when treated with bisphosphonates, Selander and co-workers found that bisphosphonate-induced apoptosis cannot be completely inhibited by anti-apoptotic agents [127]. Their study found that no difference can be established between clodronate-induced and “physiological” apoptosis based on morphological changes (monitored by transmission electron microscopy (TEM)). This finding does not exclude the existence of different biochemical pathways.

Ikegame and co-workers described the effect of calcitonin on the development of osteoclast progenitors [128]. In the first set of experiments, progenitors isolated freshly from mouse BM were treated daily with 0.1 nM sCT. Results suggested that treated cells were developing at the same rate as control cultures and were indistinguishable from controls upon morphological features. However, the mean number of nuclei per multinucleated cell was significantly lower (~5 *vs.* ~7) in treated cultures than in control cells suggesting that sCT had delayed the fusion of osteoclast precursors. CTR expression was significantly suppressed in

treated cultures when compared to untreated ones but interestingly TRAP expression did not change significantly. Though not expressing CTR, treated osteoclasts remained fully functional based on bone resorption studies. In the second set of experiments, cells were cultured for 6 days without any treatment (fully differentiated osteoclasts by this time). On day 6 they were treated with 0.1 nM of sCT. Six hours after the addition of sCT the number of CTRs became markedly reduced (reached its absolute minimum at 24 hours time and the effect lasted for 72 hours).

A recent study by Granholm and co-workers assessed the importance of cytokines and other humoral factors on CTR and CRLR-RAMP expression [112]. They found that mouse BM macrophages treated with only macrophage colony stimulating factor (M-CSF) expressed CRLR mRNA and the mRNA of all three subtypes of RAMP but did not express CTR mRNA. When BM macrophages were treated with M-CSF and receptor activator of nuclear factor kappa-B ligand (RANKL) they expressed CTR, CRLR, RAMP2 and RAMP3 mRNA whilst RAMP1 mRNA expression became down-regulated. Immunostaining followed by fluorescence-activated cell sorting (FACS) analyses confirmed the presence of the above proteins on the cell membrane. CTR expression was detected 48-72 hours after M-CSF and RANKL had been added to the culture medium. In cells treated with M-CSF only, neither calcitonin nor CRSP evoke a cAMP signal (*N.B.* CGRP, adrenomedullin and amylin did), whilst in M-CSF-RANKL treated cells all the above peptides did so. Interestingly not only calcitonin (in 1 nM concentration) but all the above mentioned peptides inhibited CTR mRNA expression in the cells, in 1000-fold higher concentration though.

Beaudreuil and co-workers found that calcitonin is a very important physiological factor in maintaining postmenopausal bone matrix density [129]. They compared CTR mRNA levels in PBMCs obtained from healthy pre- and postmenopausal and osteoporotic postmenopausal women (obtaining osteoclasts directly would not have been feasible). After analysing a relatively large number of samples (n=59) they found a 5-fold (statistically significant) difference in CTR mRNA levels between healthy and osteoporotic subjects with no difference between healthy pre- and postmenopausal women.

1.3.11 Other osteoclast regulators

RANKL is proven to be an effective activator of osteoclast formation and function. This protein is expressed and secreted by osteoblasts and BM stromal cells. RANKL is an essential factor for functional osteoclast formation. The ligand also stimulates CTR expression. Another crucial factor in osteoclast formation is M-CSF. This agent influences cells in multiple ways: it stimulates receptor activator of nuclear factor kappa-B (RANK) expression in osteoclast precursors and its membrane bound form directly affects osteoclast differentiation. This cytokine is also able to inhibit osteoclast apoptosis [130].

Interleukins (IL-1, IL-6, IL-11) represent an important group of osteoclast stimulators with IL-1 being the “most potent peptide stimulator of *in vitro* bone resorption” [130]. Currently interferons are subject to controversies regarding their role in osteoclast regulation as they seem to act differently *in vivo* and *in vitro*. *In vitro* studies with interferon γ show that the compound is an inhibitor of bone resorption. Intraperitoneal injection of the agent in rats induced osteopaenia in one study; whilst its administration to osteopetrotic patients stimulated bone resorption [130].

The high local Ca^{2+} concentration (*i.e.* 8-20 mM) that osteoclasts generate whilst resorbing the bone directly influences their activity: changing (either increasing or decreasing) the extracellular Ca^{2+} concentration evokes immediate increase in intracellular Ca^{2+} levels resulting in inhibition of cellular activity [96]. *N.B.* avian osteoclasts do differ from mammalian ones. A study on quail osteoclasts found that freshly isolated cells did not respond to elevation of Ca^{2+} levels (up to 20 mM) and only responded moderately to ionomycin [131]. On the other hand rat osteoclasts presented a significant increase in intracellular Ca^{2+} levels in both the above cases in an earlier study [132]. Bascal and co-workers concluded that rat osteoclasts express a putative Ca-receptor whilst avian cells lack it [132]. When the same quail cells were cultured for ~1 week in moderately calcium supplemented medium ($[Ca^{2+}]$=2mM) they presented the same response to changes in extracellular calcium levels as did rodent cells [131]. These data suggest that expression of the putative Ca-receptor or sensor in osteoclasts is down-regulated by high calcium levels (*N.B.* quails used in this study were egg laying hens with high bone turnover). Shankar and co-workers identified both intra- and extracellular sources responsible for the calcium-induced elevation of intracellular (cytosolic) calcium levels [133]. They found that ionomycin induced a sharp 18-fold elevation of cytosolic calcium levels even in the complete absence of free extracellular Ca^{2+} indicating that osteoclasts have a large intracellular Ca^{2+} stock [133].

Bax *et al.* found that Ni^{2+} has the same but even more intensive effect on (rat) osteoclasts as Ca^{2+} [134]: 5 mM of Ni^{2+} evoked a 6-fold increase in intracellular Ca^{2+} concentration whilst incubation in 10 mM Ca^{2+} resulted in 3-4-fold increase only. As a result, Ni^{2+} effectively inhibited osteoclastic bone resorption [134] (morphological and functional examinations confirmed that 5 mM of Ni^{2+} was not toxic to the cells).

Moonga and co-workers proved that perchlorate has an inhibitory effect on osteoclasts both *in vivo* and *in vitro* [135]. *In vivo* the maximum hypocalcaemic effect was reached when 600 μmols of perchlorate were injected in rats resulting in a ~10% decrease in serum Ca^{2+} levels at 20 minutes post-injection. Calcium levels were normal after another 20 minutes.

1.3.12 Calcitonin – can the hormone be used to treat bone diseases?

Due to the fact that calcitonin is a very potent inhibitor of osteoclasts the hormone in high doses has been clinically used since the 1960's to treat several bone diseases, especially Paget's disease of the bone and osteoporosis. High doses of sCT have been clinically used since 1967 although the way the hormone reduced serum calcium levels and skeletal events remained unknown until the late 1970's [136]. The recommended daily dose of sCT for a patient with Paget's disease is 100 IU, corresponding to around 25 μg of the peptide. Long-term treatment makes patients (and their osteoclasts) refractory to calcitonin ("escape") [98]. The most convenient formulations of sCT preparations are nasal drops and sprays (*e.g.* Fortical, Miacalcin), these drugs are licensed in Europe and the US for the treatment of postmenopausal osteoporosis [137]. Injectable formulations of sCT are also available (*e.g.* Calcimar).

1.3.13 Osteoclast-like behaviour of MM cells

Calvani and co-workers demonstrated that some MM cell lines are able to act as functional osteoclasts whilst Silvestris *et al.* pointed out the same in primary MM cells [138, 139]. Calvani *et al.* used FACS to evaluate the presence of CTRs (and other receptors) in cultured adherent U-266 and MCC-2 cells. RT-PCR was applied to determine the expression of H^+-ATPase. Bone resorption assays were also carried

out. CTR positivity was confirmed in both cell lines and in adherent and non-adherent cells too. Over-expression of the receptor was detected in adherent U-266 cells when compared to non-adherent (parental) ones. It was also demonstrated that adherent MM cells resorbed bone slices in a similar manner as do cultured osteoclasts. Cytoskeleton of adherent MM cells presented high similarity to that of cultured osteoclasts.

Silvestris and co-workers studied primary MM cells (n=19) and BM plasma cells of patients with MGUS (n=16) [138]. They found that both primary MM cells and control MM cell lines expressed high levels of CTR whilst MGUS plasma cells expressed only lower levels of the receptor (4-times lower fluorescent intensity when compared to primary MM cells). sCT had no effect on proliferation or apoptosis of MM cells. Bone resorption studies were only carried out on MM cell lines and it was confirmed that sCT had inhibitory effect on this process just like in osteoclasts. These very recent results suggest that any imaging or therapeutic radiopharmaceuticals, targeting CTR would directly target MM lesions not only osteoclasts. It is noteworthy that the mean fluorescent intensity when stained for CTR was approximately 10-fold higher in primary MM cells than MCF-7 breast cancer cells suggesting high receptor levels.

1.3.14 Myeloma bone disease

As we have described earlier MM is characterised by the uncontrolled proliferation of a malignant plasma cell clone in the BM. In the vicinity of malignant foci increased osteoclast activity will occur and this increase is not counterbalanced by osteoblasts [140]. As a result MM patients will present with bone fractures and elevated serum calcium levels. MM cells, osteoblasts and stromal cells produce high levels of osteoclast activating factors *e.g.* RANKL and IL-6 [140]. The above factors

activate existing osteoclasts and also activate the maturation of osteoclast precursors. Therefore, if untreated bone disease becomes more severe with time.

In addition to osteoclast activation in myeloma bone disease studies also suggest that the presence of MM cells induces apoptosis in osteoblasts, this observation would explain the complete lack of bone regeneration in areas surrounding MM lesions [140].

1.3.15 Conclusions

Functional CTRs are expressed in several cancers including MM. A recent study suggests that not only certain MM cell lines but primary MM cells also express CTR and receptor levels are relatively high (although no direct comparison to osteoclasts was made) [138]. In a preliminary cell uptake experiment Greenland found that MCF-7 cells took up a radiolabelled sCT derivative, the Tc-99m labelled sCTLys^{18}-hynic-TFA when compared to an empty well and that uptake could be blocked by a micromolar concentration of calcitonin thus the radiolabelled sCT derivative is likely to be a ligand for CTR (subject to further evaluation) [114]. Based on the data published by Silvestris and co-workers the fluorescent intensity of MCF-7 cells was 10-times lower than that of primary MM cells when stained for CTR [138] therefore the Tc-99m labelled sCTLys^{18}-hynic-TFA and other calcitonin derivatives [115] could be potential imaging agents for MM.

1.4 Summary

MM is an incurable haematological malignancy. None of the imaging agents that are currently used to image patients are fully MM specific, most of them are not even cancer specific. Recent studies suggest that MM cells become fully functional osteoclasts in the bone and therefore express large numbers of CTRs. The ligand for

CTR is calcitonin, a 32-amino acid peptide hormone produced by the C-cells of the thyroid. sCT is proven to be more stable *in vivo* than mammalian calcitonins and has a high affinity to the human receptors. Therefore a radiolabelled sCT derivative is likely to be a useful imaging agent to image osteoclastic lesions in MM (and other CTR+ malignancies). In this thesis we aim to synthesise and evaluate Tc-99m labelled hynic conjugated sCT derivatives as imaging agents for MM and osteoclastic malignancies.

Chapter 2: Synthesis of sCTLys^{18}-hynic-TFA and sCT(8-32)Lys^{18}-hynic-TFA

2.1 Aims

In this chapter we aimed to synthesise, purify and characterise the hynic-conjugated sCT sCTLys^{18}-hynic-TFA and its abbreviated derivative sCT(8-32)Lys^{18}-hynic-TFA that does not include the evolutionarily conserved intramolecular disulfide bond.

2.2 Introduction

In this chapter we aimed to synthesise two hynic-conjugated sCT derivatives for labelling with Tc-99m. Hynic (6-hydrazinonicotinic acid) is an efficient chelator for Tc-99m; a detailed description with radiochemical characterisation will be given in Chapter 8. sCTLys^{18}-hynic-TFA was originally made by Greenland in the early 2000's, he radiolabelled the peptide with Tc-99m and did a preliminary uptake experiment in CTR+ MCF-7 breast cancer cells [114, 115]. We aimed to synthesise the same hynic-peptide, radiolabel it and later evaluate *in vitro* and possibly *in vivo*. Whilst reviewing the literature we found a small number of publications suggesting that abbreviated calcitonin sequences could be biologically active since a weak helical structure formed in the middle region of the sequence between amino acids 8-22 is predominantly responsible for receptor binding [80]. To test this theory we also synthesised an abbreviated hynic-conjugated sCT sequence, that is sCT(8-32)Lys^{18}-hynic-TFA; the sCT sequence without the first seven amino acids (and therefore the intramolecular disulfide loop). The structure of sCTLys^{18}-hynic-TFA is shown in

Figure 2.1. The abbreviated sequence sCT(8-32)Lys^{18}-hynic-TFA is shown in Figure 2.2.

Figure 2.1: The structure of sCTLys^{18}-hynic-TFA. The hynic-TFA moiety highlighted in red.

Figure 2.2: The structure of sCT(8-32)Lys^{18}-hynic-TFA. The hynic-TFA moiety highlighted in red.

2.3 Experimental

2.3.1 Analytical methods

Instruments: High performance liquid chromatography (HPLC) equipment: Agilent 1200 series liquid chromatograph. Mass spectrometer (MS): Agilent 6520 Accurate Mass Q-TOF with dual electrospray ionisation (ESI) ion source. Mass spectra were analysed with Agilent Masshunter Workstation – Qualitative Analysis (Version B.03.01). The same software was used to calculate accurate masses. Isotope distributions were modelled with Agilent Masshunter Workstation – Isotope Distribution Calculator.

HPLC methods: Solvents: “A”: water-0.05% trifluoroacetic acid (TFA); “B”: 70% acetonitrile (MeCN) in water-0.0425% TFA. Method 1: gradient: 0-5 min: 10% B, 5-10 min: rising to 25% B, 10-40 min: rising to 75% B, 40-45 min: rising to 100% B, 45-50 min: 100% B. Equilibration: 50-51 min: falling to 10% B, 51-60 min: 10% B. Flow rate 1 ml/min, λ=214 nm. Column: Vydac Protein&Peptide C18, 4.6×150 mm, particle size 5 µm, pore size 300 Å.

Method 2: gradient: same as for method 1. Flow rate 4.5 ml/min, λ=214 nm. Column: Agilent Eclipse XDB-C18, 9.4×250 mm, particle size 5 µm, pore size 300 Å.

MS: Method M1: 0-5min: 50% B (isocratic direct infusion). Cone voltage: 100 V (positive mode ESI-MS).

Liquid chromatography-mass spectrometry (LC-MS): Method M2: gradient, flow rate, wavelength and column: same as for method 1. Cone voltage: 100V (positive mode ESI-MS).

2.3.2 Peptide synthesis

Peptides were synthesised on solid phase using a Shimadzu PSSM-8 peptide synthesiser and fluorenylmethyloxycarbonyl (Fmoc) amino acids. Syntheses were performed at the University of Kent, Canterbury with the help of Kevin Howland. Resin (NovaSyn TGR, 0.2 mmol/g substitution) and Fmoc-L-amino acids were purchased from NovaBioChem, N,N-dimethylformamide (DMF) was purchased from Rathburn Chemicals. Other chemicals and solvents were purchased from Sigma and used as received. In position 18 a hynic-conjugated Fmoc-lysine (Fmoc-N-ε-(hynic-Boc)-Lysine) was used. For completeness the synthesis of the hynic-conjugated lysine derivative will be reported in Chapter 8.

Syntheses were carried out on a 20 µmol scale (sCTLys^{18}-hynic-TFA) and 10 µmol scale (sCT(8-32)Lys^{18}-hynic-TFA). Fmoc amino acids were used in 10-fold excess except for the hynic conjugated Fmoc-lysine in position 18 which was in 4-5-fold excess to save reagent. In each step amino acids were activated with a mixture of *O*-(Benzotriazol-1-yl)-*N,N,N′,N′*-tetramethyluronium hexafluorophosphate (HBTU), 1-hydroxy-benzotriazole (HOBt), N,N-Diisopropylethylamine (DIEA) in DMF (1:1, 1:1, 2:1 reagent-to-amino acid ratio) and Fmoc groups were removed with 30% piperidine in DMF (45 minutes incubation). Coupling of each amino acid was quenched after 45 minutes by draining the reaction tubes and washing the resin with DMF. After the last coupling step the resin was washed with 3×2 ml of DMF then 5×2 ml of MeOH then dried in air. To cleave the peptides and protect the hydrazine groups with TFA resins were incubated in 2 ml of 95% TFA, 2.5% triisopropylsilane (TIS) and 2.5% water for 6 hours (following the method of Surfraz *et al.* [141] and the recommendations of Kevin Howland). After 6 hours peptides were precipitated in 20 ml of ice-cold ether in Falcon tubes. Peptides were

centrifuged and washed 3 times with 20 ml of ice-cold diethyl-ether. After the last washing step supernatants were discarded and the crude peptides dried in air for a few minutes. Falcon tubes were then sealed and transported to London.

Upon arrival in London the crudes were dissolved in 10 ml of 90% water-10% MeCN, flash frozen on liquid nitrogen and freeze-dried. Before freezing 50 µl of the above solutions were withdrawn for LC-MS analysis. Freeze dried peptides were stored at -80°C until purification.

Before purification crudes were dissolved in 14 ml (full hynic-sCT sequence) or 10 ml (abbreviated sequence) of cold 90% water-0.05% TFA ("A") and 10% (70% MeCN-30% water-0.0425% TFA) ("B"), *i.e.* the initial HPLC conditions. Aliquots (2 ml) were injected in the HPLC and purified using method 2. The stock was kept on ice between injections to minimise peptide degradation and TFA deprotection of the hynic moiety (refer to [114, 115]). Product peaks (as determined by LC-MS analysis of the crude) and depending on the peptide 2-5 other major peaks surrounding the product peak were collected and analysed by MS (full sequence, method M1) or LC-MS (abbreviated sequence, method M2). Fractions were flash-frozen on liquid nitrogen and freeze-dried. Fractions containing the desired product (*i.e.* TFA-protected hynic-peptides, sCTLys^{18}-hynic-TFA and sCT(8-32)Lys^{18}-hynic-TFA) were re-dissolved in 1-2 ml of 90% water-10% MeCN, unified, flash-frozen immediately and freeze-dried again. Before freezing a 20 µl aliquot was withdrawn from the unified product fractions and analysed by LC-MS (method M2) again to confirm purity. We attempted to separate non-TFA protected or deprotected products from protected hynic-calcitonin peptides as much as possible. After the above step the sCT(8-32)Lys^{18}-hynic-TFA peptide was ready to use.

2.3.3 Disulfide bond formation

The purified sCTLys^{18}-hynic-TFA peptide contained free thiol (reduced) groups therefore the disulfide bond had to be formed in the next step. To do so the crude peptide was dissolved in 0.1M NH_4HCO_3 (previously de-oxygenated with nitrogen) at a concentration of 0.1 mg/ml. The solution was kept at 3-5°C and conversion to the oxidised form was meant to be monitored by LC-MS on a daily basis. Due to technical problems daily monitoring could not be carried out, the solution could only be analysed after 7 days. After 7 days the solution was flash-frozen on liquid nitrogen and freeze dried. The freeze-dried product was kept at -80°C.

2.4 Results

2.4.1 Synthesis of sCTLys^{18}-hynic-TFA

The crude contained a high number of different species (Figure 2.3). Every species was analysed by MS, regions 1-3 (as marked in Figure 2.3 with their retention times (RT)) were identified as “useful” products, their mass spectra are shown in Figures 2.4–2.7. Table 2.1 reports the calculated mass of sCTLys^{18}-hynic derivatives. Note that the calculated mass in the table is the mass corresponding to the most abundant (hence not the monoisotopic) isotope peak. Isotope peak distribution of sCTLys^{18}-hynic-TFA is shown in Appendix 1.

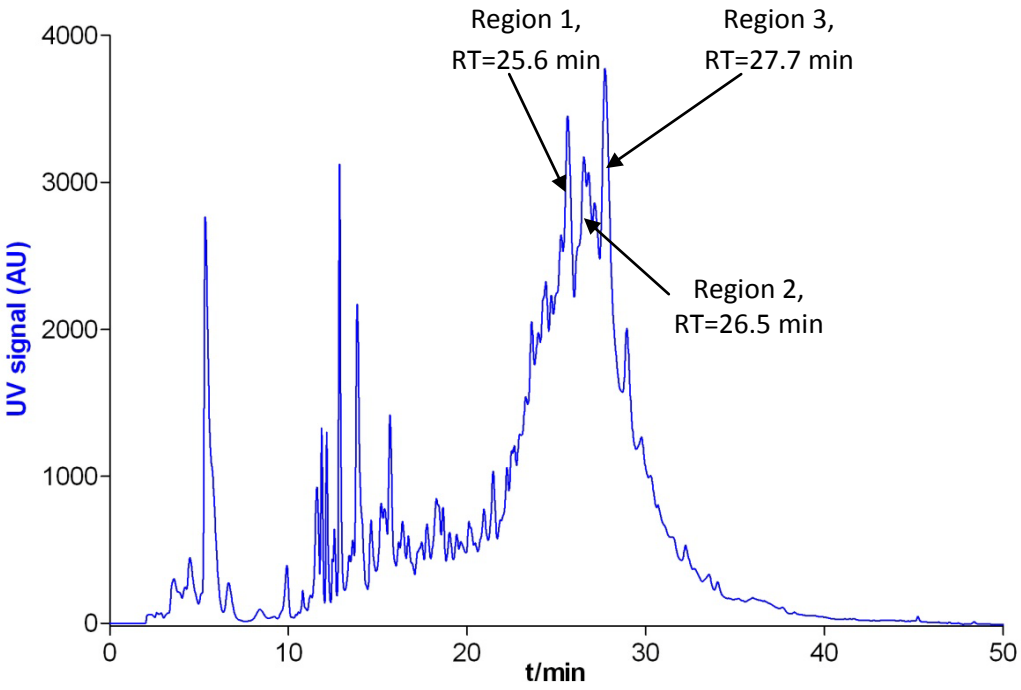

Figure 2.3: HPLC chromatogram of the crude sCTLys^{18}-hynic-TFA peptide.

Compound	Formula	Calc. mass (Da)
reduced sCTLys^{18}-hynic-TFA (1)	$C_{153}H_{246}N_{47}O_{50}S_2F_3$	3664.76
reduced sCTLys^{18}-hynic (2)	$C_{151}H_{247}N_{47}O_{49}S_2$	3568.78
reduced sCTLys^{18}-hynic, $^{\cdot}NH$ loss (3)	$C_{151}H_{246}N_{46}O_{49}S_2$	3553.77
reduced sCTLys^{18}-hynic, $^{\cdot}N_2H_2$ loss (4)	$C_{151}H_{245}N_{45}O_{49}S_2$	3538.76
sCTLys^{18}-hynic-TFA (5)	$C_{153}H_{244}N_{47}O_{50}S_2F_3$	3662.74
sCTLys^{18}-hynic (6)	$C_{151}H_{245}N_{47}O_{49}S_2$	3566.76
sCTLys^{18}-hynic, $^{\cdot}NH$ loss (7)	$C_{151}H_{244}N_{46}O_{49}S_2$	3551.75
sCTLys^{18}-hynic, $^{\cdot}N_2H_2$ loss (8)	$C_{151}H_{243}N_{45}O_{49}S_2$	3536.74

Table 2.1: Calculated masses of compounds detected in crude sCTLys^{18}-hynic-TFA. Masses corresponding to the most abundant isotope peak are shown for consistency with mass spectra.

Figure 2.4: Deconvoluted mass spectrum (abundance *vs.* M) of region 1.

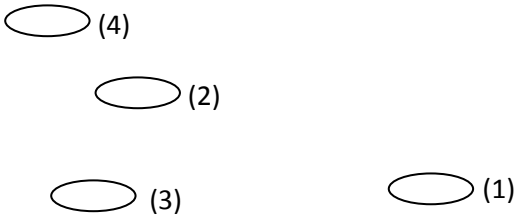

Figure 2.5: Deconvoluted mass spectrum (abundance *vs.* M) of region 2.

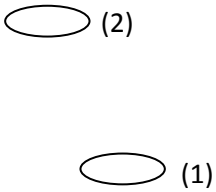

Figure 2.6: Deconvoluted mass spectrum (abundance *vs.* M) of region 3.

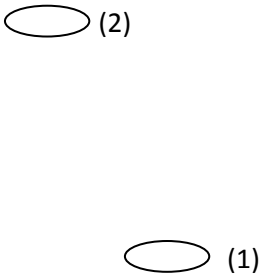

Figure 2.7: Deconvoluted mass spectrum (abundance *vs.* M) of region 3 after a 4 hour-incubation at room temperature.

Mass spectra suggested that region 1 contained the reduced sCTLys^{18}-hynic (Figure 2.4, observed mass 3568.75, calc. mass 3568.78). Region 2 contained a mixture of the reduced sCTLys^{18}-hynic and its degradation products, *i.e.* a de-aminated therefore non-chelating reduced sCTLys^{18}-hynic (Figure 2.5, observed mass 3553.72, calc. mass 3553.77) and a de-hydrazinated derivative (observed mass 3538.73, calc. mass 3538.76) with other, non-identifiable peptides in the mass range of 3400-3500. Region 3 contained a mixture of the reduced sCTLys^{18}-hynic-TFA (Figure 2.6, observed mass 3664.73, calc. mass 3664.76) and reduced sCTLys^{18}-hynic. Upon incubation at room temperature for 4 hours relative abundance of reduced sCTLys^{18}-hynic markedly increased (Figure 2.7). During purification fractions corresponding to the regions highlighted in Figure 2.3 were collected (Fraction 1: 24.8-26.0 min, fraction 2: 26.0-27.3 min, fraction 3: 27.3-28.4 min) and freezed-dried separately. Fraction 1 weighed 2.4 mg, fraction 2 weighed 2.8 mg and fraction 3 weighed 3.3 mg. After the 7 day-incubation in the cold room (disulfide bond formation) fractions 1-2 were analysed by MS (method M1), spectra are shown in Figures 2.8–2.9. Fraction 1 that had been pure reduced sCTLys^{18}-hynic prior to oxidation (Figure 2.4) contained a set of species other than sCTLys^{18}-hynic: peaks representing the (oxidised) degradation products after amine (observed mass 3551.73, calc. mass 3551.75) and hydrazine (observed mass 3536.74, calc. mass 3536.74) loss were even more abundant than the peak representing a protonated sCTLys^{18}-hynic (observed mass 3567.73, calc. mass 3566.76). Fraction 1 also included a minor peak at M=3661.75, a mass corresponding to a deprotonated sCTLys^{18}-hynic-TFA. In fraction 2 (Figure 2.9) de-hydrazinated sCTLys^{18}-hynic was oxidised (observed mass 3536.75, calc. mass 3536.74), the de-aminated peptide was oxidised but seemed to be protonated (observed mass 3552.75, calc. mass

3551.75). Fully oxidised sCTLys[18]-hynic-TFA was also present in the sample (observed mass 3662.76, calc. mass 3662.74).

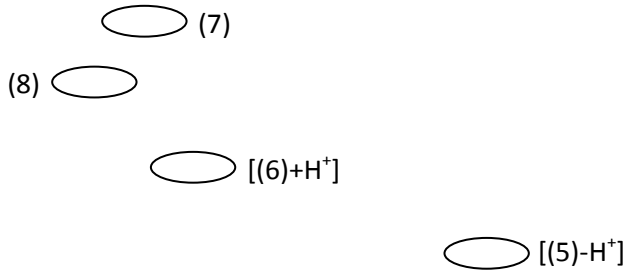

Figure 2.8: Deconvoluted mass spectrum (abundance *vs.* M) of fraction 1 after disulfide bond formation.

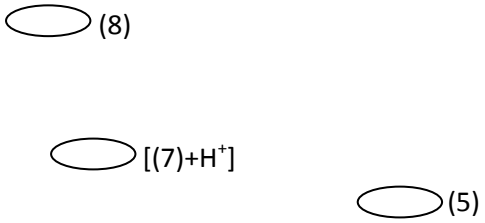

Figure 2.9: Deconvoluted mass spectrum (abundance *vs.* M) of fraction 2 after disulfide bond formation.

Results of the LC-MS analysis of fraction 3 are shown below. Figure 2.10 shows the UV chromatogram of fraction 3, Figure 2.11 highlights the 20-40 minutes region of the chromatogram. Fraction 3 contained four major components after oxidation (represented by regions α-δ in Figure 2.11). Deconvoluted mass spectra of the four regions are shown in Figures 2.12-2.15.

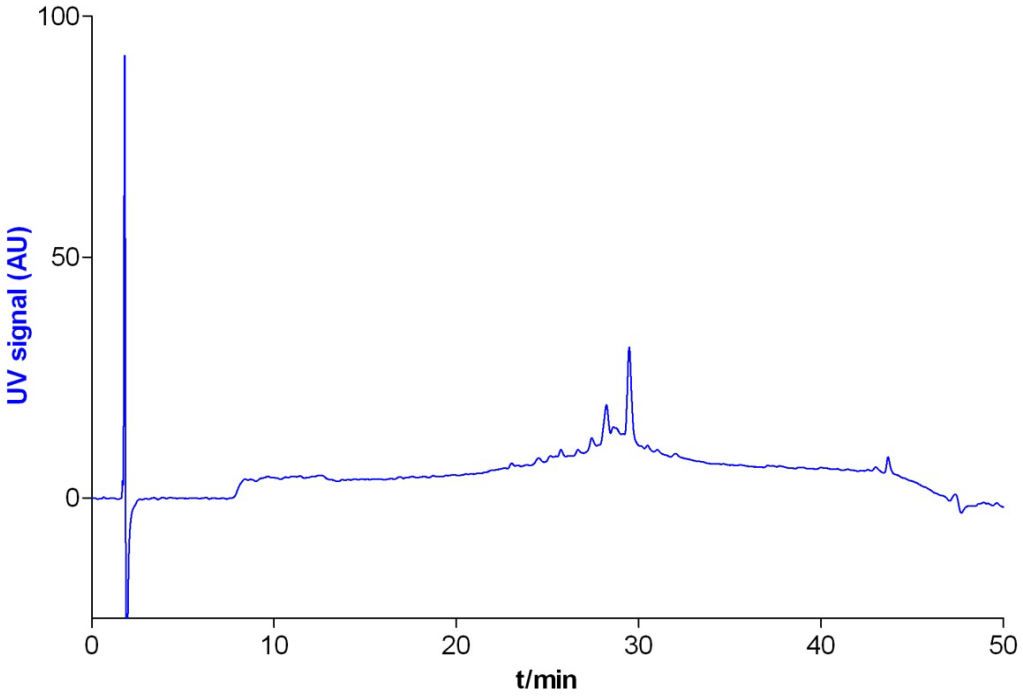

Figure 2.10: UV chromatogram of fraction 3 after disulfide bond formation.

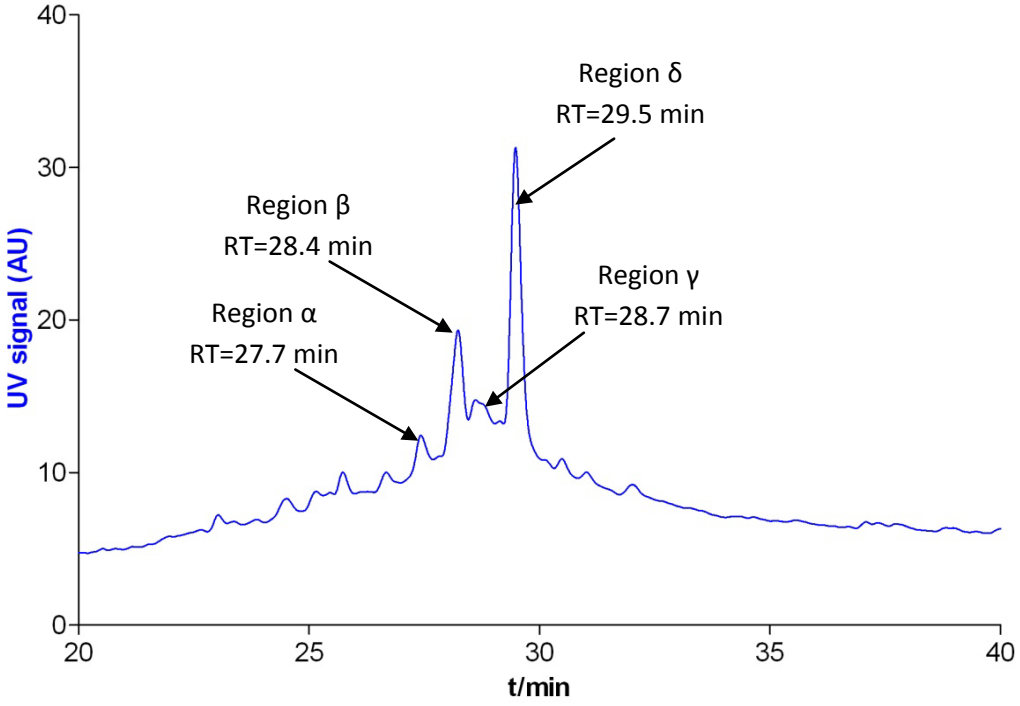

Figure 2.11: UV chromatogram of fraction 3 after disulfide bond formation. The RT=20-40 minutes region highlighted.

Region α (Figure 2.12), a minor part of fraction 3 contained the pure sCTLys[18]-hynic (retention time, RT=27.7 min, observed mass 3566.73, calc. mass

3566.76). Region β (RT=28.4 min, figure 2.13) was a mixture of the de-aminated and de-hydrazinated derivatives and some reduced sCTLys[18]-hynic. Region γ (RT=28.7 min, figure 2.14) contained unidentified by-products at the mass range of 3400-3500 and a protonated oxidised de-aminated sCTLys[18]-hynic derivative (observed mass 3552.69, calc. mass 3551.75). Region δ (RT=29.5 min, figure 2.15) was the largest fraction on the UV trace, this fraction contained the desired product *i.e.* sCTLys[18]-hynic-TFA (observed mass 3662.71, calc. mass 3662.74).

Figure 2.12: Deconvoluted mass spectrum (abundance *vs.* M) of region α.

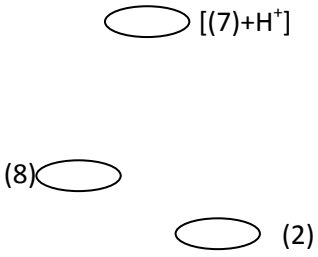

Figure 2.13: Deconvoluted mass spectrum (abundance *vs.* M) of region β.

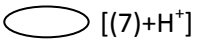

Figure 2.14: Deconvoluted mass spectrum (abundance *vs.* M) of region γ.

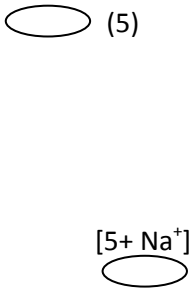

Figure 2.15: Deconvoluted mass spectrum (abundance *vs.* M) of region δ.

Fraction 3 (desired product) was freeze dried without further purification and weighed: m=2.8 mg (0.76 µmol, 3.8% yield).

2.4.2 Synthesis of sCT(8-32)Lys^{18}-hynic-TFA

The UV trace of the crude product is shown in Figure 2.16. The three major constituents (regions 1-3) were highlighted. Mass spectra representing regions 1-3 are shown in Figures 2.17-2.19, Table 2.2 lists the possible relevant species. Mass spectrometry revealed that region 1 (Figure 2.17) represented sCT(8-32)Lys^{18}-hynic (observed mass 2859.53, calc. mass 2859.52). Region 2 included unidentified species with the most abundant species being a compound with M=2752.48 (Figure 2.18). Region 3 represented sCT(8-32)Lys^{18}-hynic-TFA (Figure 2.19, observed mass 2955.51, calc. mass 2955.50) De-aminated or de-hydrazinated degradation products were not detected. Isotope peak distribution of sCT(8-32)Lys^{18}-hynic-TFA is shown in Appendix 2.

During purification three fractions were collected: fraction 1 (18.1-18.6 min), fraction 2 (18.6-20.1 min) and fraction 3 (20.1-20.6 min). Fractions 1 and 3 contained desired (useful) products; these were freeze-dried. Fraction 1 weighed 3.1 mg and fraction 3 weighed 1.9 mg. Yield: 16% (calculated upon the overall 5.0 mg mass of fractions 1 and 3).

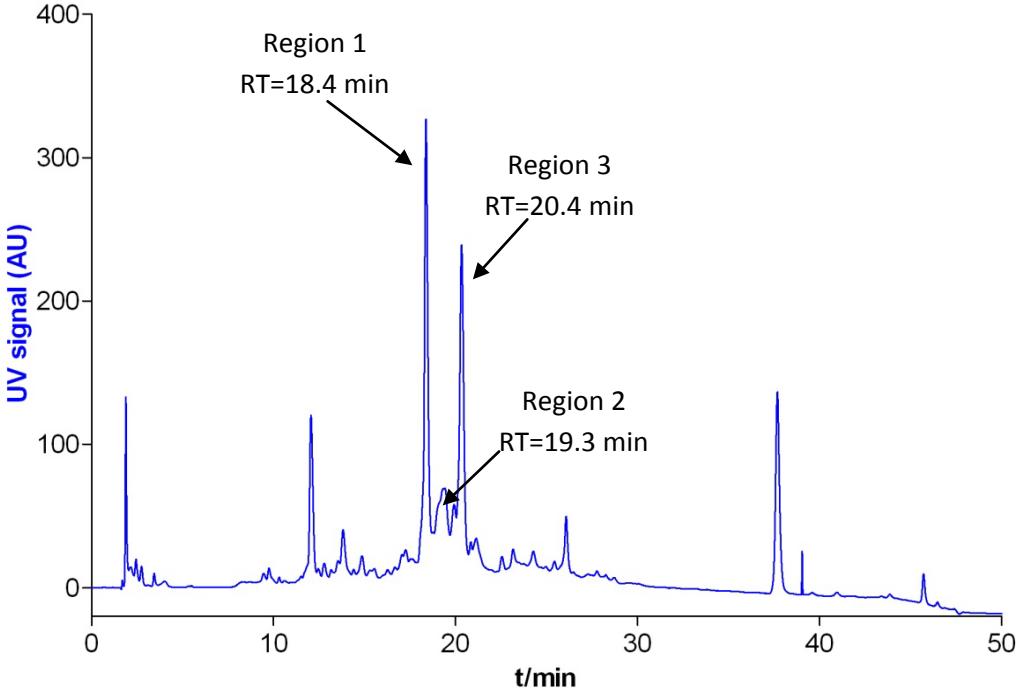

Figure 2.16: UV trace of the crude sCT(8-32)Lys^{18}-hynic-TFA.

Compound	Formula	Calc. mass (Da)
sCT(8-32)Lys^{18}-hynic-TFA (1)	$C_{127}H_{202}N_{39}O_{39}F_3$	2955.50
sCT(8-32)Lys^{18}-hynic (2)	$C_{125}H_{203}N_{39}O_{38}$	2859.52
sCT(8-32)Lys^{18}-hynic, $^{\bullet}NH$ loss (3)	$C_{125}H_{202}N_{38}O_{38}$	2844.51
sCT(8-32)Lys^{18}-hynic, $^{\bullet}N_2H_2$ loss (4)	$C_{125}H_{201}N_{37}O_{38}$	2829.50

Table 2.2: Calculated masses of compounds detected in crude sCT(8-32)Lys^{18}-hynic-TFA. Masses corresponding to the most abundant isotope peak are shown for consistency with mass spectra.

(2)

Figure 2.17: Deconvoluted mass spectrum (abundance *vs.* M) of region 1.

Figure 2.18: Deconvoluted mass spectrum (abundance *vs.* M) of region 2.

Figure 2.19: deconvoluted mass spectrum (abundance *vs.* M) of region 3.

The purified product fractions were re-analysed by LC-MS (method M2) to confirm purity. UV traces (Figures 2.20-2.21) suggest very high purity for both fractions. Fraction 1 contained the pure sCT(8-32)Lys^{18}-hynic, fraction 3 was a mixture of sCT(8-32)Lys^{18}-hynic and sCT(8-32)Lys^{18}-hynic-TFA as confirmed by retention times. For further confirmation mass spectra of the regions are also shown (Figures 2.22-2.23), spectrum of region α is only included once. Region α contained sCT(8-32)Lys^{18}-hynic and its sodium adducts, region β contained sCT(8-32)Lys^{18}-hynic, its sodium and potassium adducts and an unidentified fragment (Figure 2.23, M=2786.43).

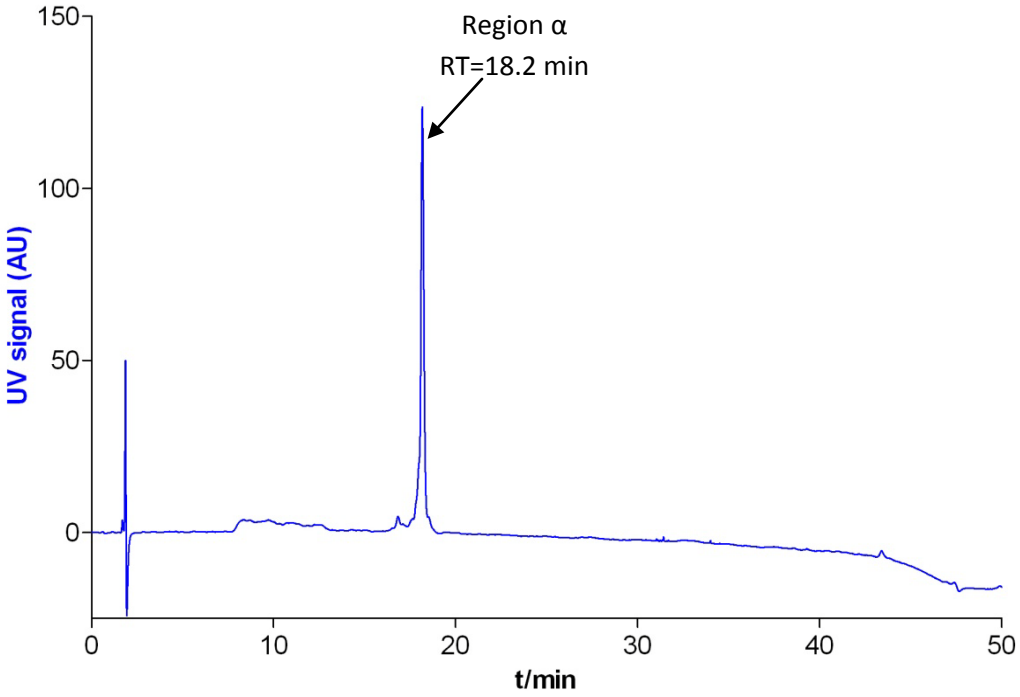

Figure 2.20: UV trace of purified fraction 1.

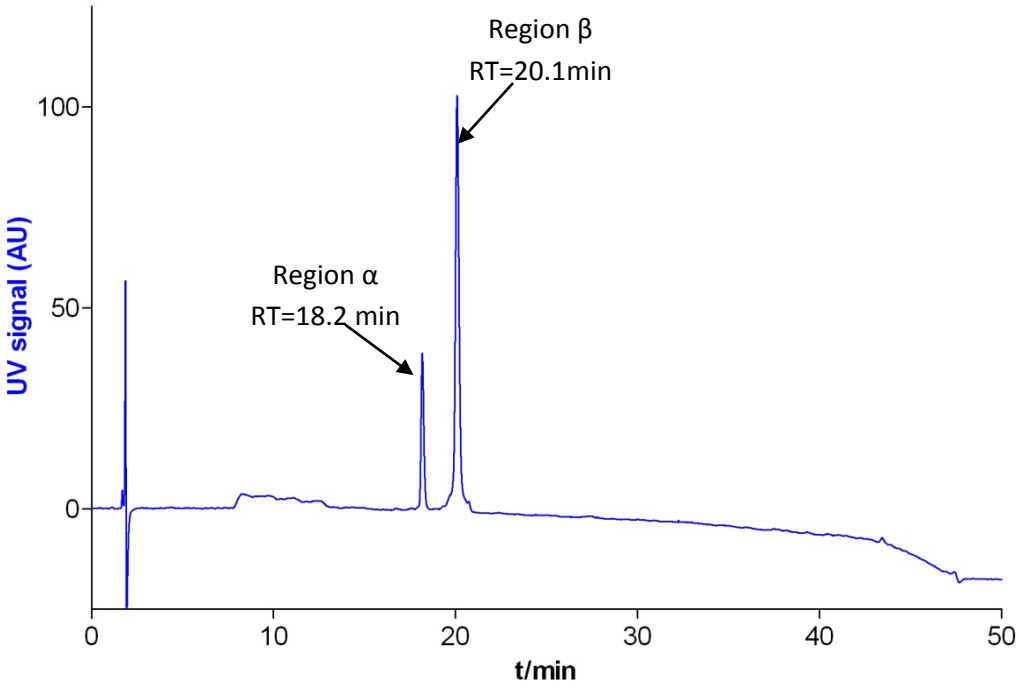

Figure 2.21: UV trace of purified fraction 3.

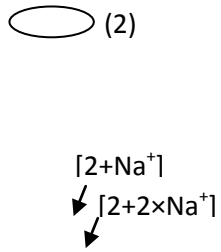

Figure 2.22: Deconvoluted mass spectrum (abundance *vs.* M) of region *α*.

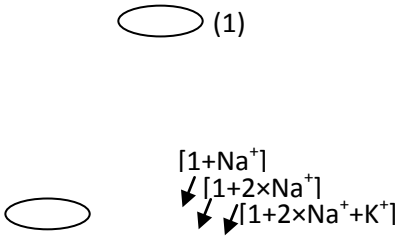

Figure 2.23: Deconvoluted mass spectrum (abundance *vs.* M) of region β.

2.5 Discussion

The synthesis of sCTLys^{18}-hynic-TFA was carried out 3 times. The first two syntheses did not yield enough peptide to radiolabel: after purification the unified reduced product fractions contained <1 mg of the reduced product. After disulfide bond formation no visible amount of peptide was present in the product vials. Results reported above belong to the third synthesis. On the other hand in the same facility using the same reagents synthesis of sCT(8-32)Lys^{18}-hynic-TFA was successful on first attempt with a reasonably good yield (16%). In comparison yield of the first successful synthesis of the full sequence was only 3.8%. Regarding the full sequence containing 32 amino acids (31 peptide bonds) the maximum achievable yield would be 20% if the average conversion was 95% in each coupling step and 53% if the average conversion was 98%. In comparison the maximum achievable yield when making the abbreviated sequence (25 amino acids and 24 peptide bonds)

would be 29% if the average conversion was 95% and 62% assuming 98% conversion.

The crude sCTLys^{18}-hynic-TFA contained a large number of different species. Unfortunately fractions were only analysed by mass spectrometry (not connected to an HPLC) hence quantifying the amount/ratio of different species within fractions would have been difficult. Among other compounds the crude included de-aminated and de-hydrazinated derivatives of sCTLys^{18}-hynic-TFA. In theory these derivatives could be fragments formed in the mass spectrometer however this is unlikely as the mass spectrum of the fraction containing the oxidised sCTLys^{18}-hynic (Figure 2.4) (acquired using the same method) did not contain any of them. In their study on the same hynic-sCT peptide Greenland *et al.* also identified a de-aminated by-product and speculated that it was a result of hynic-peptide degradation rather than fragmentation occurring during the ionisation process [115]. The same LC-MS method did not reveal any de-aminated or de-hydrazinated derivative in the crude or pure sCT(8-32)Lys^{18}-hynic-TFA, this may correlate with the absence of thiol groups in the sequence. To our knowledge no other authors reported on similar degradation processes.

When purifying the crudes we found that the purified TFA-protected fractions contained significant amounts of deprotected hynic-peptide (Figures 2.6 and 2.21). At first glance this finding is a little bit strange as for both sequences there is an approximately 2 minute difference between the RT of the TFA protected and unprotected species. *N.B.* Greenland *et al.* and Surfraz *et al.* found that the TFA-protected hynic-moiety can easily be deprotected under relatively mild acidic conditions (*i.e.* incubation at room temperature in a medium containing 0.1% TFA for 3 h or 1M HCl for 1 h) [115, 141]. In a more recent study Surfraz *et al.* proved

that TFA-deprotection happens under even milder conditions, *i.e.* there is no need to deprotect hynic-peptides prior to radiolabelling, deprotection happens *in situ* during the labelling process and TFA-protected and (previously) deprotected hynic-peptides label identically [142]. Thus, under certain (acidic) conditions the TFA protective group can easily be cleaved in an hour. Therefore, taking into account that the fractions were collected in a solution containing around 0.05% TFA we can argue that at time of collection fractions corresponding to the (reduced) sCTLys^{18}-hynic-TFA and sCT(8-32)Lys^{18}-hynic-TFA only contained the (reduced) sCTLys^{18}-hynic-TFA and sCT(8-32)Lys^{18}-hynic-TFA and the (reduced) sCTLys^{18}-hynic and sCT(8-32)Lys^{18}-hynic were formed whilst the sample was standing at room temperature. To confirm our hypothesis the vial containing a sample of the reduced sCTLys^{18}-hynic-TFA was left in the autosampler of the mass spectrometer and analysed again after 4 hours (Figures 2.6 and 2.7). Results of the second analysis proved the above hypothesis *i.e.* using the same sample and method the relative abundance of the peak corresponding to the deprotected hynic-peptide was much higher than 4 hours before suggesting progression of the deprotection process.

To oxidise the free thiol groups in the reduced sCTLys^{18}-hynic and sCTLys^{18}-hynic-TFA sequences solutions were prepared at low concentration, mild basic pH and kept at low temperature to avoid the formation of peptide oligomers (intermolecular disulfide bond formation) and degradation of the peptide sequence. These conditions were based on Greenland's work ([114, 115]) and discussions with Kevin Howland [143]. Analysis of the fraction previously containing sCTLys^{18}-hynic suggested that the TFA-deprotected species underwent significant degradation (de-amination and de-hydrazination), this phenomenon was also reported by Greenland [115]. We emphasise again that although many other authors have used

hynic peptides with free hydrazine groups to our knowledge no other studies reported on degradation of the hynic moiety thus this phenomenon seems to be unique to the hynic conjugated sCT and is likely to be related to the presence of thiol groups in the sequence. Hynic is usually considered as a fairly stable chelator, the only (long-term) degradation that reduces the shelf-life of hynic-based radiopharmaceuticals is hydrazone formation (as reported by Harris and co-workers [144]).

Based on its UV trace the purified sCTLys^{18}-hynic-TFA (Figure 2.11) was far from being pure. Mass spectrometric analysis identified the major peaks on the chromatogram. Despite using a very resolving gradient most of the peaks were overlapping. Based on the UV trace the region representing the desired product *i.e.* sCTLys^{18}-hynic-TFA was the largest; quantification however could not have led to any major conclusion regarding the purity of the sample due to the quick degradation in solution. At acidic pH and room temperature the TFA protecting group starts to hydrolyse immediately and deprotection completes within a few hours. We also found that in the labelling mixture (at acidic pH and room temperature) deamination of the unprotected hynic moiety completes within 30 minutes (for experimental data refer to Figure 3.13). Taking into account the relatively quick degradation of sCTLys^{18}-hynic and cleavage of the TFA group we should note that the UV spectrum (Figure 2.11) and corresponding mass spectra only reflect the composition of the mixture at the moment when it was injected in the LC-MS instrument, further and non-negligible degradation is likely to have happened to the stock afterwards (*N.B.* we were aiming to freeze and freeze-dry the fraction as quickly as possible but then it had to be reconstituted again to prepare kits for radiolabelling). To summarise, it is not possible to produce highly pure sCTLys^{18}-hynic-TFA.

Considering the above processes and the very low yield of the synthesis sCTLys^{18}-hynic-TFA (represented by the UV trace in Figure 2.11) was aliquoted to kits without further purification. This is not elegant but is a reasonable step to take due to the difficulties in synthesising such a long sequence. Having non-chelating calcitonin derivatives present (at tracer level) should not compromise the *in vitro* or *in vivo* characterisation of the radiolabelled hynic-sCT peptide. For consistency the purified sCT(8-32)Lys^{18}-hynic-TFA was aliquoted to kits, sCT(8-32)Lys^{18}-hynic was kept as a backup.

LC-MS analysis of several samples gave results that were not easy to explain at first glance. A couple of species in the sCTLys^{18}-hynic-TFA samples were detected with a mass 1 Da higher or lower than their theoretical mass (*e.g.* Figures 2.8, 2.13, 2.14). Greenland also recorded similar observations [114]. In addition to deconvoluted spectra we also analysed raw spectra and m/z of ions were consistent with their deconvoluted masses hence it was not the deconvolution algorithm that went wrong.

One may notice that there was a 0.3 min shift in retention times when comparing data obtained for the crude sCT(8-32)Lys^{18}-hynic-TFA and the purified product (Figures 2.16, 2.20, 2.21). Although the same column and gradient were used, measurements were carried out on different days with different batches of solvents and at different room temperatures; these factors may have caused the shifting.

2.6 Determination of peptide content

2.6.1 Materials, methods and calculations

Note: these experiments were carried out after most of the *in vivo* studies had been done. The aim was to find an explanation to the relatively low specific activity of Tc-99m labelled sCTLys^{18}-hynic-TFA (refer to labelling studies, *vide infra*).

Peptide content of sCTLys^{18}-hynic-TFA and sCT(8-32)Lys^{18}-hynic-TFA was evaluated semi-quantitatively *i.e.* the theoretical maximal peptide content was determined. Weighed stocks of freeze-dried sCTLys^{18}-hynic-TFA and sCT(8-32)Lys^{18}-hynic-TFA were dissolved in 90% water-0.05% TFA ("A") and 10% (70% MeCN-30% water-0.0425% TFA) ("B") at a concentration of 1 mg/ml. Note that both peptide stocks had been weighed on the same balance after one another, both stocks were stored in 50 ml Falcon tubes.

HPLC analysis: peptide stock solutions were stored on ice. 20 µl were injected in an HPLC (method 1), UV spectrum acquired at 214 nm, a wavelength highly specific to peptide bonds. Both peptides were analysed 3 times in total. An acetyl-sCT standard with known peptide content (Sigma SCP0059, lot ME0812, 97% purity (α) and 82% peptide content(β)) was also analysed and used as a basis of comparison. The stock containing 1 mg of solid material in a septum-sealed glass vial was dissolved in 1000 µl of 90% A-10% B and analysed the same way as the hynic-peptides.

UV chromatograms were integrated and average area under the curve (AUC) calculated for all three peptides ( ). When analysing the data the following simplifications were made: sCT is a large peptide with a low number of aromatic side-chains hence mostly the peptide bonds contribute to its extinction coefficient at 214 nm. Hynic peptides have a non-natural aromatic side chain that will affect their

extinction coefficient which we did not account for (*N.B.* the sequence is long therefore the above effect should not be very significant). Hynic is conjugated to the ε-amine group of lysine-18 via an isopeptide bond which we accounted for.

Peptide content of the hynic-peptides was then calculated as follows: if $\varepsilon_{s,214}$ is the absorption of 1 nmol of peptide bonds in the acetyl-sCT standard it can be calculated as $\frac{\varepsilon_{s,214}}{N}$ where "N" is the number of peptide bonds in the molecule (calculated), "n" is the nominal number of moles in nmol calculated as the fraction of the injected mass (20 ng) and the molecular weight in units of ng/nmol; α_s is the peptide content (known) of the standard and β_s is the purity of the standard (known). An analogous equation can be drawn for the sCTLys^{18}-hynic-TFA and sCT(8-32)Lys^{18}-hynic-TFA peptides. The number of peptide bonds in each peptide and the number of moles can be calculated; the only unknown will then be the $\alpha_h \cdot \beta_h$ product. The purity could be determined based on the UV trace however due to the presence of multiple species and the quick degradation we decided not to do so. It is safer to use the $\alpha_h \cdot \beta_h$ product and it is fit for our purpose (*i.e.* to determine the actual amount of hynic-peptides). *N.B.* due to the presence of non-hynic peptide impurities the α factor will be overestimated thus what we will determine is in fact the highest possible value of the above product; the actual hynic-peptide content will be lower. Assuming that the absorption of 1 nmol of peptide bonds in the hynic-sCT peptides equals to that in the acetyl-sCT standard $\alpha_h \cdot \beta_h$ can easily be calculated for both the sCTLys^{18}-hynic-TFA and sCT(8-32)Lys^{18}-hynic-TFA.

2.6.2 Results

The absorbance of 1 nmol peptide bond at 214 nm, based on the acetyl-sCT standard: $\varepsilon_{s,214}$=114.73 nmol^{-1}. $\alpha \cdot \beta$ values were then calculated for the two hynic peptides (Table 2.3).

compound	AUC	N	n/nmol	$\alpha \cdot \beta$
acetyl-sCT (standard)	16811±677	32	5.76	0.80±0.03
sCTLys^{18}-Hynic-TFA	7184±336	32	5.46	**0.36±0.02**
sCT(8-32)Lys^{18}-Hynic-TFA	13851±619	25	6.76	**0.71±0.03**

Table 2.3: Results of peptide content calculations. AUC is the average AUC (standard error of the mean, SEM) (n=3), N is the number of peptide bonds in the sequence, n/nmol is the nominal amount of peptide injected in each run, $\alpha \cdot \beta$ is the product of the actual purity and peptide content.

2.6.3 Discussion

Based on its UV trace peptide content of the sCTLys^{18}-hynic-TFA is very low, a "10 µg kit" (*vide infra*) contains no more than 3.6 µg sCTLys^{18}-hynic-TFA. Peptide content of the abbreviated hynic-peptide sequence was comparable to that of the calcitonin standard, after purification 10 µg of the purified product contained up to 7.1 µg of sCT(8-32)Lys^{18}-hynic-TFA.

2.7 Preparation of tricine-peptide kits

Pure TFA-protected hynic-calcitonin peptides (Fraction 3 of the sCTLys^{18}-hynic-TFA and fraction 3 of sCT(8-32)Lys^{18}-hynic-TFA) were dissolved in ice-cold 100 mg/ml tricine (N-(2-Hydroxy-1,1-bis(hydroxymethyl)ethyl)glycine, >99% purity) in distilled water (dH_2O) at a concentration of 0.1 mg peptide/ml of buffer. 100 µl aliquots, containing 10 µg of hynic-peptide and 10 mg of tricine were pipetted into polypropylene microcentrifuge tubes that were kept on ice. Tubes were covered with kitchen foil, flash frozen on liquid nitrogen and freeze-dried. After

freeze-drying tubes were sealed and kept at -80°C. The above kits will be referred to as “10 μg kits”.

Several microcentrifuge tubes were prepared with 500 μl of the above solution for Tc-99 labelling (*i.e.* “cold” or “carrier-added”) and subsequent LC-MS analysis (“50 μg kits”).

2.8 Conclusions

The sCTLys^{18}-hynic-TFA is a non-natural peptide-sequence that is very difficult to make. Despite having access to a fully equipped peptide synthesis facility and a very experienced peptide chemist at the University of Kent only one out of three syntheses was successful with a very low yield. The non-TFA protected fraction of the synthesised peptide underwent quick degradation that seems to be unique to this hynic-peptide; this process also compromised the yield. We finally isolated enough of the peptide for radiolabelling and *in vitro* and *in vivo* evaluation. Due to the de-amination and de-hydrazination processes described in this chapter the preparation contained a significant amount of non-chelating fragments. This needs to be borne in mind when analysing radiolabelling data.

The abbreviated peptide is much easier to synthesise and purify than the full hynic-calcitonin sequence. The synthesis (on a non-microwave assisted synthesiser) and purification can be carried out in 3 days whilst taking into account the longer sequence and the time required for disulfide bond formation the synthesis of sCTLys^{18}-hynic-TFA requires at least 11-12 days. The sCT(8-32)Lys^{18}-hynic-TFA sequence behaves as an “ordinary” hynic-peptide *i.e.* it is fairly stable, can be made and purified easily. Taking into account the above factors, the higher stability (no de-amination occuring) and the high achievable purity (strictly a single, narrow and symmetrical peak in the UV trace), if the abbreviated sequence turns out to be

biologically active with an affinity similar to the full hynic-sCT it should clearly be the choice for CTR imaging.

2.9 Summary

We synthesised and purified two hynic conjugated sCT derivatives, sCTLys^{18}-hynic-TFA and sCT(8-32)Lys^{18}-hynic-TFA. Synthesising and purifying the full sequence were challenging due to the quick degradation that takes place at acidic pH; the abbreviated sequence demonstrated higher stability probably due to the lack of a disulfide bond (or thiol groups) in the sequence. We prepared lyophilised kits by freeze-drying aliquots of the hynic-peptides from a concentrated tricine solution. These kits are ready for radiolabelling upon reconstitution and addition of a reducing agent.

Chapter 3: Radiolabelling sCTLys^{18}-hynic-TFA and sCT(8-32)Lys^{18}-hynic-TFA

3.1 Aims

In his thesis and paper Greenland gave a thorough description on how he radiolabelled the sCTLys^{18}-hynic-TFA using tricine as co-ligand and also characterised the labelled species [114, 115]. First we aimed to reproduce his results. After numerous unsuccessful attempts we decided to develop our own labelling protocol.

3.2 Introduction

Figure 3.1: The structure of hynic (a) and the most widely used co-ligands: tricine (b), EDDA (c), nicotinic acid (d); the structure of a hynic-technetium complex with tricine as co-ligand (e).

In this section we summarise the main practical aspects of the chemistry of technetium-hynic complexes. Chapter 8 of this thesis is focussing on hynic, a detailed background on the chelator, the putative structure of its coordination sphere and the characterisation of novel hynic derivatives that helped us to understand structural aspects will be described there.

Hynic (Figure 3.1 a) was first synthesised and used to indirectly radiolabel an antibody in 1990 [145]. Hynic soon turned out to be a very efficient ligand for technetium: Tc-hynic complexes presented high *in vitro* and *in vivo* stability, the chelator was easy to make and functionalise (*e.g.* [145, 146] and refer to [147] for *in vivo* stability). Therefore it was an ideal candidate to conjugate with the sCT sequence for Tc-labelling. To achieve site specificity we made a hynic-conjugated lysine derivative and used that for solid phase synthesis of the peptide (following Greenland's method [114, 115]).

Although hynic binds technetium very strongly it is unable to saturate the octahedral coordination sphere of Tc(V). It either acts as a monodentate ligand or more likely as a bidentate chelator [148-150]. Therefore other ligands, so-called co-ligands are needed to saturate the coordination sphere of the radiometal. These co-ligands are usually weak(er) chelators for Tc (than hynic), *e.g.* glucoheptonate, tricine, ethylenediaminediacetic acid (EDDA), nicotinic acid *etc*. Structures of the most widely used co-ligands and the structure of a Tc-hynic complex with tricine co-ligand are shown in Figure 3.1. It was recognised in the early days that co-ligands can have a substantial effect on the stability and biodistribution of technetium labelled hynic-conjugated peptides and proteins [151]. Since then a large number of studies has focussed on the role of co-ligands in Tc-hynic complexes [148]. In the past decade tricine has been the most widely used co-ligand in Tc-hynic complexes.

It forms hydrophilic complexes (renal extraction) and is easy and convenient to use (*e.g.* not toxic, does not require heating or specific pH, fairly good chelator for Tc and has an active role in the labelling process [148]). Depending on the peptide or protein sequence (*i.e.* the neighbouring side-chains) one or two tricine molecules will fill up the free coordination sites of Tc [115, 152, 153]. Tricine looked to be an ideal co-ligand and Greenland also used it when he radiolabelled sCTLys^{18}-hynic-TFA thus we also decided to use this co-ligand.

The labelling is carried out using a Mo-99/Tc-99m generator eluate that contains Tc-99m-pertechnetate in (sterile) saline. Pertechnetate is a fairly inert anion that would not bind to any chelator. The oxidation state of Tc in pertechnetate is +7. The radiometal has to be reduced to +5 in order to make it capable of undergoing complexation. Free Tc(V) does not exist under normal conditions, it either forms a complex with suitable ligands or gets oxidised back to Tc(VII) (pertechnetate). Thus the radiometal has to be reduced *in situ* in the labelling mixture. Tricine is a weak chelator for Tc-99m and has to be in high excess (compared to the hynic conjugated peptide/protein) to achieve sufficient labelling yields [154]. Thus many authors speculated what was then confirmed by mass spectrometry (see *e.g.* [148, 149, 155]): upon being reduced in a solution containing a large excess (usually milligrams) of tricine the reduced radiometal will form Tc-tricine complexes with a structure of $[(TcO)^{3+}tricine_n\text{-}5H]^{2-}$ (n=1-4) [149, 155]. These complexes are stable in solution and, when a hynic conjugated molecule is added they will radiolabel the hynic moiety with hynic replacing the oxo group and tricine in two binding sites. The formation of these intermediates is probably crucial in order to achieve high labelling yields and avoid the formation of colloidal technetium, *i.e.* a hydroxy-oxo precipitate of the radiometal [154].

Pertechnetate is either reduced by the ligand itself (water soluble phosphines, *e.g.* [156]) or a reducing agent has to be added to the labelling mixture. The most widely used reducing agent used with hynic-conjugated biomolecules is $SnCl_2$. Other possible reducing agents are SnF_2 or $NaBH_4$.

In this chapter we aimed to radiolabel sCTLys^{18}-hynic-TFA and sCT(8-32)Lys^{18}-hynic-TFA with Tc-99m then characterise the labelled species by instant thin layer chromatography (ITLC) and HPLC. Factors affecting labelling yields were also assessed.

3.3 Materials and methods

3.3.1 Materials and analytical methods

Tin(II) chloride dihydrate (Ph Eur, >98%) was purchased from Sigma. 5M HCl was purchased from Fisher and diluted to 0.01M in dH_2O. Water (LC grade) was purchased from Fisher, other solvents and TFA were purchased from Sigma. ^{99m}Tc-TcO_4^- was obtained from the Nuclear Medicine Department at Guy's Hospital.

HPLC and LC-MS instrumentation were described in Chapter 2, section 2.3.1. For gamma detection a LabLogic B-FC-3200 NaI detector was installed after the UV detector of both instruments. UV trace, radioactive counts and total ion chromatograms were co-registered. ITLC analysis was carried out on polysilicic acid gel coated glass microfiber papers (Agilent ITLC-SA, part number A120B12). ITLC strips were developed in saline eluant to check for pertechnetate impurity (routinely performed at the end of radiolabelling experiments) or a mixture of aqueous and organic solvents to check for colloidal impurities (*vide infra*). After developing ITLC strips were evaluated on a LabLogic MINI-SCAN radio TLC linear scanner

connected to a LabLogic B-FC-3200 NaI detector for gamma photon detection. Strips were developed at a speed of 0.25 mm/min.

After radiolabelling mixtures were analysed by HPLC (method 1) or LC-MS (method M2). ITLC-SA strips were developed in saline as mobile phase unless stated otherwise. pH of reaction mixtures was determined by Fisherbrand pH-Fix 0-14 colour fixed indicator sticks followed by a more accurate assessment using Fluka pH-Indicator strips (Range 1.8-3.8 and 3.8-5.5).

To assess the amount of colloidal impurities in labelling mixtures ITLC-SA strips were developed in mixtures of aqueous and organic solvents. The following solvent mixtures were used: different ratios of MeCN in water (from 10 to 90% in 10% increments); 50% acetone-water; 1:1:1, 1:2:2, 1:1:2 and 1:2:1 mixture of saline, acetone and MeCN; different ratios of methanol and 10% NH_4OAc in water (10-90 to 90-10 in 10% increments).

3.3.2 Tc-99m labelling of tricine controls C1-3 and the effect of $SnCl_2$ and pH on the formation of non-soluble radioactive species

In control experiments 44-50 MBq (at time of elution) of $^{99m}Tc\text{-}TcO_4^-$ eluate in 300 µl of saline were added to 10 mg tricine in a microcentrifuge tube. To this mixture 10 µl of freshly prepared 10 (C1), 5 (C2) or 1 (C3) mg/ml $SnCl_2 \cdot 2H_2O$ in 0.01M HCl were added as reducing agent. After a short centrifugation to remove drops from the wall of the microcentrifuge tube the mixture was incubated on a shaker at a constant temperature of 37°C. Mixtures were analysed by ITLC after 30, 60 and 120 minutes and pH of the mixtures was also assessed.

3.3.3 Determination of the ideal labelling time

A "10 µg kit" of sCTLys^{18}-hynic-TFA[7] was labelled with 241 MBq of ^{99m}Tc-TcO_4^- (for labelling protocol refer to section 3.3.4). Samples were withdrawn after 10, 20, 30 and 60 minutes and analysed by ITLC-SA and saline as mobile phase.

3.3.4 Tc-99m labelling of hynic-calcitonin conjugates

To a freeze-dried "10 µg kit" of sCTLys^{18}-hynic-TFA or sCT(8-32)Lys^{18}-hynic-TFA a total volume of 300 µl of saline and high specific activity ^{99m}Tc-TcO_4^- eluate were added. To the above mixture 10 µl freshly-prepared 1 mg/ml $SnCl_2 \cdot 2H_2O$ in 0.01M HCl were added. After a short centrifugation the mixture was incubated on a shaker for 30 minutes at a constant temperature of 37°C. Mixtures were analysed by ITLC-SA/saline and occasionally by HPLC.

3.3.5 Determination of the maximum achievable specific activity

After synthesising the hynic-peptides approximately 30 sCTLys^{18}-hynic-TFA kits were radiolabelled (labelling time 30-35 min) to get used to peptide labelling and to make sure that radiolabelling results are reproducible. sCTLys^{18}-hynic-TFA were labelled with different activities in the range of 50-400 MBq (decay corrected to time of elution; approximately 14-110 MBq/µg of sCTLys^{18}-hynic-TFA) hence we had a good record of activities and corresponding radiochemical purities (RCP). RCP, defined as the area under the product peak divided by the AUC for the whole range of chromatogram was determined by ITLC.

To determine the maximum achievable specific activity when labelling sCT(8-32)Lys^{18}-hynic-TFA kits, kits were labelled with ascending amounts of generator eluate from 100 to 550 MBq (decay corrected to time of elution,

[7] Note that a sCTLys^{18}-hynic-TFA kit contained no more than 3.6 µg of hynic-peptide and a sCT(8-32)Lys^{18}-hynic-TFA kit contained a maximum of 7.1 µg of the abbreviated hynic-sCT sequence.

corresponding to 14-77 MBq/µg of sCT(8-32)Lys^{18}-hynic-TFA) with 50 MBq increments. At the range of 300-500 MBq kits were labelled at least twice on different days to determine reproducibility. RCP was determined by ITLC.

3.3.6 Carrier level labelling of hynic-calcitonin conjugates

To freeze-dried "50 µg kits" containing 50 µg (nominal amount) sCTLys^{18}-hynic-TFA or sCT(8-32)Lys^{18}-hynic-TFA and 50 mg tricine in a screw-cap microcentrifuge tube 200 µl of saline, 50 µl of 0.3 mg/ml $K^{99}TcO_4$ in saline and 10 µl ^{99m}Tc-TcO_4^- eluate were added. After gentle mixing 10 µl freshly-prepared 2 mg/ml $SnCl_2 \cdot 2H_2O$ in 0.01M HCl were added. The mixture was incubated on a shaker at a constant temperature of 37°C for 30 minutes then analysed by LC-MS.

3.4 Results

3.4.1 Tc-99m labelling of tricine controls C1-3 and the effect of $SnCl_2$ and pH on the formation of non-soluble radioactive species

Results of pH measurements were as follows: C1 pH 1.8-2.1, C2 pH 3.8, C3 pH 4.4-4.6. ITLC chromatograms developed after 30 minutes are shown in Figures 3.2-3.4. No significant changes were detected at later time points. In C1, the control that contained the highest amount of $SnCl_2 \cdot 2H_2O$ and was therefore the most acidic 33% of the radioactivity was present in the form of a hydrophobic chemical species (R_f=0)[8]. The "product peak" (R_f=1) was a doublet (Figure 3.2). The second control (C2) contained half as much of Sn(II) as C1 and was less acidic; the ratio of baseline-bound activity was 18% (Figure 3.3). Sample C3 contained 10-times less $SnCl_2 \cdot 2H_2O$ than C1 and the ratio of the hydrophobic chemical species was only 2% (Figure 3.4). Other control chromatograms are reported in Appendix 3.

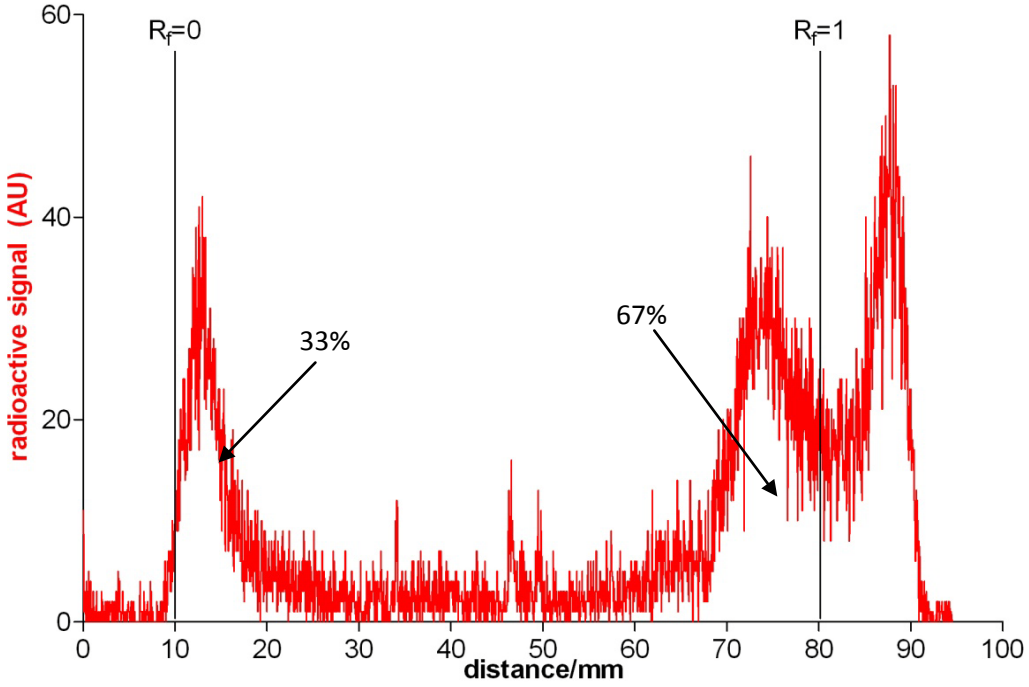

Figure: 3.2 ITLC chromatogram of C1 after 30 min incubation at 37°C.

[8] R_f: retention factor

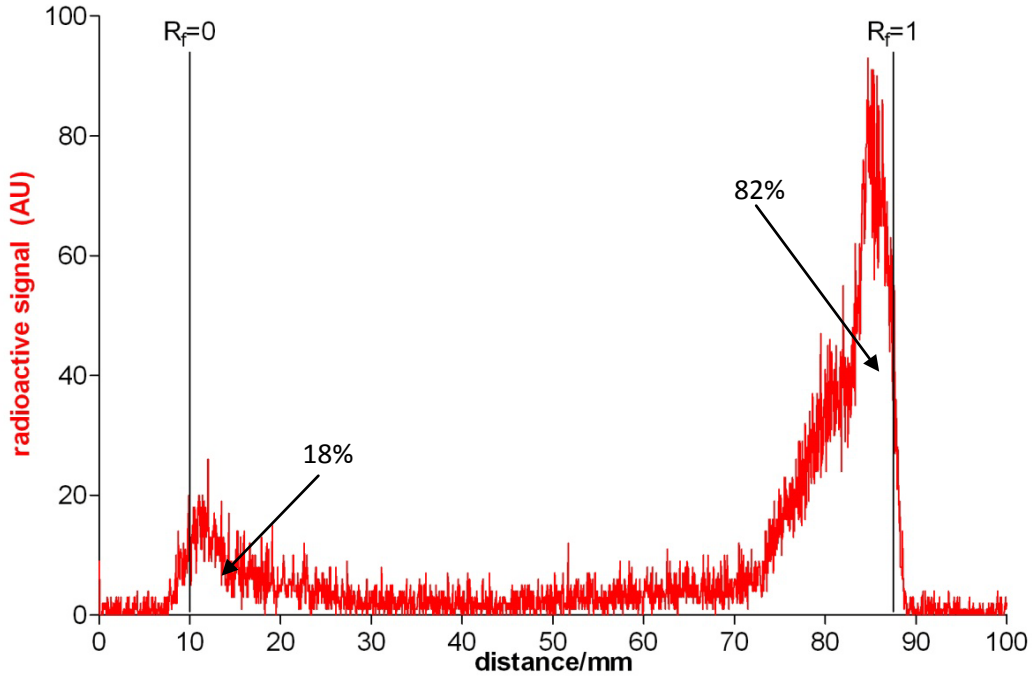

Figure 3.3: ITLC chromatogram of C2 after 30 min incubation at 37°C.

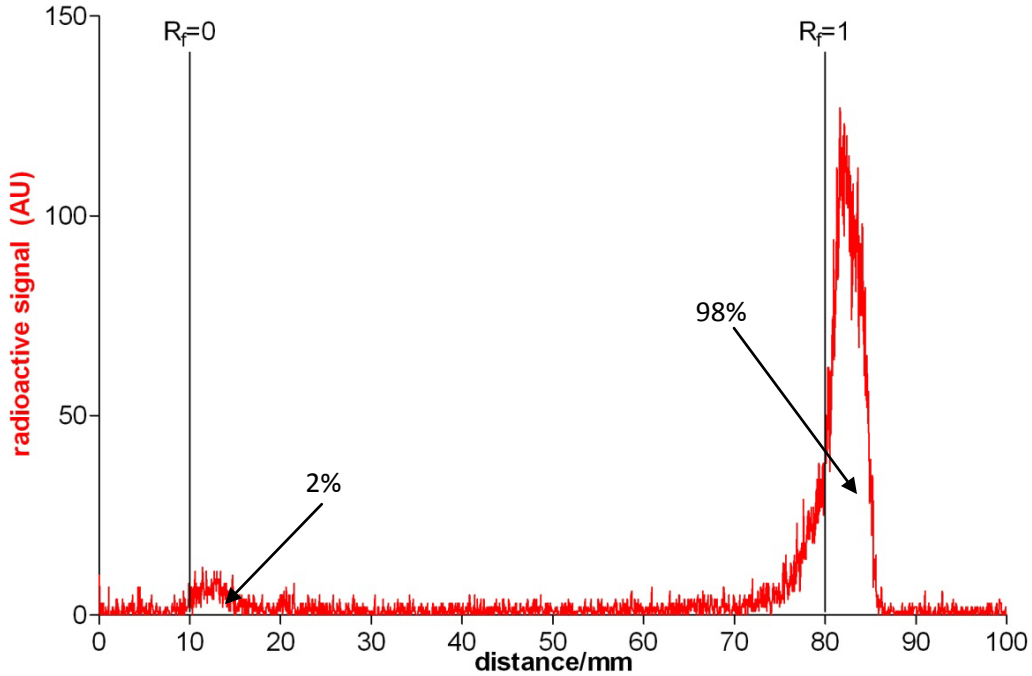

Figure 3.4: ITLC chromatogram of C3 after 30 min incubation at 37°C.

3.4.2 Determination of the ideal labelling time

241 MBq of Tc-99m-pertechnetate were added to the "10 µg" sCTLys[18]-hynic-TFA kit (activity at time of elution). pH of the labelling mixture was 4.6.

Samples were withdrawn after 10, 20, 30 and 60 minutes and analysed by ITLC. Chromatograms are shown in Figures 3.5-3.8. Approximately 75% conversion was reached in 10 minutes (Figure 3.5) and 98% conversion in 30 min (Figure 3.7). By 60 minutes the conversion was 100% (Figure 3.8).

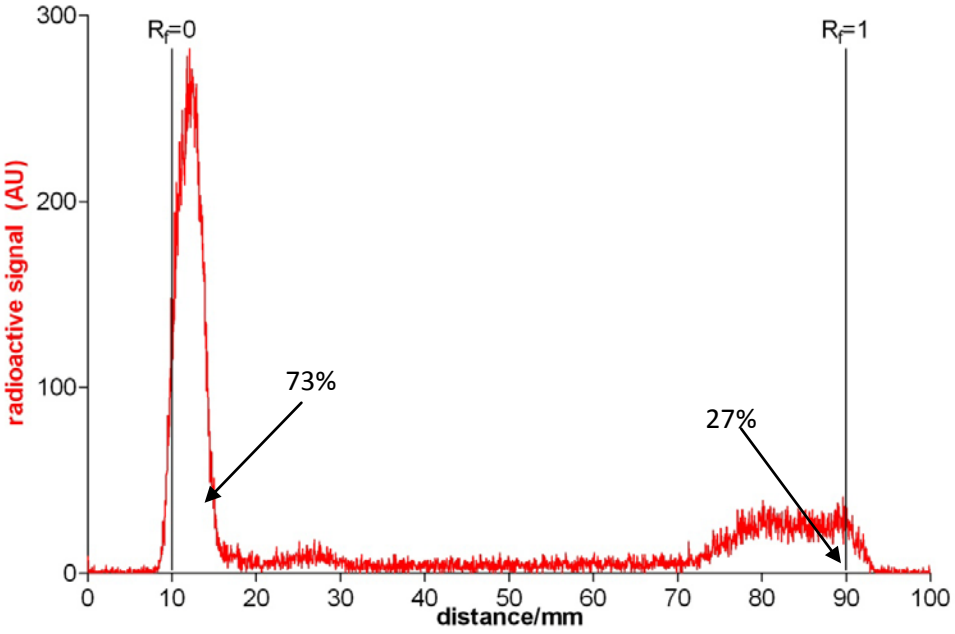

Figure 3.5: ITLC chromatogram of the labelling mixture after 10 min incubation at 37°C.

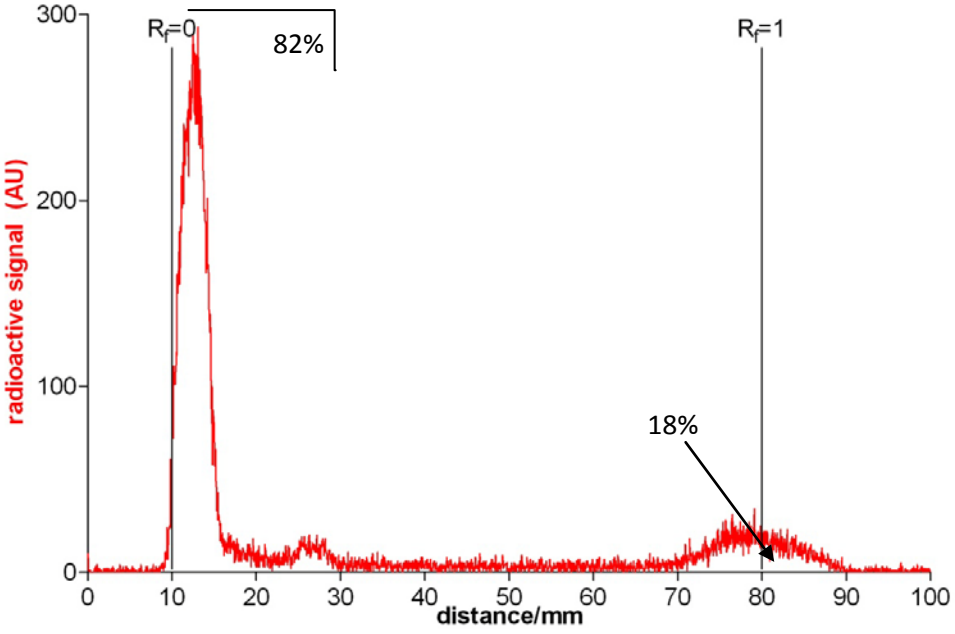

Figure 3.6: ITLC chromatogram of the labelling mixture after 20 min incubation at 37°C.

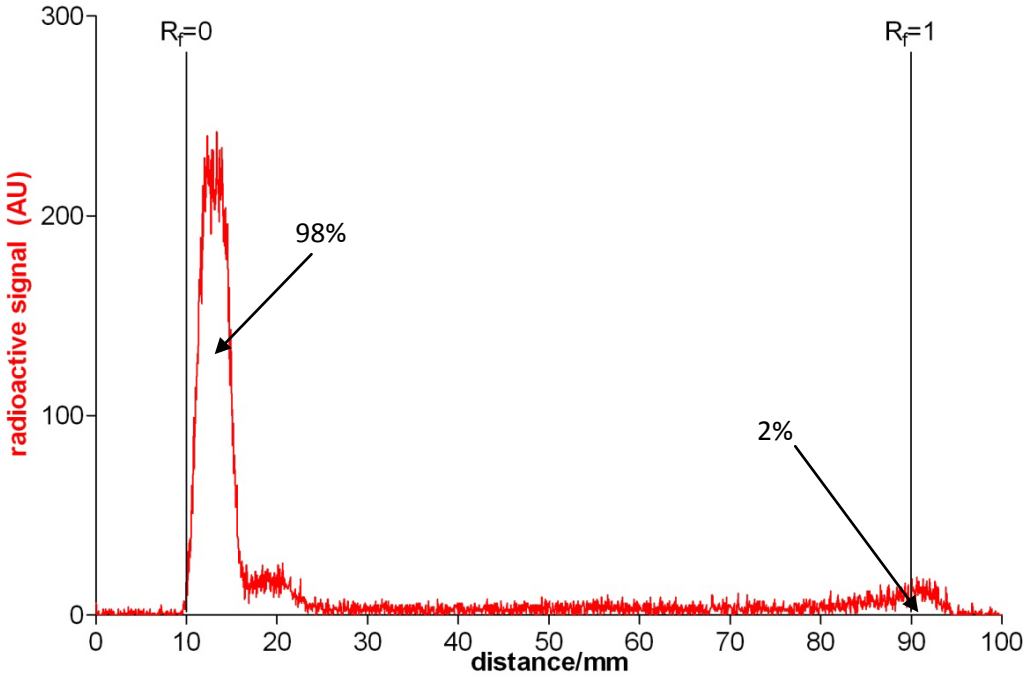

Figure 3.7: ITLC chromatogram of the labelling mixture after 30 min incubation at 37°C.

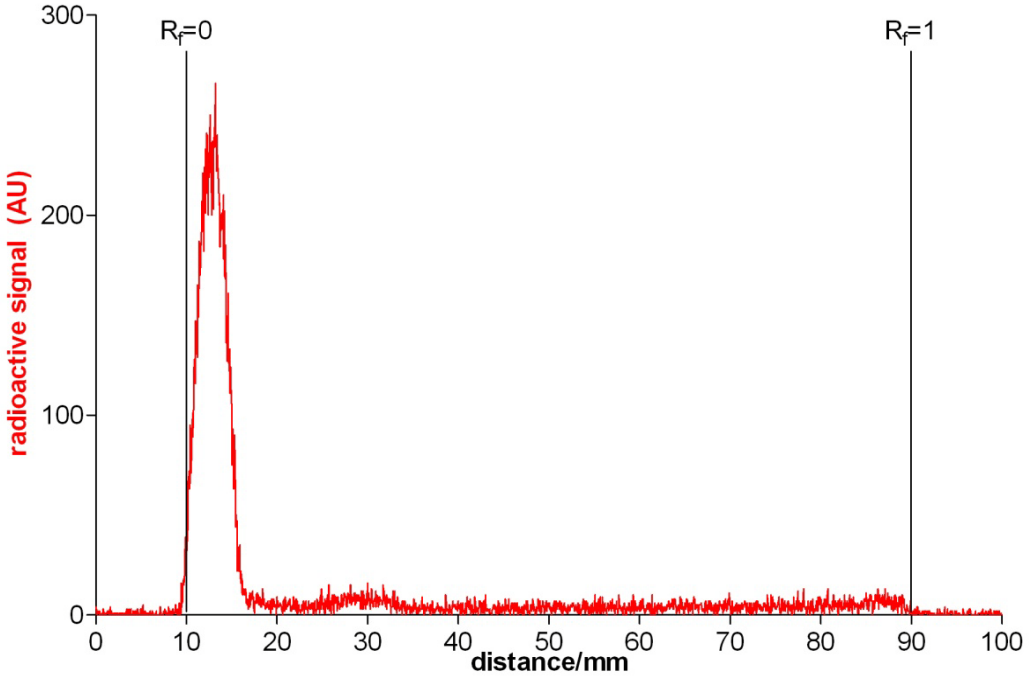

Figure 3.8: ITLC chromatogram of the labelling mixture after 60 min incubation at 37°C.

3.4.3 Determination of maximum achievable specific activities and chromatographic characterisation

The HPLC radiochromatogram of the Tc-99m labelled sCTLys^{18}-hynic-TFA contained a set of overlapping peaks in the region of RT=20-31 min. The UV trace contained a single very intensive UV peak at RT=2 min (Figure 3.9). The Tc-99m labelled sCT(8-32)Lys^{18}-hynic-TFA mostly eluted as a single peak at RT=19.1 min with a series of minor peaks surrounding the base of the major product peak (Figure 3.10). The Tc-99m labelled sCT(8-32)Lys^{18}-hynic-TFA was represented by a single peak at the baseline of the ITLC chromatogram (R_f=0; Figure 3.11). For a representative ITLC chromatogram of Tc-99m labelled sCTLys^{18}-hynic-TFA refer to Figure 3.8.

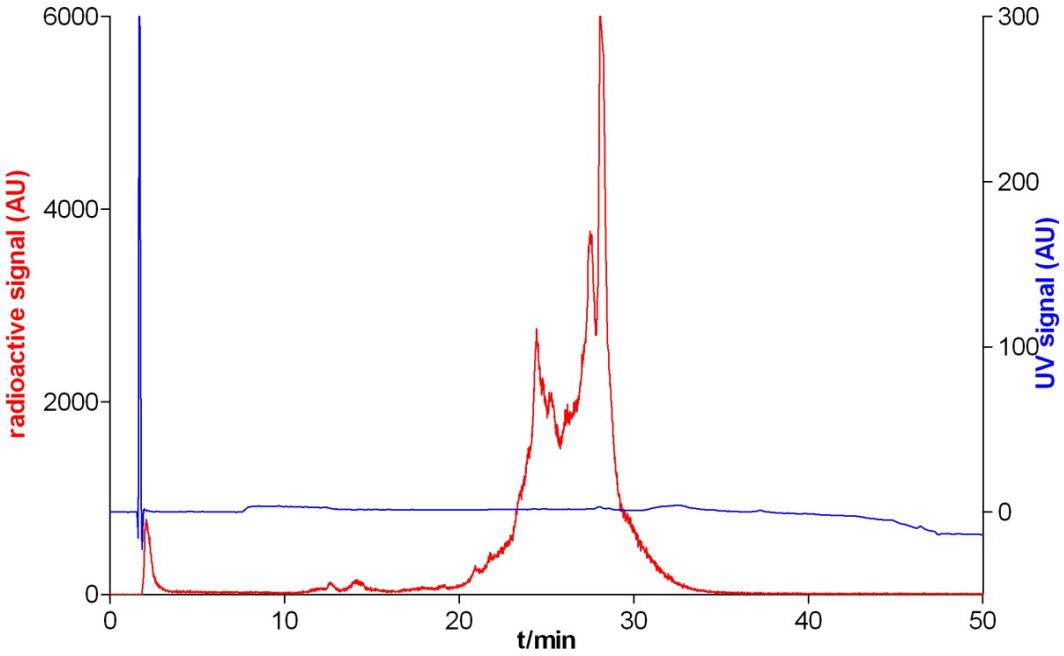

Figure 3.9: Representative HPLC chromatogram of Tc-99m labelled sCTLys^{18}-hynic-TFA.

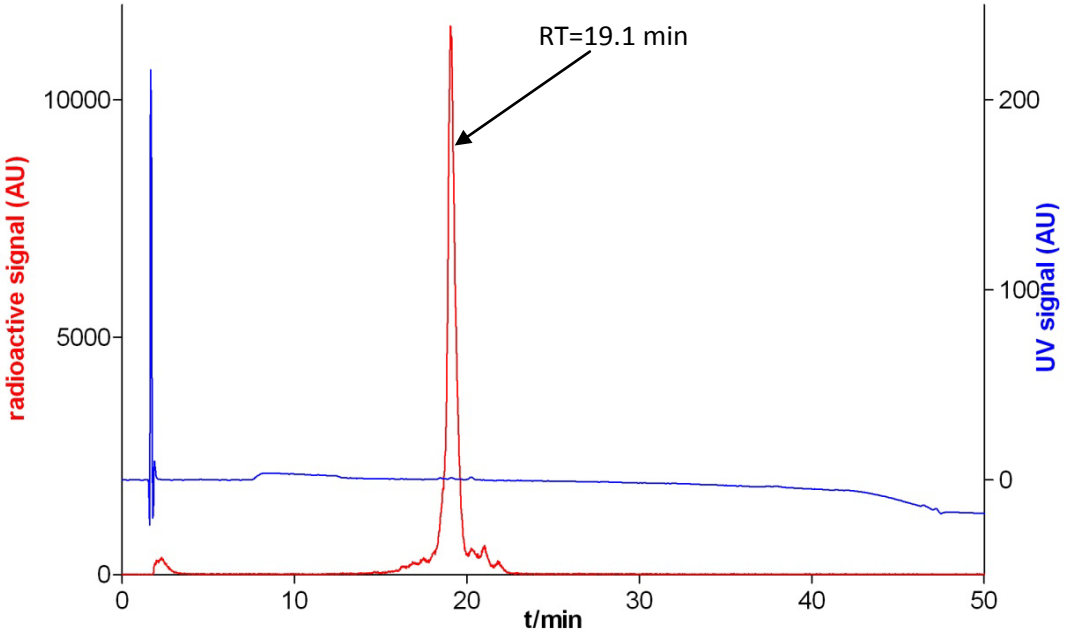

Figure 3.10: Representative HPLC chromatogram of the Tc-99m labelled sCT(8-32)Lys^{18}-hynic-TFA.

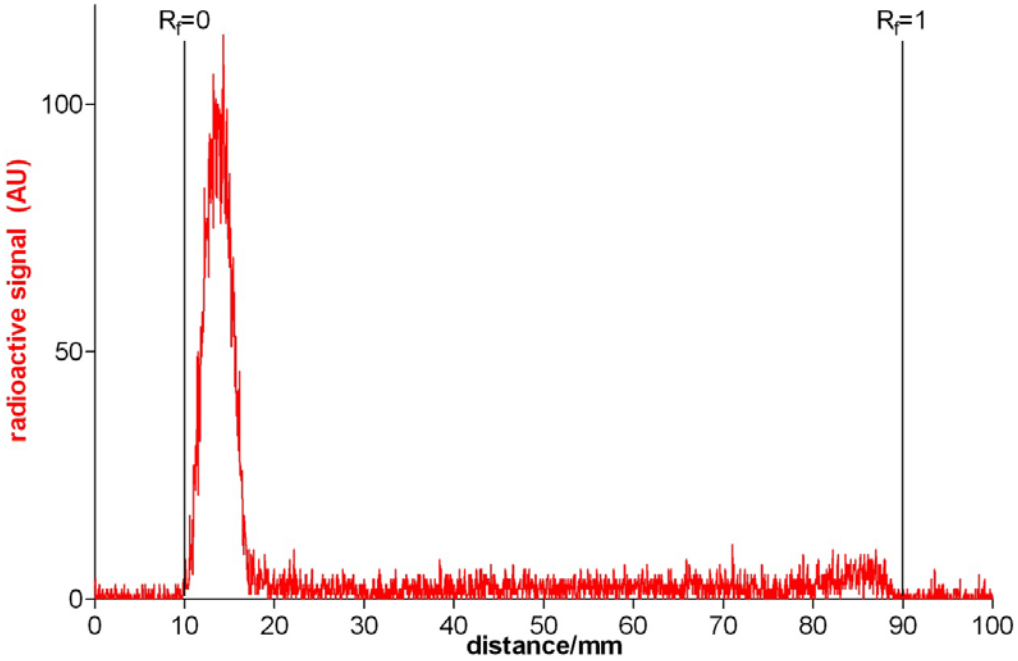

Figure 3.11: Representative ITLC chromatogram of the Tc-99m labelled sCT(8-32)Lys^{18}-hynic-TFA.

We found that a 10 µg kit of sCTLys^{18}-hynic-TFA can be labelled reproducibly with 160-200 MBq (45-55 MBq/µg at time of elution) Tc-99m with an RCP>95%. No more than 160 MBq should be used on Mondays (no elution over the

weekend thus these eluates have very low specific activity). When we obtained very high specific activity eluates a “10 µg kit” could reproducibly be labelled with up to 250 MBq of Tc-99m.

Except for Mondays a “10 µg kit” of sCT(8-32)Lys^{18}-hynic-TFA could be labelled with up to 500 MBq (at time elution) of Tc-99m (RCP>95%) corresponding to a specific activity of 70 MBq/µg. On Mondays activities above 350 MBq resulted in RCP<95%.

None of the attempts to assess the amount of colloidal impurities in labelling mixtures were successful. Chromatograms obtained in ITLC-SA/organic solvent systems (refer to section 3.3.1) were either identical to those obtained with saline eluant (*i.e.* labelled peptides staying at the baseline and hydrophilic impurities eluting with the solvent front) or were represented by a smear between R_f=0-1.

3.4.4 Carrier level labelling of hynic-calcitonin conjugates

Although the radiochromatogram of the sCTLys^{18}-hynic-TFA labelled at carrier level was very noisy it was identical to the chromatogram obtained after analysing the hynic-peptide radiolabelled at tracer level (Figure 3.12). LC-MS analysis identified a new and abundant species with a (deconvoluted) mass of 3880.74, eluting at RT=28.3 min (Figure 3.13). Calculations suggest that the above mass corresponds to an MeCN adduct of a [^{99}Tc-sCTLys^{18}-hynic-tricine] species after the loss of five protons (calc. mass 3880.7363, observed mass 3880.74) (Table 3.1). Neither unlabelled sCTLys^{18}-hynic nor the TFA protected derivative was detected by MS, only the de-aminated and de-hydrazinated fragments were present in the mixture (Figure 3.13).

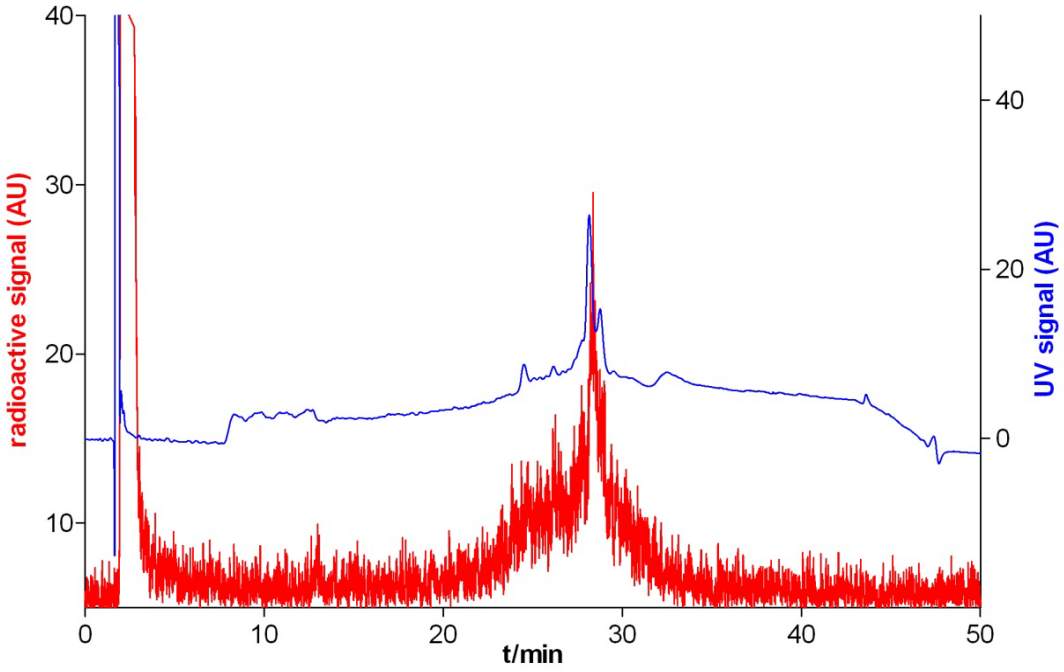

Figure 3.12: UV and radiochromatogram of the Tc-99 labelled sCTLys^{18}-hynic-TFA.

Figure 3.13: Deconvoluted mass spectrum (abundance *vs.* M) of the Tc-99 labelled sCTLys^{18}-hynic-TFA between RT=28.222-28.594 min.

Compound	Formula	RT/min	Species	Calc. mass or m/z
[^{99}Tc+sCTLys^{18}-Hynic+tricine+MeCN-5H]	$C_{159}H_{256}N_{49}O_{54}S_2$ [^{99}Tc]	27.678 28.258	M	3880.7363
			$[M+4H]^{4+}$	971.1914
			$[M+3H]^{3+}$	1294.5861
			$[M+2H]^{2+}$	1941.3754

Table 3.1: Calculated mass or m/z of detected Tc-99-sCTLys^{18}-hynic-TFA complexes and corresponding ions. Most abundant isotope peaks included.

In an attempt to identify more isomeric complexes or a $tricine_2$ complex of the radiopeptide we performed molecular feature extraction (MFE) on the chromatography data. MFE confirmed that there were no $tricine_2$ complexes present and revealed an isomeric [^{99}Tc-sCTLys^{18}-hynic-tricine] complex eluting at RT=27.678 (Figure 3.14).

a

b

c

d

Figure 3.14: Extracted ion (a) and compound (b) chromatograms with the corresponding MFE spectrum (c) and raw mass spectrum (d) of the compound eluting at RT=27.678 min.

a

b

c

d

e

Figure 3.15: Extracted ion (a) and compound (b) chromatograms with the corresponding MFE spectrum (c-d) and raw mass spectrum (e) of the compound eluting at RT=28.258 min.

MFE also identified the complex that we had found before (Figure 3.15). Due to the low reliability of MFE spectra raw spectra that reflect the real isotope peak distribution of ions are also included (for reference spectrum see Appendix 4).

LC-MS analysis of the Tc-99 labelled sCT(8-32)Lys^{18}-hynic-TFA suggested that tracer and carrier level labelling resulted in chemically identical species *i.e.* a single radioactive product peak eluted at RT=19.1 min (Figure 3.16). The UV peak representing the Tc-99 complex was also identified (Figure 3.16: region 1, RT=18.8 min). Mass spectrometry suggested that the product was the MeCN adduct of the [^{99}Tc-sCT(8-32)Lys^{18}-hynic-tricine] complex after the loss of five protons (observed mass 3173.50, calc. mass 3173.4915, refer to Table 3.2). The non MeCN adducted complex was also present (observed m/z for $[M+3H]^{3+}$ 1045.1625, calc. m/z 1045.1623; Figure 3.17 c and Figure 3.21). Region 2 (overlapping with Region 1) contained some of the labelled product and an unidentified species (Figure 3.18, M=2915.52). sCT(8-32)Lys^{18}-hynic-TFA was also present (Region 3, RT=20.3 min and confirmed by mass spectrometry, Figure 3.19). Region 3 included an unidentified non-radioactive species too (Figure 3.18, M=3370.87). The TFA deprotected species sCT(8-32)Lys^{18}-hynic (RT=18.2 min) was not detected in the sample.

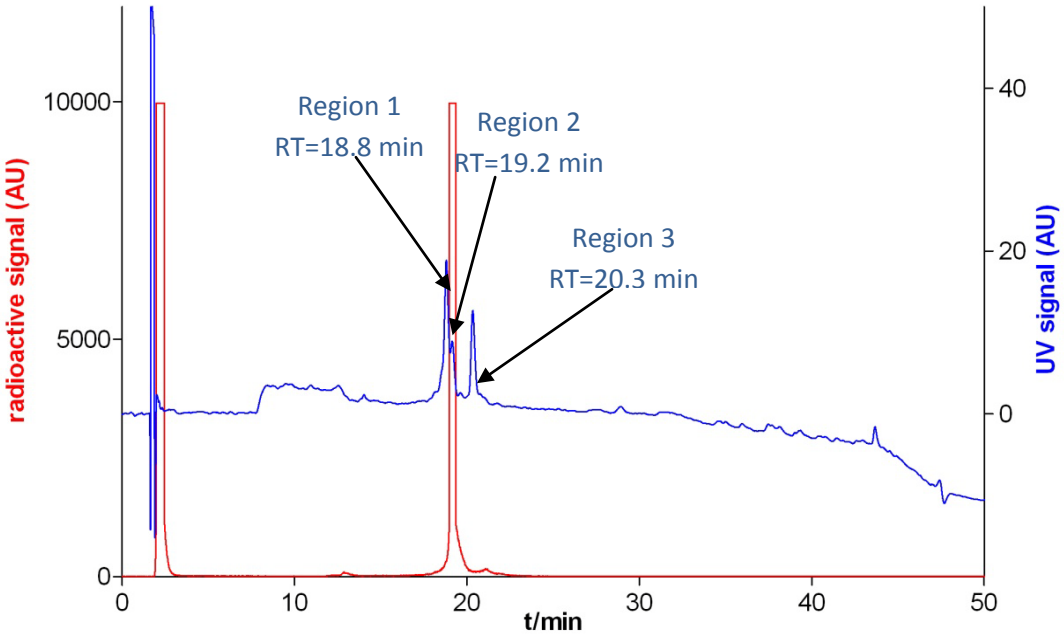

Figure 3.16: UV and radiochromatogram of the Tc-99 labelled sCT(8-32)Lys^{18}-hynic-TFA.

Compound	Formula	RT/min	Species	Calc. mass or m/z
[^{99}Tc+sCT(8-32)Lys^{18}-Hynic+tricine-5H]	$C_{131}H_{211}N_{40}O_{43}$ [^{99}Tc]	19.108	M	3132.4650
			$[M+4H]^{4+}$	784.1235
			$[M+3H]^{3+}$	1045.1623
			$[M+2H]^{2+}$	1567.2398
[^{99}Tc+sCT(8-32)Lys^{18}-Hynic+tricine+MeCN-5H]	$C_{133}H_{214}N_{41}O_{43}$ [^{99}Tc]	19.083	M	3173.4915
			$[M+4H]^{4+}$	794.3802
			$[M+3H]^{3+}$	1058.8378
			$[M+2H]^{2+}$	1587.7530

Table 3.2: Calculated mass or m/z of detected Tc-99-sCT(8-32)Lys^{18}-hynic-TFA complexes and corresponding ions. Most abundant isotope peaks shown.

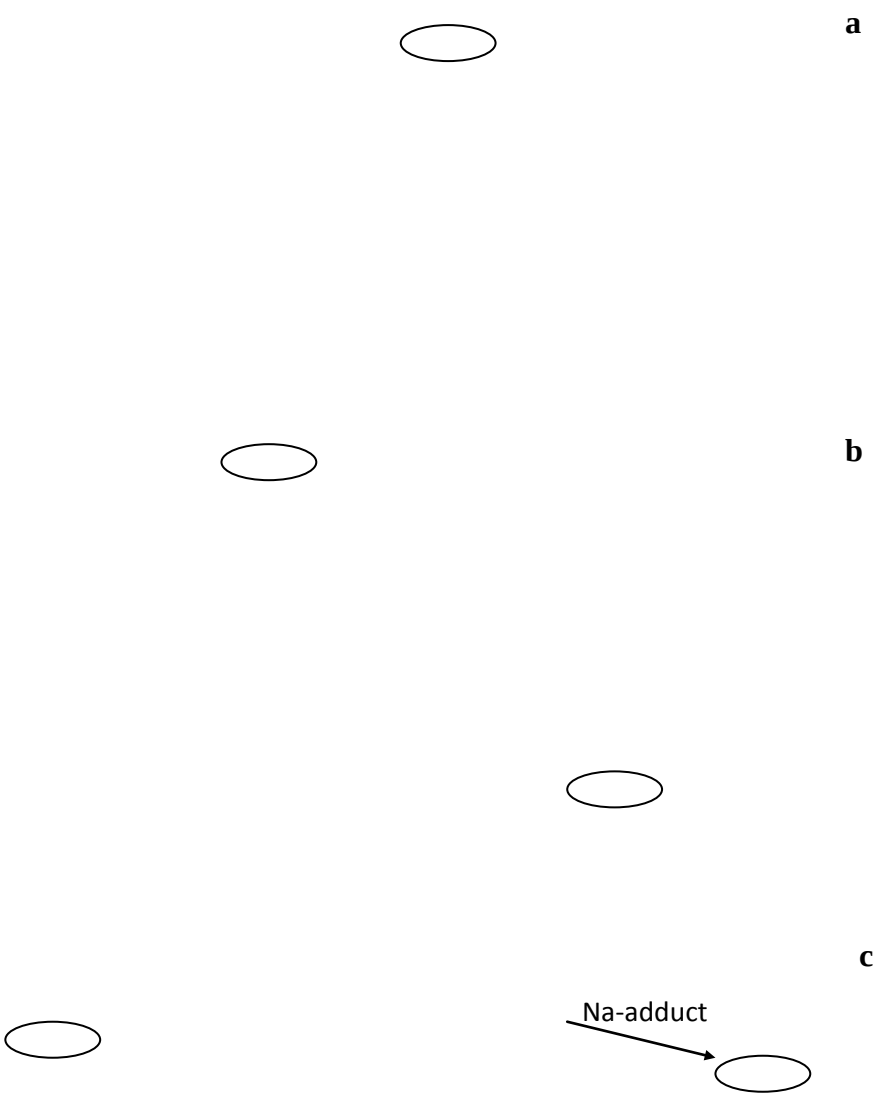

Figure 3.17: Deconvoluted (a) and raw (b, c) mass spectra representing region 1 as defined in Figure 3.16.

Figure 3.18: Deconvoluted mass spectrum representing region 2 as defined in Figure 3.16.

Figure 3.19: Deconvoluted mass spectrum representing region 3 as defined in Figure 3.16.

MFE was carried out to reveal possible isomeric complexes and other species with low abundance; results are shown in Figures 3.20-3.21. MFE identified the MeCN adduct of the [^{99}Tc-sCT(8-32)Lys^{18}-hynic-tricine] complex that is represented by Region 1 on the UV chromatogram and what we had identified based on the raw spectrum (Figures 3.16-3.17). MFE results for the same compound are summarised in Figure 3.20, the figure also includes raw spectra reflecting the real isotope peak distribution of the doubly charged ion (for reference spectrum see Appendix 5).

The extraction algorithm identified a less abundant compound (Figure 3.21) *i.e.* the [^{99}Tc-sCT(8-32)Lys^{18}-hynic-tricine] complex after the loss of five protons ([M+3H]$^{3+}$ 1045.1613, calc. 1045.1623). Neither the MFE nor the raw spectrum

matched the theoretical isotope peak distribution (Figure 3.21d and Appendix 5); this is probably due to the very low abundance of this species. The [^{99}Tc-sCT(8-32)Lys^{18}-hynic-tricine$_2$] complex was not detected.

Figure 3.20: Extracted ion (a) and compound (b) chromatograms with the corresponding MFE spectrum (c, d) and raw spectrum (e) of the compound eluting at RT=19.083 min.

a

b

c

d

Figure 3.21: Extracted ion (a) and compound (b) chromatograms with the corresponding MFE spectrum (c) and raw spectrum (d) of the compound eluting at RT=19.108 min.

3.5 Discussion

By labelling tricine controls C1-C3 we aimed to optimise the amount of reducing agent used in labelling experiments. The Tc-tricine complexes as well as pertechnetate are very hydrophilic. Pertechnetate travels with the solvent front in the ITLC-SA/saline system (R_f=1), refer to Appendix 3. Based on their HPLC profile the Tc-tricine complexes co-elute with pertechnetate thus we expect them to have an R_f close to 1. In C1, the most acidic sample containing the highest amount of $SnCl_2$ the "product peak" was a doublet (Figure 3.2) and the baseline-bound activity was 33%. This is likely to be an artefact, probably due to incorrect spotting of the sample. However it may also represent two chemical species, most likely Tc-tricine

complexes and pertechnetate (*N.B.* we did not aim to characterise these peaks). The ratio of baseline-bound activity in sample C3 that contained 10-times less $SnCl_2 \cdot 2H_2O$ than C1 was only 2% (Figure 3.4). Although we have no direct evidence it is very likely that the hydrophobic radioactive species remaining at the baseline were colloidal particles. In a system containing tricine, pertechnetate and (in C1 a large amount of) Sn(II) and Cl^- we cannot think of the formation of any other possible hydrophobic species. The question is what kind of colloidal species could be formed? One possibility is the formation of TcO_2 or at basic pH a hydroxy-oxo particle. However at acidic pH, especially pH 1.8 none of the above could be formed. Another possibility is the formation of stannous radiocolloid. Stannous(II)-fluoride radiocolloid is a clinically used agent for leukocyte labelling. Unfortunately this imaging agent is poorly characterised hence not too much is known about its formation and structure [157]. Synthesising the Tc-99m labelled radiocolloid is very easy and, although the compound has not yet been properly characterised based on the steps of synthesis (*e.g.* [157, 158]) it is very likely that we "accidentally" synthesised an analogous compound. The reason for having only 2% of the activity in colloidal form in C3 can be explained by the low concentration of Sn(II) in that sample. Based on the results we decided to use 10 µl of a 1 mg/ml solution of $SnCl_2 \cdot 2H_2O$ (*i.e.* same as for C3) as reducing agent for hynic-peptide labelling. Having a strong chelator such as hynic in solution would probably further reduce the amount of colloidal species as it would compete for the radiometal with the stannous colloid particles under formation. Therefore in the labelled hynic-calcitonin samples the ratio of colloidal impurities would not exceed 2%.

By analysing the radiolabelled $sCTLys^{18}$-hynic-tricine-TFA at different time points we determined the optimal labelling time of the hynic-calcitonin peptides.

Based on the results after 10 minutes 75% of the activity was peptide (baseline) bound (Figure 3.5) proving that hynic binds technetium very rapidly (click chemistry) and confirming results described in Chapter 8. Note: the only reason why we chose to label our hynic-peptides at 37°C instead of room temperature is that we have had a constant problem with the heating and air-conditioning in our laboratories with temperatures fluctuating between 12-30°C. Thus the term “room temperature” would have been a very vague definition and could have compromised reproducibility.

After 30 min conversion was 98% (Figure 3.7) thus we speculated that 30 min could be the ideal labelling time for radiolabelling our hynic-peptide kits. Although under the actual conditions (overall activity and specific activity) 100% conversion could be achieved in 60 min (Figure 3.8) we should take into account that the rate of conversion is a function of the radioactivity and specific activity of the generator eluate. Therefore these data are not considered as reproducible and only give us a rough idea on the rate of conversion. Actual RCPs will always be evaluated after each and every experiment. Regarding the actual sample RCP exceeding 95% is the generally accepted threshold for imaging hence a sample with RCP=98% could be used in a clinical setting.

As larger labelled peptides and antibodies in general the Tc-99m labelled sCTLys^{18}-hynic-TFA and sCT(8-32)Lys^{18}-hynic-TFA stay at the baseline in the ITLC-SA/saline (or aqueous mobile phase) system. Technetium colloids are expected to stay at the baseline too whilst other impurities such as pertechnetate and Tc-tricine complexes move with the solvent front. Therefore determination of colloidal technetium content requires the use of a different system. To determine colloidal technetium organic or a mixture of organic and aqueous solvents were used

as mobile phase with ITLC-SA strips. There are several examples in the literature, such as 50% MeCN-water [141], 50% acetone-water [150]; Greenland used a 1:1:1 mixture of saline, acetone and MeCN [114]. Ideally in these systems the labelled peptide or antibody will leave the baseline and only colloidal species stay there. We tried all the above solvent mixtures as well as different ratios of MeCN in water (from 10 to 90% in 10% increments) and 1:2:2, 1:1:2, 1:2:1 mixtures of saline, acetone and MeCN. Dr. Rafael Torres from the Division of Imaging Sciences suggested using mixtures of methanol and 10% NH_4OAc in water. We tested this solvent system too at different ratios: 10-90 to 90-10 in 10% increments. Unfortunately none of the above methods led to success. The result was either the same as with saline eluant (so the labelled peptide did not leave the baseline) or a smear with no peaks at all. Thus we did not manage to determine directly the ratio of colloidal technetium in the labelling mixture. On the other hand with indirect measurements we proved that no/only negligible amounts of colloidal species were present (*vide supra*).

On HPLC chromatograms small hydrophilic impurities elute at RT=2.1 min (also refer to Appendix 3). Based on LC-MS studies pertechnetate and Tc-tricine complexes are indistinguishable at least with this method (*vide infra*); they both elute straight after the void volume without any interaction with the column. At first glance the HPLC chromatogram of the labelled sCTLys^{18}-hynic-TFA looks very bad, the labelled peptide is represented by a large set of overlapping peaks between RT=20-30 min (Figure 3.9). The high number of peaks with similar retention times represents isomeric complexes (for evidence refer to mass spectrometry data). The formation of a high number of isomers when labelling hynic conjugates has been a long-term problem [148]. When labelling hynic analogues for LC-MS studies we

also identified isomeric species (Chapter 8, [149]). Liu *et al.* published a number of studies on the identification and characterisation of isomeric hynic complexes and the role of co-ligands; their papers will be reviewed in Chapter 8 or [148]. In one of their studies Liu and co-workers reported very similar chromatograms for a labelled hynic-peptide to what we have found with the labelled sCTLys^{18}-hynic-TFA. They also identified 8 isomeric complexes of the very same Tc-99m labelled hynic-peptide with tricine as co-ligand [159].

The UV chromatogram only contained one (and very intensive) peak corresponding to tricine. Neither the sCTLys^{18}-hynic-TFA nor its Tc-99m complex was detected since their concentration was so low. The radio HPLC chromatogram of the Tc-99m labelled sCT(8-32)Lys^{18}-hynic-TFA consisted of a single and narrow peak at RT=19 min (with a minor pertechnetate or Tc-tricine peak at RT=2.1 min). The base of the product peak was broadened with a minor peak at RT=21 min, suggesting the presence of an isomer or fragment. Based on the HPLC chromatogram of the purified sCT(8-32)Lys^{18}-hynic-TFA it is unlikely that the sample contained another hynic peptide that could be responsible for this observation. Similarly to the full radiopeptide sequence the UV chromatogram only contained one peak corresponding to tricine. Due to their very low concentration neither the sCTLys^{18}-hynic-TFA nor its Tc-99m complex was detected.

After every single injection and at the end of every single run the HPLC column was monitored with a contamination monitor. The radiochromatogram will only account for the radioactive species that leave the column – we had to make sure that no activity was retained. We speculated that colloidal species – depending on their size – will either be retained by the column or if they are small enough they will

pass through the column and appear on the chromatogram. Thus, this was an indirect way to test the samples for colloidal impurities.

After injecting one of the labelled peptides and holding the contamination monitor above the HPLC column the count rate was in the order of 10^3. At the end of the run, holding the monitor in roughly the same position the count rate was not or only a bit higher than background (*i.e.* order of 10 suggesting that no more than 1% of the injected activity remained on the column). During multiple runs when the retained activity accumulated the "background" was considered as the count rate at the end of the previous run.

Considering the low peptide content and purity (*N.B.* de-amination/hydrazination) of sCTLys^{18}-hynic-TFA being able to label a "10 µg kit" of the peptide with 200 MBq of Tc-99m is a very good result. Based on the decay law we can calculate the number of moles in 200 MBq of carrier-free Tc-99m, that is around 10 pmol. *N.B.* Tc-99m eluted from a generator will never be carrier free, the overall concentration of Tc-99 and Tc-99m pertechnetate in the generator eluate is 0.1-0.4 nmol/GBq [160]. Thus 20 pmol is the minimum amount of pertechnetate present in 200 MBq of generator eluate. The maximum amount of sCTLys^{18}-hynic-TFA in a "10 µg kit" was 3.6 µg (around 980 pmol) (refer to section 2.6). These data suggest that sCTLys^{18}-hynic was in less than 50-fold excess to Tc-99m. Note that 980 pmol or 3.2 µM is the maximum amount of hynic-peptide present and 20 pmol or 0.065 µM is the minimum amount of pertechnetate present in the labelling mixture therefore 50-fold excess is the theoretical maximum excess of hynic-peptide. These results confirm that hynic is a very efficient chelator for technetium (for a titration study refer to Chapter 8 or [149]).

A “10 µg kit” of the abbreviated hynic-sCT sequence can reproducibly be labelled with 500 MBq of Tc-99m (except for Mondays), that is much higher than what we had achieved with the full sequence. These results are consistent with the higher peptide content and lower molecular weight of the sCT(8-32)Lys^{18}-hynic-TFA peptide. Based on the peptide content calculations a 10 µg kit contained no more than 7.1 µg (2.4 nmol or 7.8 µM in the labelling mixture) of sCT(8-32)Lys^{18}-hynic-TFA. Taking into account that 500 MBq generator eluate contains 0.05-0.2 nmol or 0.16-0.65 µM (in the labelling mixture) of pertechnetate these data suggest that sCT(8-32)Lys^{18}-hynic-TFA was in only 12-50-fold excess to the radiometal. These results again clearly demonstrate the efficiency of hynic in chelating technetium.

In the carrier level labelled sCTLys^{18}-hynic-TFA sample we identified two isomeric complexes (Figures 3.14-3.15), both are the MeCN adducts of [Tc-sCTLys^{18}-hynic-TFA-tricine] after the loss of five protons in other words the formal oxidation state of Tc was +5. Calculating the oxidation state of metals this way has been generally accepted in the literature although it does not give direct evidence as Mössbauer or EXAFS spectroscopy. By definition the deconvoluted mass corresponds to the mass of an uncharged (neutral) species. If the oxidation state of the metal was 0 the deconvoluted mass of the complex would be the sum of the mass of ligands and the mass of the metal. In positive mode ESI-MS and acidic solvent system ionisation of neutral species usually happens via protonation thus deconvolution means the multiplication of the detected m/z by the charge (z) and the subsequent subtraction of the appropriate number (z) of protons (~ 1 Da): ~1 Da if the ion was singly charged, ~ 2 Da if it was doubly charged *etc.* After deconvoluting our data we found that the mass of the neutral complex was ~5 Da less than the sum

of the mass of ligands and the radiometal. The only possible way for a complex to stay neutral after losing five protons is that the metal had an oxidation state of +5. The +5 oxidation state is in agreement with Greenland's data and the literature [114, 148, 149]. Greenland only identified one isomer, we did two. Based on the shape of the radiochromatogram it is likely that there were more isomers or peptide fragments present. Similarly to Greenland we did not detect complexes with two tricine co-ligands confirming that a histidine neighbouring to the hynic moiety in the peptide sequence replaces one tricine co-ligand (also confirmed by Surfraz *et al.* [153]). A putative structure of the coordination sphere is shown in Figure 3.22.

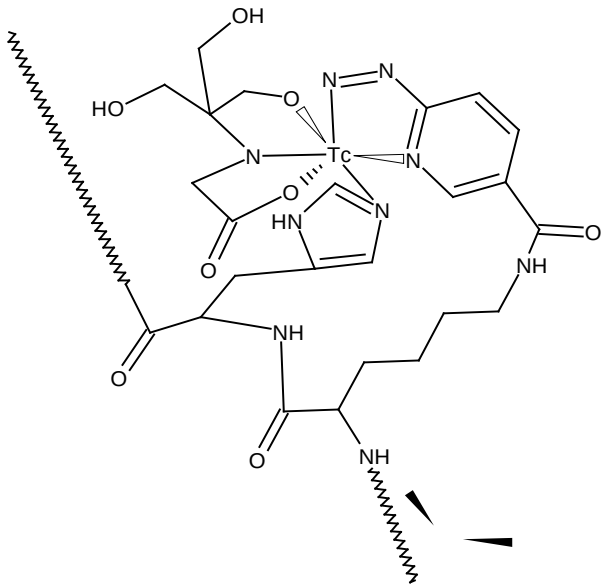

Figure 3.22: Putative structure of the coordination sphere in the [Tc(V)-sCTLys^{18}-hynic-tricine] complex.

In the sample containing the carrier level labelled sCT(8-32)Lys^{18}-hynic-TFA we identified an MeCN adduct of the [Tc(V)-sCT(8-32)Lys^{18}-hynic-tricine] complex and in much lower abundance the non-adducted complex too; the two species were eluting closely to each other (Figure 3.17). Similarly to the full sequence we could not detect Tc complexes with two tricine co-ligands. Considering that the amino acid

sequence surrounding the coordination sphere is identical to that in the full sequence this observation is in accordance with the data above. Based on the shape of the peak on the radiochromatogram (*i.e.* a single narrow peak) it is likely that only one isomeric species was present (in detectable quantity) or we simply could not separate isomers. Due to better labelling yields we also detected the UV peak corresponding to the [Tc(V)-sCT(8-32)Lys^{18}-hynic-tricine] complex (Figure 3.16).

Neither of the carrier level labelled hynic-calcitonin peptides contained unlabelled peptides with free hydrazine groups, only the de-aminated and/or de-hydrazinated derivatives were present. The carrier level labelled abbreviated sequence contained the TFA protected species. These data suggest that (at least in the labelling mixture) after the TFA protected hynic moiety has hydrolysed the remaining free hydrazine group is unstable and it either chelates technetium or gets degraded within no more than 30 minutes.

The fact that the MFE algorithm was misled by probably background ions was unexpected especially because most product ions were abundant enough and clearly separated from background. However raw spectra were consistent with theoretical isotope peak distributions.

3.6 Conclusions

We have radiolabelled the sCTLys^{18}-hynic-TFA and sCT(8-32)Lys^{18}-hynic-TFA with Tc-99m in presence of tricine co-ligand. HPLC analysis revealed that when radiolabelled the full hynic-calcitonin sequence forms a large number of isomeric species or fragments resulting in a broad peak on the chromatogram whilst the labelled abbreviated sequence was represented by a single peak that makes it more favourable for radiopharmaceutical development.

Carrier level labelling of the hynic-calcitonin peptides confirmed that they form complexes with one tricine co-ligand suggesting that the histidine neighbouring to the hynic-conjugated lysine in the sequence takes part in the coordination. Based on their HPLC chromatograms technetium complexes formed by hynic-calcitonin conjugates were identical at carrier and tracer level.

3.7 Summary

We radiolabelled sCTLys^{18}-hynic-TFA and sCT(8-32)Lys^{18}-hynic-TFA with Tc-99m and Tc-99 and characterised the labelled species chemically and radiochemically. We achieved high specific activities confirming the efficiency of hynic as a chelator for technetium and enabling the *in vitro* and *in vivo* evaluation of the radiopeptides.

Chapter 4: *In vitro* stability of Tc-99m labelled sCTLys^{18}-hynic-TFA and Tc-99m labelled sCT(8-32)Lys^{18}-hynic-TFA radiopeptides

4.1 Aims

As a preparation for *in vitro* uptake experiments and subsequent *in vivo* studies we aimed to evaluate the stability of the radiolabelled hynic-calcitonin derivatives in human serum. In another set of experiments we investigated the metabolic fate of the radiopeptides by incubating them in freshly isolated and prepared mouse kidney homogenates.

4.2 Introduction

Greenland was the first to synthesise and radiolabel the sCTLys^{18}-hynic-TFA in the early 2000's, he also assessed the *in vitro* (serum) stability of the Tc-99m labelled radiopeptide and found that the labelled peptide was stable for at least half an hour in serum (no further time points were assessed) [114]. He observed no serum protein bound radioactivity or significant release of radioactivity in his experiment. As a result Greenland concluded that the radiopeptide was stable enough for *in vitro* uptake experiments. Being a novel compound the serum stability of the Tc-99m labelled sCT(8-32)Lys^{18}-hynic-TFA sequence had to be assessed. Since the coordination sphere and the neighbouring amino acids are identical in both radiopeptides we do not expect major differences in their *in vitro* stability.

Assessing the stability and metabolism of radiolabelled compounds in organ homogenates (usually liver and kidney homogenates) is a widely used technique. It gives an idea on the metabolic fate of the compounds and makes it easy to study the

kinetics of the metabolic process. Both hynic-calcitonin sequences are hydrophilic compounds hence the main route of their extraction from the circulation is likely to be renal. Therefore we decided to assess their metabolic fate and stability on incubation in mouse kidney homogenates by analysing the radiopeptide-kidney homogenate mixtures at different time points by HPLC.

4.3 Materials and methods

4.3.1 Materials

Human serum was isolated aseptically from A+ male buffy coat provided by the National Blood Service by density gradient centrifugation. To remove contaminants (platelet/protein aggregates) the isolated serum was filtered on a 0.22 µm filter into sterile Falcon tubes then kept at -20°C. Mouse kidneys were obtained from C57Bl/6J mice; mice were culled by cervical dislocation and their kidneys were excised immediately. Kidneys were gently homogenised by a syringe plunger using BD Falcon 40 µm cell strainers connected to 50 ml Falcon tubes containing ice-cold Hanks' balanced salt solution (HBS) (20 ml/kidney). Instruments and materials described in previous chapters were used.

4.3.2 Radiolabelling hynic-conjugated calcitonin analogues

To a freeze-dried "10 µg kit" of sCTLys^{18}-hynic-TFA (1) or sCT(8-32)Lys^{18}-hynic-TFA (2) in a screw-cap microcentrifuge tube 160-210 (1) or 350-450 (2) MBq (at time of elution) of high specific activity ^{99m}Tc-TcO_4^- generator eluate in 300 µl of saline were added. To the above mixture 10 µl freshly-prepared 1 mg/ml $SnCl_2 \cdot 2H_2O$ in 0.01M HCl were added. The microcentrifuge tube was sealed, centrifuged and placed in a shaker heated to 37°C for 30 min, pH 4.6. RCP was

above 95% (typically 98-100%) in each case as assessed by ITLC-SA and saline as mobile phase and HPLC.

4.3.3 Stability studies

100 µl of labelled radiopeptide were added to 400 µl of human serum or mouse kidney homogenate in HBS in a 1.5 ml microcentrifuge tube. The tube was placed into a heated shaker and shaken at a constant temperature of 37°C for up to 24 hours. 50 µl aliquots were withdrawn at regular intervals (*vide infra*), centrifuged at 12,000 RPM for 1 minute to isolate (cell) aggregates and, depending on time of injection 5-20 µl (approximately 50-700 kBq) were injected in the HPLC (method 1). After each run the residual activity of the HPLC column was determined using a contamination monitor to make sure no activity was retained by the column.

Radiopeptide samples were also analysed by size exclusion chromatography (SEC) on a Phenomenex BioSep SEC-s2000 (300×7.8 mm, 5 µm pore size) column with isocratic PBS eluant at a flow rate of 1 ml/min for 30 minutes.

4.4 Results

4.4.1 Serum stability of Tc-99m labelled sCTLys^{18}-hynic-TFA

Samples were analysed after 60, 120, 180 minutes and 20 hours in serum. Results are shown in Figures 4.1-4.6. A control (0 min) is also shown, that sample was taken just before adding the radiopeptide to serum. Note that neither the HPLC column (method 1) nor the machine (tubing) retained any measurable radioactivity as assessed after each run thus the radiochromatograms below account for the whole amount of injected activity. Unfortunately the full hynic-sCT sequence could not be characterised by SEC: after the radiopeptide peak had eluted the radioactive signal did not return to background and remained at a level of approximately half of the

peak height for several hours suggesting that the column retained and slowly released a significant amount of the radiolabelled sCTLys[18]-hynic-TFA. Therefore we only analysed the serum-radiopeptide mixtures by HPLC method 1.

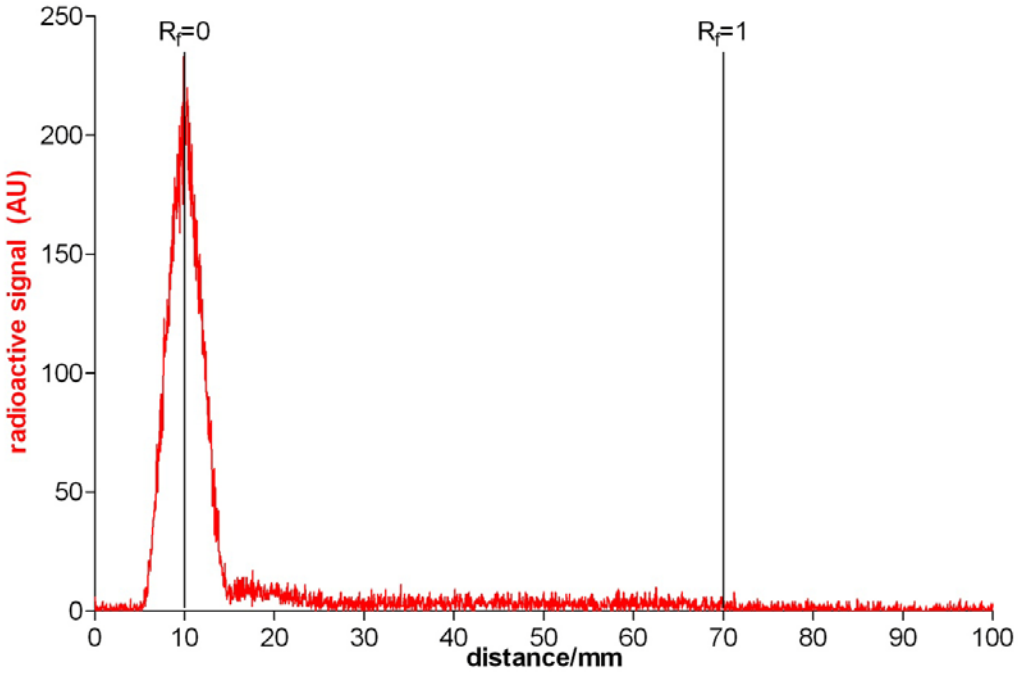

Figure 4.1: ITLC chromatogram of the Tc-99m labelled sCTLys[18]-hynic-TFA at 0 min (control sample, no serum).

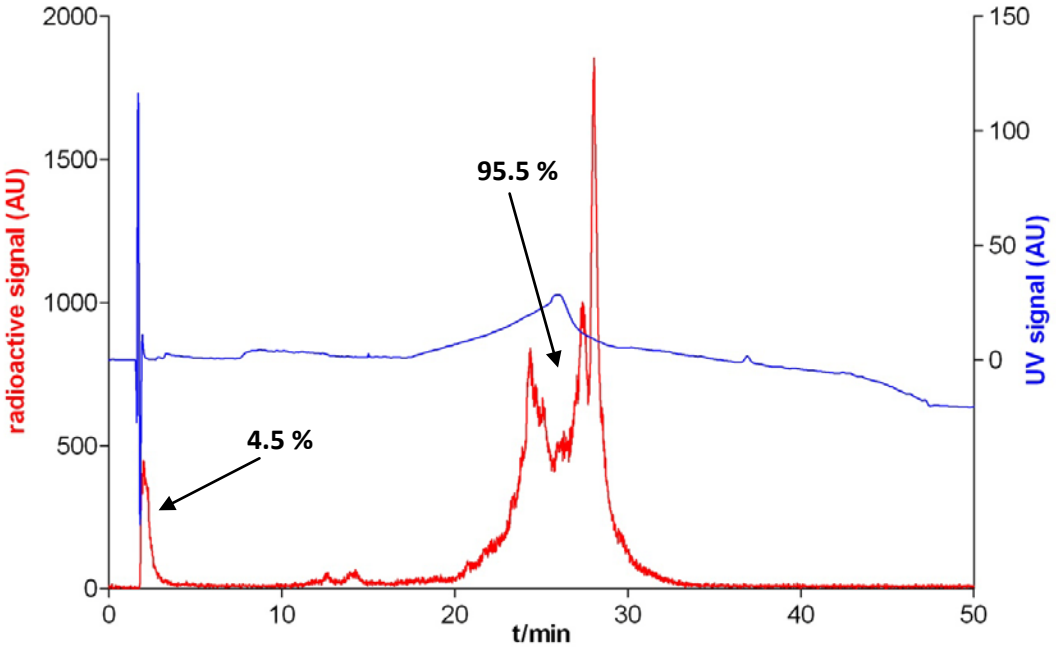

Figure 4.2: UV and radiochromatogram of the Tc-99m labelled sCTLys[18]-hynic-TFA at 0 min (control sample, no serum).

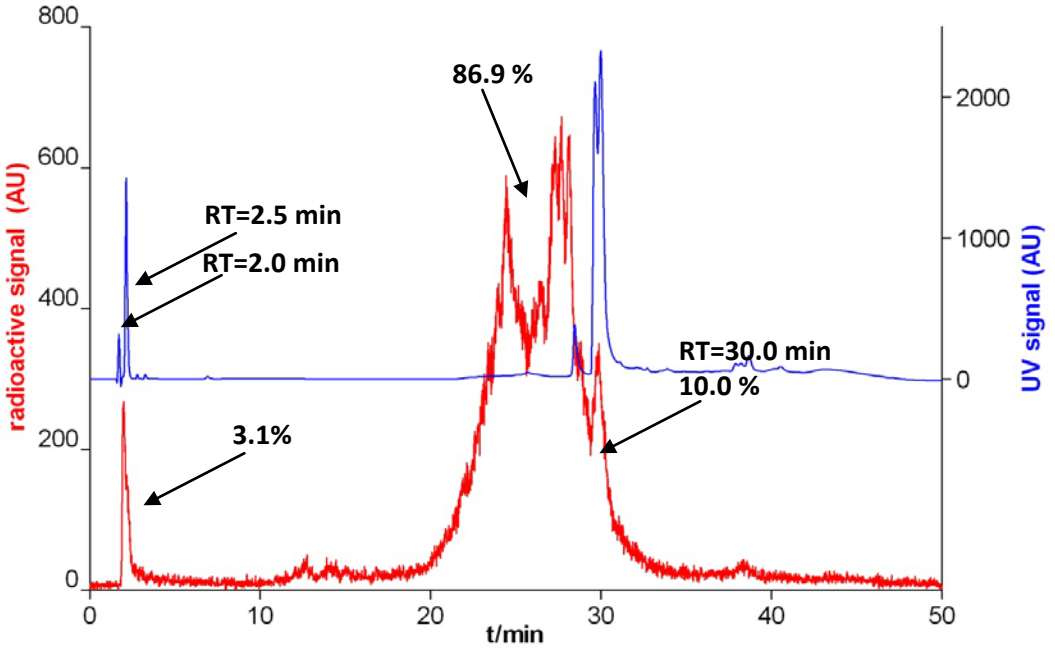

Figure 4.3: UV and radiochromatogram acquired after incubating the Tc-99m labelled sCTLys^{18}-hynic-TFA in serum at 37°C for 60 min.

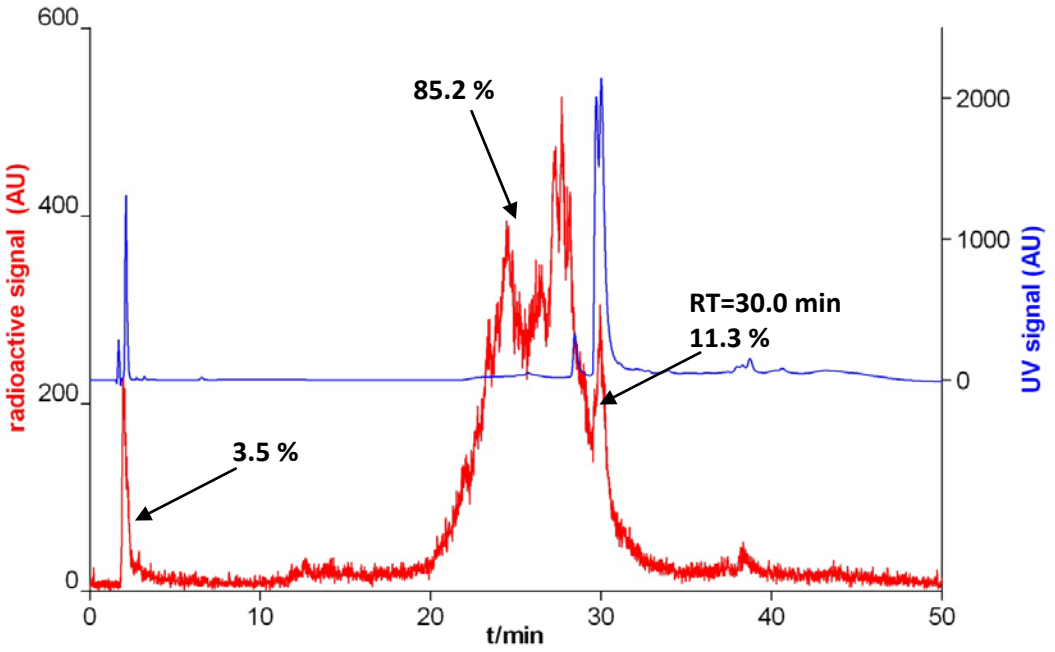

Figure 4.4: UV and radiochromatogram acquired after incubating the Tc-99m labelled sCTLys^{18}-hynic-TFA in serum at 37°C for 120 min.

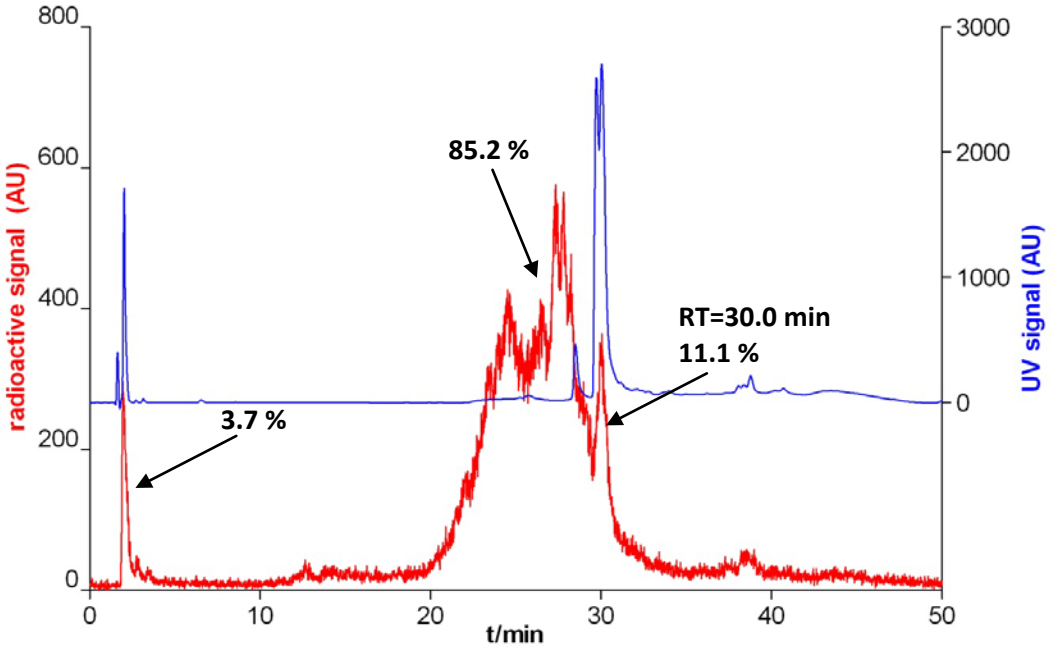

Figure 4.5: UV and radiochromatogram acquired after incubating the Tc-99m labelled sCTLys[18]-hynic-TFA in serum at 37°C for 180 min.

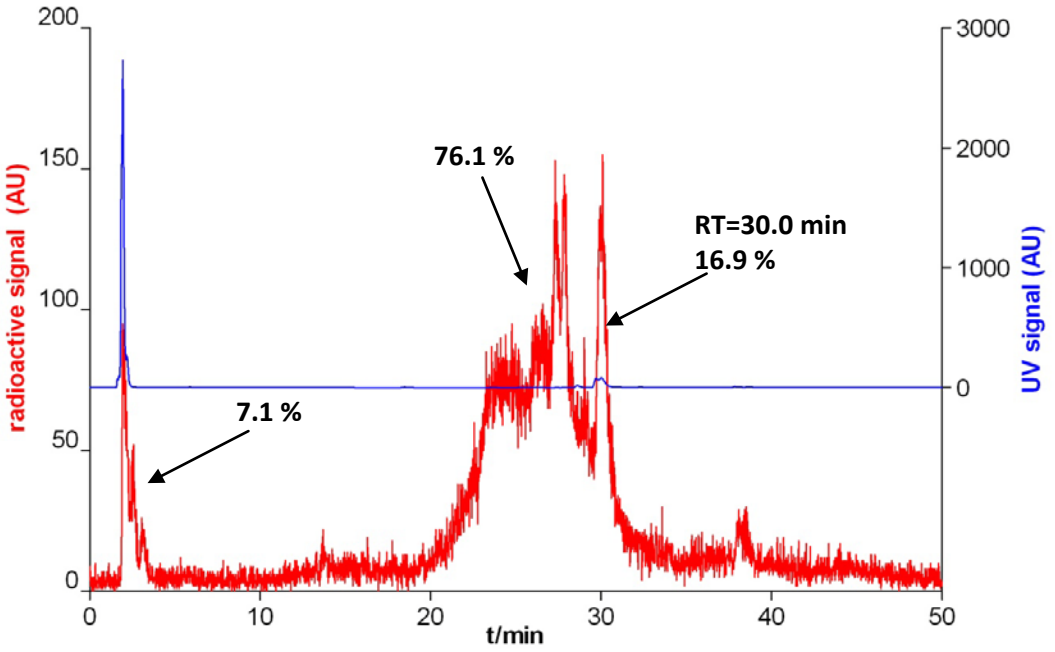

Figure 4.6: UV and radiochromatogram acquired after incubating the Tc-99m labelled sCTLys[18]-hynic-TFA in serum at 37°C for 20 hours.

The radiolabelled Tc-99m-sCTLys[18]-hynic-TFA was >99% pure based on ITLC and 95.5% pure based on HPLC (Figures 4.1-4.2). After a 60-minute

incubation (Figure 4.3) at 37°C in serum the number of (detected) isomeric complexes increased, the narrow peak at RT=28 min split to at least two more peaks. The ratio of unbound radioactivity slightly decreased to 3.1%. We also detected new radioactive species at RT=30 minutes accounting for 10.0% of the injected activity. The UV chromatogram contained a set of very intensive peaks representing serum proteins eluting after 30 min and a minor peak eluting at 28 min corresponding to serum constituents. After 120 (Figure 4.4) and 180 (Figure 4.5) minutes in serum, radiochromatograms did not change significantly. After 20 hours (Figure 4.6) the ratio of serum bound activity increased to 16.9%, the ratio of unbound activity doubled to 7.1% and as a result only 76.1% of the overall activity accounted for the Tc-99m labelled sCTLys^{18}-hynic-TFA. The UV peak associated with serum proteins significantly diminished in the UV spectrum and a major peak appeared at RT=2 min; this symptom is typical to overloaded HPLC columns. *N.B.* the very small UV peak that remained at RT=30min is probably the small fraction of proteins that is actually bound to the radiopeptide.

4.4.2 Serum stability of Tc-99m labelled sCT(8-32)Lys^{18}-hynic-TFA

Samples were analysed after 60 and 120 minutes in serum. A control (0 min) is also shown, that sample was analysed (ITLC and HPLC) just before adding the radiopeptide to serum. Note that neither the HPLC column (method 1) nor the machine (tubing) retained any measurable radioactivity as assessed after each run thus the radiochromatograms below account for the whole amount of injected activity. Similar to the full radiopeptide the abbreviated sequence could not be characterised by SEC: after the radiopeptide peak had eluted the radioactive signal did not return to background and remained at a level of approximately half of the peak height for several hours suggesting that the column retained and slowly

released a significant amount of the radiolabelled sCT(8-32)Lys^{18}-hynic-TFA. Therefore we only analysed the serum-radiopeptide mixtures by HPLC method 1.

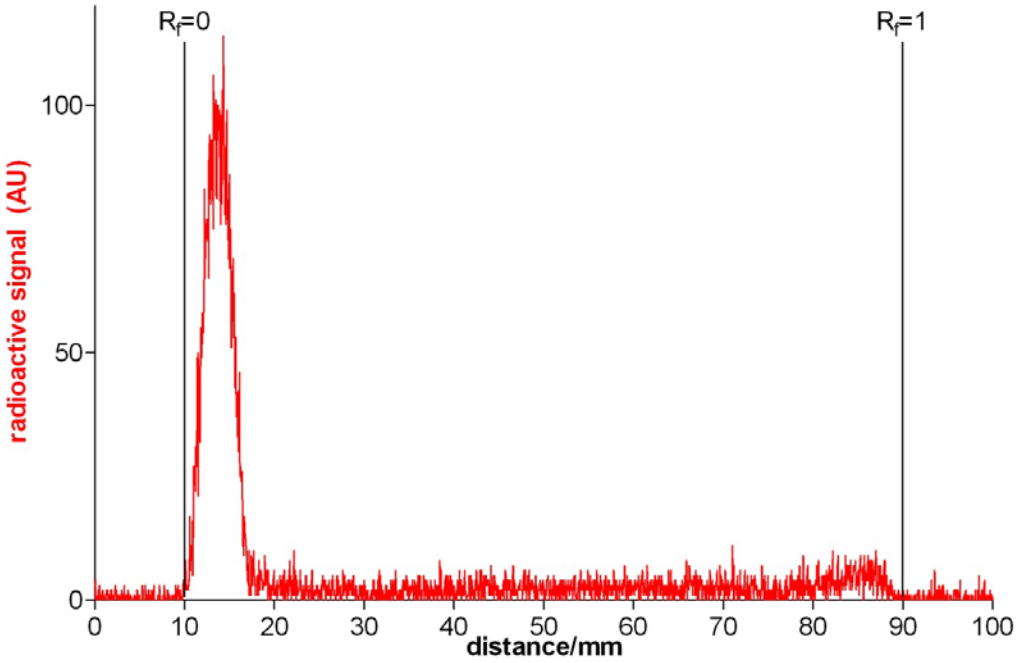

Figure 4.7: Radio ITLC of the Tc-99m labelled sCT(8-32)Lys^{18}-hynic-TFA at 0 min (control sample, no serum).

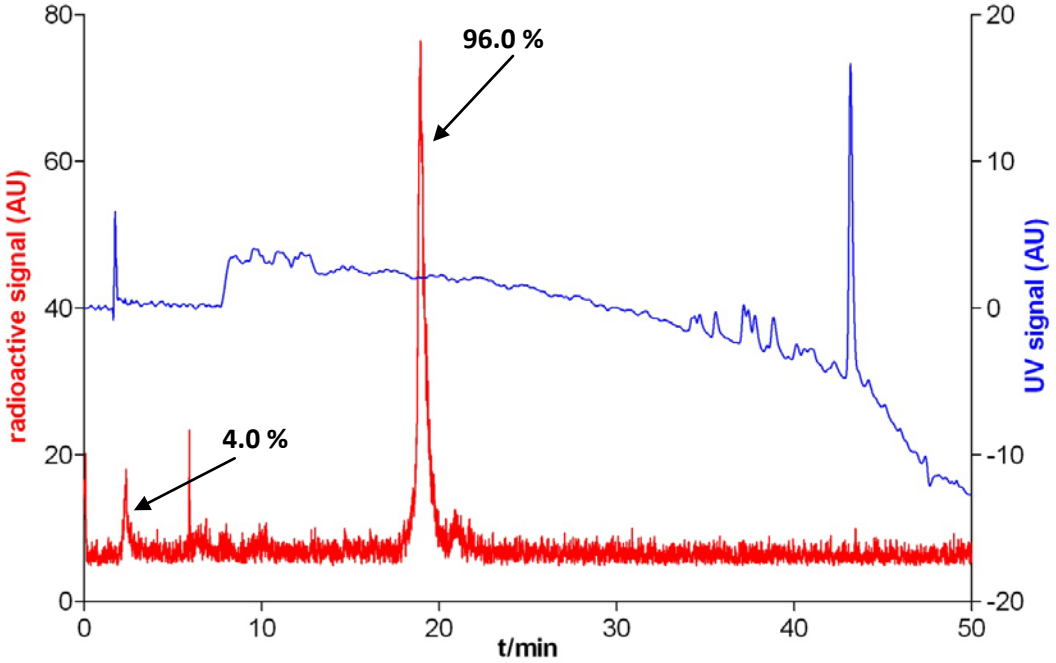

Figure 4.8: UV and radiochromatogram of the Tc-99m labelled sCT(8-32)Lys^{18}-hynic-TFA at 0 min (control sample, no serum).

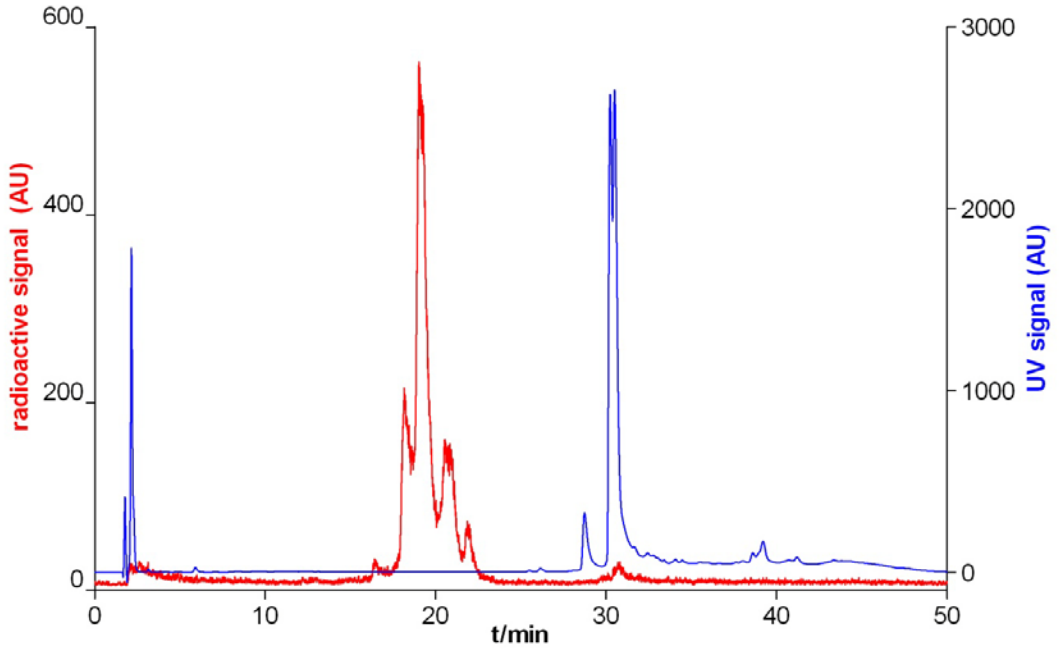

Figure 4.9: UV and radiochromatogram acquired after incubating the Tc-99m labelled sCT(8-32)Lys^{18}-hynic-TFA in serum at 37°C for 60 min.

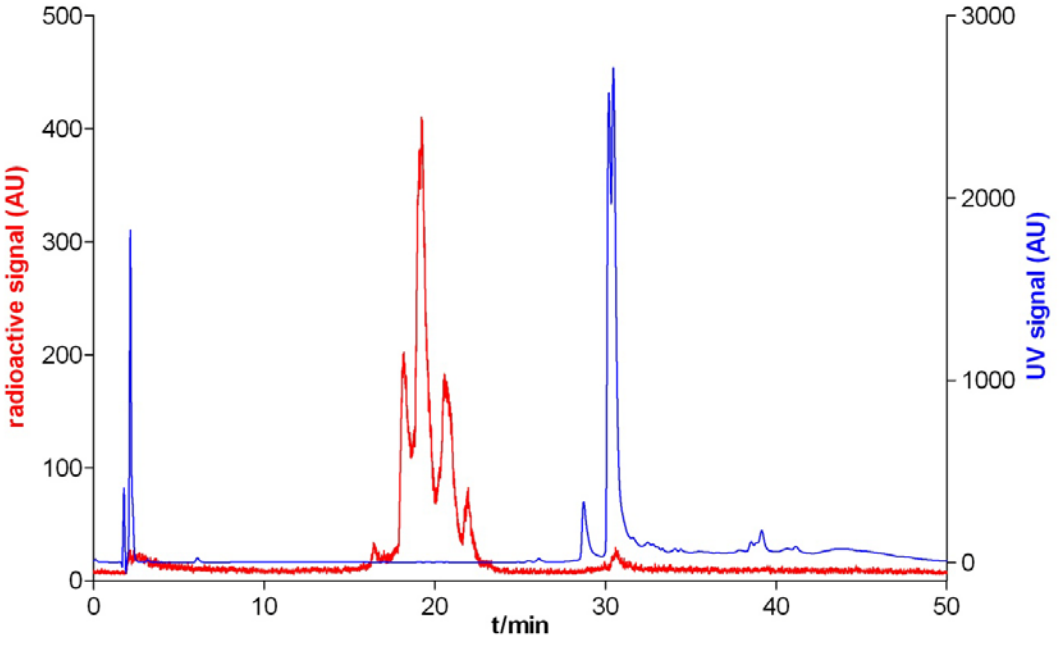

Figure 4.10: UV and radiochromatogram acquired after incubating the Tc-99m labelled sCT(8-32)Lys^{18}-hynic-TFA in serum at 37°C for 120 min.

The radiolabelled sCT(8-32)Lys^{18}-hynic-TFA peptide was ~100% pure as assessed by ITLC (Figure 4.7) and 96.0% pure as assessed by HPLC (Figure 4.8). After 60 minutes incubation in serum the peak representing the Tc-99m labelled

sCT(8-32)Lys^{18}-hynic-TFA split to a quadruplet of narrow peaks, RT=18-22 min (Figure 4.9) with no significant change occurring in the following 60 minutes (Figure 4.10).

4.4.3 Stability of Tc-99m labelled sCTLys^{18}-hynic-TFA on incubation in mouse kidney homogenate

The radiopeptide was incubated in a solution containing 5.5×10^6 cells in HBS. Initial RCP was 100% as assessed by ITLC. Samples were withdrawn after 5 (Figure 4.11), 60 (Figure 4.12) and 120 (Figure 4.13) minutes of incubation and processed as described above. After 5 minutes a large ratio of radioactivity was in the form of a small hydrophilic radioactive species (Figure 4.11) and by 60 minutes only a small "bump" represented the radiopeptide (Figure 4.12). Interestingly a number of intermediates appeared on the radiochromatogram after 60 minutes (RT=10-16 min) whose ratio significantly decreased by 2 hours (Figure 4.13). After 2 hours most of the radioactivity was in the form of a very hydrophilic radioactive species whilst the product peak completely disappeared with a minor set of peaks (degradation intermediates) being present (RT=10-16 min). The UV chromatograms contained a peak representing tricine at around RT=2.1 min and a set of peaks between RT=30-40 min.

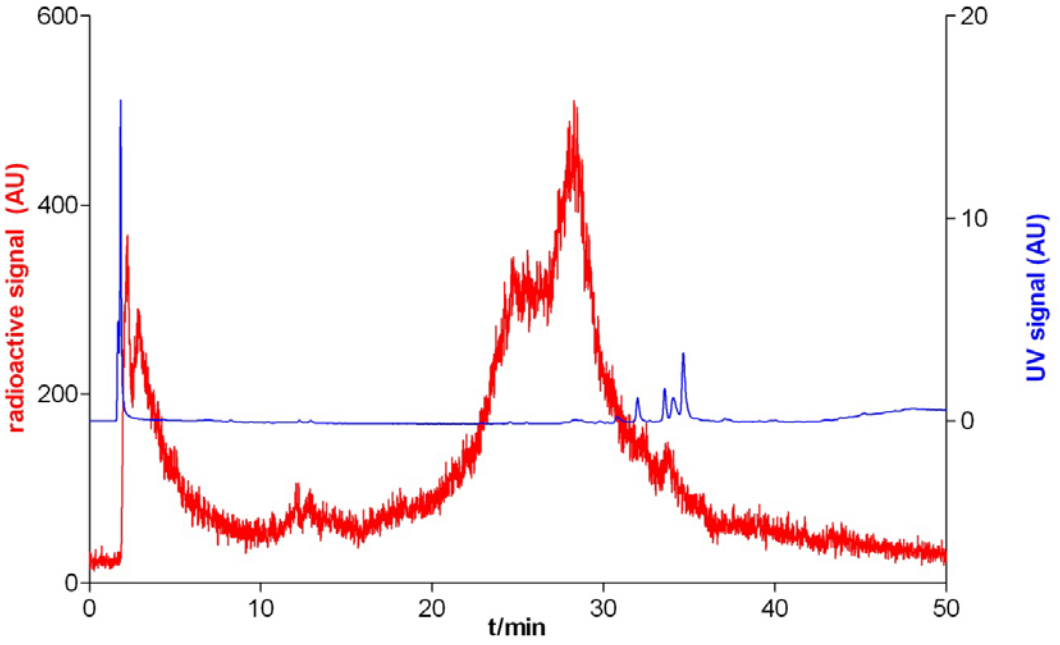

Figure 4.11: UV and radiochromatogram acquired after incubating the Tc-99m labelled sCTLys^{18}-hynic-TFA in mouse kidney homogenate at 37°C for 5 min.

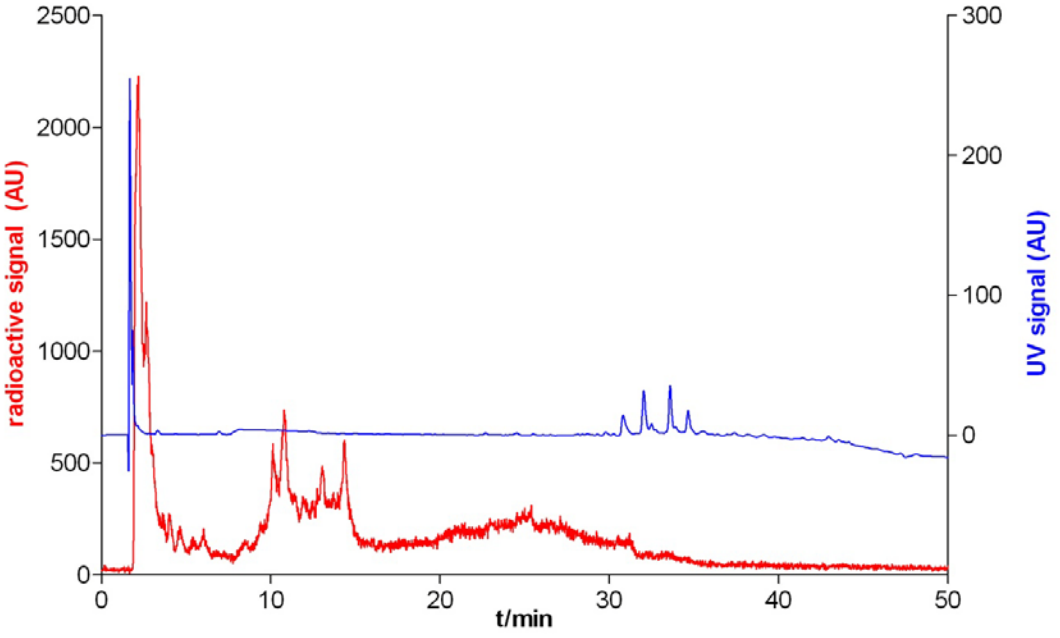

Figure 4.12: UV and radiochromatogram acquired after incubating the Tc-99m labelled sCTLys^{18}-hynic-TFA in mouse kidney homogenate at 37°C for 60 min.

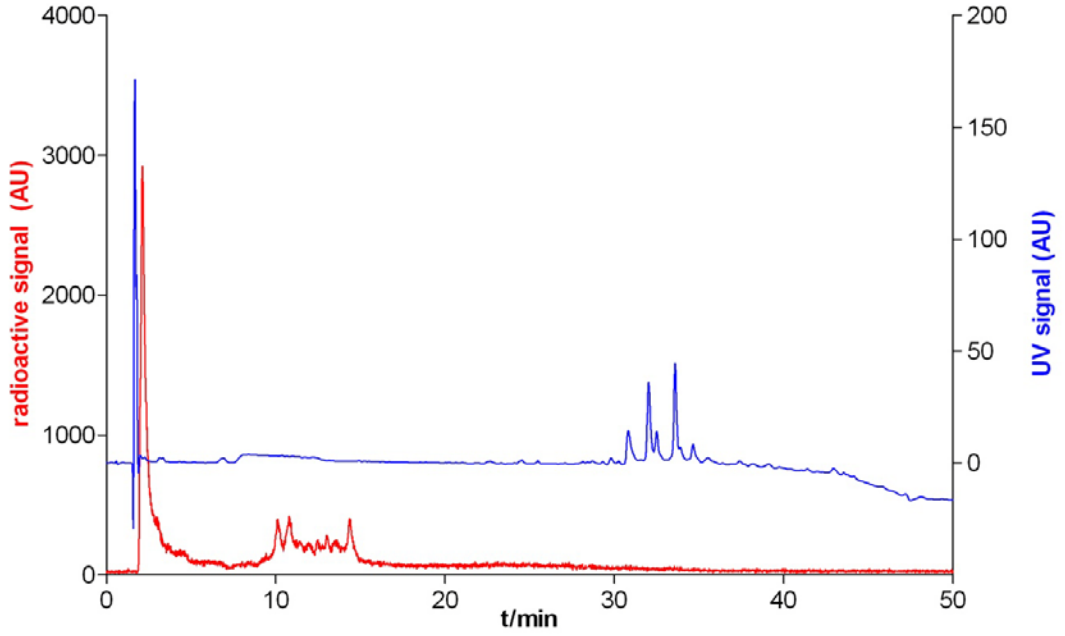

Figure 4.13: UV and radiochromatogram acquired after incubating the Tc-99m labelled sCTLys^{18}-hynic-TFA in mouse kidney homogenate at 37°C for 120 min.

4.4.4 Stability of Tc-99m labelled sCT(8-32)Lys^{18}-hynic-TFA on incubation in mouse kidney homogenate

The radiopeptide was incubated in a solution containing 4.8×10^{6} cells homogenised in HBS. Initial RCP was 100% (determined by ITLC). Samples were withdrawn after 5 (Figure 4.14), 60 (Figure 4.15) and 120 (Figure 4.16) minutes of incubation and processed as described above. After 5 minutes the peak representing the radiolabelled peptide split to four major peaks and a skewed peak representing small hydrophilic radioactive species was also present (Figure 4.14). After 60 minutes in kidney homogenate the radiopeptide was not detected in the sample. A set of peaks between 10-17 minutes and a major peak representing small hydrophilic species were present (Figure 4.15). After 120 minutes the radiochromatogram did not change significantly (Figure 4.16).

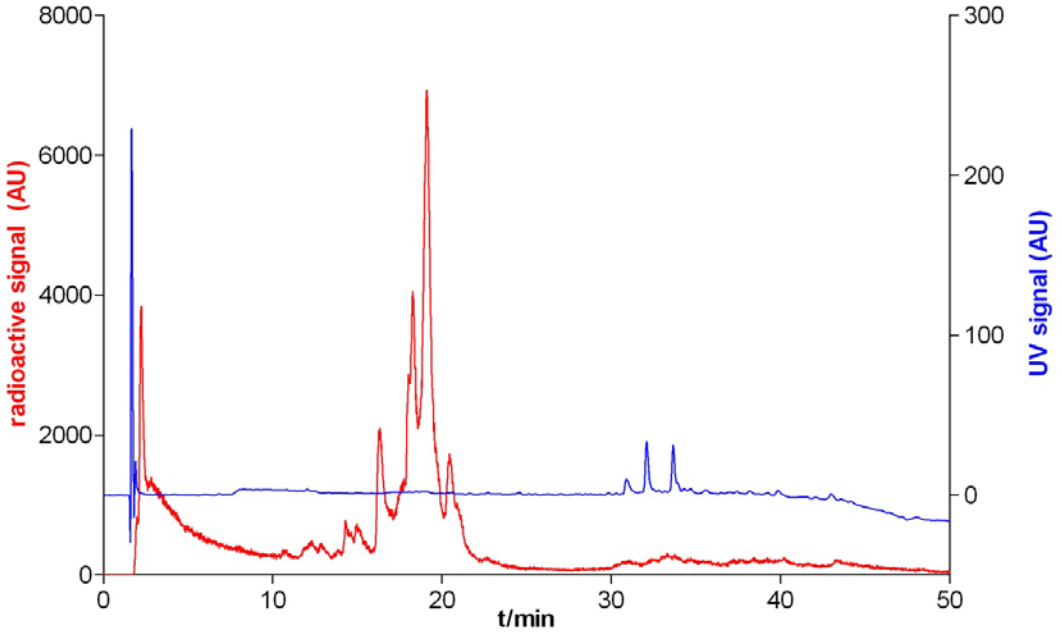

Figure 4.14: UV and radiochromatogram acquired after incubating the Tc-99m labelled sCT(8-32)Lys^{18}-hynic-TFA in mouse kidney homogenate at 37°C for 5 min.

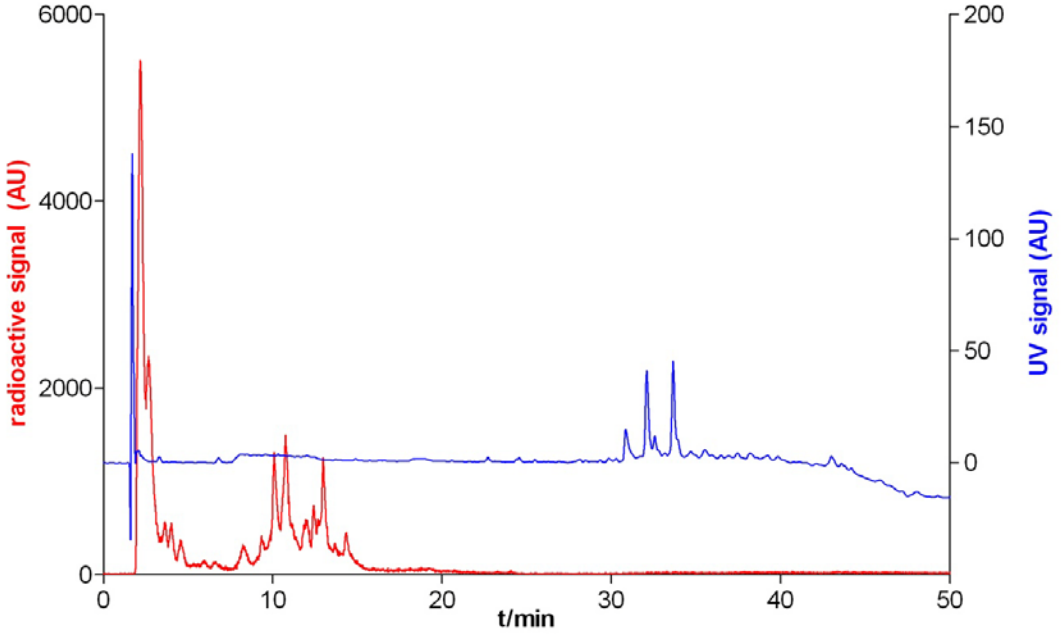

Figure 4.15: UV and radiochromatogram acquired after incubating the Tc-99m labelled sCT(8-32)Lys^{18}-hynic-TFA in mouse kidney homogenate at 37°C for 60 min.

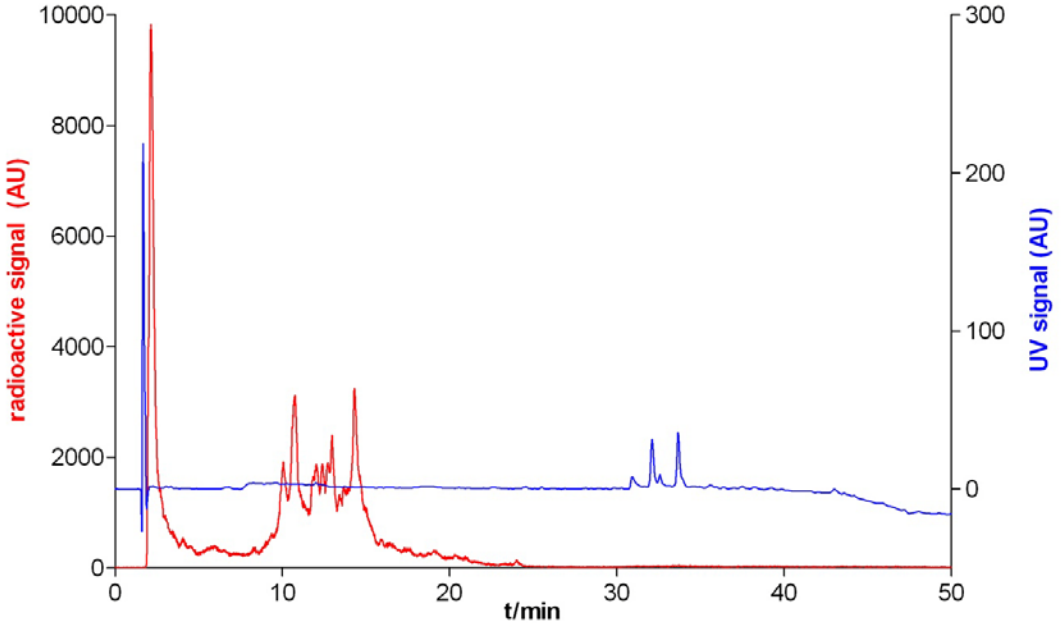

Figure 4.16: UV and radiochromatogram acquired after incubating the Tc-99m labelled sCT(8-32)Lys^{18}-hynic-TFA in mouse kidney homogenate at 37°C for 120 min.

4.5 Discussion

Before assessing its serum stability RCP of the sCTLys^{18}-hynic-TFA was assessed by HPLC and ITLC and results were conflicting: ITLC suggested >99% purity whilst RCP was only 95.5% based on the HPLC chromatogram. This finding is somehow controversial and is probably an artefact occurring in the HPLC. The impurity eluted at 2-2.5 min, a retention time associated with pertechnetate and the Tc-tricine complex (and possibly other small hydrophilic species). The radiochromatogram suggested the presence of multiple isomeric peptide species as previously seen (refer to Chapter 3, section 3.4.3). The UV chromatogram of the labelled radiopeptide did not contain any product peaks as expected since the concentration was so low.

Upon incubation in serum even after 1 hour the shape of the “peak” representing the radiopeptide markedly changed suggesting the formation of

fragments or isomers. Using the same radiopeptide but different HPLC gradient Greenland reported that the initially single and sharp peak representing the Tc-99m labelled sCTLys^{18}-hynic-TFA became significantly broader after a 30 minute incubation in serum and commented that this finding may also be due to the formation of ternary complexes with small molecules in serum. We should also note that in theory tricine, which is not a strong chelator for Tc-99m could be replaced (ligand exchange) by another strong(er) chelating compound present in serum. Apart from broadening of the product peak he found that the radiopeptide remained stable for 30 minutes with no radioactivity being released [114].

A radioactive peak emerged at RT=30.0 min (Figure 4.3-4.6); based on the UV chromatogram this radioactivity could be associated with serum proteins. This finding is not completely unexpected as *e.g.* Ono and co-workers reported on transchelation occurring between Tc-99m labelled hynic-conjugated peptides and serum proteins [161]. The minor peak appearing in the UV chromatogram at RT=2 min is related to tricine co-ligand whilst the larger peak at RT=2.5 min (Figure 4.3) is associated with small hydrophilic molecules in serum. Regarding serum protein-binding findings conflict with the results of Greenland who found no serum protein-binding after a half an hour incubation in serum [114]. Since he did not assess stability for longer we cannot compare our data directly, although it is unlikely that trans-chelation to serum proteins only begins after 31 minutes of incubation. We could argue that the radioactive peak arising at RT=30.0 min is an isomeric Tc-99m sCTLys^{18}-hynic-TFA complex and the fact that it elutes the same time as serum proteins is just coincidence. This explanation would resolve the above conflict. However we have no experimental evidence that would support this assumption. SEC normally separates radiopeptides from serum proteins better than reverse phase

chromatography; unfortunately SEC turned out to be useless when we tried to use it to characterise the hynic-sCT radiopeptides.

In terms of binding the radiometal the Tc-99m labelled sCTLys^{18}-hynic-TFA was fairly stable in serum, after 20 hours only 7.1% of the activity was released from the radiopeptide. *N.B.* the new peak emerging at RT=30 min was probably protein associated radiopeptide formed via trans-chelation to serum proteins. After 60 minutes radiochromatograms did not change significantly suggesting that equilibrium in the formation of isomers/fragments was reached in the first 60 minutes.

When assessing the RCP of the Tc-99m labelled sCT(8-32)Lys^{18}-hynic-TFA prior to incubation in serum we found that ITLC and HPLC chromatograms conflicted with each other, similarly to the full length radiopeptide. In this case it is likely that we simply did not inject enough of the sample for accurate detection in the HPLC (Figure 4.8).

Before adding the abbreviated radiopeptide to serum it was represented by a single narrow peak at RT=19 min on the HPLC chromatogram (Figure 4.8) as described earlier (Chapter 3, section 3.4.3). Since the initial product peak was a singlet suggesting the presence of a single isomeric species or that our HPLC method is unable to separate the isomeric complexes it is likely that the 3 “new” product peaks emerging after 60 minutes in serum (Figure 4.9) are ternary peptide complexes or complexes where the tricine co-ligand had been exchanged for/partially replaced by a small serum molecule. It is noteworthy that only a negligible amount of radioactivity was bound by serum proteins even after 120 minutes (Figure 4.10) whilst assuming that the peak appearing in Figures 4.3-4.6 represented a serum-bound fraction of the full radiopeptide sequence 11.3% of the Tc-99m labelled

sCTLys^{18}-hynic-TFA peptide was bound by serum proteins after 2 hours (Figure 4.4). The coordination sphere of Tc-99m in the radiolabelled sCT(8-32)Lys^{18}-hynic-TFA peptide is assumed to be identical to the coordination sphere of the radiometal in the full radiopeptide and the secondary structures of the sequences are also meant to be very similar as this is the reason why the abbreviated sequence would bind to the receptor. The presence of the first seven amino acids may be involved in a steric or electronic effect that facilitates serum protein binding. Another possibility is that disulfide bond exchange may cause links to other molecules or peptide degradation by serum peptidases.

Based on the above data the Tc-hynic bond in the Tc-99m labelled sCT(8-32)Lys^{18}-hynic-TFA peptide, similarly to the full hynic-sCT sequence is stable in serum for at least 2 hours although several new radioactive peptide species appear after a 60 minute incubation in serum with retention times very similar to that of the labelled radiopeptide suggesting some alterations in the coordination sphere of the radiometal.

After a 5 minute incubation in mouse kidney homogenate (Figure 4.11) the radiolabelled sCTLys^{18}-hynic-TFA released some activity in the form of hydrophilic species eluting between RT=2-5 min (skewed peak), the shape of the peptide peak became similar to what we had observed upon incubating the radiopeptide in serum. Similarly to the full hynic-calcitonin sequence the Tc-99m labelled sCT(8-32)Lys^{18}-hynic-TFA released some radioactivity in the form of hydrophilic radioactive species (Figure 4.14) upon a 5 minute incubation in mouse kidney homogenate and the peak pattern of the radiopeptide became very similar (*i.e.* a quadruplet of peaks) to the peak pattern developing upon incubation in serum suggesting that an analogous isomerisation or ligand exchange process occured.

Incubation of the Tc-99m labelled sCTLys^{18}-hynic-TFA and sCT(8-32)Lys^{18}-hynic-TFA in mouse kidney homogenate resulted in the formation of radioactive degradation intermediates appearing in the region of RT=9-16 min within an hour (Figures 4.12 and 4.15). Based on our previous experience small peptides elute in this region. The UV traces suggest the presence of protein fractions in the homogenate with retention times similar to those of serum proteins (RT=31-35 min, *e.g.* Figure 4.12) but we did not detect protein-bound radioactivity.

Based on chromatography data obtained after 120 minutes (Figure 4.13 and 4.16) by which time the peaks representing the labelled peptides completely disappeared and those corresponding to degradation intermediates diminished the final degradation product was a small hydrophilic species eluting at RT=2.5 min. A major UV peak emerging at around RT=2.5 min, a retention time matching that of tricine suggested that the final product could be a Tc-tricine complex or another very hydrophilic species that runs through the C-18 column without interaction.

4.6 Conclusions

We assessed the serum stability of the Tc-99m labelled sCTLys^{18}-hynic-TFA and Tc-99m labelled sCT(8-32)Lys^{18}-hynic-TFA peptides. We found that both radiopeptides were fairly stable in serum for at least 2 hours *i.e.* they did not release radioactivity and there was minimal binding of radioactivity to serum proteins. After being incubated in serum for 60 minutes both peptides presented a set of new radioactive species with retention times very similar to those of the radiopeptides. These species are likely to be either isomeric Tc-tricine-hynic-peptide complexes or ternary complexes where the tricine co-ligand had partially been replaced by a small serum molecule or newly-formed complexes where the tricine moiety had been

exchanged for a small serum molecule. We did not observe significant binding of Tc-99m to serum proteins or the release of small hydrophilic species.

Incubating the radiopeptides in kidney homogenates suggested that both compounds are metabolised very rapidly resulting mainly in very hydrophilic radioactive species.

4.7 Summary

We assessed the *in vitro* stability of the Tc-99m labelled sCTLys^{18}-hynic-TFA and sCT(8-32)Lys^{18}-hynic-TFA. We found that both radiopeptides were stable on incubation in human serum. Thus if they retained their affinity to CTR (this is to be assessed by *in vitro* uptake experiments) they could be used to image CTR+ lesions *in vivo*.

Chapter 5: *In vitro* uptake of Tc-99m labelled sCTLys^{18}-hynic-TFA and Tc-99m labelled sCT(8-32)Lys^{18}-hynic-TFA radiopeptides in MCF-7 breast cancer cells

5.1 Aims

In this set of experiments we aimed to establish whether the Tc-99m labelled hynic-calcitonin peptides retain their affinity to CTR using the CTR+ MCF-7 breast cancer cell line. We aimed to establish the time course of uptake to find the optimal time point for later inhibition assays and investigate whether uptake of the radiopeptides was specific in an inhibition assay with ascending concentrations of cold (*i.e.* non-radioactive) sCT.

5.2 Introduction

Greenland carried out a preliminary uptake study with the Tc-99m labelled sCTLys^{18}-hynic-TFA on MCF-7 breast cancer cells (*N.B.* the cell line does express CTR). He found that MCF-7 cells took up the radiopeptide after 30 minutes of incubation and that 1 μM sCT completely blocked the uptake [114, 115]. Since the current study is focussing on targeting MM (and evaluating the radiopeptide in the 5T33 murine MM model), refer to Chapters 6-7 we had intended to use 5T33 murine MM cells for *in vitro* evaluation too. However FACS analysis suggested that 5T33 cells are CTR- *in vitro* (see Chapter 7) thus we decided to use the MCF-7 cell line.

5.3 Materials and methods

5.3.1 Materials

MCF-7 cells were obtained from a master stock prepared by Dr. Amanda Weeks at the Division of Imaging Sciences. Cells were maintained in culture medium 1 (Appendix 6) in T75 or T175 tissue culture flasks in a tissue culture incubator (5% CO_2 in 95% air) with humidified atmosphere at a constant temperature of 37°C and passaged after a gentle scraping every 4-5 days and diluted at a ratio of 1:5-1:6 for maintenance (approximate concentration 2×10^5 cells/ml). Lyophilised sCT was purchased from Cambridge Biosciences (cat. no. SP2557a) and kept at -80°C until use. Radioactive samples were measured on a Wallac 1282 Compugamma Universal Gamma Counter.

5.3.2 Experimental protocols

2×10^5 MCF-7 cells in 1 ml of culture medium 1 were plated in each well of a 24-well plate. 1 ml culture medium 1 (with no cells) was added to 4 wells in each set of experiment to correct for non-specific binding to plastic (negative control). Uptake studies were carried out 3 days later when cells had formed a confluent and strongly adherent layer at the bottom of wells.

For kinetic studies 1/10,000 of a labelled kit, corresponding to 10 kBq of radiolabelled hynic-sCT were added to each well (0.28 nM (full sequence)/0.34 nM (abbreviated sequence) final maximum carrier concentration). Plates were sealed, gently shaken for 2 minutes then incubated at 37°C in a tissue culture incubator. At every time point (15, 30, 60, 120) 4 wells were processed as described below.

An inhibition assay was carried out to assess the specificity of the uptake of Tc-99m labelled sCTLys^{18}-hynic-TFA. Ascending amounts of sCT (inhibitor) in 30

µl of PBS were added to wells resulting in a final concentration of 0 (positive control), 3.3, 10, 25, 50, 100, 250, 500 nM of sCT (each point in quadruplets). No sCT was added to negative control wells. After addition of the blocking agent plates were sealed and gently shaken for 1 minute and 1/6,000 of a labelled kit in 30 µl PBS was added to each well corresponding to approximately 25 kBq or 1.67 ng or 0.45 nM sCTLys^{18}-hynic-TFA carrier. Plates were sealed and shaken again for 1 minute then kept in a tissue culture incubator for 2 hours and processed according to the protocol below. Note that since peptide content of the hynic-peptides was well below 1 the carrier concentrations reported above are in fact theoretical maximum carrier concentrations; actual carrier concentrations were much lower.

To assess the specificity of the uptake of Tc-99m labelled sCT(8-32)Lys^{18}-hynic-TFA the same assay was carried out using 0 (positive and negative controls), 1.25, 2.5, 5, 10, 25, 50, 100, 1000 nM cold sCT in quadruplets. After gentle mixing 1/10,000 of a labelled sCT(8-32)Lys^{18}-hynic-TFA kit was added to each well, corresponding to 25 kBq or 1 ng or 0.34 nM sCT(8-32)Lys^{18}-hynic-TFA carrier. After gentle mixing plates were kept in a tissue culture incubator for 2 hours and processed according to the protocol below.

After incubation with one of the radiopeptides and cold sCT (optional for inhibition assays) contents of wells were processed as follows:

1. The supernatant (1ml) was removed using a 1 ml pipette
2. Wells were washed with 3×1 ml of ice-cold PBS
3. 0.5 ml 1 M NaOH were added to wells to detach and lyse the cells
4. After a 5-minute incubation in a tissue culture incubator cell lysates were pipetted against the bottom of the well several times then transferred into a pre-labelled FACS tube

5. Wells were washed with 1×1 ml of ice-cold PBS to remove residues of cell lysates. The washing medium was added to the FACS tube containing the appropriate cell lysate.

FACS tubes were sealed and gamma counted. The average non-specific binding was calculated as the mean count rate of the 4 negative control samples in every experiment. This value was then subtracted from the count rate of every cell lysate (corrected uptake). Corrected uptake values, defined as the difference of the measured count rate and the sum of the average "uptake" in negative control wells (*i.e.* non-specific binding to plastic) and the average background count rates were calculated. Average corrected uptake values and SEM were then calculated for each quadruplet.

5.3.3 Data analysis

Inhibition assays were evaluated using Prism 5.04 for Windows. For each quadruplet total inhibitor concentration was calculated as the sum of carrier concentration (either 0.45 or 0.34 nM) and the concentration of cold sCT added. Average corrected uptake values were plotted as a function of the logarithm of total inhibitor concentration and a sigmoidal dose-response curve was fitted in no more than 1000 iterative steps then IC50 values were calculated.

5.4 Results

5.4.1 Time course of the uptake of radiolabelled hynic-calcitonin peptides

Results of the uptake experiments are shown in Figures 5.1-5.2. Non-specific binding to the plastic was 265±56 cpm (Tc-99m-sCTLys^{18}-hynic-TFA) and 54±16 (Tc-99m-sCT(8-32)Lys^{18}-hynic-TFA) and had been subtracted from the data

presented in Figures 5.1-5.2. Uptake of the radiopeptides increased with time and was the highest after 120 minutes.

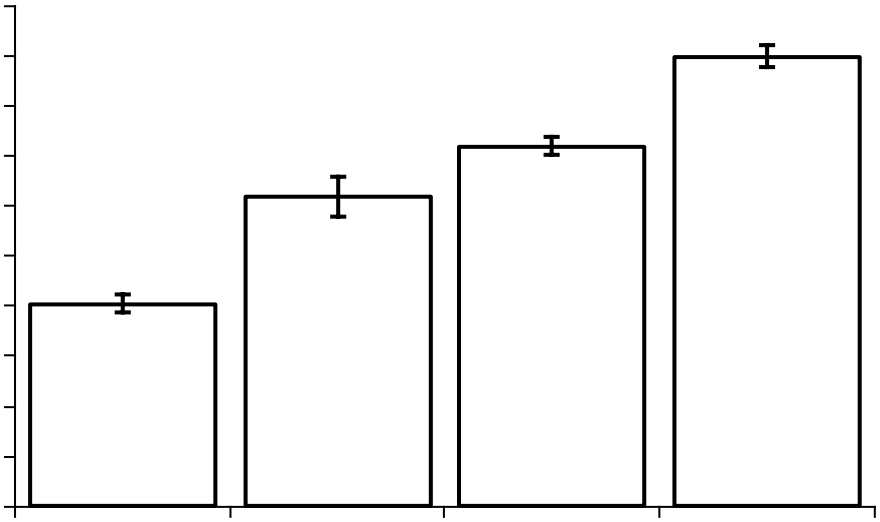

Figure 5.1: Uptake of the Tc-99m labelled sCTLys^{18}-hynic-TFA in MCF-7 cells at different time points.

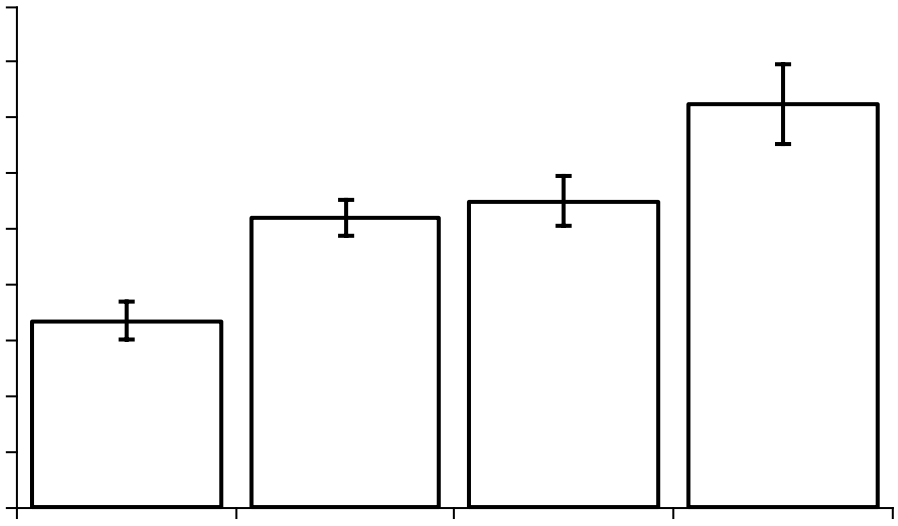

Figure 5.2: Uptake of the Tc-99m labelled sCT(8-32)Lys^{18}-hynic-TFA in MCF-7 cells at different time points.

5.4.2 Inhibition assays

Inhibition curves are shown in Figures 5.3-5.4. Note that SEM of each data point is shown on the graphs, in some cases it was very low hence cannot be seen. Based on the graphs ascending amounts of sCT gradually blocked the uptake of the Tc-99m labelled sCTLys^{18}-hynic-TFA and sCT(8-32)Lys^{18}-hynic-TFA and 100 nM of sCT completely blocked the uptake of both radiopeptides. We found that IC50 values were 7.3±1.1 nM (mean±SEM) with sCTLys^{18}-hynic-TFA and 4.8±1.1 nM (mean±SEM) with sCT(8-32)Lys^{18}-hynic-TFA.

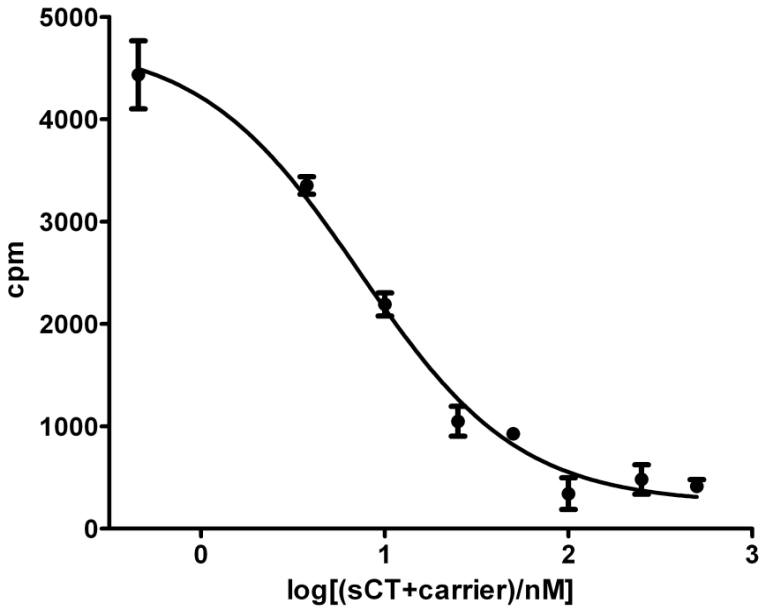

Figure 5.3: Results of the inhibition assay with Tc-99m labelled sCTLys^{18}-hynic-TFA and sCT.

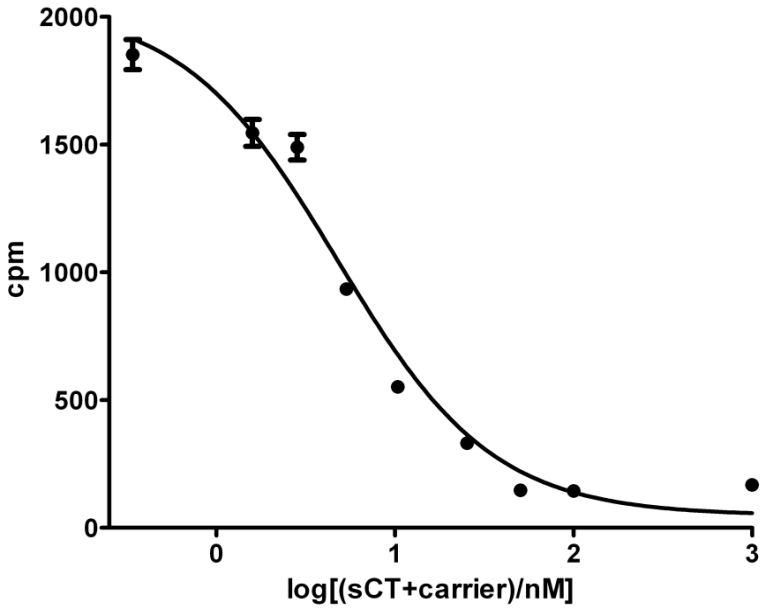

Figure 5.4: Results of the inhibition assay with Tc-99m labelled sCT(8-32)Lys^{18}-hynic-TFA and sCT.

5.5 Discussion

Greenland's results suggested that the Tc-99m labelled sCTLys^{18}-hynic-TFA was a ligand for CTR *i.e.* it was taken up by CTR+ MCF-7 cells and uptake could be blocked by a large excess of cold sCT [114, 115]. Our time course experiments confirmed Greenland's results *i.e.* the full hynic-sCT sequence was taken up by MCF-7 cells. Time course experiments suggested that the abbreviated sequence was also taken up by MCF-7 cells. Note that time course experiments with the two radiopeptides were carried out on different days, hence actual count rates from the two sets of experiments should not be compared to one another. We found that uptake gradually increased with time and was high enough after 2 hours therefore decided to carry out the inhibition assays after 2 hours of incubation. This thesis did not aim to give a full characterisation on the *in vitro* receptor binding properties of the hynic-calcitonin derivatives therefore we did not assess uptake in later timepoints. We only aimed to prove that both peptides were taken up by CTR+ cells

and their uptake was specific (inhibition assays) so that we can justify *in vivo* imaging experiments and in case of a positive outcome get closer to their translation into human medicine. We speculated that very long incubation of the labelled hynic-peptides and cold sCT with live cells could potentially have caused problems.

By using ascending amounts of cold sCT we confirmed Greenland's preliminary data *i.e.* uptake of Tc-99m labelled sCTLys^{18}-hynic-TFA in MCF-7 cells was specific. We found that uptake of the abbreviated sequence was also specific and inhibition curves as well as the actual IC50 values were very similar to each other. In other words we proved that hynic conjugated sCT will retain its biological affinity if we eliminate the (highly conserved) first seven amino acids hence the intramolecular disulfide bond from the sequence.

Given that IC50=[radioligand]+K_d (for evaluation of the binding equation see *e.g.* the Prism software) and the large molar excess of hynic-peptide to Tc-99m-pertechnetate the amount of Tc-99m labelled sCTLys^{18}-hynic-TFA or sCT(8-32)Lys^{18}-hynic-TFA was negligible compared to the amount of free (unlabelled) sCTLys^{18}-hynic-TFA or sCT(8-32)Lys^{18}-hynic-TFA (refer to Chapter 3 or an overview is given by Meszaros *et al.* [149]) thus in equation 1 [radioligand]≈0 and IC50=K_d. As a result K_d(Tc-99m-sCTLys^{18}-hynic-TFA)=7.3±1.1 nM and K_d(Tc-99m-sCT(8-32)Lys^{18}-hynic-TFA)=4.8±1.1 nM. These data even suggest that the abbreviated sequence has slightly higher affinity to the receptor than the full hynic-calcitonin sequence although the difference is not statistically significant.

To summarise both radiopeptides bind to CTR with a nanomolar affinity. Greenland evaluated the I-125-iodo-Tyr^{22}-sCT gold standard and found an average K_d of 209 pM. Note that replacing one hydrogen with iodine on a tyrosine residue results in a very minor structural modification whereas attaching a Tc-hynic-tricine

complex to a peptide sequence is likely to evoke significant changes in its hydrophilicity and secondary structure. Therefore the fact that both Tc-99m labelled hynic-calcitonin analogues (and especially the abbreviated one) had nanomolar affintity to CTR looks very promising.

5.6 Conclusions and summary

We proved that both the Tc-99m-sCTLys^{18}-hynic-TFA and Tc-99m-sCT(8-32)Lys^{18}-hynic-TFA were taken up by CTR+ MCF-7 cells and uptake was specific *i.e.* it could be blocked in a dose dependent manner by adding cold sCT. Therefore both radiopeptides are suitable ligands for CTR and could potentially be used for *in vivo* imaging. The combined stability data and receptor binding assays confirm that an *in vivo* study is justified and not unethical on the basis of *in vitro* results.

Chapter 6: The 5T33 murine MM model

6.1 Aims

In this chapter we aim to give a brief overview on the 5T33 murine MM model and assess whether it is suitable for the *in vivo* evaluation of the Tc-99m labelled sCTLys^{18}-hynic-TFA and sCT(8-32)Lys^{18}-hynic-TFA.

6.2 Introduction

We are pleased to have access to the non-commercialised murine MM model, the enhanced green fluorescent protein transfected 5T33 cell line (eGFP-5T33) (kindly provided by Dr Abedi-Valugerdi, Division of Hematology, Department of Medicine, Karolinska Institutet at Karolinska University Hospital, Stockholm, Sweden). The cell line has been studied at Department of Haematological Medicine at King's College London for a number of years. Thus we decided to use it for the *in vivo* evaluation of the Tc-99m labelled hynic conjugated sCT derivatives. Compared to MM xenograft models (*e.g.* intrafemoral U266 xenografts [162]) this is a syngeneic disease model hence it does not require the use of immuno-compromised animals (*vide infra*).

6.3 The 5T murine model of MM

In the late 1980's Radl and co-workers found that C57BL/KaLwRij mice older than 2 years spontaneously develop MM with a relatively high incidence (1:200). In their early study they described and characterised 9 different MM subtypes occurring in the inbred strain [163]. Due to their very high genetic similarity the disease can be transferred from one mouse to another by a simple i.v. inoculation. All but one of the nine 5T (*e.g.* 5T2, 5T33) sublines presented osteolytic

lesions and high serum Ig values and therefore mimicked the human disease. Moreover lesions were usually (but not exclusively) restricted to the BM and other haematopoietic organs (that is the spleen and liver). Radl and colleagues found that MM cells first appeared focally in the BM and then as the disease progressed malignant cells gradually replaced the normal haematopoietic tissue. Focal destruction of the cortical bone was also described, with high intensity in the proximity of blood vessels. In more progressed stages MM cells broke through the bone and were present in surrounding tissues (mainly muscles) as well. *N.B.* till 1992 5T cell lines were maintained and passaged *in vivo*. Attempts to culture the cell lines *in vitro* whilst retaining their properties led to success in 1992 when Manning and co-workers reported on the successful isolation and *in vitro* culturing of the 5T33 cell line [164]. The same study gives a thorough description of the 5T33 *in vivo* MM model. The most noteworthy finding was that i.v. inoculation with only 500 5T33 cells could result in paralysis and death 36 days after inoculation. Progression of the disease correlates well with the number of injected cells (Figure 6.1).

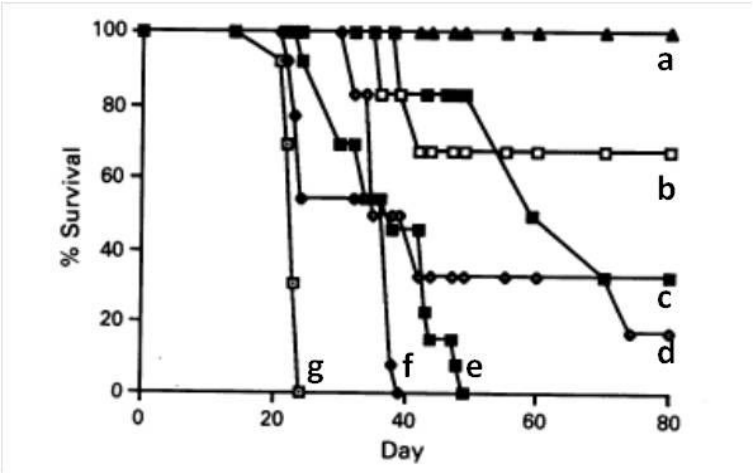

Figure 6.1: Effect of i.v. injection of 5T33 MM cell numbers on survival of C57Bl/KaLwRij mice. Mice were inoculated i.v. with 100 (a), 500 (b), 1000 (c), 5000 (d), 10^4 (e), 10^5 (f) and 10^6 (g) 5T33 cells; n=6-13 per group. Graph reproduced from [164].

In 1997 Garrett *et al*. also established a 5T33 cell line originating from a different *in vivo* passage; one of the authors was Radl who first described the 5T lines [165]. Properties of the "newly isolated" line were evaluated and were basically the same as those described by Manning *et al.* earlier. Garrett and co-workers evaluated blood ionised calcium levels of MM bearing C57Bl/KaLwRij mice and found elevated calcium levels 2 weeks post-injection of 10^5 5T33 cells. Hypercalcaemia became more and more severe as the disease progressed [165]. A number of studies using the 5T33 model were published soon after the *in vitro* culturing of the cell line had become possible [166-169].

A detailed study on the 5T disease models (5T33 and 5T2) was published by Vanderkerken and co-workers. The paper gives a thorough description and comparison of the above models [168]. Distribution of MM lesions was evaluated by histological examination, using antibodies developed against the M-proteins produced by the MM cell lines. Results (Figure 6.2) suggest that the 5T33 model is more aggressive than the 5T2 one. Not only the time points were different (4 *vs.* 13 weeks): only 10^5 cells were used to inoculate the animals with the 5T33 subtype whilst 2×10^6 cells were injected in the 5T2 model. Kinetic studies using the 5T33 model suggest that lesions become detectable in the BM, spleen and liver at the same time point (*i.e.* after 2 weeks when using 10^5 cells/mouse). However, kidneys, testes, lungs, intestines, the heart, blood and thymus remain disease-free confirming the high stroma-dependency of 5T33 cells [168].

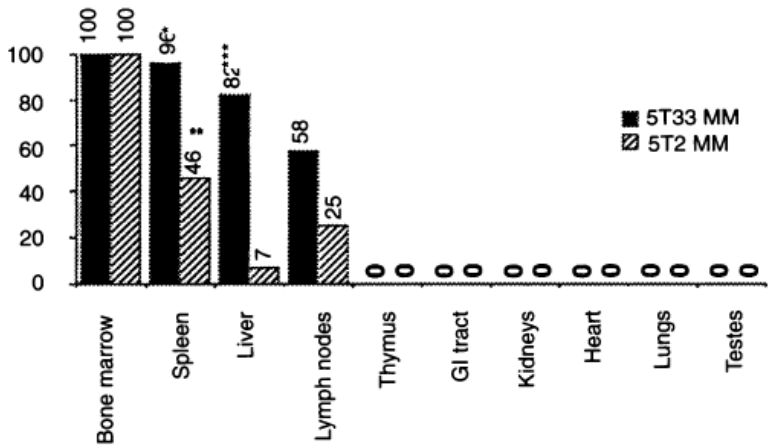

Figure 6.2: Organ involvement in the 5T2 and 5T33 murine MM models. Thirty mice were inoculated with 2×10^6 5T2 cells and sacrificed 13 weeks after inoculation (grey bars). Thirty mice were inoculated with 10^5 5T33 cells and sacrificed 4 weeks after inoculation (black bars). *: 20-30-fold splenomegaly, **: 1.5-fold splenomegaly, ***; 3-fold hepatomegaly. Note: The y axis refers to the percentage of animals whose organs were affected by the disease. Graph reproduced from [168].

Vanderkerken *et al.* assessed early tissue distribution in the 5T2 model using Cr-51 labelled 5T2 cells. Their results are summarised in Figure 6.3 [170]. They found that an hour after inoculation most of the radioactivity was present in the liver, spleen, BM, lungs (probably due to cells getting retained in microcapillaries), kidneys and urine (due to excretion of Cr-51 released from cells). With time activity disappeared from the lungs and ratio of injected activity increased in the liver, spleen and more markedly in the BM (refer to Figure 6.3). These data suggest that 5T2 cells have a very high affinity to the liver, spleen and BM and home in the above organs from very early stages.

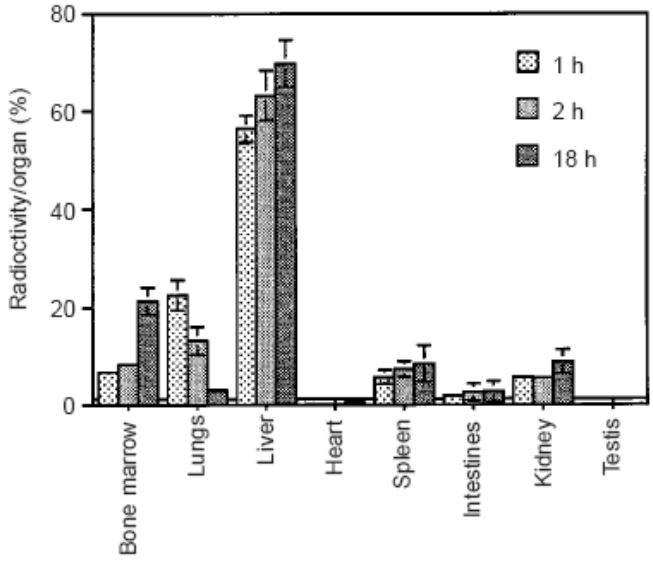

Figure 6.3: Early tissue distribution of Cr-51-labelled 5T2MM cells in C57BL/KaLwRij mice. Mice were inoculated i.v. and sacrificed 1, 2 and 18 h after inoculation (n=4/group). BM represents the radioactivity of ribs, vertebrae and fore and hind legs. Figure was reproduced from [170].

In 2004 Alici *et al.* transduced the eGFP DNA in the 5T33 cell line without causing significant alterations to its (*in vitro*) behaviour [169]. A kinetic study was carried out after i.v. inoculation of C57BL/KaLwRij mice with 10^5 fluorescent cells. Mice were sacrificed at different time points and certain organs were homogenised and analysed by FACS to assess the size of the eGFP+ cell population. Results summarised in Table 6.1 suggested the main organs involved in the 5T33 MM are the BM, spleen and liver. Disease progress was not completely uniform *i.e.* some animals were paraplegic whilst others had no outward symptoms by 4 weeks. BM MM cell counts in paraplegic animals were significantly higher than in asymptomatic subjects at the same time point.

	1	2	3	4 (no paraplegia)	4 (paraplegia)
Bone marrow	0.03 (0.02)	0.04 (0.02)	0.33 (0.18)	3.11 (0.14)	12.98 (1.86)
Spleen	0.06 (0.02)	0.60 (0.04)	1.93 (0.45)	3.92 (0.40)	3.66 (1.54)
Liver	0.07 (0.08)	0.20 (0.02)	0.33 (0.08)	2.20 (0.53)	1.81 (0.22)
Lymph nodes	0.02 (0.02)	0 (0)	0.50 (0.17)	0.63 (0.19)	0.72 (0.10)
Thymus	0 (0)	0 (0)	0 (0)	0 (0)	0 (0)

Table 6.1: Tissue distribution of eGFP-5T33 cells in C57BL/KaLwRij mice. Mice were sacrificed 1, 2, 3 and 4 weeks after i.v. inoculation with 10^5 eGFP-5T33 cells. Data shown as mean% of $eGFP^+$ cells (SEM), n>3. Table was reproduced from [169].

Vanderkerken *et al*. recently reviewed a number of publications focussing on the 5T2 and 5T33 murine MM models [171]. They found that MM cells cultured *in vitro* and those freshly isolated from sick animals differ in many respects *i.e. in vivo* MM cells express antigens and receptors that are not present in cells *in vitro* (*e.g.* CD44v6, matrix metalloproteinases). Moreover, after a few hours of incubation *in vitro*, 5T cells isolated from mice would no longer express the above receptors and antigens and become indistinguishable from *in vitro* cultured cells. This finding suggests a high microenvironment-dependency for the 5T33 model and highlights the limitations of *in vitro* uptake studies.

6.4 Radionuclide imaging and therapy in the 5T MM models

Only a limited number of studies have been published on the evaluation of radiopharmaceuticals in the 5T MM models. A report from 1993 evaluated Sm-153-EDTMP (lexidronam), a therapeutic bone targeting radiopharmaceutical in the 5T33 murine MM model [167]. The radiopharmaceutical was used both as a single agent and in combination with melphalan and/or BM transplantion. Lexidronam itself could significantly increase the lifetime of MM bearing mice. The increase with lexidronam as single agent was slightly higher than that with melphalan as single agent. Melphalan and lexidronam together (both toxic to the BM) significantly

decreased the lifetime of animals. However when the combined melphalan-lexidronam treatment was followed by BM transplantation lifetime increased significantly, compared to controls and single agent therapies. For some reason mice treated with Sm-153-EDTMP were not imaged. Although the radiopharmaceutical was administered to ablate the entire BM imaging could have provided further evidence regarding the accumulation of Sm-153-EDTMP in MM lesions.

In a recent study, C57BL/KaLwRij mice bearing subcutaneous 5TGM1 (a variant of the 5T33 cell line) myeloma grafts were infected i.v. or intratumorally with virus vectors encoding the NIS gene and were imaged with I-123; images suggested radiotracer uptake in the tumour [51].

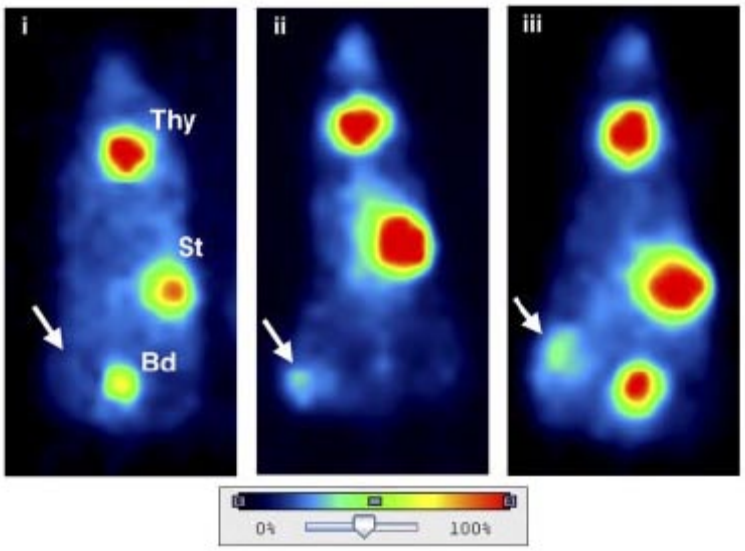

Figure 6.4: 5TGM1 MM bearing mice imaged with I-123. Radiotracer accumulation was observed in the tumour (arrow), thyroids (Thy), stomach (St) and bladder (Bd). A tumour bearing mouse was imaged after intratumoral injection of PBS (mock) (i), intratumoural (ii) or i.v. (iii) injection of the NIS virus vector on day -1 and 0. Figure reproduced from [51].

Interestingly even the infection itself (*N.B.* an oncolytic virus) could significantly increase the survival of animals and decrease tumour volumes by ~60%. When I-131 (suitable for imaging and therapy) was administered 90%

decrease in tumour volumes was observed. The route of virus vector administration (i.v. or intratumoral) did not affect the effectiveness of I-131 treatment significantly.

6.5 Imaging disease progress in the 5T33 MM model using In-111-oxine labelled eGFP-5T33 cells

6.5.1 Aims

The literature only reports on the tissue distribution of 5T33 cells at 3 and 7 days post-injection (see *e.g.* [168, 169]), Vanderkerken and colleagues only evaluated early (1, 2 and 18 hours) tissue distribution in the 5T2 model by using Cr-51 labelled cells [170]. There is a common belief that intravenously injected tumour cells, or at least a part of them will be retained in the lungs. Weeks after inoculation no (detectable amounts) of tumour cells are present in the lungs [168] however this may be caused by slow proliferation or low viability due to the non-optimal microenvironment. The use of radiolabelled cells combined with imaging is probably the easiest way to monitor early tissue distribution. The aims of these experiments were to find out whether 5T33 cells can be labelled with In-111-oxine and whether the labelling affects their viability. In the next step we aimed to assess the early tissue distribution in the 5T33 MM model by using In-111-oxine labelled eGFP-5T33 cells. We also designed a control study to determine the fate of radioactivity released from dying In-111-oxine 5T33 cells *in vivo*.

6.5.2 Materials and methods

6.5.2.1 Animals and materials

eGFP-5T33 cells were maintained in culture medium 2 (Appendix 6) in T75 or T175 tissue culture flasks in a tissue culture incubator (5% CO_2 in 95% air) with humidified atmosphere at a constant temperature of 37°C and passaged after a gentle scraping every 3 days and diluted at a ratio of 1:6-1:7 for maintenance (approximate concentration 2×10^5 cells/ml). Six-to-seven weeks old male C57Bl/KaLwRij mice were purchased from Harlan UK and allowed to acclimatise for 2 weeks after arrival. In-111-oxine was obtained from the Nuclear Medicine Department at Guy's Hospital. Sterile PBS (Dulbecco's Phosphate Buffered Saline, for *in vitro* diagnostic use) was purchased from Sigma. For i.v. injections Terumo insulin syringes (0.3 ml) fitted with 29 g (13 mm) needle were used. Cell concentrations and viability were calculated by a Countess automated cell counter (Invitrogen, USA) using trypan blue exclusion. Trypan blue (0.4%) and counting slides were supplied by Invitrogen. Prior to counting cell suspensions were diluted 1:1 in 0.4% Trypan blue, 10 µl of the above mixture were pipetted onto the counting slide and counted (as per manufacturer's instructions). Blank controls, *i.e.* a 1:1 dilution of PBS and trypan blue were counted before every experiment to check for aggregated trypan blue. If the concentration of trypan blue "particles" exceeded 2×10^4/ml a fresh vial was used instead.

Every experiment described in the section below was carried out under personal project licence (PPL) 70/7238 (In vivo imaging in cancer models, PPL holder Phil Blower) and personal investigator licence (PIL) 70/23500 (PIL holder Levente Meszaros) and fully complied with Home Office guidelines. Mice were scanned on a Bioscan NanoSPECT/CT (Mediso, Hungary) system (*In vivo* studies,

series 1) or a Bioscan NanoSPECT/CT Plus system (Mediso, Hungary) (*In vivo* studies, series 2). Both scanner systems were equipped with four heads, each with nine 1 mm pinhole collimators, in helical scanning mode. CT images were obtained with a 55 kV X-ray source, 1000 ms exposure time in 360 projections. Images were reconstructed in a 256 × 256 matrix using the HiSPECT (Scivis GmbH, Germany) reconstruction software and fused using Bioscan InVivoScope (Bioscan, France) software. Radioactive samples were measured in a Capintec CRC-25 dose calibrator.

6.5.2.2 In-111-oxine labelling of eGFP-5T33 cells

After gentle scraping three 700 µl aliquots, each containing 1.3×10^6 eGFP-5T33 cells (98% viable, referred to as "$Viability_i$" in Table 6.2) were withdrawn from a T75 cell culture flask (stock) and pipetted into three 15 ml centrifuge tubes. Cells were washed twice in 10 ml PBS. After the second washing step cells were resuspended in 2 ml PBS. To tube 1, 700 µl of PBS were added dropwise. To tube 2 4.7 MBq In-111-oxine in 700 µl PBS were added dropwise. To tube 3 10.2 MBq In-111-oxine in 700 µl PBS were added dropwise. Tubes were incubated at room temperature for 20 minutes and gently shaken in every 3 minutes. After 20 minutes 7 ml of PBS were added to each tube, tubes were then centrifuged (2000 RPM, 5 min) and pellets washed two more times in 10 ml of PBS. Supernatants (SN) were collected separately in each step. After the last washing step pellets were resuspended in 5 ml of culture medium 2 (referred to as "$concentration_{0h}$" in Table 6.2) and viabilities (referred to as "$viability_{0h}$" in Table 6.2) assessed. Contents of tubes 1 and 3 were transferred into a T25 flask and kept in a tissue culture incubator for 24 h. After 24 h cells were gently scraped, 100 µl were withdrawn from each flask to assess cell concentrations (referred to as "$concentration_{24h}$" in Table 6.2) and viabilities (referred to as "$viability_{24h}$" in Table 6.2).

6.5.2.3 *In vivo* studies, series 1

The protocol described in section 6.5.2.2 was followed for cell labelling. Briefly 3×10^6 eGFP-5T33 cells in 6 ml of PBS were radiolabelled with 5.0 MBq of In-111-oxine. 3.1 MBq were taken up by cells (~1 Bq/cell, 62% labelling yield), by the end of the labelling process 90% of the labelled cells were viable. The washed cell pellet containing 3.1 MBq of the radiotracer was re-suspended in 400 µl of PBS.

Prior to inoculation mice were anaesthetised with isoflurane, detailed protocols for which are reported in Chapter 7. Mouse 1 (M1) was injected i.v. (tail vein) with 190 µl (1.5 MBq) of the above suspension corresponding to 1.45×10^6 cells. M2 was inoculated with 85 µl (0.6 MBq, 5.8×10^5 cells) and M3 was injected with 125 µl (0.9 MBq, 8.7×10^5 cells) of the labelled MM cell suspension.

M1 was placed on the SPECT scanner bed immediately after injection and imaging was started at 5 minutes post-injection with 70 sec/image projection (42 min for a whole-body scan) under general anaesthesia with 1.5% isoflurane in oxygen. The bed heating was broken and the temperature in the pre-clinical laboratory was 21°C thus a small portable radiator was placed near the scanner hoping to provide sufficient heating for the mouse. Six consecutive SPECT scans were acquired, started at 5, 50, 97, 150, 220 and 270 minutes post-injection. After the last SPECT scan a whole-body CT scan was acquired and M1 was placed in a heated recovery cage. Unfortunately M1 died in the recovery cage probably due to severe hypothermia (*N.B.* its paws were very cold). The carcass was placed in a 50ml centrifuge tube then its activity estimated by a dose calibrator: 1.2 MBq at 5h post injection (injected activity: 1.5 MBq).

At 6 hours post-injection M3 was anaesthetised, placed on the SPECT scanner bed and imaged under general anaesthesia (1.5% isoflurane in oxygen) for

45 minutes (one whole-body scan, 70 sec/image projection). A whole-body CT scan was acquired after the SPECT scan then M3 was placed in a heated recovery cage. After recovery M3 was placed in its home cage and M2 and M3 were transferred back to the biological services unit (BSU).

At 24 hours post-injection M3 was taken to the pre-clinical laboratory, anaesthetised, placed on the SPECT scanner bed and imaged under general anaesthesia for 80 minutes (one whole-body scan, 120 sec/image projection.) A whole-body CT scan was acquired after SPECT scans then M3 was placed in a heated recovery cage. After recovery M3 was transferred back to the BSU. The same procedure was carried out at 48h (160 sec/image projection, 96 minutes scan), 72h (200 sec/image projection, 122 min scan), 120h (245 sec/image projection, 147 min scan) and 168h (300 sec/image projection, 180 min scan). Due to the low amount of activity present the experiment was terminated after the 168h scan when mice were culled by cervical dislocation. A Gaussian noise filtration algorithm was applied to smooth images acquired beyond 6 hours due to the low amount of activity present.

6.5.2.4 *In vivo* studies, series 2

For cell labelling the protocol described in section 6.5.2.2 was followed. Briefly, 2×10^7 eGFP-5T33 were radiolabelled with 20.4 MBq of In-111-oxine in 10 ml PBS. 18.9 MBq of the radiotracer was taken up by the cells (93% labelling yield) corresponding to ~1 Bq/cell; 80% of the labelled cells were viable at the end of the labelling process. The washed cell pellet labelled with 18.9 MBq of In-111-oxine was re-suspended in 400 µl of PBS.

Prior to inoculation the mouse was anaesthetised with isoflurane then injected with 200 µl (9.9 MBq, 10^7 cells) of the above suspension. After injection mouse was placed on the NanoSPECT/CT Plus scanner bed and imaged at 25, 90,

145 minutes post-injection under anaesthesia (1.5% isoflurane in oxygen). A whole body CT scan was acquired after the last SPECT scan. After the last scan the mouse was placed back in its home cage to recover. It was anaesthetised again at 6 hours post-injection and imaged on the NanoSPECT/CT Plus system, a whole body CT scan was acquired after the SPECT scan. Each SPECT scan was acquired in fine mode and 60 sec frame time and was approximately 60 minutes long. Due to the refurbishment of the BSU there was no holding room available for radioactive animals at the time the experiment was carried out. Therefore the mouse was culled by cervical dislocation after the last scan.

In this set of experiments we also designed a control study to evaluate the fate of radioactivity released from dying In-111-oxine labelled 5T33 cells. 5×10^6 eGFP-5T33 cells were radiolabelled with 6.5 MBq of In-111-oxine. 5.1 MBq were taken up by cells (~1Bq/cell, 78% labelling yield). At the end of the labelling process labelled cells were transferred to a microcentrifuge tube, centrifuged and the supernatant discarded. The (dry) pellet was consecutively flash-frozen on liquid nitrogen and thawed in a 37°C waterbath three times. It was then resuspended in 400 µl PBS and 200 µl (2.6 MBq, 2.5×10^6) were injected via the tail vein of a previously anaesthetised mouse. A whole body CT scan was acquired then SPECT scans were started at 30 min and 105 min post-injection under isoflurane anaesthesia (1.5% isoflurane in oxygen). After the second scan the mouse was placed in its home cage to recover. At 8 hours post-injection mouse was culled by cervical dislocation. The carcass was scanned (whole body SPECT and CT scans acquired) and disposed of. Scanning was performed on the NanoSPECT/CT Plus system in fine mode and 60 sec frame time. Each scan took approximately 60 minutes. After reconstruction images were noise-filtered due to the low amount of activity present.

6.5.3 Results

6.5.3.1 In-111-oxine labelling of eGFP-5T33 cells

Results are summarised in Table 6.2. Cells became radiolabelled so although they were only exposed to the labelling solution for 20 min they were radioactive for the entire culture period.

	Tube 1	**Tube 2**	**Tube 3**
Number of cells	1.3×10^6	1.3×10^6	1.3×10^6
$Viability_i$	98%	98%	98%
In-111-oxine added	-	4.7 MBq	10.2 MBq
Activity of SN	-	1.7 MBq	7.8 MBq
Activity of 1st wash	-	0.1 MBq	0.1 MBq
Activity of 2nd wash	-	0.1 MBq	0 MBq
Activity of pellet	-	2.39 MBq	2.1 MBq
Lost activity	-	0.41 MBq	0.1 MBq
$Cell\ concentration_{0h}$	2.1×10^5/ml	2.4×10^5/ml	2.4×10^5/ml
$Viability_{0h}$	85%	88%	91%
$Cell\ concentration_{24h}$	6.1×10^5/ml	-	2.1×10^5/ml
$Viability_{24h}$	92%	-	75%
Labelling yield	-	51%	21%
Activity/cell	-	1.8 Bq	1.6 Bq

Table 6.2: Results of the In-111-oxine labelling of eGFP-5T33 cells. $Viability_i$ is the viability at the beginning of the procedure, activity of SN is the activity of the supernatant after cell labelling and centrifugation, activity of 1st and 2nd wash are activities of the SN discarded after the 1st and 2nd washing steps, lost activity is the difference of the overall activity ("In-111-oxine added") and the sum of the activities of the SN, 1st and 2nd wash and pellet. $Cell\ concentration_{0h}$ and $viability_{0h}$ refer to the cell concentration and viability after labelling and re-suspension in 5 ml of culture medium 2. $Cell\ concentration_{24h}$ and $viability_{24h}$ refer to the cell concentration and viability after 24 h in culture. Labelling yield was calculated as the ratio of the "activity of pellet" and "In-111-oxine added", activity/cell was calculated as the ratio of "activity of pellet" and "$cell\ concentration_{0h}$" multiplied by the volume (5 ml).

The labelling procedure, *i.e.* a series of incubation and washing steps slightly altered cell viabilities, the initial 98% viability fell to 85-91% by the end of the labelling process ("$viability_{0h}$"). Interestingly the percentage of viable cells was lowest in the control tube (tube 1) *N.B.* results shown in the table reflect a single measurement per tube thus a couple of percent difference can be accounted for as experimental or instrumental error.

By using low and high(er) activities of In-111-oxine we were aiming to determine the maximum amount of In-111-oxine that can be taken up by 10^6 viable eGFP-5T33 cells. Based on our data 1.2-1.3×10^6 MM cells (approximately 10^6 viable by the end of the labelling process) can take up a maximum of 2.4 MBq of the radiotracer; activity taken up by the cells will not be higher if we double the dose. More than 2 MBq of radioactivity taken up by a million cells means more than 2 decays per cell per second. Taking into account that In-111 is an Auger electron emitter radioisotope such a high activity is likely to cause radiation damage to the cells. Cell concentrations and viabilities assessed 24 hours after labelling confirm the above hypothesis: cell concentration in the control tube (tube 1) increased nearly 3-fold in 24 hours whilst $concentration_{24h}$ in tube 3 was slightly less than $concentration_{0h}$ suggesting that labelled cells did not divide or their division rate markedly slowed down. Viability of control cells was in the normal range (*i.e.* above 90%) whilst only 75% of the labelled cells remained viable. Again, these observations suggest that 2 Bq In-111/eGFP-5T33cell do influence the radiolabelled cells however most of them remain alive *in vitro* for at least 24 hours. For tubes 2 and 3 the difference between the added and recovered (pellet and supernatant) activity is referred to as "lost activity". A significant amount seems to have been lost from tube 2. Activity may have been lost during pipetting (*i.e.* sticking to the

plastic). We should also take into account that the dose calibrator loses accuracy at low ranges and, especially for In-111 the geometry of the source is also critical [172].

6.5.3.2 *In vivo* studies, series 1

Results of the imaging experiment are shown in Figure 6.5. After injection MM cells were retained in the lungs, probably after first pass (Figure 6.5 a). Soon after that lungs started to clear with cells migrating to the liver and spleen and some activity appearing in the kidneys (Figure 6.5 b-c). By 150 minutes post-injection most of the injected activity was in the liver and spleen (image not shown) and after 6 hours no detectable amount was present in the lungs. A small amount of radioactivity was detected in the kidneys and bladder (Figure 6.5 c) probably due to labelled cells dying and releasing In-111 *in vivo.*

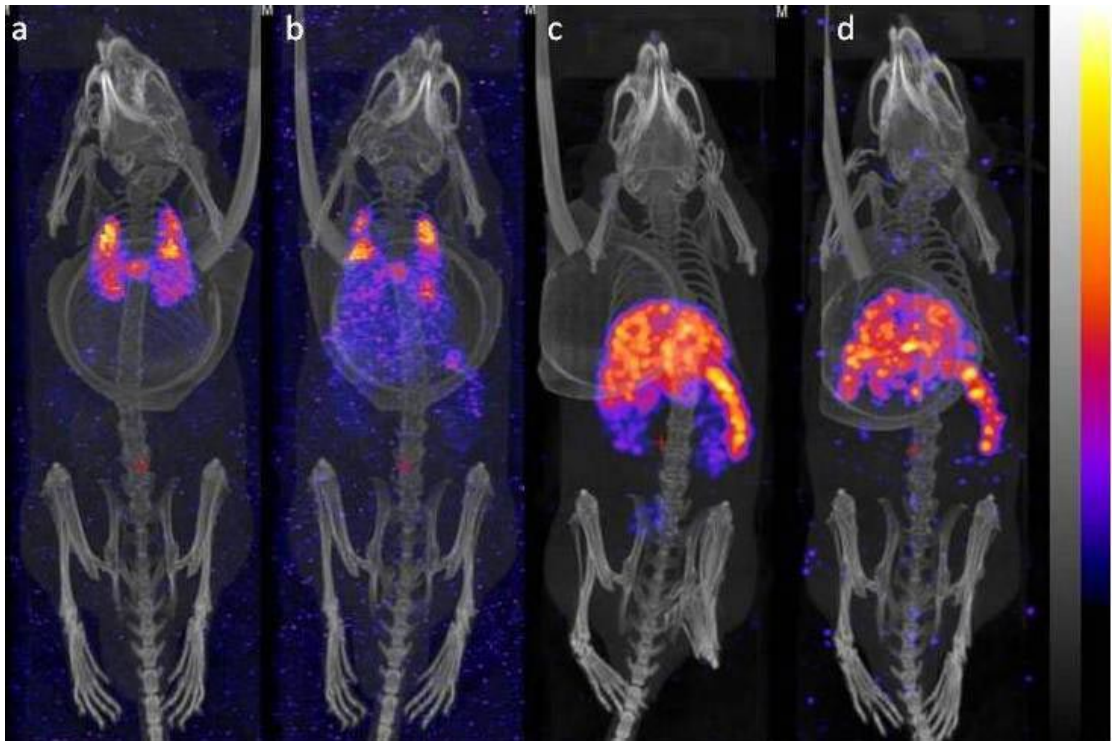

Figure 6.5: Tissue distribution of In-111-oxine labelled eGFP-5T33 cells in C57BL/KaLwRij mice. M1 at 5 (a) and 50 (b) minutes post-injection; M3 at 6 (c) and 168 (d) hours post-injection of In-111-oxine labelled eGFP-5T33 cells (note: images c and d were noise-filtered)

From 24 hours until (at least) 168 hours post-injection radioactivity was only detected in the spleen and liver (Figure 6.5 d). The signal was very weak by day 7 (*N.B.* no more than 150 kBq of In-111 were present) thus imaging was terminated.

6.5.3.3 *In vivo* studies, series 2

Images obtained with the radiolabelled eGFP-5T33 cells are shown in Figure 6.6. In this set of experiments 6-10-times higher activity was injected per mouse than in the first series reported in section 6.5.3.2. After 25 min (Figure 6.6 a) most of the injected activity was in the lungs however significant amounts were already present in the liver, kidneys, spleen and bones. Lungs gradually cleared with time and only a negligible amount of radioactivity was present after 6 hours (Figure 6.6 d). Activity clearing from the lungs radioactivity accumulated in the liver, spleen and bones (femora, tibiae, pelvis, lower vertebrae and joints) and we also observed moderate accumulation in the kidneys (Figure 6.6 a-d).

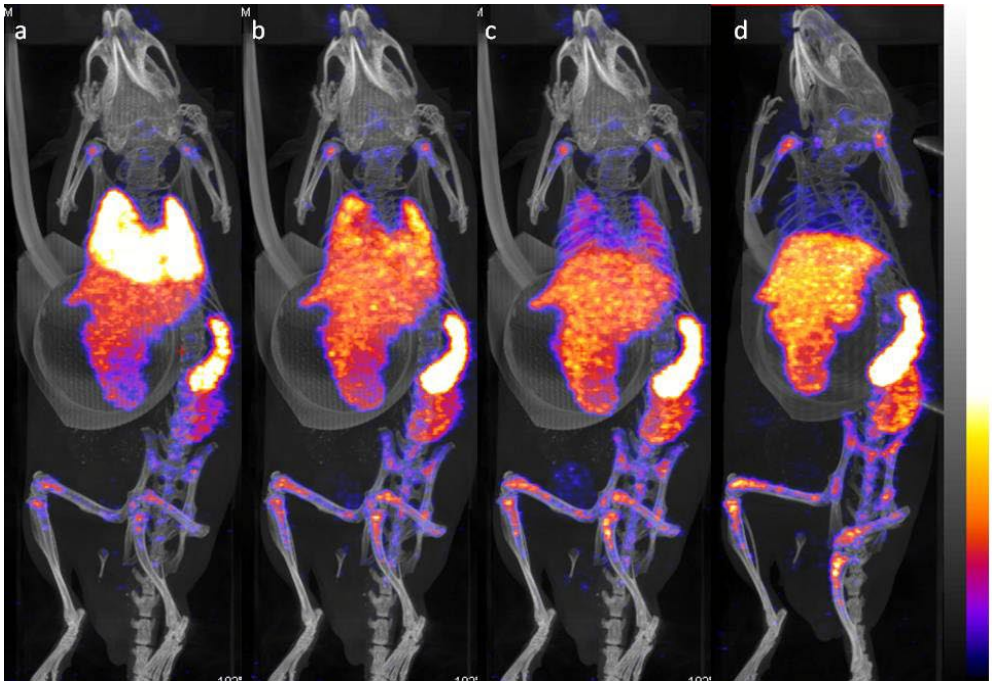

Figure 6.6: Early tissue distribution of In-111-oxine labelled eGFP-5T33 cells in a C57BL/KaLwRij mouse. Images were obtained 25 (a), 90 (b), 145 minutes (c) and 6 hours (d) after i.v. injection of In-111-oxine labelled eGFP-5T33 cells.

Upon injecting repeatedly flash-frozen and thawed In-111-oxine labelled eGFP-5T33 cells radioactivity only accumulated in the liver and kidneys and possibly there was minor accumulation in the spleen (Figure 6.7); no lung-associated radioactivity was detected even at 30 minutes post-injection (Figure 6.7 a). Images obtained at 30 and 105 minutes post-injection were indistinguishable (Figure 6.7 a-b). By 8 hours the liver mostly cleared up and released activity accumulated in the kidneys (Figure 6.7 c).

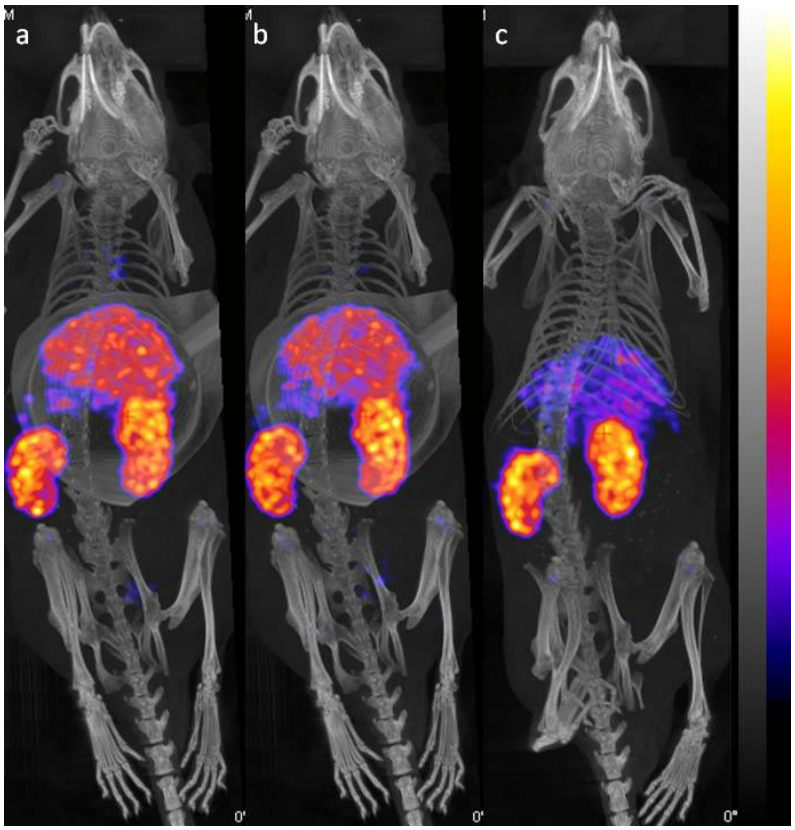

Figure 6.7: Early tissue distribution of dead In-111-oxine labelled eGFP-G5T33 cells in a C57BL/KaLwRij mouse. SPECT/CT images were obtained 30 (a), 105 minutes (b) and 8 hours (c) after i.v. injection of dead In-111-oxine labelled eGFP-5T33 cells.

6.5.4 Discussion

We managed to radiolabel eGFP-5T33 cells with In-111-oxine at a very high activity concentration (activity/cell): 2 Bq/cell was the maximum activity concentration that we could achieve; this corresponds to 2 decays/cell/second.

Considering that In-111 is an Auger electron emitter such a high activity concentration is likely to have influenced cells hence the slower (*in vitro*) proliferation rate of labelled cells (Table 6.2). For clinical studies with In-111-oxine labelled autologous leukocytes, GE Healthcare recommends to radiolabel 3-4×10^8 white blood cells with 7.4-18.5 MBq of the radiotracer (this would give 0.03-0.06 Bq/cell) and reports on an average labelling yield of 77% [173]; we labelled 100-times less MM cells (plasma cells) with one-third of the above activity. *N.B.* we only needed this amount of activity for imaging, much less would have been enough for a biodistribution study.

In the first series of imaging studies we used low activities to track the *in vivo* fate of eGFP-5T33 cells. The fact that we detected imageable amounts of In-111 in the liver and spleen even at 7 days post-injection with no signal in the kidneys and bladder suggests that the radiolabelled eGFP-5T33 cells (or at least most of them) remained viable *in vivo*. We would have expected to see a continuous "leaking" to the kidneys and bladder in the first few hours or days then a complete disappearance of the radioactive signal from the liver and spleen if cells had started to die due to radiation damage. This finding confirms our *in vitro* results *i.e.* most of the labelled cells remain alive for at least 24 hours (although their proliferation rate is lower than that of non-labelled cells).

Data obtained in the first series of imaging experiments (Figure 6.5) suggest that 5T33 cells have a very high affinity to the spleen and liver (*i.e.* main haemopoietic organs in the mouse). Although MM cells are retained in the lungs after being injected i.v. they immediately cleared from this organ whereas they remained retained in the spleen and liver. Based on the images it is likely that cells leaving the lungs migrated to the spleen and liver. By 6 hours post-injection the

lungs are completely clear on the images (Figure 6.5 c). Initial retention in the lungs is probably physical (embolism) or there may be a transient endothelial binding as capillaries in the lungs are the first capillary system to be encountered after injection. However there must be a much stronger mechanism that attracts MM cells exclusively to the liver and spleen. This “strong effect” is likely to be the haemopoietic microenvironment as a whole; in accordance with reports on the very strong stroma-dependency of MM cells [7]. The second series of imaging studies (Figure 6.6) in which we used 10-times higher activity (and cell number) confirmed the initial accumulation in the lungs and the very high affinity of MM cells to the spleen and liver. Due to the higher activity injected these imaging studies also revealed the very high affinity of 5T33 cells to the BM. Only 25 minutes after inoculation a large amount cells were present in the femora, tibiae and vertebrae and bone-associated activity markedly increased with time.

Comparing our data with the results of Vanderkerken and colleagues we can conclude that 5T2 and 5T33 MM cells behave very similarly after being injected i.v. in C57Bl/KaLwRij mice. Vanderkerken and co-workers found that 60 minutes post-injection around 20% of the Cr-51 labelled 5T2 cells were retained in the lungs and more than 60% were in the liver [170]. Although we did not quantify the biodistribution of In-111-oxine labelled eGFP-5T33 cells by counting dissected organs *ex vivo* based on the image acquired at 50 min post-injection (Figure 6.5 b) a very significant amount of activity was still retained in the lungs. We could also image significant activities in the kidneys at early time points, according to the cited study this is probably due to In-111 labelled proteins released from dead cells *in vivo*. We did a control study as part of the second series of imaging studies to confirm the fate of radioactivity released from dead or dying cells *in vivo*. At 30

minutes post-injection of the previously flash-frozen and thawed In-111-oxine labelled eGFP-5T33 cells activity was only detected in the liver and kidneys (Figure 6.7 a) but not in the bladder. This suggests that radioactivity released from cells was in multiple forms: a fraction of In-111 was bound by smaller and hydrophilic species such as peptides or protein fragments, this fraction accumulated in the kidneys. Another fraction of In-111, probably bound by larger proteins released from radiolabelled cells accumulated in the liver. The intracellular fate of In-111-oxine is not fully characterised. We only know that "within the cell, indium becomes firmly attached to cytoplasmic components; the liberated oxyquinoline is released by the cell" [173]. The above cytoplasmic components can possibly be proteins or nucleic acids/nucleotides present in the cytoplasm and cell organelles. By 8 hours post-injection the amount of radioactivity present in the liver significantly decreased whilst activity in the kidneys increased (Figure 6.7 c) suggesting that liver-bound radioactive species were metabolised and released metabolic products were trapped by the kidneys.

Vanderkerken *et al.* found that after 18 hours more than 20% of the injected 5T2 cells were present in the "bone marrow", defined as the whole skeleton apart from the bones of the head [170]. We could not visualise bone-associated activity in the first series of imaging studies because counts were too low; however the second series revealed a significant amount of activity in the bones (*vide supra*). Having used only one mouse we cannot assess our data quantitatively but it is clear that bone-associated radioactivity was significant even after 25 minutes.

6.6 Conclusions and summary

We have access to the 5T33 murine MM model that is relatively easy to use and mimics the human disease in immunocompetent mice. The cell line had been

transfected with eGFP therefore cells are fluorescent which makes their detection easy in organ homogenates isolated from inoculated mice. By using In-111-oxine labelled eGFP-5T33 cells we confirmed that cells have a very high affinity to haemopoietic tissues *i.e.* the liver, spleen and BM. We proved that eGFP-5T33 cells accumulate in the BM of C57Bl/KaLwRij mice from as early as 25 minutes post-inoculation. Based on its characteristics it is likely to be an ideal model for testing the Tc-99m labelled hynic-calcitonin radiopeptides although based on the results reported in this chapter we do not know anything about the CTR expression of eGFP-5T33 cells *in vivo*.

Chapter 7: Imaging MM lesions with Tc-99m labelled sCTLys^{18}-hynic-TFA and sCT(8-32)Lys^{18}-hynic-TFA in the 5T33 murine MM model

7.1 Aims and introduction

The aims of this set of experiments were to assess the *in vivo* MM targeting properties of the Tc-99m labelled hynic-sCT radiopeptides. FACS studies (*vide infra*) suggest that eGFP-5T33 cells do not express CTR *in vitro* however we would expect a high density of CTR+ osteoclasts surrounding MM lesions in the bones. Vanderkerken *et al.* found that 5T33 cells express a large number of receptors and surface markers *in vivo* that they do not express *in vitro* [168] thus cells may start expressing CTR after having been injected i.v. (or refer to [138]). We also carried out negative control experiments using non-inoculated healthy C57Bl/KaLwRij mice to see whether the hepatic, splenic and BM uptake of the intact radiopeptide in eGFP-5T33 MM bearing mice is specific. With FACS analyses we aimed to confirm that radiopeptide uptake in target organs was specific (*i.e.* (increased levels of) CTR were present) and that uptake correlated with CTR levels. As part of the imaging experiments we also aimed to assess the *in vivo* stability and metabolic fate of the Tc-99m labelled hynic-calcitonin derivatives.

7.2 Materials and methods

7.2.1 Materials and instruments

Six-to-seven weeks old male C57Bl/KaLwRij mice were purchased from Harlan UK and allowed to acclimatise at the Rayne BSU for 2 weeks after arrival.

^{99m}Tc-TcO_4^- was obtained from the Nuclear Medicine Department at Guy's Hospital. Tin(II) chloride dihydrate (Ph Eur, >98%) was purchased from Sigma, 5M HCl was purchased from Fisher and diluted to a concentration of 0.01M in dH_2O. 10 µg sCTLys^{18}-hynic-TFA and sCT(8-32)Lys^{18}-hynic-TFA kits were prepared as described earlier. Saline (0.9% in dH_2O) was prepared using sodium chloride (for molecular biology) from Sigma and dH_2O and filtered on a 0.22 µm filter. Sterile PBS (Dulbecco's Phosphate Buffered Saline, for *in vitro* diagnostic use) and bovine serum albumin (BSA) were purchased from Sigma. Acetyl sCT was purchased from Sigma (97% purity and 82% peptide content, 1 mg solid/vial). Vials were kept at -80°C. For i.v. injections Terumo insulin syringes (0.3 ml) fitted with 29 g (13 mm) needle were used. Spleen and liver samples were homogenised with BD Falcon 40 µm cell strainers. 10% formalin was purchased from Sigma. Radioactive samples were measured on a Capintec CRC-25 dose calibrator and/or a Wallac 1282 Compugamma Universal Gamma Counter. Data were processed and analysed in MS Excel, GraphPad Prism, SpCalc 2.12a and computer programmes developed by us.

eGFP-5T33 cells were maintained as described in Chapter 6. Passage numbers 5-30 were used for inoculation. Cell concentrations and viability were calculated by a Countess automated cell counter (Invitrogen, USA) using trypan blue exclusion assay. Trypan blue (0.4%) and counting slides were supplied by Invitrogen. A rat kidney was kindly provided by Dr Rick Southworth (Division of Imaging Sciences and Biomedical Engineering, King's College London).

7.2.2 Radiolabelling and quality control of sCTLys^{18}-hynic-TFA

To a freeze-dried kit containing 10 µg of sCTLys^{18}-hynic-TFA (10 µg kit) in a screw-cap microcentrifuge tube 160-210 MBq (at time of elution) of high specific activity ^{99m}Tc-TcO_4^- in a total volume of 300 µl of saline were added. (More than

one kit was used when necessary.) To the above mixture 10 μl freshly-prepared 1 mg/ml $SnCl_2 \cdot 2H_2O$ in 0.01M HCl were added. The microcentrifuge tube was sealed, centrifuged to remove and mix small drops from its wall and placed in a shaker heated to 37°C for 30 min. pH of the labelling mixture was 4.5. RCP was above 95% (typically 98-100%) in each case as assessed by ITLC-SA and saline as mobile phase. Depending on the study (*i.e.* imaging or *ex vivo* tissue counting) and activity, 30-50 μl (10-20 MBq at time of injection) of the above mixture were withdrawn then diluted to 200 μl in PBS (pH 6 after dilution) in a syringe. Contents of the syringe were injected i.v.

7.2.3 Radiolabelling and quality control of sCT(8-32)Lys^{18}-hynic-TFA

To a freeze-dried kit containing 10 μg of sCT(8-32)Lys^{18}-hynic-TFA ("10 μg kit") in a screw-cap microcentrifuge tube 350-500 MBq (at time of elution) of ^{99m}Tc-TcO_4^- in a total volume of 300 μl of saline were added. To the above mixture 10 μl freshly-prepared 1 mg/ml $SnCl_2 \cdot 2H_2O$ in 0.01M HCl were added. The microcentrifuge tube was sealed, centrifuged and placed in a shaker heated to 37°C for 30 min. pH of the labelling mixture was 4.6. RCP was 100% in each case as assessed by ITLC-SA and saline as mobile phase. Depending on the study (*i.e.* imaging or *ex vivo* tissue counting) and activity 10-25 μl (10-20 MBq at time of injection) of the above mixture were withdrawn then diluted to 200 μl in PBS (pH 6 after dilution) in a syringe. Contents of the syringe were injected i.v.

7.2.4 Imaging and *ex vivo* tissue counting experiments

Study groups for the *in vivo* evaluation of the Tc-99m labelled hynic-calcitonin radiopeptides are summarised in Figures 7.1-7.2. Three healthy controls were used to assess the whole body biodistribution of the Tc-99m labelled sCTLys^{18}-

hynic-TFA. These animals were included in a separate control group due to the i.v. injections going badly, meaning lots of unsuccessful attempts and resulting para-venous injections (control group 1). A negative control group of 9 mice (control group 2) was used as a basis of comparison with MM bearing animals; note that only the main thoraco-abdominal organs and one femur were excised in this group (the same organs as in disease bearing animals). A control group of 3 mice was used to assess the normal biodistribution of Tc-99m labelled sCT(8-32)Lys^{18}-hynic-TFA, this will be quoted as "control group" in section 7.3.3. MM bearing mice were inoculated with 10^6 eGFP-5T33 cells on day 0 (protocols are shown below) and used as follows. Seven MM bearing mice were used to assess the biodistribution of the Tc-99m labelled sCTLys^{18}-hynic-TFA 11 days after inoculation ("11 days group" in section 7.3.1). Twelve MM bearing mice were used on day 14 ("14 days group" in section 7.3.1) and 6 MM bearing animals were used 15 days after inoculation ("15 days group" in section 7.3.1) to assess the disease targeting properties of the full Tc-99m labelled hynic-sCT sequence. Another three mice were co-injected with acetyl-sCT and the Tc-99m labelled sCTLys^{18}-hynic-TFA 15 days post-inoculation as part of a control study ("15 days (block)" group in section 7.3.1, for further details refer to section 7.2.5). To assess the disease targeting properties of Tc-99m labelled sCT(8-32)Lys^{18}-hynic-TFA 6 MM bearing mice were used 15 days post-inoculation ("15 days group" in section 7.3.3). In every group mice were culled 100 minutes post-injection of the Tc-99m labelled sCTLys^{18}-hynic-TFA or sCT(8-32)Lys^{18}-hynic-TFA by cervical dislocation.

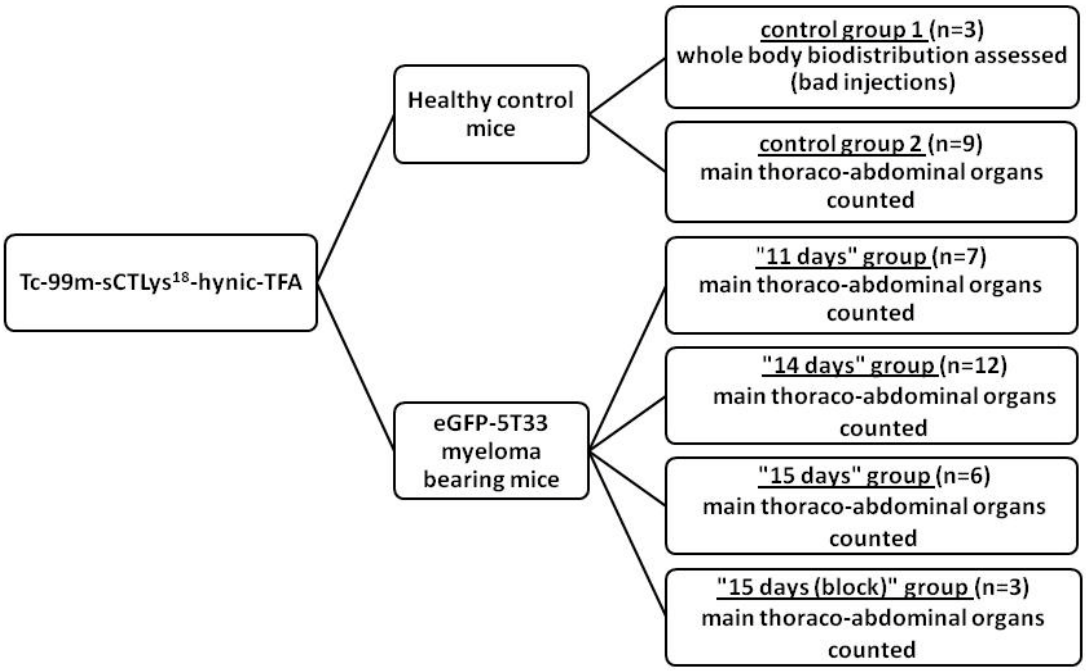

Figure 7.1: Scheme of the *in vivo* evaluation of the Tc-99m labelled sCTLys^{18}-hynic-TFA as reported in section 7.3.1.

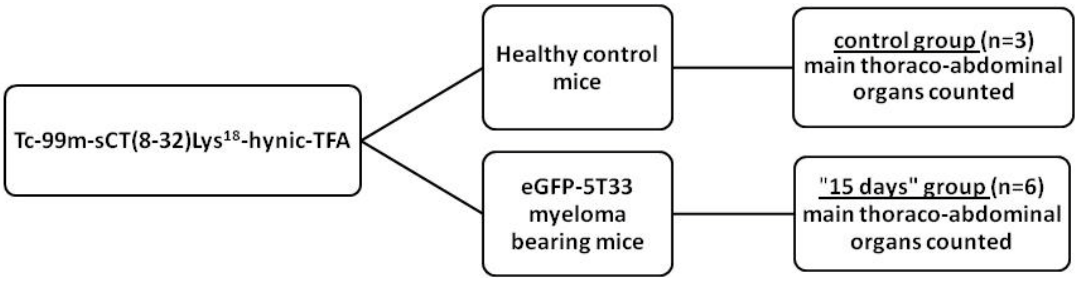

Figure 7.2: Scheme of the *in vivo* evaluation of the Tc-99m labelled sCT(8-32)Lys^{18}-hynic-TFA as reported in section 7.3.3.

For imaging MM lesions C57Bl/KaLwRij mice were inoculated with eGFP-5T33 cells. Control animals were imaged without inoculation. Mice were scanned on a Bioscan NanoSPECT/CT (Mediso, Hungary) system equipped with four heads, each with nine 1 mm pinhole collimators in helical scanning mode. CT images were obtained with a 55 kV X-ray source, 1000 ms exposure time in 360 projections. Images were reconstructed in a 256 × 256 matrix using the HiSPECT (Scivis GmbH, Germany) reconstruction software and fused using Bioscan InVivoScope (Bioscan, France) software.

Prior to inoculations actual cell concentrations and viabilities in *in vitro* cell cultures were assessed as follows: 20 µl of the cell suspension (withdrawn from the culture flask after gentle scraping) were diluted 1:1 in 0.4% Trypan blue, and 10 µl of the above mixture were pipetted onto the counting slide and counted (as per manufacturer's instructions). Blank controls, *i.e.* a 1:1 dilution of PBS and trypan blue were counted before every experiment to account for aggregated trypan blue (background). If the concentration of trypan blue "particles" exceeded 2×10^4/ml a fresh vial was used instead.

Every experiment described in the sections below was carried out under PPL 70/7238 (In vivo imaging in cancer models, PPL holder Phil Blower) and PIL 70/23500 (PIL holder Levente Meszaros) and fully complied with Home Office guidelines.

Animals were inoculated according to the protocol below:

1) Mice were transferred to the pre-clinical laboratory and left to acclimatise
2) eGFP-5T33 cells were counted and their viability assessed. Cells were used if their viability was above 90%.
3) Cells were transferred to a Falcon tube aseptically and centrifuged at 2000 RPM for 5 min then the supernatant was discarded
4) The pellet was re-suspended in 1 ml of sterile PBS then diluted to 50 ml in PBS
5) Cells were centrifuged at 2000 RPM for 5 min then the supernatant was discarded
6) Steps 4-5 were repeated
7) After step 6 the supernatant was discarded, cells were re-suspended in 1 ml of sterile PBS and diluted to a concentration of $5x10^6$ viable cells/ml

8) 200 µl of the above suspension was withdrawn in an insulin syringe fitted with a 29 g needle (10^6 cells/syringe)
9) Syringe was transferred to the pre-clinical laboratory
10) Mouse was anaesthetised with isoflurane in induction box, O_2 flow rate of 1 l/min and isoflurane levels of 2.5-3.0%
11) Mouse was transferred to mask to maintain anaesthesia : O_2 flow rate of 1 l/min and isoflurane levels of 1.5-2.0%
12) The injection site was wiped with an ethanol wipe to sterilise it
13) Cells were injected via tail vein
14) After injection the tail was wiped with Savlon to avoid infection of injection site
15) Mouse was marked
16) Mouse was transferred to a recovery cage
17) After recovery mouse was transferred to home cage and the home cage transferred back to BSU

After inoculation mice were monitored and scored at least once a day (a distress score sheet is shown in Appendix 7). Due to the very severe side-effects in this cancer model, should any of the animals have been scored 10 or above and/or presented any other serious symptoms they would have been culled immediately using a Schedule 1 procedure. Inoculated mice were kept for 11, 14 or 15 days. At the above time points mice were injected i.v. with Tc-99m labelled sCTLys^{18}-hynic-TFA or sCT(8-32)Lys^{18}-hynic-TFA and either imaged or used for *ex vivo* tissue counting studies. Imaging, biodistribution and dissection protocols are shown below. *N.B.* the time of the first injection on a day is referred to as reference time: activities

and count rates of syringes, excised tissues and standards (calibrants) were corrected back to this time point.

Imaging protocol:

1) Mouse was anaesthetised with isoflurane in induction box, O_2 flow rate of 1 l/min and isoflurane levels of 2.5-3.0%
2) Mouse was transferred to mask to maintain anaesthesia : O_2 flow rate of 1 l/min and isoflurane levels of 2.5%
3) Tail was heated with heat lamp
4) Mouse was injected with the Tc-99m-sCTLys^{18}-hynic-TFA or Tc-99m-sCT(8-32)Lys^{18}-hynic-TFA intravenously (tail vein); volume: 200 µl.
5) Isoflurane on nanoSPECT/CT bed was set to: O_2 flow rate of 1 l/min and isoflurane level of 2.5%
6) Mouse was transferred to a tray and then to the mouse bed (lined with bench coat) in the nanoSPECT/CT.
7) A whole body CT scan was acquired
8) A whole body helical SPECT scan was started at 30 min post-injection at 70 sec/projection unless stated otherwise; a whole body scan took around 50-60 minutes
9) Mouse was culled by cervical dislocation at 100 min post-injection of the Tc-99m-sCTLys^{18}-hynic-TFA or Tc-99m-sCT(8-32)Lys^{18}-hynic-TFA and main thoraco-abdominal organs were excised for *ex vivo* tissue counting.

Ex vivo tissue counting protocol:

1) Mouse was anaesthetised with isoflurane in induction box, O_2 flow rate of 1 l/min and isoflurane levels of 2.5-3.0%
2) Mouse was transferred to mask to maintain anaesthesia : O_2 flow rate of 1 l/min and isoflurane levels of 2.5%
3) Tail was heated with a heat lamp
4) Mouse was injected with Tc-99m-sCTLys^{18}-hynic-TFA or Tc-99m-sCT(8-32)Lys^{18}-hynic-TFA intravenously (tail vein); volume: 200 µl.
5) Mouse was placed in a recovery cage and transferred to home cage after recovery
6) The mouse was culled by cervical dislocation at 100 min post-injection of the Tc-99m-sCTLys^{18}-hynic-TFA or Tc-99m-sCT(8-32)Lys^{18}-hynic-TFA

Dissection protocol:

1) Dead mouse was transferred to the dissection area
2) Carcass was weighed
3) The carcass was dissected and relevant tissues *i.e.* a femur and thoraco-abdominal organs except the thymus and reproductive organs were collected (unless stated otherwise)
4) Tissues were collected in pre-weighed scintillation vials
5) Vials were weighed with organs and tissue weights calculated
6) Organs were counted on the gamma counter (10 sec/sample, 110-155 keV energy window, no more than 10% dead-time)

Target organ (*i.e.* liver, spleen and BM) samples from MM-bearing animals were fixed as follows for later FACS analyses. Femora were cleaned of muscle and kept in PBS at 4°C overnight. The following day joints were chopped off and BMs flushed

with 6 ml ice-cold PBS using a 25 g needle connected to a 5 ml syringe. Marrows were homogenised by pipetting then centrifuged (2000 RPM, 5 min). Supernatants were discarded and pellets resuspended in 1 ml of ice-cold formalin. Samples were then diluted to 5 ml in formalin and kept at 4°C. Spleen (10-30 mg/mouse) and liver samples (300-600 mg/mouse) were put in ice-cold PBS straight after being removed from the carcass and kept at 4°C overnight. The following day organ samples were placed onto a 40 μm cell strainer connected to a 50 ml Falcon tube and pushed through the strainer gently using a syringe plunger and ice-cold PBS to wash cells into the centrifuge tube. Samples were centrifuged (2000 RPM, 5 min), supernatants discarded and pellets re-suspended in 1 ml ice cold formalin. Spleen samples were diluted to 10 ml and liver samples to 25 ml in formalin and kept at 4°C for FACS analysis. Every sample was filtered prior to FACS analysis using a 40 μm cell strainer in order to remove larger cell aggregates and contaminants such as mouse hair that could have blocked the FACS machine.

7.2.5 Control experiments - blocking the *in vivo* uptake of Tc-99m labelled sCTLys^{18}-hynic-TFA with cold sCT

C57Bl/KaLwRij mice (n=3) were inoculated i.v. with 10^6 eGFP-5T33 cells and used 15 days after inoculation. On the day of the experiment sCTLys^{18}-hynic-TFA kits were radiolabelled as described earlier. Approximately 30 minutes before injection 150 μl ice-cold PBS were added to each acetyl-sCT vial resulting in immediate dissolution of contents. Vials were then kept on ice. Before injection 30 μl (10-12 MBq at time of injection) of the labelled kit were withdrawn in an insulin syringe followed by 150 μl (1 mg) of the cold (non-radioactive) peptide. Peptides were co-injected after 2-3 minutes incubation at room temperature (once syringes had warmed up).

7.2.6 Gamma counter calibration

The gamma counter was calibrated with a set of standards (*i.e.* samples with known activity). For details on calibration data refer to Appendix 8.

7.2.7 Data analysis

Excised tissues were gamma counted and activities calculated. SUVs were calculated as SUV= ——— ——— where A_{organ} refers to the activity of a certain organ (at reference time) and A_{total} refers to the overall injected activity (tail excluded) at reference time. Student's t test was used to compare radiopeptide uptake in different groups of mice.

7.2.8 FACS analyses

Liver, spleen and BM homogenates were analysed on a BDFACSCanto II (BD BioSciences, Oxford, UK) flow cytometer. The flow cytometer is fitted with a 488 nm (20 mW) solid state laser and a 633 nm (17 mW) He-Ne laser and programmed with detector bands that cover most of the visible spectrum between 500-800 nm. Samples were stained for CTR (RPE (R-phycoerythrin), λ_{Ex}=488 nm and λ_{Em}=585/42 nm), CD138 which is a plasma cell marker (APC (Allophycocianin), (λ_{Ex}=633 nm and λ_{Em}=660/20 nm) and also monitored for endogenous expression of eGFP (FITC channel, λ_{Ex}=488 nm and λ_{Em}=530/30 nm). For CTR staining a rabbit anti rat calcitonin receptor antibody (AHP635 from AbD Serotec) was used as primary antibody in a ratio of 1:10 (where 1:1 refers to 1 mg antibody/ml) in 5% BSA in PBS; the antibody is known to cross-react with mouse and human CTR (refer to manufacturers data). The antibody is recommended for immunohistochemical staining, the manufacturer did not assess it for flow

cytometry. At the time the study was designed there was no anti mouse CTR antibody recommended for FACS on the market. We first had to assess whether the antibody of our choice was suitable for FACS analysis. The manufacturer used rat kidney sections as positive control tissue in immunohistochemistry hence we decided to use rat kidney homogenate previously fixed in formalin. The staining protocol described below was followed except that we did not stain the samples for CD138. The antibody was tested in different dilutions: 1:100, 1:50 and 1:10, results of FACS analyses are reported in Appendix 9. We found that sufficient staining can be achieved in 1:10 dilution hence we decided to use the antibody in this ratio for our analyses. After the rat kidney homogenate had been stained we also evaluated the antibody for the mouse receptor using formalin-fixed mouse kidney homogenate. Note that the mouse kidney homogenate was stained for CD138 too. We also stained and analysed formalin-fixed eGFP-5T33 cells obtained from an *in vitro* culture.

Secondary antibody for CTR staining: RPE conjugated sheep anti rabbit antibody (STAR35A, AbD Serotec) was used 1:5 (as recommended by the manufacturer) in 5% BSA in PBS. CD138 staining was carried out using monoclonal anti-mouse syndecan-1-APC antibody recommened for FACS (FAB2966A, R&D Systems) in a dilution of 1:5. Due to the (emission) spectral overlap between eGFP and RPE two samples, one with a strong FITC but no RPE and another with strong RPE but no FITC signal were analysed prior to the organ homogenates. Bleeding over was calculated between the two fluorochromes and compensation settings were calculated by the instrument. Thus all the data presented in this chapter had been automatically compensated.

Protocol for staining and processing samples for FACS:

1) 10^6 cells that had previously been fixed in formalin were pipetted into a well of a U-bottom 96 well-plate
2) The plate was centrifuged at 1500 RPM for 5 min and the supernatant was discarded
3) Contents of each well were re-suspended in 200 µl of PBS
4) The plate was centrifuged at 1500 RPM for 5 min and the supernatant discarded
5) Pellets in each well were re-suspended in 25 µl 5% BSA in PBS containing the anti-CTR primary antibody 1:10
6) The plate was incubated in the dark at room temperature for 60 min
7) The plate was centrifuged at 1500 RPM for 5 min and the supernatant discarded
8) Contents of each well were re-suspended in 200 µl of PBS
9) Steps 7-8 were repeated twice
10) Pellets were re-suspended in 25 µl of 5% BSA in PBS containing the RPE conjugated sheep anti-rabbit antibody (1:5) and the monoclonal anti-mouse syndecan-1-APC Antibody (1:5)
11) The plate was incubated in the dark at room temperature for 60 min
12) The plate was centrifuged at 1500 RPM for 5 min and the supernatant discarded
13) Contents of each well were re-suspended in 200 µl of PBS
14) Steps 12-13 were repeated twice

15) Pellets were re-suspended in 200 µl of PBS and the resulting suspensions were transferred to FACS tubes containing 500 µl of PBS; samples were then analysed on the FACS machine

7.2.9 *In vivo* stability of Tc-99m labelled hynic-calcitonin derivatives

Upon dissecting two healthy control C57Bl/KaLwRij mice that had been injected i.v. with the Tc-99m labelled sCTLys^{18}-hynic-TFA (sample 1) or sCT(8-32)Lys^{18}-hynic-TFA (sample 2) under anaesthesia with no recovery and culled at 100 min post-injection contents of their bladder were withdrawn in an insulin syringe. pH of urine samples was determined by spotting several microlitres of the sample onto a pH paper. Immediately after the pH had been determined contents of the insulin syringes were emptied into microcentrifuge tubes. Tubes were centrifuged at 12,000 RPM for 1 minute to sediment larger particles/cell debris that may have contaminated the sample. After centrifugation 10 µl of the "supernatants" were withdrawn and injected in the LC-MS system and analysed by method M2.

We processed urine samples as quickly as possible in order to avoid *ex vivo* degradation of metabolites thus analyses were started no more than 10 minutes after the samples had been withdrawn from the bladder and no more than 15 minutes after mice had been culled.

7.3 Results

7.3.1 Imaging normal and MM bearing mice with Tc-99m labelled sCTLys^{18}-hynic-TFA

Injections were carried out under general anaesthesia. Animals injected with the radiopeptide only, irrespectively of their disease status recovered from anaesthesia within minutes without presenting signs of distress during or after

injection. Mice co-injected with the radiopeptide and cold sCT (“15 days (block)” group) were seriously distressed. Seconds after co-injecting the cold and radiopeptide mice started to hyperventilate, became tachycardic and woke up. Their eyeballs were significantly swollen. In the recovery cage animals hunched up and did not move around. They were closely monitored in the following 100 minutes; their condition slowly and gradually improved. Therefore results of the blocking experiment have to be interpreted with caution.

In normal mice most of the injected radiopeptide rapidly accumulated in the kidneys (Figure 7.3, Table 7.1) and some was subsequently excreted to the bladder.

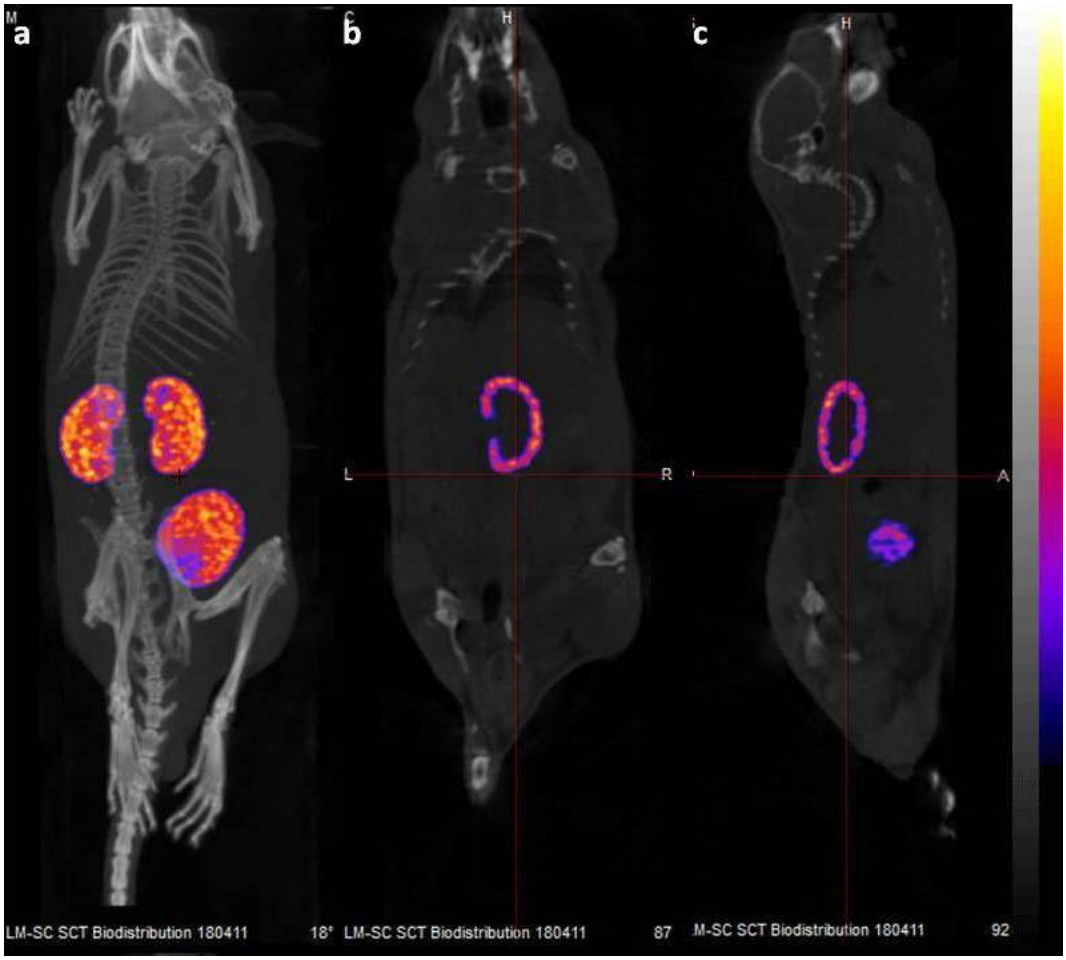

Figure 7.3: Healthy control mouse scanned 30 min post-injection of Tc-99m-sCTLys^{18}-hynic-TFA. Maximum intensity projection (MIP) (a), coronal image section (b), sagittal image section (c).

	Control group 1 n=3
Brain	0.02 (0.02)
Trachea+thyroids	0.95 (0.26)
Heart	0.17 (0.01)
Thymus	0.20 (0.05)
Lungs	0.83 (0.05)
Liver	0.48 (0.04)
Spleen	0.69 (0.01)
Stomach	1.30 (0.25)
Large intestine	0.41 (0.09)
Small intestine	0.60 (0.06)
Pancreas	0.12 (0.02)
Kidneys	33.65 (2.56)
Testicles	0.09 (0.02)
Muscle	0.30 (0.11)
Spine	0.30 (0.05)
Femur	0.34 (0.12)
Blood	0.34 (0.02)
Carcass	0.02 (0.00)

Table 7.1: Whole body biodistribution of Tc-99m labelled sCTLys^{18}-hynic-TFA in normal mice (control group 1). Uptake is reported in mean SUV (SEM) for each organ.

Coronal and sagittal image sections (Figure 7.3 b-c) suggest that renal uptake is limited to the cortex with no visible radiopeptide accumulation in the medulla. We also found moderate lung and gut uptake (Table 7.1). Due to the very low level of uptake in most of the organs we decided to dissect the main thoraco-abdominal organs and one femur in subsequent studies.

No outward signs of disease were recorded in any of the inoculated animals (*i.e.* distress scores remained 0). Average SUVs for every dissected organ and group (including control group 2) are shown in Table 7.2. Note that kidneys in the "11 days" and "15 days (block)" groups were not counted due to problems with the gamma counter. Figure 7.4 compares the radiopeptide accumulation in three target organs.

	Control group 2 n=9	"11 days" group n=7	"14 days" group n=12	"15 days" group n=6	"15 days" (block) n=3
Heart	0.22 (0.02)	0.38 (0.03)	0.43 (0.05)	0.52 (0.05)	0.36 (0.02)
Lungs	1.07 (0.12)	1.48 (0.14)	0.94 (0.07)	0.72 (0.06)	0.78 (0.09)
Liver	**0.62 (0.05)**	**0.89 (0.06)**	**0.98 (0.04)**	**1.26 (0.11)**	**1.46 (0.10)**
Spleen	**1.67 (0.29)**	**2.14 (0.52)**	**4.34 (0.54)**	**6.57 (0.80)**	**3.67 (0.54)**
Stomach	0.40 (0.05)	1.36 (0.13)	0.90 (0.12)	0.42 (0.07)	1.26 (0.15)
Intestines	0.15 (0.02)	0.30 (0.02)	0.22 (0.01)	0.22 (0.02)	0.19 (0.01)
Kidneys	35.44 (1.25)	not collected	36.36 (1.99)	43.72 (2.85)	not collected
Muscle	0.14 (0.02)	0.21 (0.02)	0.25 (0.03)	0.29 (0.04)	0.09 (0.01)
Femur	**0.27 (0.03)**	**0.65 (0.16)**	**1.18 (0.24)**	**0.48 (0.02)**	**0.25 (0.04)**
Blood	0.46 (0.06)	0.70 (0.08)	1.08 (0.19)	1.83 (0.46)	0.82 (0.03)

Table 7.2: Biodistribution of Tc-99m labelled sCTLys^{18}-hynic-TFA in control and MM bearing mice. Uptake is reported in mean SUV (SEM) for each organ.

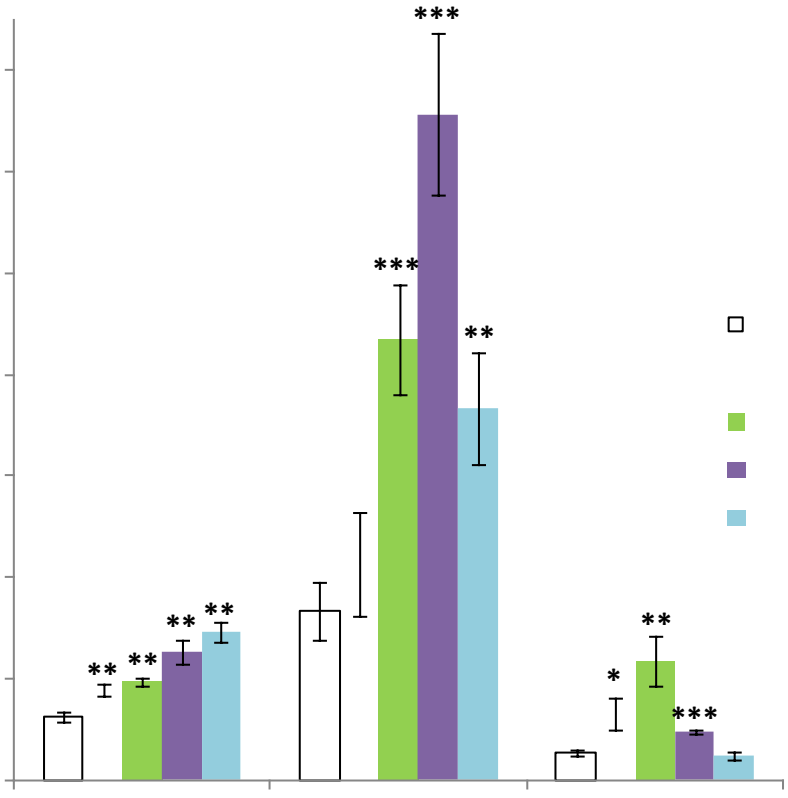

Figure 7.4: Mean SUV (SEM) of Tc-99m labelled sCTLys^{18}-hynic-TFA in target organs of control and MM bearing mice. Significance of difference to controls: *: p<0.1, **: p<0.01, ***: p<0.001.

Our data suggest that Tc-99m-sCTLys^{18}-hynic-TFA uptake was significantly higher in the target organs (liver, spleen and BM) of MM bearing animals than in healthy controls. Results of t-tests for every group and organ are reported in

Appendix 10. Radiopeptide uptake in the kidneys remained the same as in controls confirming rapid renal extraction and urinary excretion. Fifteen days after inoculation with 10^6 eGFP-5T33 cells spleen uptake was nearly 4-times higher and liver uptake was more than twice as high as in controls (Table 7.2 and Figure 7.4). Significant increase occurred in spleen SUVs from day 14 to day 15 ($p<0.05$) and liver SUVs too ($p=0.05$). By day 11 only liver and femoral SUVs increased significantly ($p<0.01$ and $p<0.1$ when compared to controls), between day 11 and 14 we observed a more than 2-fold increase in spleen SUVs. There was a significant decrease in femoral uptake from day 14 to 15 ($p=0.02$) but it still remained higher than in controls ($p<0.001$).

Liver uptake was statistically the same in the “15 days” and “15 days (block)” group ($p=0.24$). Co-injection of the radiopeptide with 1 mg of acetyl-sCT blocked spleen uptake in eGFP-5T33 MM bearing mice by 44% when compared to the “15 days” group: it was still higher than in control group 2 ($p=0.04$) and the “11 days” group ($p=0.09$) but significantly lower than in non-blocked mice 15 days after inoculation ($p=0.02$). Femoral (BM) uptake in the “15 days (block)” group was statistically the same as in “control group 2” ($p=0.67$) and lower than in non-blocked animals ($p=0.02$). To summarise there was a steady increase in radiopeptide uptake in target organs (except for femoral uptake) which was partially offset by the block. Other organs did not show this increase therefore observations with the Tc-99m labelled $sCTLys^{18}$-hynic-TFA fit our previous *in vivo* results with In-111-oxine labelled eGFP-5T33 cells.

Figure 7.5 b-c show representative MIP images obtained 30 minutes post-injection in the “11 days” and “15 days” groups. Due to the very high kidney uptake image settings had to be altered to be able visualise the liver and spleen; the same

settings were applied to a control image (Figure 7.5 a, mouse belonging to “control group 2”) to show that what we had observed in MM bearing mice was associated with the presence of MM. Figure 7.6 shows an MIP image of a mouse from the “11 days” group, kidneys and bladder had been removed in the InVivoScope software.

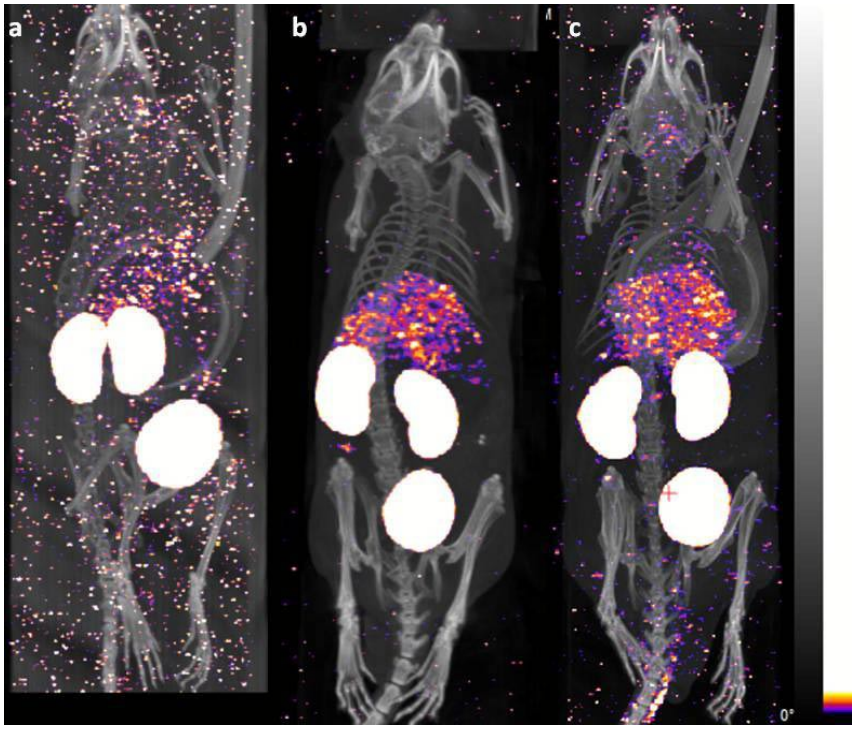

Figure 7.5: Representative MIP images acquired 30 minutes post-injection of Tc-99m labelled sCTLys^{18}-hynic-TFA in normal and MM bearing mice. Mouse from control group 2 (a), mouse from “11 days” group (b), mouse from “15 days” group (c).

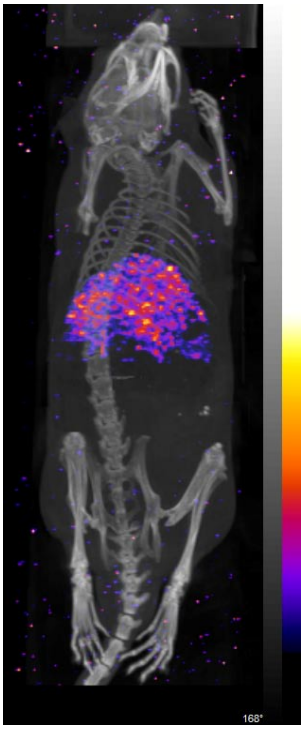

Figure 7.6: Representative MIP image acquired 30 minutes post-injection of Tc-99m labelled sCTLys^{18}-hynic-TFA in a mouse from the "11 days" group. Kidneys and bladder were removed after image reconstruction.

Radiopeptide uptake in some non-target tissues and organs such as the lungs, muscle, heart, stomach, intestines and blood was also significantly different between different groups of mice (results of t-tests are reported in Appendix 10). Difference in radiochemical purities (*i.e.* presence of pertechnetate and colloidal technetium) can explain differences in stomach, intestinal and lung uptakes. Blood SUVs gradually increased with time after inoculation suggesting the presence of increasing amounts of circulating plasma cells or other CTR positive white blood cells resulted by abnormal BM and lymphatic function. Increased blood radiopeptide levels show a good correlation with uptake in (heavily) perfused organs such as the heart and thigh muscle (Figure 7.7) Kidney uptake in the "15 days" group was significantly higher than in the control group ($p<0.05$) and "14 days" group ($p<0.1$), this phenomenon may also be related to increased blood radiopeptide levels.

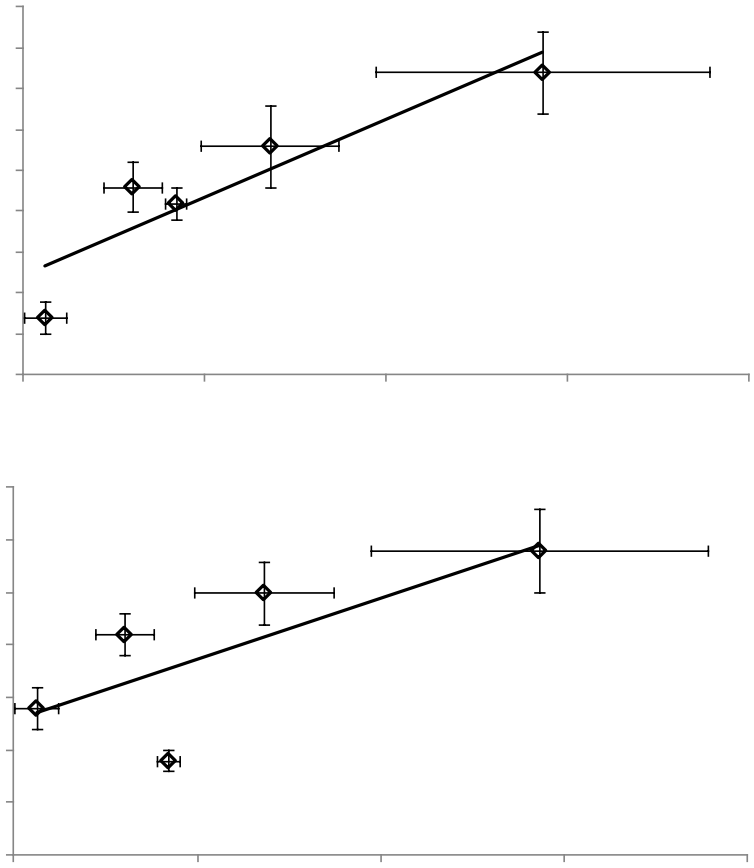

Figure 7.7: Correlation between blood and heart (a) and blood and muscle uptake (b) of the Tc-99m labelled sCTLys^{18}-hynic-TFA.

7.3.2 FACS analyses of organ homogenates obtained from mice imaged with the Tc-99m labelled sCTLys^{18}-hynic-TFA

7.3.2.1 Control samples

We first stained a rat kidney homogenate with the primary CTR antibody to see if it was suitable for FACS studies. We found that the antibody was suitable for FACS in a 1:10 dilution, results of these studies are summarised in Appendix 9.

In the next step a mouse kidney homogenate (positive control for CTR and negative control for eGFP) was stained and analysed by FACS (Figure 7.8). FACS analysis suggests that kidney cells are eGFP- as expected (Figure 7.8 a). Staining for CTR suggested that autofluorescence of kidney cells in the PE window (Figure 7.8

b) as well as the non-specific binding of the secondary antibody were negligible (Figure 7.8 c). We found that a large population of kidney cells was CTR+ (Figure 7.8 d) confirming that the rabbit anti rat CTR antibody cross-reacted with the mouse receptor and proving that the antibody was suitable for FACS.

In vitro cultured eGFP-5T33 cells were also stained and analysed by FACS (Figure 7.9). Cells were eGFP+ as expected (Figure 7.9 a). Autofluorescence of eGFP-5T33 cells in the PE channel as well as the non-specific binding of the RPE-conjugated sheep anti rabbit IgG antibody were negligible (Figure 7.9 b-c). Nearly 98% of *in vitro* cultured eGFP-5T33 cells were CTR- with a minor population showing CTR positivity (Figure 7.9 d). CTR positivity was not exclusively associated with eGFP positivity (Figure 7.9 h). As expected the eGFP-5T33 MM cells showed a strong positivity for the plasma cell marker CD138 (Figure 7.9 f). Autofluorescence in the APC channel was negligible, Figure 7.9 e. Figure 7.9 g suggests that eGFP positivity was strongly associated with CD138 positivity (*N.B.* the size of Q2 in Figure 7.9.g is almost identical to the size of P3 in Figure 7.9 f).

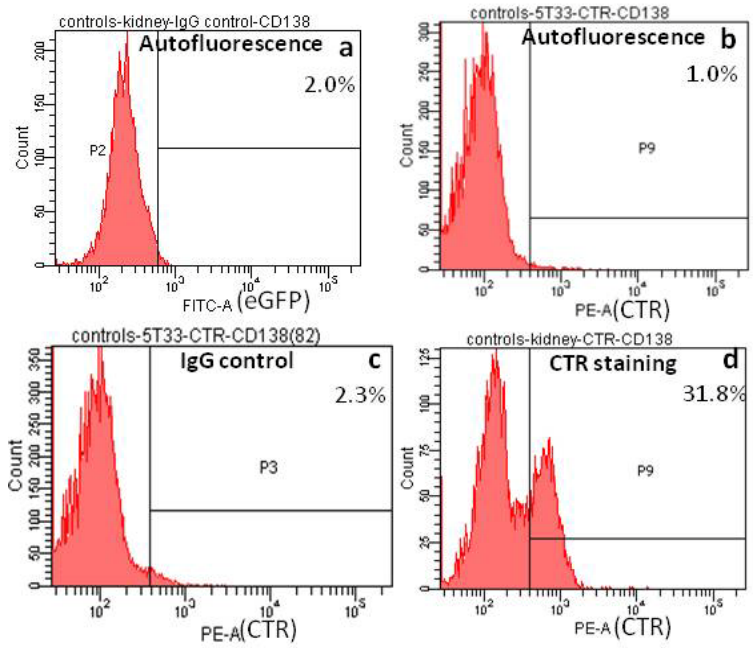

Figure 7.8: Results of the FACS analysis of a mouse kidney homogenate stained for CTR. Autofluorescence in the FITC channel (a), autofluorescence in the PE channel (b), non-specific binding of the secondary antibody (c) and histogram showing a large CTR+ cell population (d).

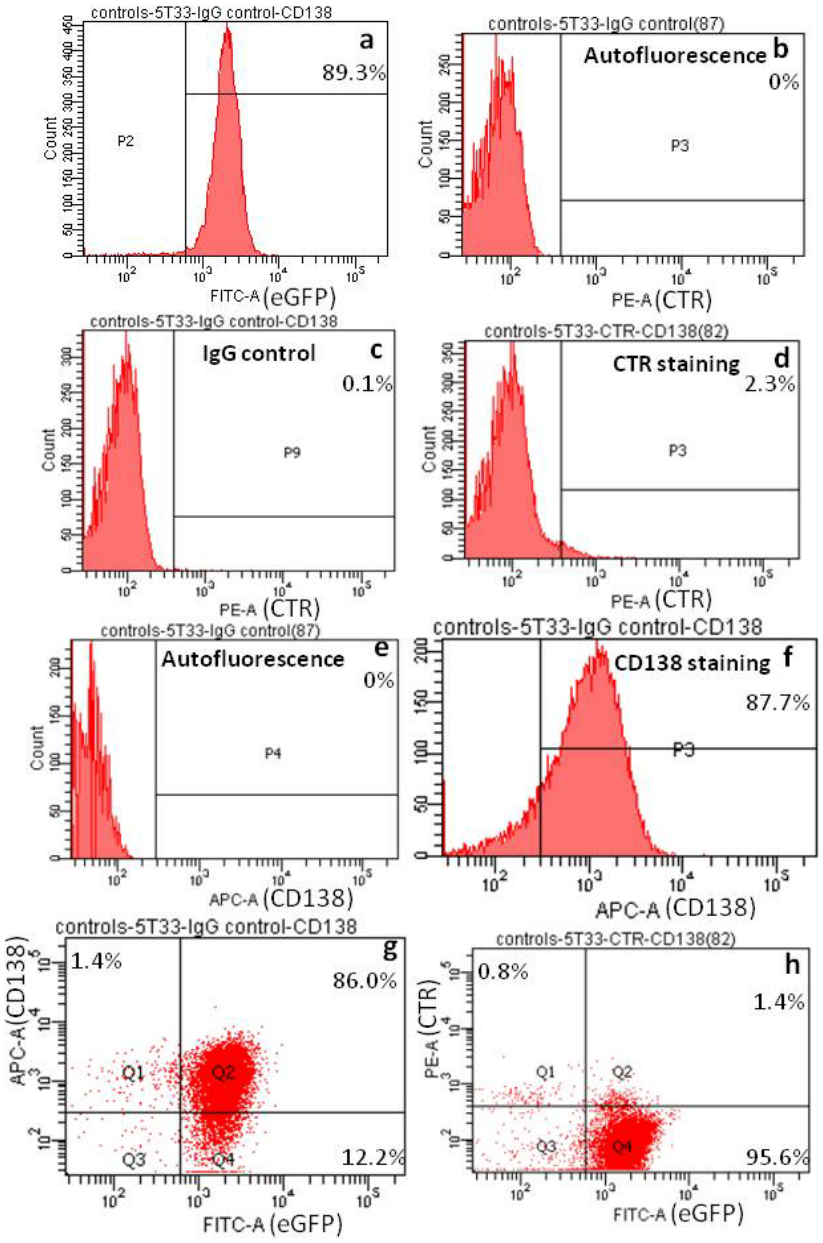

Figure 7.9: Results of the FACS analysis of *in vitro* cultured eGFP-5T33 cells stained for CTR and CD138. eGFP signal in the FITC channel (a), autofluorescence in the PE channel (b), non-specific binding of the secondary antibody (c), results of the staining for CTR (d), autofluorescence in the APC channel (e), results of CD138 staining (f), scatter diagrams (CD138 *vs.* eGFP (g) and CTR *vs.* eGFP (h)).

7.3.2.2 FACS analyses of organ homogenates

Liver, spleen and BM samples were isolated from every mouse in the “11 days”, “14 days” and “15 days” groups and also from three healthy controls.

Representative FACS results of liver samples are shown in Figure 7.10. Scatter diagrams are shown instead of histograms as this is a better representation to show CTR expression in eGFP+ and CD138+ populations. Figure 7.10 a-b confirm the low levels of autofluorescence and non-specific binding of secondary antibody in liver samples. Figure 7.10 c-d belong to a representative healthy control sample, it contained low levels of CTR+ cells and negligible CD138+ and eGFP+ populations. Results belonging to a representative MM bearing mouse are shown in Figure 7.10 e-f. In this sample the overall size of CTR+ population was 7.7%, most of the CTR+ cells were eGFP- (Figure 7.10 e, Q1-1). The size of eGFP+ population was low. However all the eGFP+ cells were CTR+ too (*N.B.* the size of Q4-1 was 0%) suggesting that unlike *in vitro* cultured eGFP-5T33 cells those homing in the liver do express CTR. The size of the CD138+ population was 1.9%, two thirds of these cells were eGFP+ too (Figure 7.10 f). In Figure 7.10 g-h we show FACS analysis results of one of the liver samples with the highest levels of CTR+ cells. Only 0.3% of the cells were eGFP+ however more than 14% of them were CTR+ (Figure 7.10 g). The size of the CD138+ population was minor (Figure 7.10 h).

Representative FACS results of spleen samples are shown in Figure 7.11. Figure 7.11 a-b confirm the low levels of autofluorescence and non-specific binding of secondary antibody in spleen samples. The size of the CTR+ population in a representative healthy control sample was above 10% (Figure 7.11 c) this is probably due to CTR+ white blood cells homing in the spleen. The size of the CD138+ population in healthy controls was minor (Figure 7.11 d).

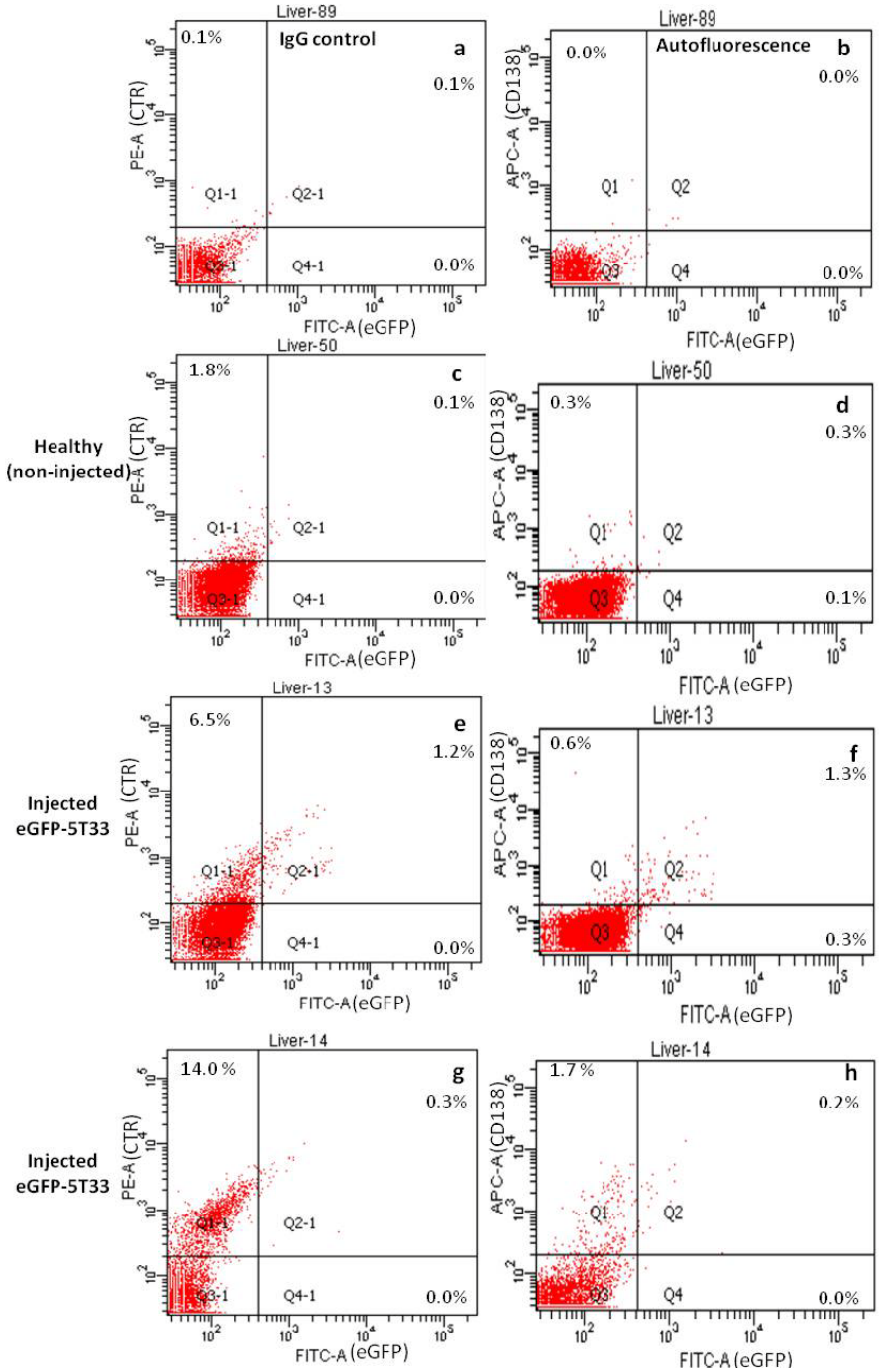

Figure 7.10: Results of the FACS analyses of liver samples stained for CTR and CD138. IgG control sample (a); autofluorescence control sample (b); representative sample from healthy control CTR *vs.* eGFP (c) and CD138 *vs.* eGFP (d) scatter diagrams; representative sample from MM bearing mouse CTR *vs.* eGFP (e) and CD138 *vs.* eGFP (f) scatter diagrams; MM bearing mouse with high levels of CTR+ cells CTR *vs.* eGFP (g) and CD138 *vs.* eGFP (h) scatter diagrams.

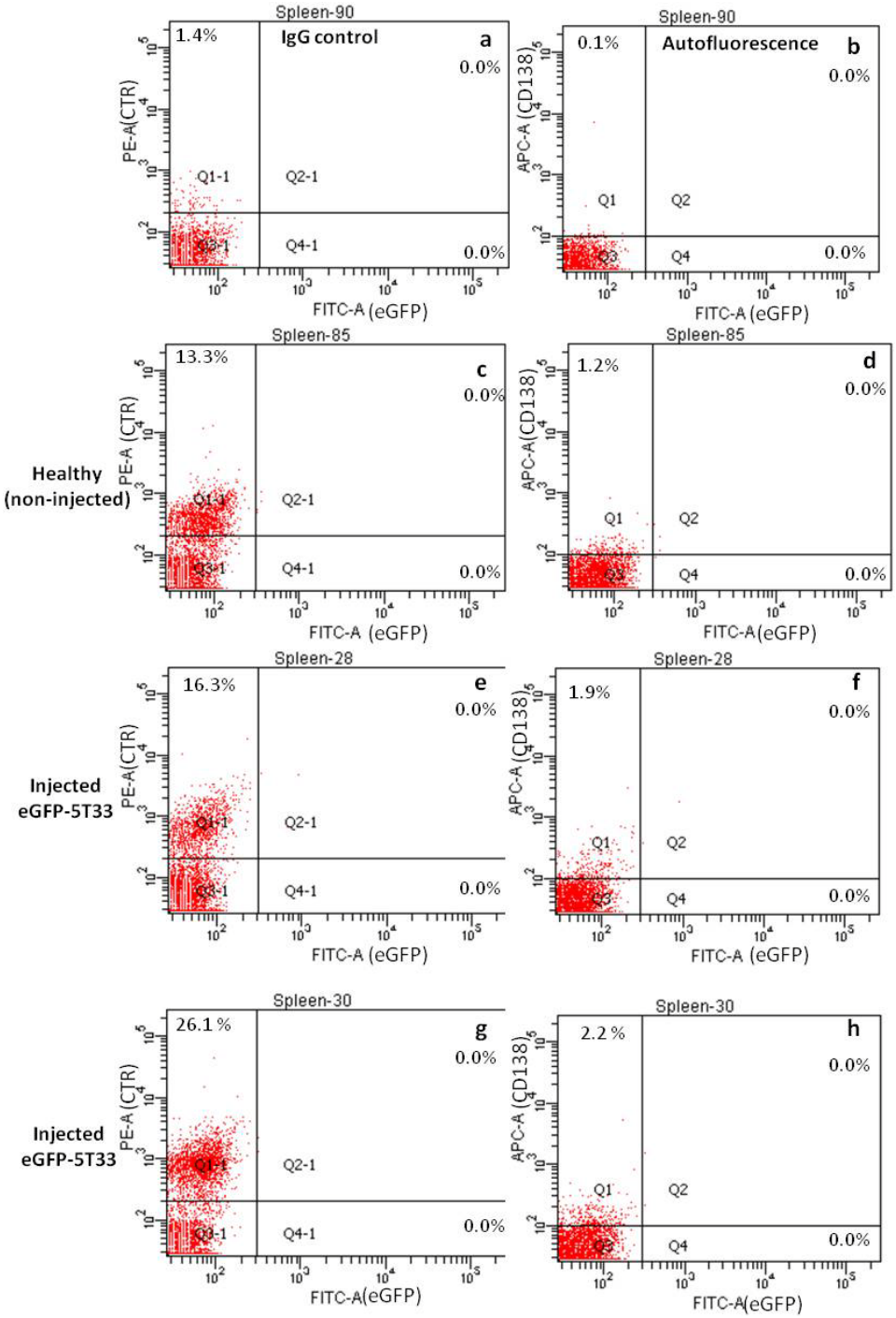

Figure 7.11: Results of the FACS analyses of spleen samples stained for CTR and CD138. IgG control sample (a); autofluorescence control sample (b); representative sample from healthy control CTR *vs.* eGFP (c) and CD138 *vs.* eGFP (d) scatter diagrams; representative sample from myeloma bearing mouse CTR *vs.* eGFP (e) and CD138 *vs.* eGFP (f) scatter diagrams; myeloma bearing mouse with high levels of CTR+ cells CTR *vs.* eGFP (g) and CD138 *vs.* eGFP (h) scatter diagrams.

A representative spleen sample obtained from a myeloma bearing mouse contained only slightly higher numbers of CTR+ and CD138+ cells than healthy controls (Figures 7.11 e-f) with no eGFP+ cells present. In Figure 7.11 g-h FACS analysis results of one of the spleen samples with the highest levels of CTR+ cells are shown. The size of the CTR+ population was twice as high as in the healthy control (Figure 7.11 g) however there were still no eGFP+ cells present. The size of the CD138+ population remained moderate (Figure 7.11 h).

Representative FACS results of BM samples are shown in Figure 7.12. Figure 7.12 a-b confirm the low levels of autofluorescence and non-specific binding of secondary antibody in BM samples. The size of the CTR+ population in a representative healthy control sample was high and comparable to the size of the CTR+ population in healthy spleen samples (Figure 7.12 c) this is probably due to CTR+ white blood cells and progenitors homing in the BM. The size of the CD138+ population in the BM of healthy controls was minor (Figure 7.12 d). A representative BM sample obtained from a MM bearing mouse contained only slightly higher numbers of CTR+ and CD138+ cells than samples obtained from healthy controls (Figures 7.12 e-f). However there was a cell population accounting for approximately 1% of the BM cells that was clearly eGFP+ (Q2-1, Q4-1, Q2, Q4 in Figures 7.12 e-f). Around half of these cells were also CTR+ and CD138+. In samples with very high levels of CTR+ cells (Figure 7.12 g-h) we observed approximately 2-3-fold increase in the size of the CTR+ population. The size of eGFP+ and CD138+ populations did not increase compared to representative “average” MM bearing mice.

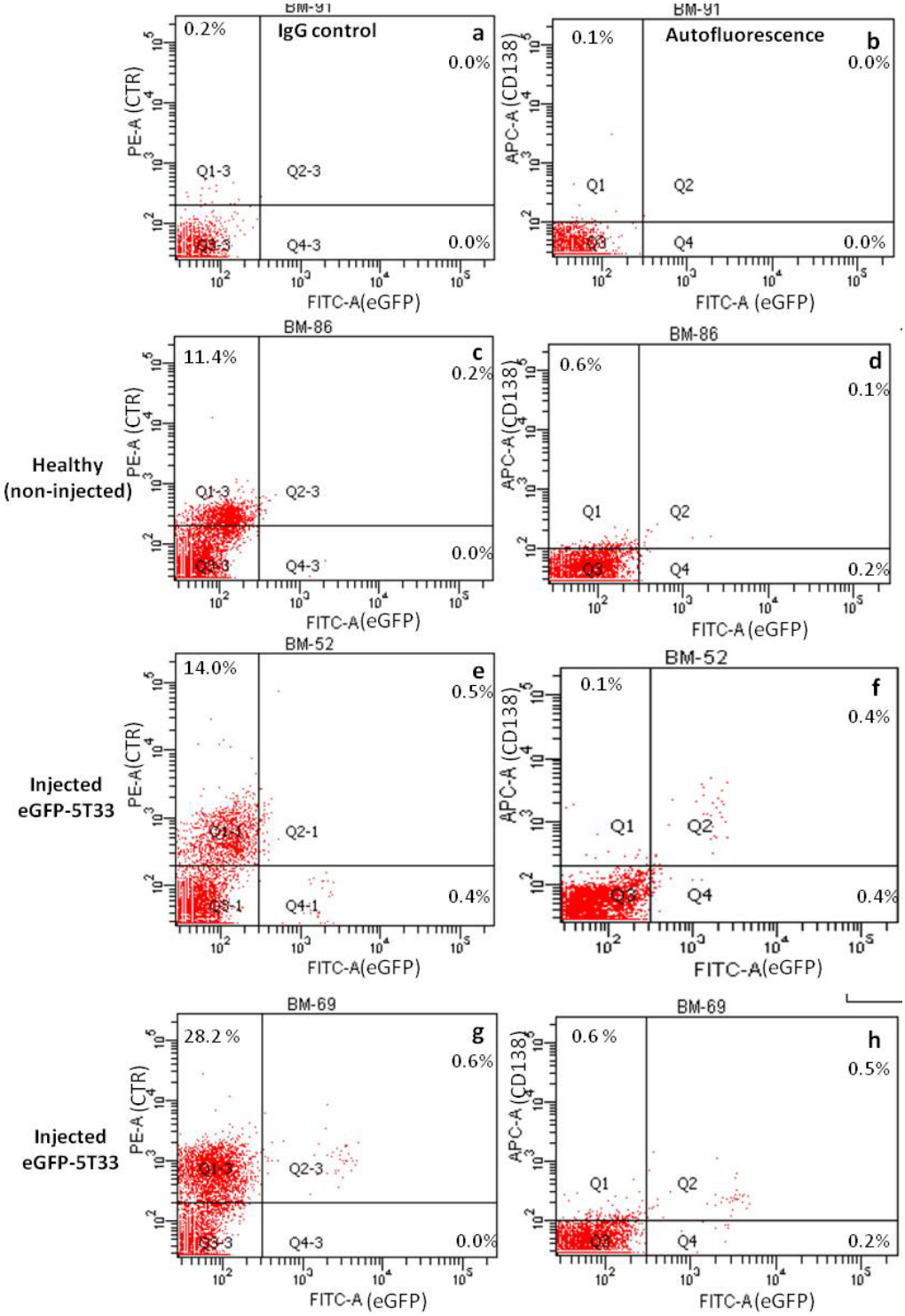

Figure 7.12: Results of the FACS analyses of BM samples stained for CTR and CD138. IgG control sample (a); autofluorescence control sample (b); representative sample from healthy control CTR *vs.* eGFP (c) and CD138 *vs.* eGFP (d) scatter diagrams; representative sample from MM bearing mouse CTR *vs.* eGFP (e) and CD138 *vs.* eGFP (f) scatter diagrams; MM bearing mouse with highest levels of CTR+ cells CTR *vs.* eGFP (g) and CD138 *vs.* eGFP (h) scatter diagrams.

Results of the FACS analyses of CTR and CD138 stained healthy control samples and samples obtained from MM bearing mice are reported in Table 7.3. Samples were also monitored on the FITC channel for endogenous expression of eGFP. We found low levels of CTR expression in healthy liver samples whilst the size of CTR+ cell population in spleen and BM control samples exceeded 10% probably due to a large number of (partly CTR+) leukocytes residing in these organs. The size of CD138+ populations in healthy controls was low, the size of eGFP+ populations was close to zero as expected (note that these animals had not been injected with eGFP-5T33 cells).

	negative control group (n=3)			"11 days" group (n=7)		
	P(CTR+)/%	P(CD138+)/%	P(eGFP+)/%	P(CTR+)/%	P(CD138+)/%	P(eGFP+)/%
Liver	2.3 (1.3)	0.4 (0.2)	0.2 (0.1)	11.4 (1.0)**	1.8 (0.3)**	1.0 (0.2)**
Spleen	13.1 (2.7)	1.3 (0.2)	0.0 (0.0)	27.1 (1.7)**	2.2 (0.3)*	0.0 (0.0)
BM	12.8 (0.3)	0.8 (0.2)	0.4 (0.2)	19.2 (2.0)**	1.0 (0.1)	0.3 (0.0)
	"14 days" group (n=12)			"15 days" group (n=6)		
	P(CTR+)/%	P(CD138+)/%	P(eGFP+)/%	P(CTR+)/%	P(CD138+)/%	P(eGFP+)/%
Liver	14.4 (1.5)**	2.2 (0.3)**	1.4 (0.2)**	9.9 (1.4)**	1.3 (0.2)*	0.3 (0.1)
Spleen	15.5 (2.7)	1.9 (0.4)	0.0 (0.0)	21.3 (2.6)*	1.5 (0.2)	0.0 (0.0)
BM	38.8 (2.8)**	0.5 (0.1)*	1.1 (0.1)	17.1 (2.7)	0.9 (0.2)	0.1 (0.1)

Table 7.3: Mean (SEM) CTR+, CD138+ and eGFP+ population sizes in different groups of control and eGFP-5T33 MM bearing mice. Significance of difference to controls are also reported: *:$p<0.05$, **: $p<0.01$.

In general, the eGFP+ population was very small in every organ and group. The size of the CD138+ cell population was slightly higher but still remained below 3%. The above findings suggest that only a low amount of MM cells were present in the samples. On the other hand we detected large CTR+ populations in every organ and group (especially in liver and BM samples when being compared to controls). Liver samples obtained from MM bearing mice contained significantly larger populations of CTR+ cells than controls ($p<0.01$). Compared to day 14 the size of the CTR+ population in liver samples shrank by day 15 but still remained higher

than in healthy controls ($p<0.01$). These results conflict with biodistribution data: liver uptake on day 15 was significantly higher than on day 14. It is therefore very likely that other, unidentified factors also affect liver uptake in disease bearing mice. We should also take into account that although the same cell line and mouse strain were used experiments and inoculations were carried out on different days. Experimental errors such as different cell counts, differences in inoculation (better or worse injections) and different passage numbers could have affected organ uptakes.

We found no eGFP+ cells in the spleen of eGFP-5T33 MM bearing mice. The size of the CTR+ population was significantly higher than in the control group in the “11 days” and “15 days” groups. The CD138+ population remained minor.

Ex vivo tissue counting experiments found that normalised radiopeptide uptake was far the highest in the spleen of 5T33 MM bearing mice. Radiopeptide uptake gradually increased with time after inoculation however the sizes of CTR+ populations did not reflect this tendency. The CTR+ population in the spleen was the largest on day 11 then unexpectedly low on day 14 with a slight increase by day 15. No significant differences were found in mean fluorescent intensities among the 4 groups. Therefore similarly to liver samples factors other than the size of CTR+ population affected the uptake of Tc-99m labelled sCTLys^{18}-hynic-TFA.

In BM samples the CTR+ population was already significantly higher on day 11 than in controls then doubled up by day 14 and dropped to the normal level by day 15. This fluctuation is unexpected however seems to reflect changes in uptake values: BM SUVs gradually increased until day 14 then dropped to the normal level on day 15. Taking into account what we had observed in liver and spleen samples the above tendency may just be coincidence.

Since the size of CTR+ populations seems to vary randomly among groups (refer to Table 7.3) we decided to study the whole set of 25 MM bearing mice imaged with the Tc-99m labelled sCTLys^{18}-hynic-TFA as one group, irrespective of the time they had been bearing MM for. Treating the data this way would also serve our main aim (*i.e.* confirming the presence of CTR+ cells in target organs and determining whether there is correlation between the size of the CTR+ population and radiopeptide uptake) better. We also aimed to investigate the relationship between CTR positivity and eGFP and/or CD138 positivity.

7.3.2.3 Correlation between the size of CTR+ population and SUVs

We plot the SUVs in the liver (Figure 7.13 a), spleen (Figure 7.13 b) and BM (Figure 7.13 c) as a function of the size of CTR+ population (in %). We found no (linear) correlation between the percent of CTR+ cells and Tc-99m-sCTLys^{18}-hynic-TFA uptake values in any of the target organs. Since the ultimate evidence for the presence of MM cells in the target organs was eGFP expression we speculated that there might be correlation between radiopeptide uptake and MM involvement. Thus we plotted the SUV *vs.* P(eGFP+) function in the liver and BM (Figure 7.14 a-b). Note that we did not find eGFP+ cells in spleen samples (Table 7.3). Results suggested that there was no correlation between uptake of the radiopeptide and the size of eGFP+ cell population in target organs.

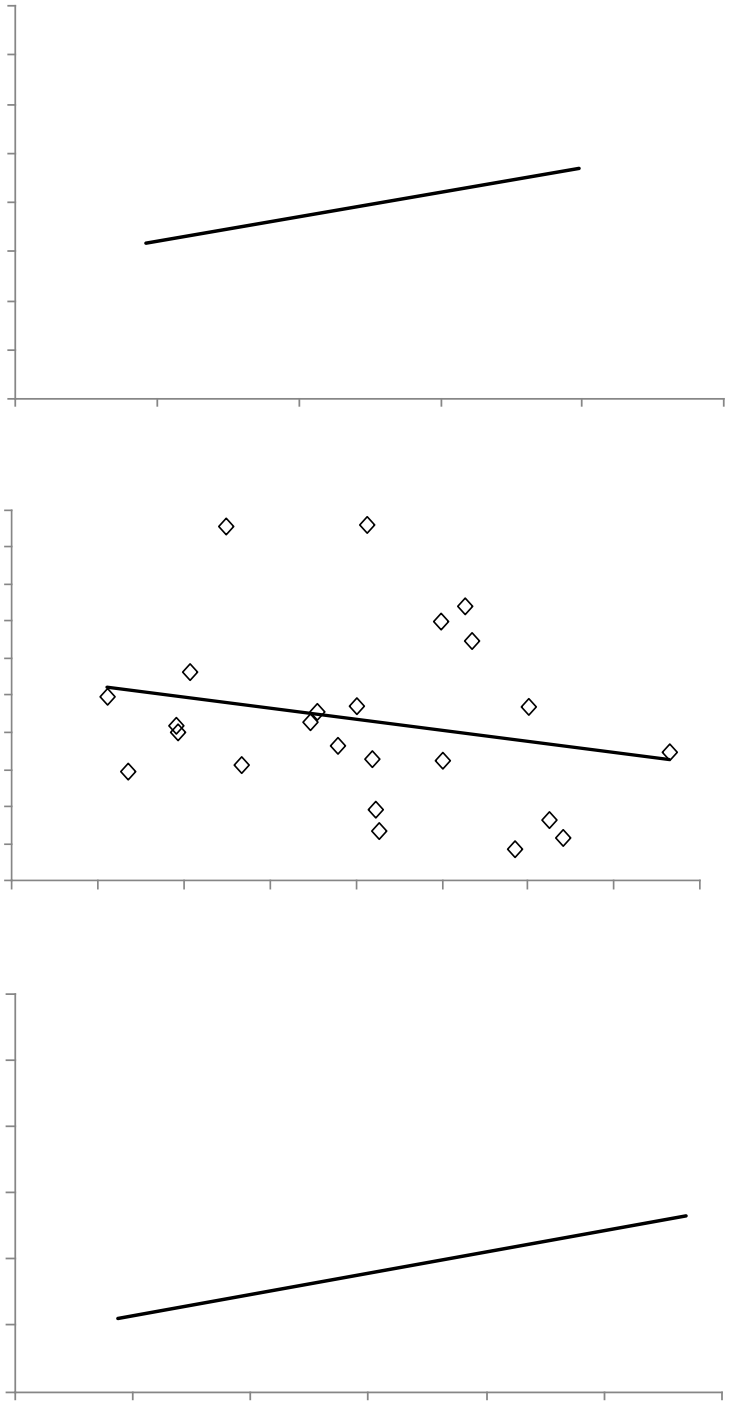

Figure 7.13: Correlation between uptake of Tc-99m-labelled sCTLys^{18}-hynic-TFA and the size of CTR+ population in the liver (a), spleen (b) and BM (c) of eGFP-5T33 MM bearing mice. Normal dots represent one animal, bold dots represent two animals.

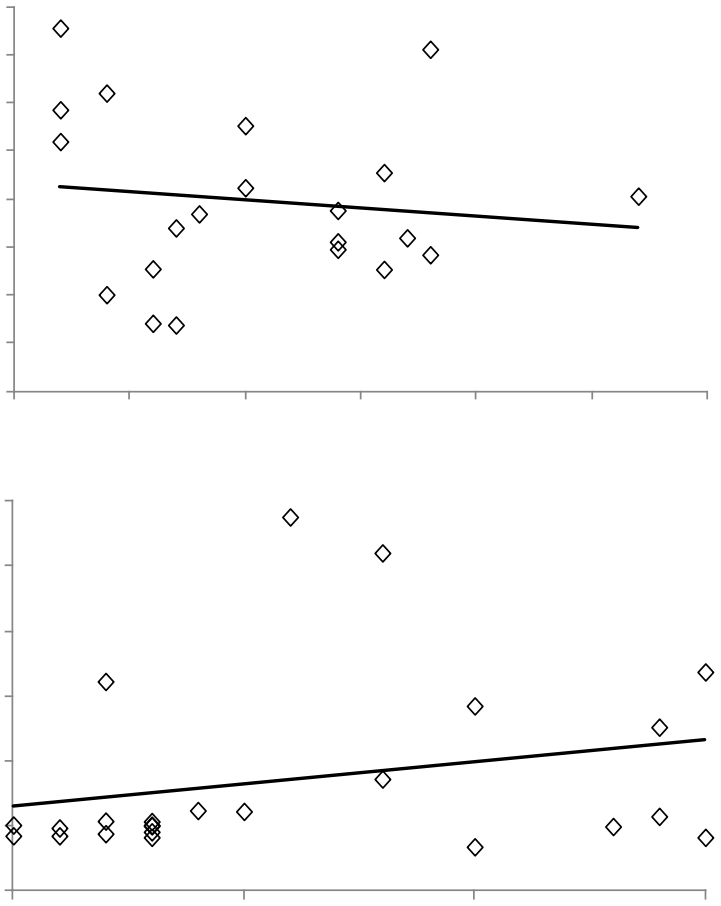

Figure 7.14: Correlation between uptake of Tc-99m-labelled sCTLys^{18}-hynic-TFA and the size of eGFP+ population in the liver (a) and BM (b) of eGFP-5T33 MM bearing mice. Normal dots represent one animal, bold dots represent two animals.

We also assessed correlation between the radiopeptide uptake in target organs and the size of the CTR+ and CD138+ subpopulation as CD138 is a plasma cell marker and eGFP-5T33 cells are CD138+. Results are reported in Figure 7.15 a-c.

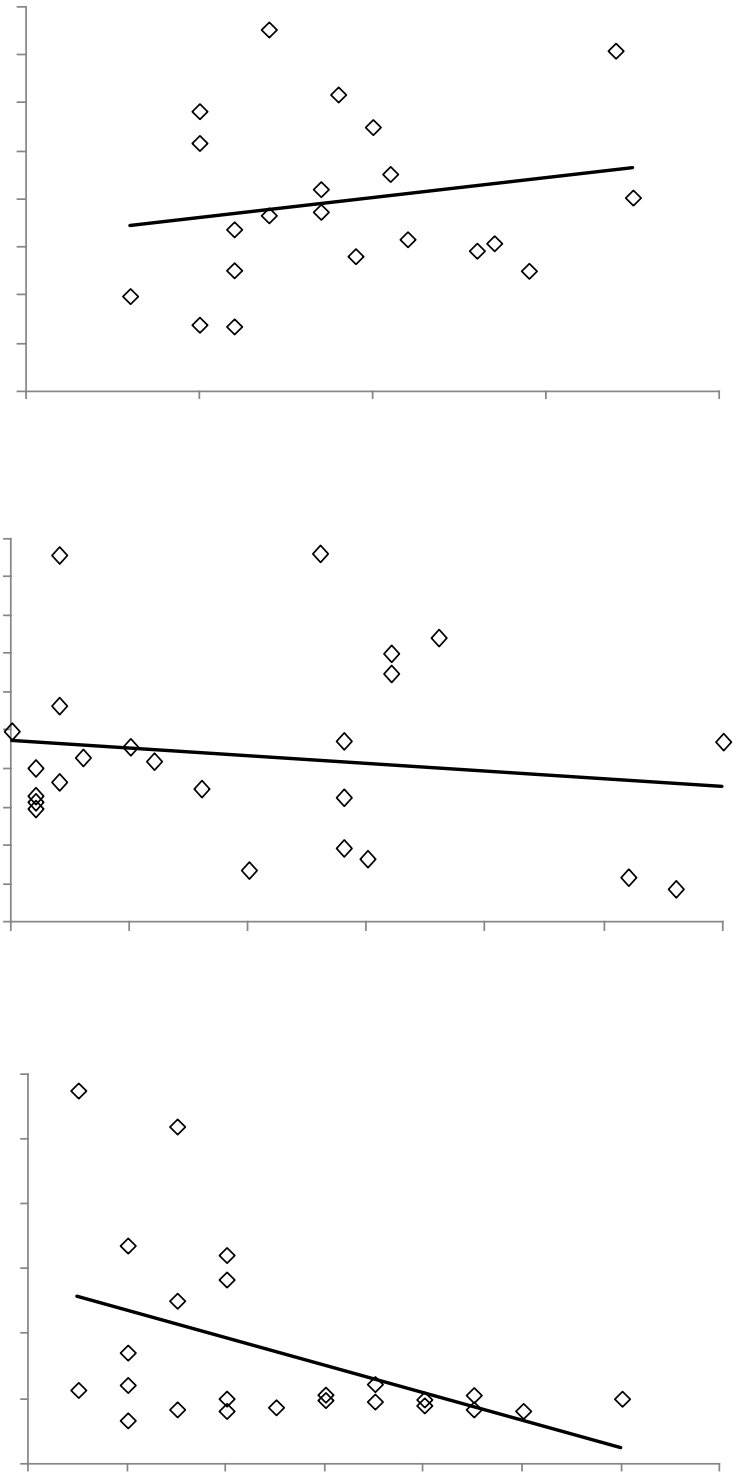

Figure 7.15: Correlation between uptake of Tc-99m-labelled sCTLys^{18}-hynic-TFA and the size of CTR+ and CD138+ subpopulation in the liver (a), spleen (b) and BM (c) of eGFP-5T33 MM bearing mice. Normal dots represent one animal, bold dots represent two animals.

7.3.2.4 Correlation between the size of CTR+, CD138+ and eGFP+ cell populations in the liver

We aimed to determine whether there is correlation between the sizes of different cell populations in order to better characterise the biology of eGFP-5T33 MM. We found strong positive linear correlation between the size of the CTR+ and CD138+ cell populations (Figure 7.16 a) and the size of the eGFP+ and CD138+ populations (Figure 7.16 b). Slightly weaker positive linear correlation was established between the percent of CTR+ and eGFP+ cells (Figure 7.16 c). In other words we found that CTR positivity was strongly associated with CD138 positivity (Figure 7.16 a), eGFP positivity was strongly associated with CD138 positivity (as expected) (Figure 7.16 b) and eGFP positivity was strongly associated with CTR positivity (Figure 7.16 c) suggesting that eGFP-5T33 cells do express CTR *in vivo* when homing in the liver. In addition to the above observations correlation parameters were nearly identical. Mathematically this would suggest that CD138+ and eGFP+ populations are in fact the same cell populations. To prove this hypothesis we analysed our data again and found that in liver samples nearly all CD138+ cells were eGFP+ too (Figure 7.17, slope≈1) in other words our hypothesis was true. Since in our system eGFP positivity is a highly specific marker of eGFP-5T33 cells we can also conclude that all the CD138+ plasma cells that we detected in liver homogenates were eGFP-5T33 MM cells. We also analysed the eGFP+ and CTR+ subpopulation and found that all the eGFP+ cells were CTR+ too (Figure 7.18, slope≈1). *N.B.* we did not detect CTRs on *in vitro* cultured eGFP-5T33 cells thus the above results are another example of how the phenotype of 5T33 cells can change *in vivo*. By combining the results shown in Figures 7.17-18 a simple consideration proves that in the liver every eGFP+ cell was also CTR+ **and** CD138+.

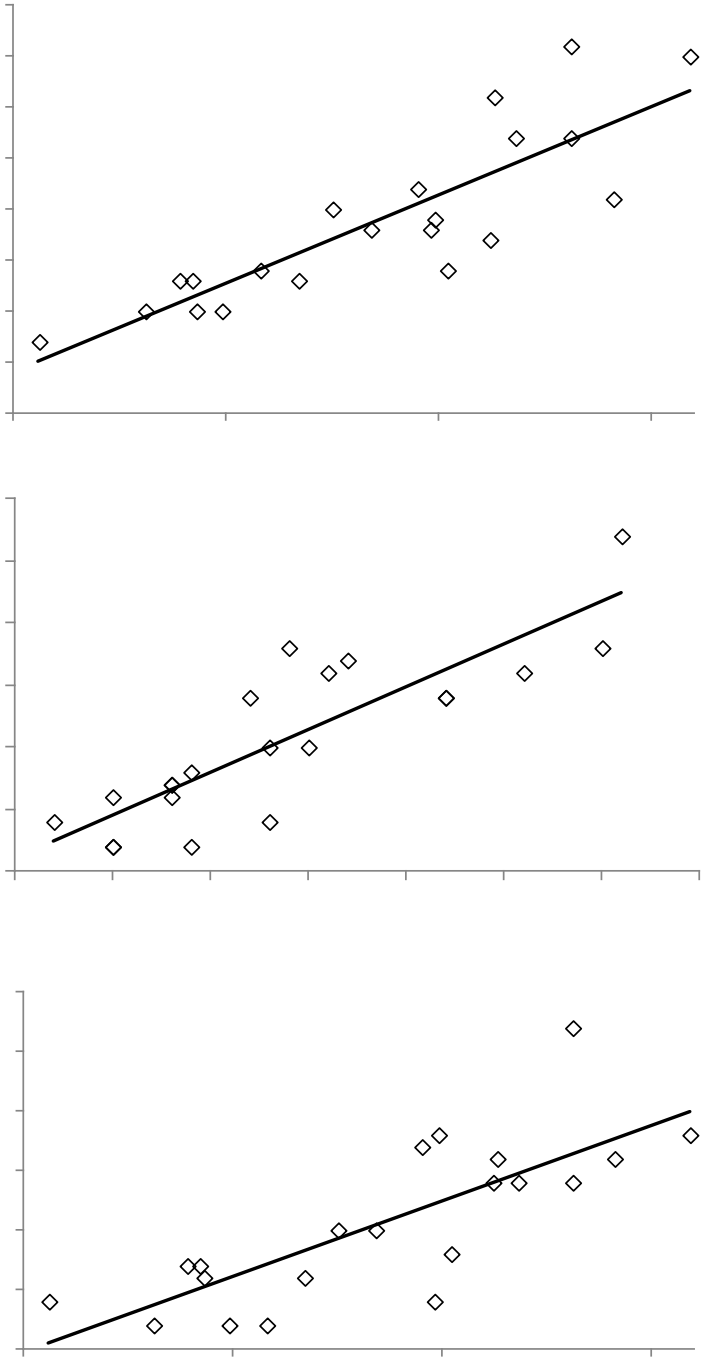

Figure 7.16: a: size of the CD138+ population as a function of the size of the CTR+ population; b: size of the eGFP+ population as a function of the size of the CD138+ population; c: size of the eGFP+ population as a function of the size of the CTR+ population in the liver of eGFP-5T33 MM bearing mice. Normal dots represent one animal, bold dots represent two animals.

In the samples that we analysed MM cells only accounted for a small fraction of CTR+ cells. Based on the above data it is likely that the presence of (CTR+) eGFP-5T33 cells evoke CTR expression in other liver cells or possibly the formation of a new cell type that is CTR+ (neoplasm) and this effect is proportional to the size of the 5T33 population.

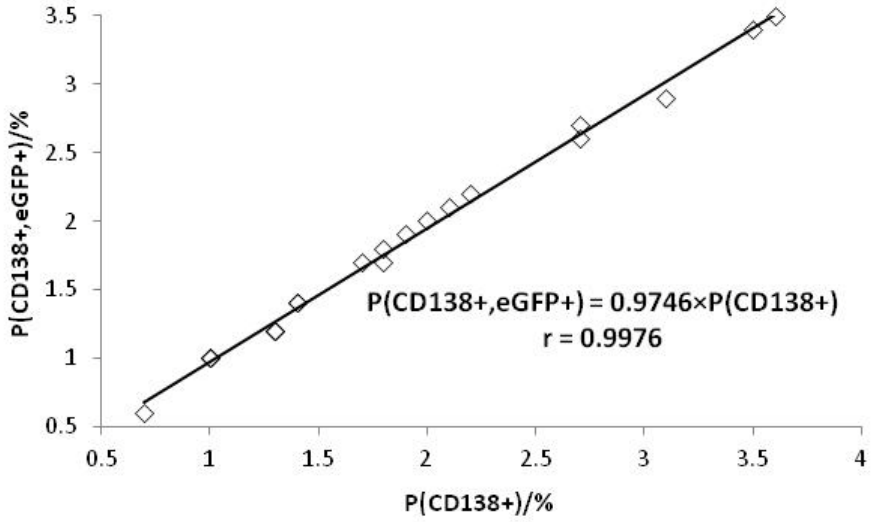

Figure 7.17: Size of the CD138+ and eGFP+ subpopulation as a function of the size of CD138+ population in the liver of eGFP-5T33 MM bearing mice. Normal dots represent one animal, bold dots represent two animals.

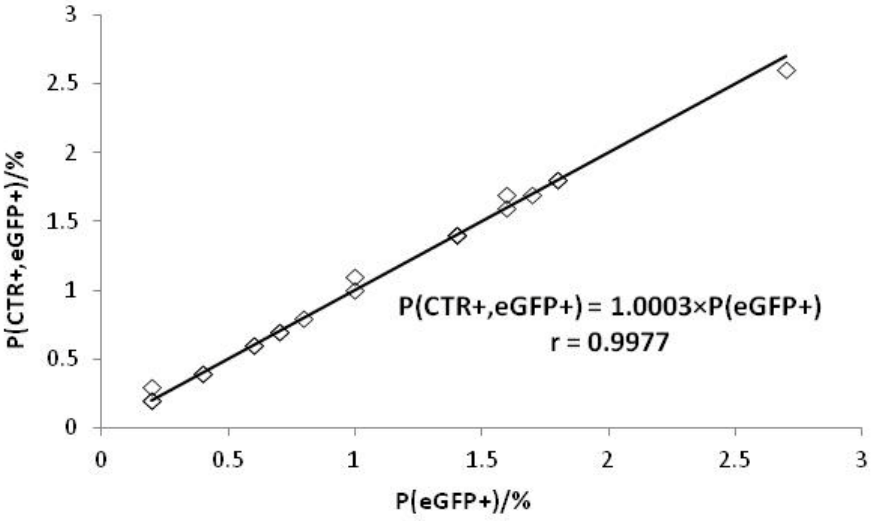

Figure 7.18: Size of the CTR+ and eGFP+ subpopulation as a function of the size of eGFP+ population in the liver of eGFP-5T33 MM bearing mice. Normal dots represent one animal, bold dots represent two animals.

7.3.2.5 Correlation between the size of CTR+, CD138+ and eGFP+ cell populations in the spleen

In the spleen of eGFP-5T33 MM bearing mice there was a positive linear correlation between the size of the CTR+ and CD138+ cell populations (Figure 7.19), similar to what we have described in the liver.

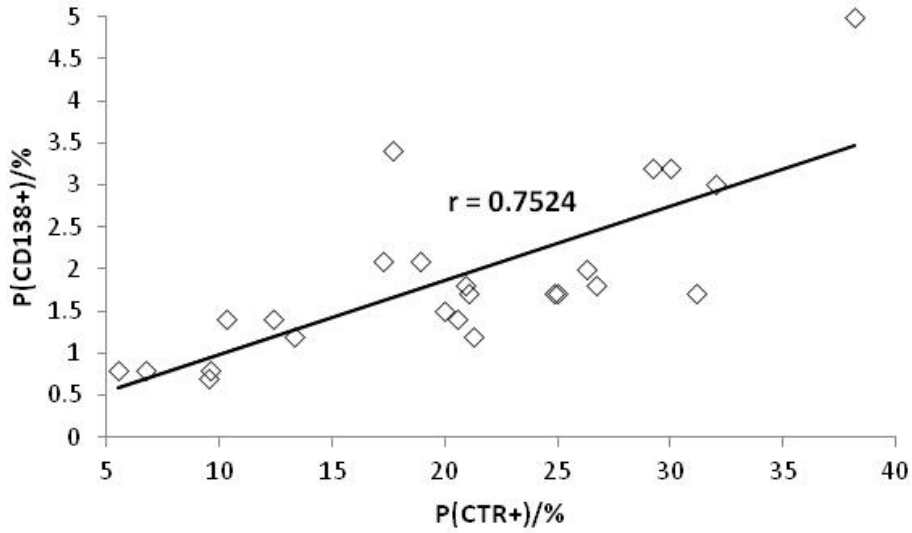

Figure 7.19: Size of CD138+ splenocyte population as a function of the size of CTR+ splenocyte population. Normal dots represent one animal, bold dots represent two animals.

In all but three of the spleen samples no eGFP+ cells were detected, the maximum eGFP+ population size was 0.2%. This is unexpected as based on imaging with In-111-oxine labelled eGFP-5T33 cells MM cells accumulate in the liver, spleen and BM immediately after inoculation and stay in these organs for at least seven days. It is noteworthy that in spleen samples obtained from control animals the average size of the CTR+ population was around 13% whilst in quite a few of MM bearing mice the above population size was between 5-15% only (refer to Figure 7.19), this finding needs to be investigated in the future. Correlation between the sizes of the CD138+ population and CD138+, CTR+ subpopulation was weak

(Figure 7.20). Figure 7.20 would suggest the existence of two different and well-separating sets of points. After checking the corresponding data we found that this separation was not associated with any experimental condition such as time of inoculation, cell passage numbers *etc*. suggesting that the separation of data was a random event.

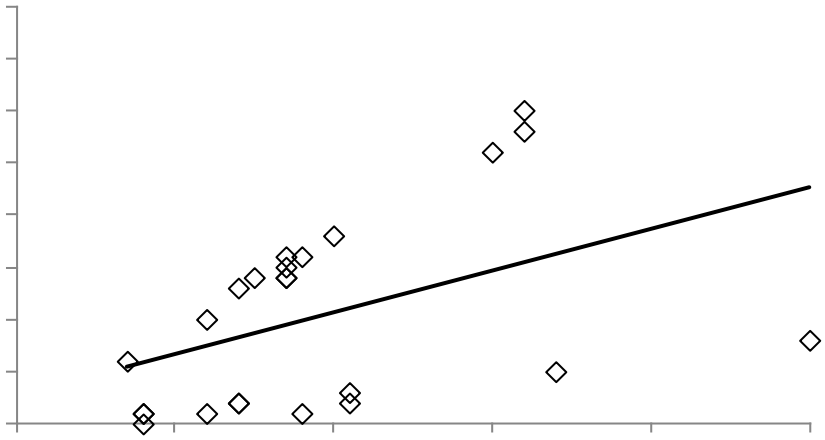

Figure 7.20: Size of the CD138+ and CTR+ subpopulation as a function of the size of CD138+ population in the spleen of eGFP-5T33 MM bearing mice. Normal dots represent one animal, bold dots represent two animals.

Our finding that the size of the CD138+ splenocyte population was in strong linear correlation with the size of the CTR+ cell population with the total lack of eGFP+ tumour cells and the lack of (strong) correlation between the size of CD138+ population and CD138+, CTR+ subpopulation suggests that disease progress in the spleen follows a pathway different to that occurring in the liver.

7.3.2.6 Correlation between the size of CTR+, CD138+ and eGFP+ cell populations in the BM

In BM samples isolated from MM bearing mice we found very weak negative linear correlation between the size of CTR+ and CD138+ (Figure 7.21 a) and

CD138+ and eGFP+ populations (Figure 7.21 b). *N.B.* in some of the samples the size of CTR+ and CD138+ populations were below the "normal" levels (~12% and ~0.8%, respectively), at this stage of our studies we have no explanation to this phenomenon. It is also noteworthy that in some samples as much as 50-55% of the BM cells were CTR+. We found a strong positive linear correlation between the size of the CTR+ and eGFP+ cell populations in the BM (Figure 7.21 c). This finding is similar to what we have described in liver samples. When plotting the P(CTR+, eGFP+) *vs.* P(eGFP+) (Figure 7.22) function we established a strong positive linear correlation and a slope≈1 suggesting that eGFP+ cells present in the BM were also CTR+ (again, similar to what we have found in the liver). We also plotted the P(eGFP+, CD138+) *vs.* P(CD138+) function and found a strong positive linear correlation (Figure 7.23). In this case the slope of the linear function was well below 1 suggesting that (i) eGFP-5T33 cells homing in the BM are CD138+ and (ii) there are additional CD138+ cells (possibly normal plasma cells) present. Based on the strong correlation there is likely to be a connection between the number of MM cells and other CD138+ cell types; yet again another proof that MM cells can influence their microenvironment as well as be influenced by their microenvironment. Based on the above data disease progress in the BM follows a third pathway *i.e.* it is partially different to what we have found in the liver and spleen. First, there was only a weak (and negative) correlation between the size of P(CTR+) and P(CD138+) and P(CD138+) and P(eGFP+) (Figure 7.21 a-b). In the liver a strong positive linear correlation was established for both pairs of cell populations. Due to the complete lack of eGFP+ cells in spleen samples we could only assess the first function where the correlation was strong and positive (Figure 7.19). In the spleen CD138+ cells were also CTR+ (similar to the liver) whilst we could not prove the same in the BM.

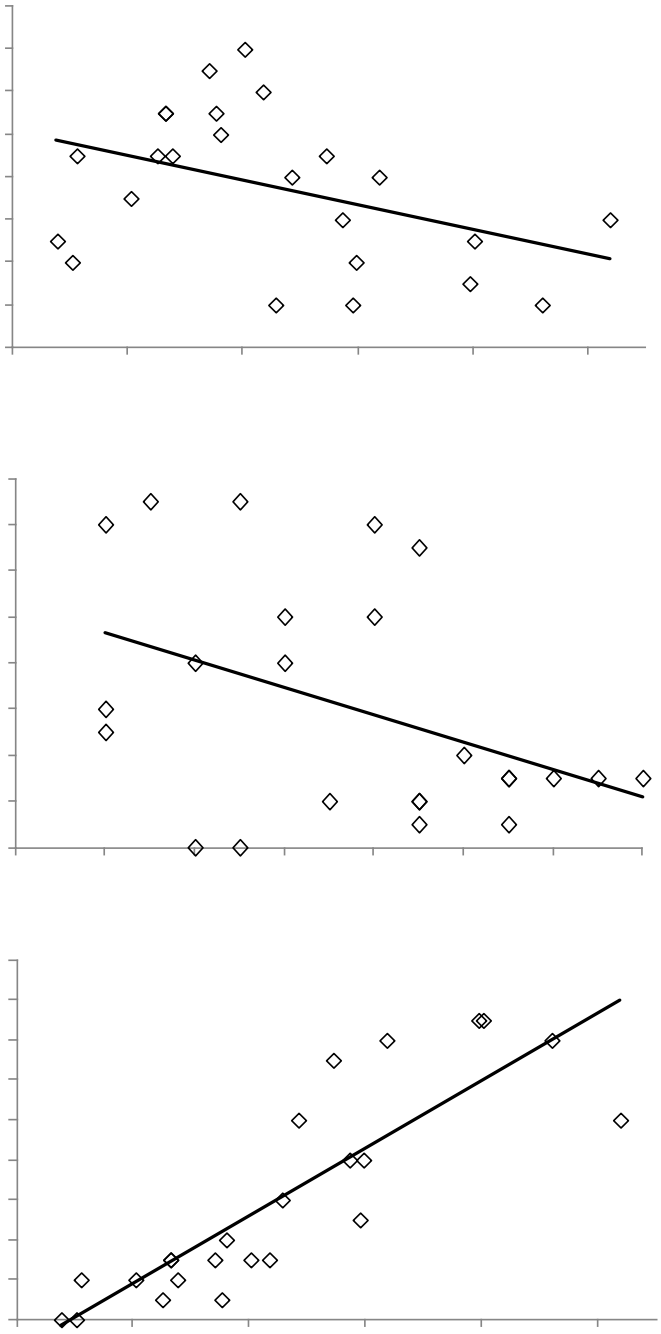

Figure 7.21: a: size of the CD138+ population as a function of the size of the CTR+ population; b: size of the eGFP+ population as a function of the size of the CD138+ population; c: size of the eGFP+ population as a function of the size of the CTR+ population in BM samples. Normal dots represent one animal, bold dots represent two animals.

However in the BM cells from the eGFP+ population (*i.e.* eGFP-5T33 clones) were also CTR+ (Figure 7.22) accounting for a small fraction of CTR+ cells.

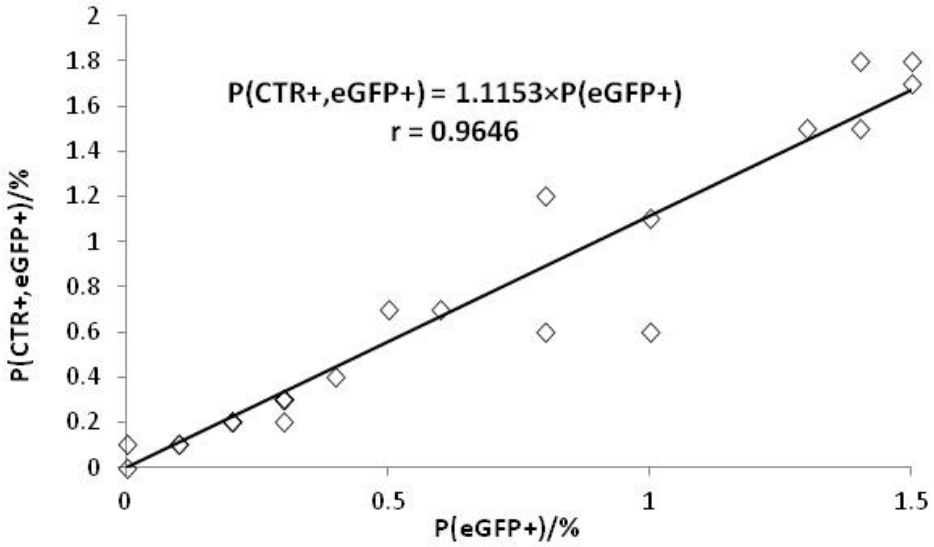

Figure 7.22: Size of the CTR+ and eGFP+ subpopulation as a function of the size of eGFP+ population in the BM of eGFP-5T33 MM bearing mice. Normal dots represent one animal, bold dots represent two animals.

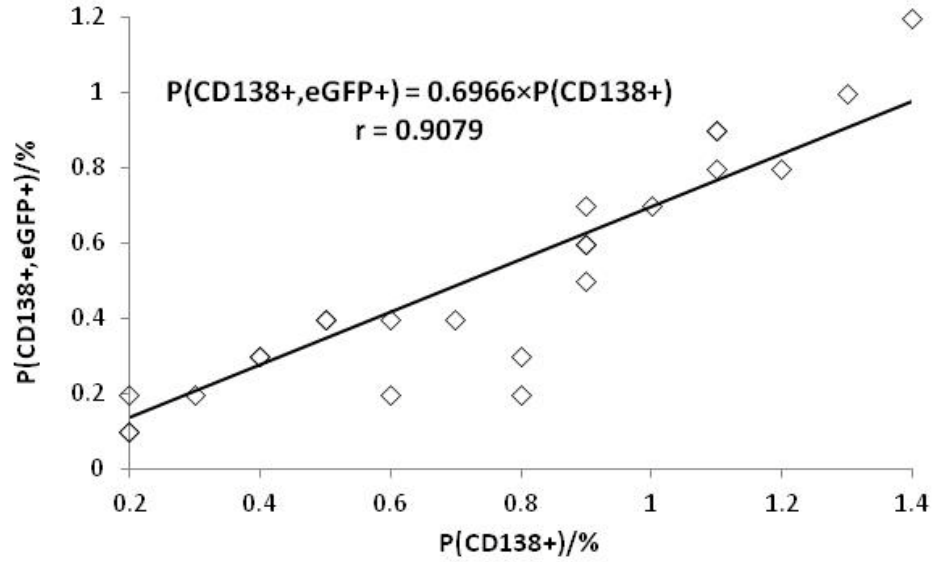

Figure 7.23: The size of the CD138+ and eGFP+ subpopulation as a function of the size of CD138+ population in the BM of eGFP-5T33 MM bearing mice. Normal dots represent one animal, bold dots represent two animals.

7.3.3 Imaging normal and MM bearing mice with Tc-99m labelled sCT(8-32)Lys^{18}-hynic-TFA

Briefly, control mice ("control group", n=3) were used without inoculation, disease bearing mice were used 15 days after i.v. inoculation ("15 days" group, n=6) with 10^6 eGFP-5T33 cells. Results of the imaging and biodistribution experiments are shown in Table 7.4 and Figure 7.24. Biodistribution pattern of the abbreviated peptide sequence is analogous to that of the radiolabelled sCTLys^{18}-hynic-TFA in normal mice. Image pattern of the abbreviated sequence was identical to that of the full hynic-sCT radiopeptide in a healthy control mouse (Figure 7.25).

	Control group n=3	"15 days" group n=6
Heart	0.42 (0.15)	0.33 (0.02)
Lungs	1.18 (0.54)	0.44 (0.03)
Liver	**0.79 (0.09)**	**1.19 (0.04)**
Spleen	**0.65 (0.17)**	**4.00 (0.49)**
Stomach	1.17 (0.66)	0.58 (0.21)
Intestines	0.50 (0.06)	0.24 (0.04)
Kidneys	35.03 (2.62)	28.28 (1.18)
Muscle	0.26 (0.06)	0.33 (0.03)
Femur	**0.44 (0.10)**	**0.38 (0.04)**
Blood	1.51 (0.72)	1.04 (0.23)

Table 7.4: Biodistribution of Tc-99m labelled sCT(8-32)Lys^{18}-hynic-TFA in control and MM bearing mice. Uptake is reported in mean SUV (SEM) for each organ.

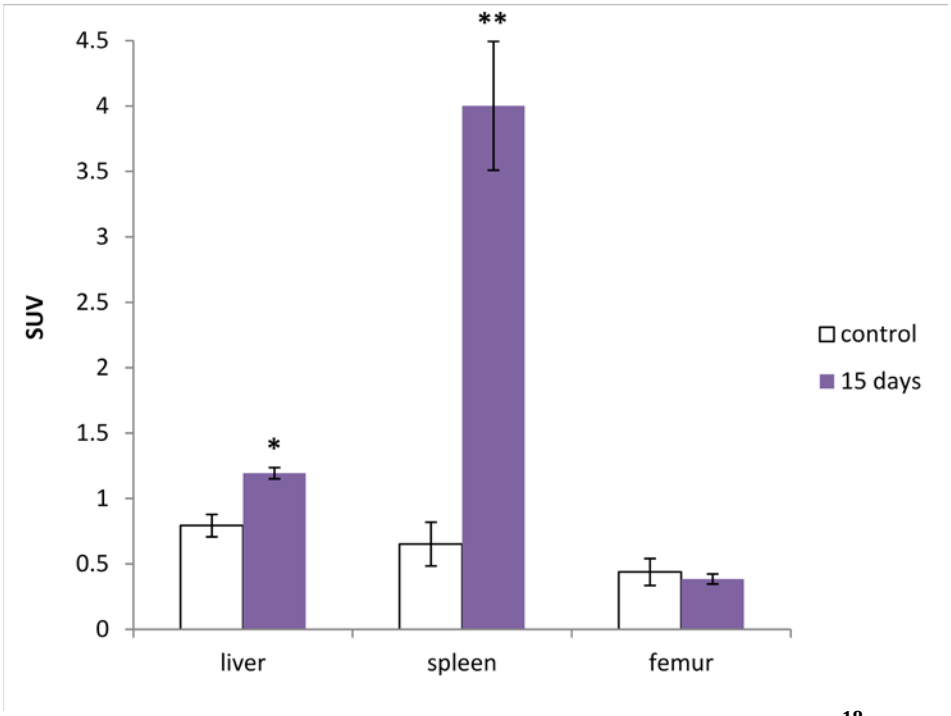

Figure 7.24: Mean SUV (SEM) of Tc-99m labelled sCT(8-32)Lys^{18}-hynic-TFA in target organs of control and MM bearing mice. Significance of difference to controls: *: p<0.05, **: p<0.001.

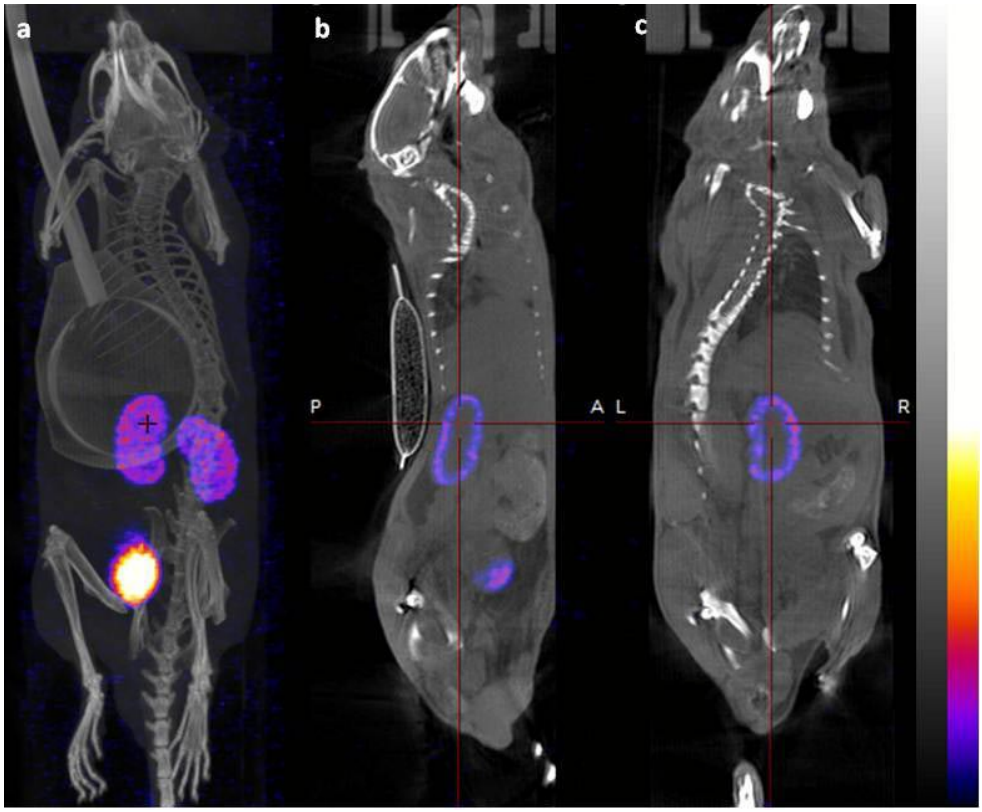

Figure 7.25: Healthy control mouse scanned 30 min post-injection of Tc-99m-sCT(8-32)Lys^{18}-hynic-TFA. Maximum intensity projection (MIP) (a), sagittal image section (b), coronal image section (c).

When a mouse belonging to “15 days” group was imaged with the Tc-99m-sCT(8-32)Lys^{18}-hynic-TFA the image scale had to be altered in order to visualise organs other than the kidneys and bladder (Figure 7.26, similar to the full sequence). An image obtained with a control mouse was manipulated the same way (Figure 7.26 a), this proved that liver uptake in Figure 7.26 b is associated with the disease. There is also significant uptake in the thyroids and salivary glands that is due to the presence of pertechnetate impurity.

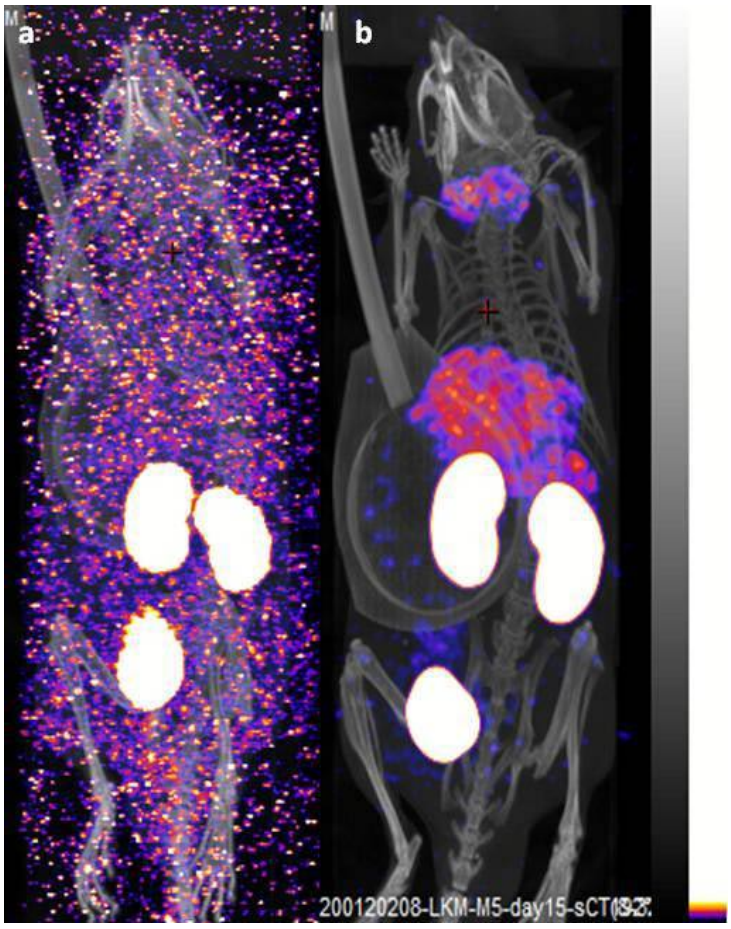

Figure 7.26: Representative MIP images acquired 30 minutes post-injection of Tc-99m labelled sCT(8-32)Lys^{18}-hynic-TFA in normal and MM bearing mice. Mouse from the control group (a), mouse from “15 days” group (b).

In every non-target organ of MM bearing mice (“15 days” group) uptake of the abbreviated radiopeptide was statistically the same as in control animals ($p>0.1$, null and alternative hypotheses are the same as those reported in Appendix 10)

except for the intestines and lungs. Difference in intestinal uptake is likely to be the result of different levels of pertechnetate impurity being present, difference in lung accumulation might be caused by colloidal impurities. In the liver and spleen of MM bearing mice radiopeptide uptake was significantly higher than in controls ($p<0.05$ and $p<0.001$ respectively). There was no statistically significant difference between the femoral (BM) uptake in control and MM bearing mice.

Based on the results of our preliminary imaging experiment the abbreviated hynic-calcitonin sequence does target the liver and spleen of eGFP-5T33 MM bearing mice however it does not seem to target BM lesions. Further studies on a higher number of animals should be carried out for a more complete evaluation.

7.3.4 FACS analyses of organ homogenates obtained from mice imaged with the Tc-99m labelled sCT(8-32)Lys^{18}-hynic-TFA

Although we used the same disease model we decided to include these data in a separate section. We had two reasons to do so. First, these experiments were carried out 2 months after we had finished the characterisation of the full hynic-sCT radiopeptide thus animals used in this experiment were inoculated with a different batch of eGFP-5T33 cells. Secondly, mice were injected with a different radiopeptide (thus they were "treated" differently). Results of FACS analyses are summarised in Table 7.5. Negative controls reported in section 7.3.2 were used as bases of comparison (also reported in Table 7.5).

	negative control group (n=3)			"15 days" group (n=6)		
	P(CTR+)/%	P(CD138+)/%	P(eGFP+)/%	P(CTR+)/%	P(CD138+)/%	P(eGFP+)/%
Liver	2.3 (1.3)	0.4 (0.2)	0.2 (0.1)	12.5 (3.3)**	1.2 (0.2)*	0.2 (0.1)
Spleen	13.1 (2.7)	1.3 (0.2)	0.0 (0.0)	23.0 (3.6)*	1.2 (0.2)	0.0 (0.0)
BM	12.8 (0.3)	0.8 (0.2)	0.4 (0.2)	22.9 (2.5)**	1.5 (0.2)*	0.3 (0.1)

Table 7.5: Mean (SEM) CTR+, CD138+ and eGFP+ population sizes in different groups of eGFP-5T33 MM bearing mice. Significance of difference to controls: *:$p<0.1$, **: $p<0.05$.

We found that average sizes of CTR+, CD138+ and eGFP+ populations were statistically the same as in the “15 days” group injected with the Tc-99m labelled sCTLys^{18}-hynic-TFA ($p>0.5$). After assessing correlation between the ratio of CTR+ cells and radiopeptide uptake in each target organ (Figure 7.27) we found that results were very similar to those obtained with the full radiopeptide sequence *i.e.* no (linear) correlation can be established between the size of CTR+ population and SUVs in any of the target organs.

N.B. when analysing results for spleen samples one could consider the point with the highest ratio of CTR+ cells (and lowest SUV) being an outlier. By ignoring that point we can establish a strong linear correlation (Figure 7.27 b, dashed line and bold symbols). From a purely mathematical point of view this step can fully be justified. However since samples were gamma counted, stained and analysed as part of the same worklist we could not give a good reason for omitting that particular point.

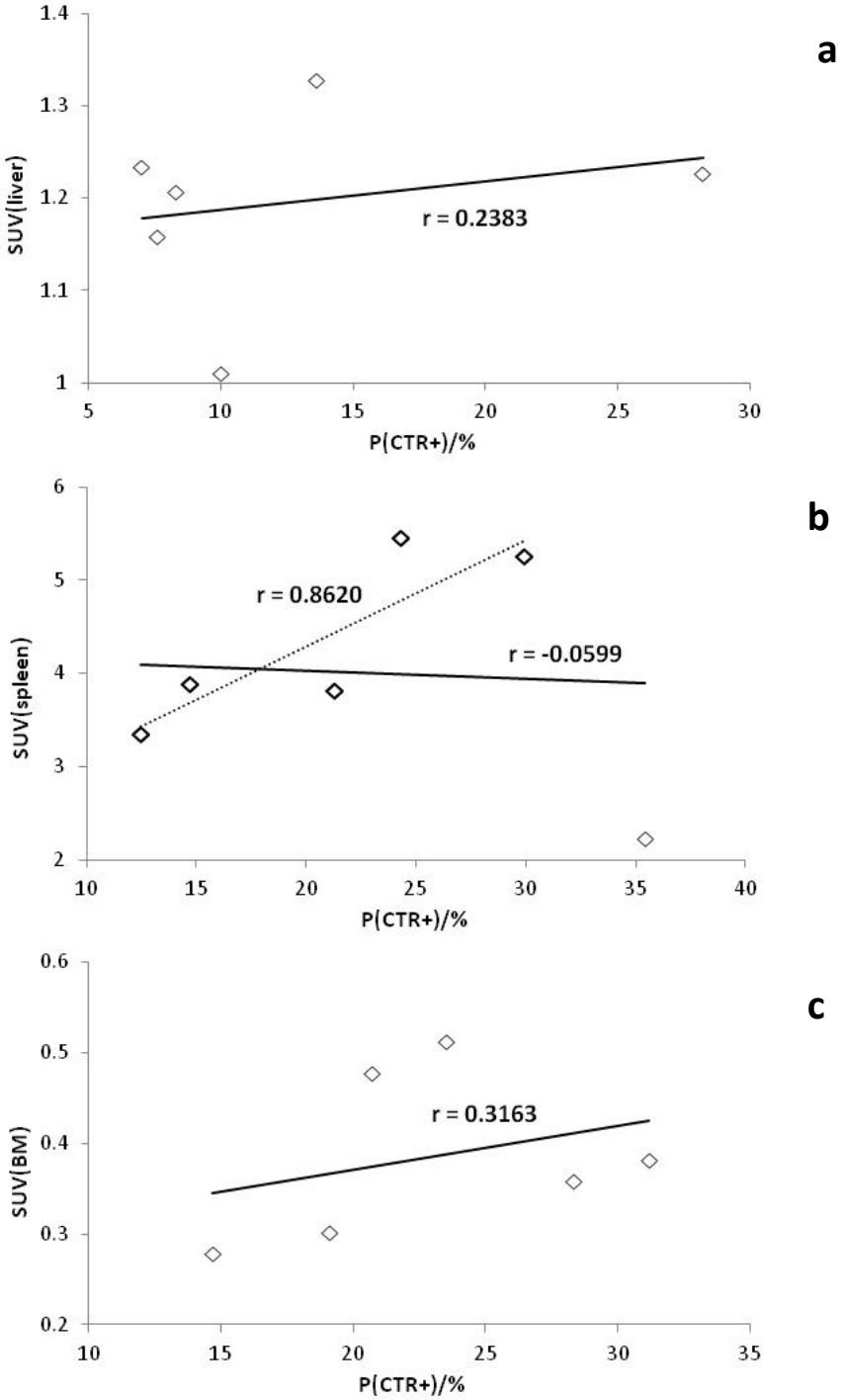

Figure 7.27: Correlation between uptake of Tc-99m-labelled sCT(8-32)Lys^{18}-hynic-TFA and the size of CTR+ population in the liver (a), spleen (b) and BM (c) of eGFP-5T33 MM bearing mice. The bold line on graph b is a trendline fitted on all six data points, the dashed line represents a trendline fitted on the five bold dots only (the sixth point considered as outlier).

7.3.4.1 Correlation between the size of CTR+, CD138+ and eGFP+ cell populations in the liver

Correlation was established between different cell populations (Figure 7.28), similar to our results in mice injected with the full radiopeptide. These data suggest that characteristics of the disease model did not change in this group of mice.

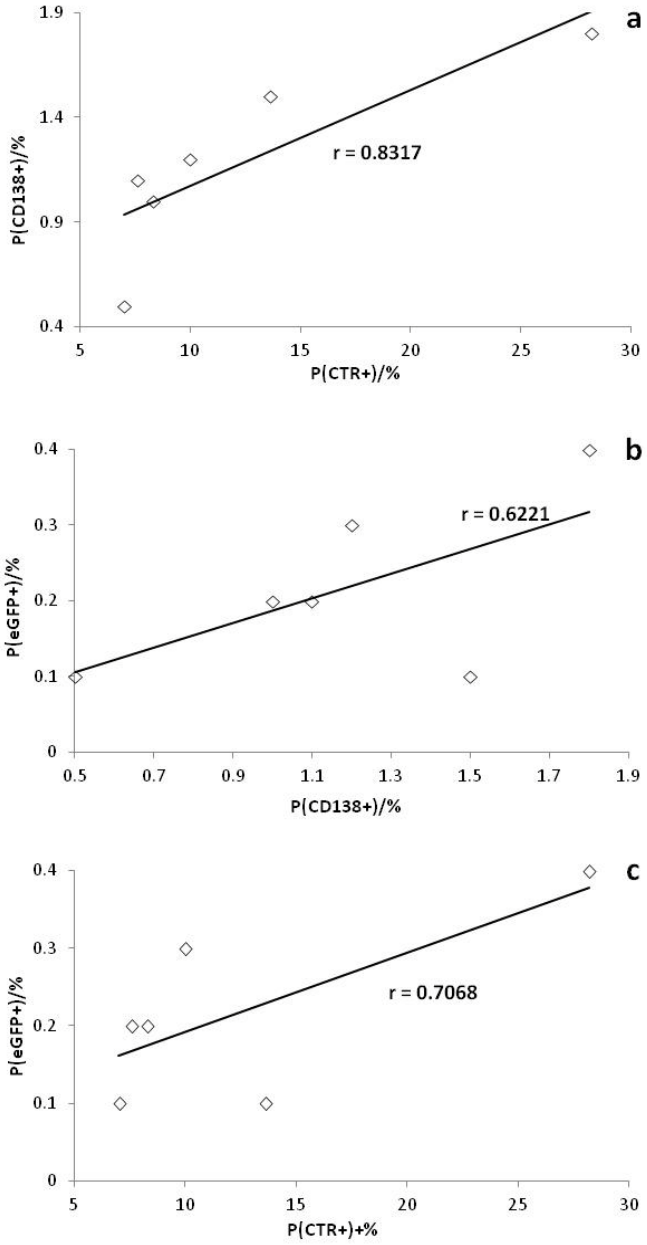

Figure 7.28: a: size of the CD138+ population as a function of the size of the CTR+ population; b: size of the eGFP+ population as a function of the size of the CD138+ population; c: size of the eGFP+ population as a function of the size of the CTR+ population in liver samples.

This is further confirmed when we plot the P(CTR+, eGFP+) *vs.* P(eGFP+) and P(CD138+, eGFP+) *vs.* P(CD138+) functions (Figures 7.29-7.30). The slope of both linear functions was very close to 1 and the correlation coefficient was very high confirming what we have established earlier, that is (irrespective of the injected radiopeptide) eGFP-5T33 cell clones homing in the liver are CTR+ and CD138+.

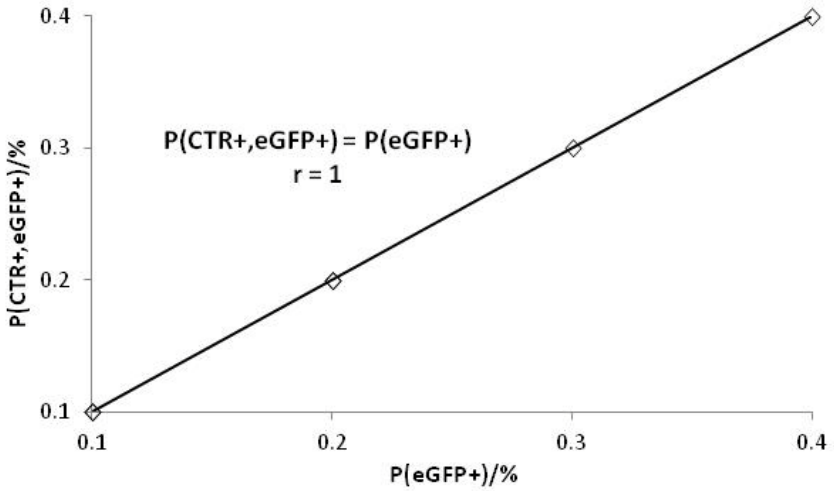

Figure 7.29: The size of the CTR+ and eGFP+ subpopulation as a function of the size of eGFP+ population in the liver of eGFP-5T33 MM bearing mice.

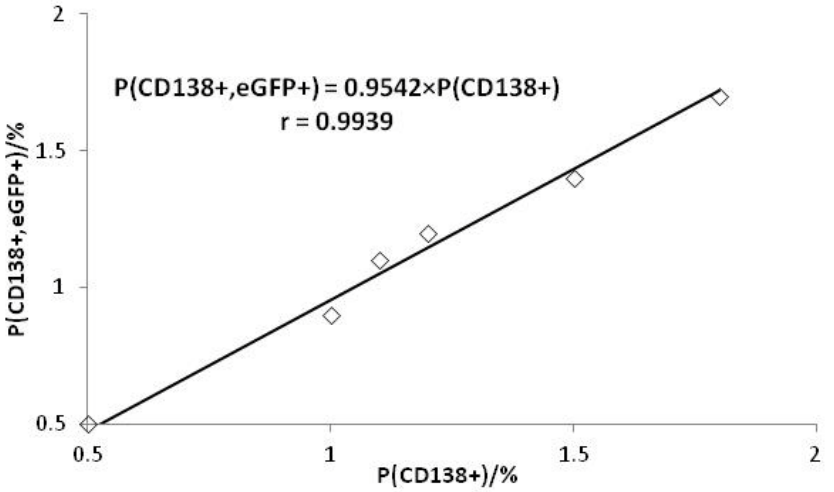

Figure 7.30: The size of the CD138+ and eGFP+ subpopulation as a function of the size of CD138+ population in the liver of eGFP-5T33 MM bearing mice.

7.3.4.2 Correlation between the size of CTR+, CD138+ and eGFP+ cell populations in the spleen

Results shown in Figure 7.31 are analogous to what we have found in the larger set of animals injected with the full radiopeptide sequence *i.e.* weak linear correlation can be established between the size of CTR+ and CD138+ cell populations. Again no eGFP+ cell populations were detected in spleen samples.

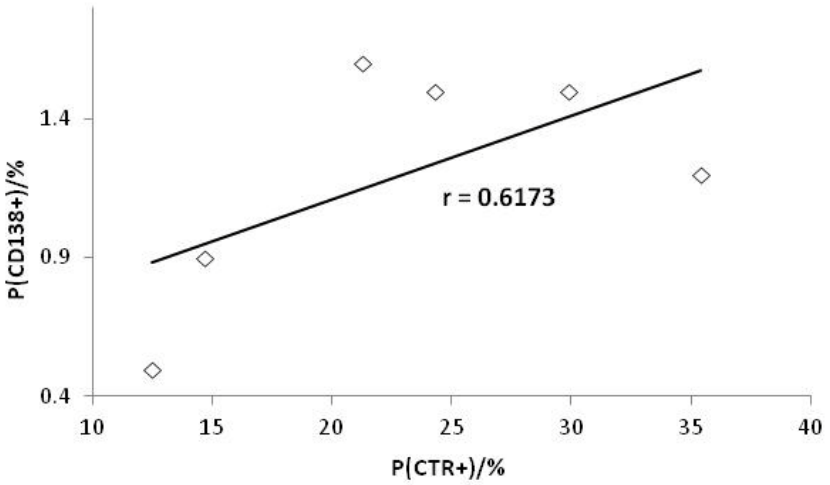

Figure 7.31: The size of the CD138+ splenocyte population as a function of the size of the CTR+ splenocyte population.

7.3.4.3 Correlation between the size of CTR+, CD138+ and eGFP+ cell populations in the BM

Results are shown in Figure 7.32. These findings are very different to what we have found in the other set of mice (refer to Figure 7.21). Differences are very significant (*i.e.* weak negative correlation in Figure 7.21 a-b *vs.* strong positive linear correlation in Figure 7.32 a-b) and probably can not be explained simply by the difference in group sizes. Based on Figure 7.32 b a very strong positive correlation can be established between P(CD138+) and P(eGFP+). The slope of the linear function is 0.37, this would suggest that every single MM cell "generates" two other CD138+ cells in the BM.

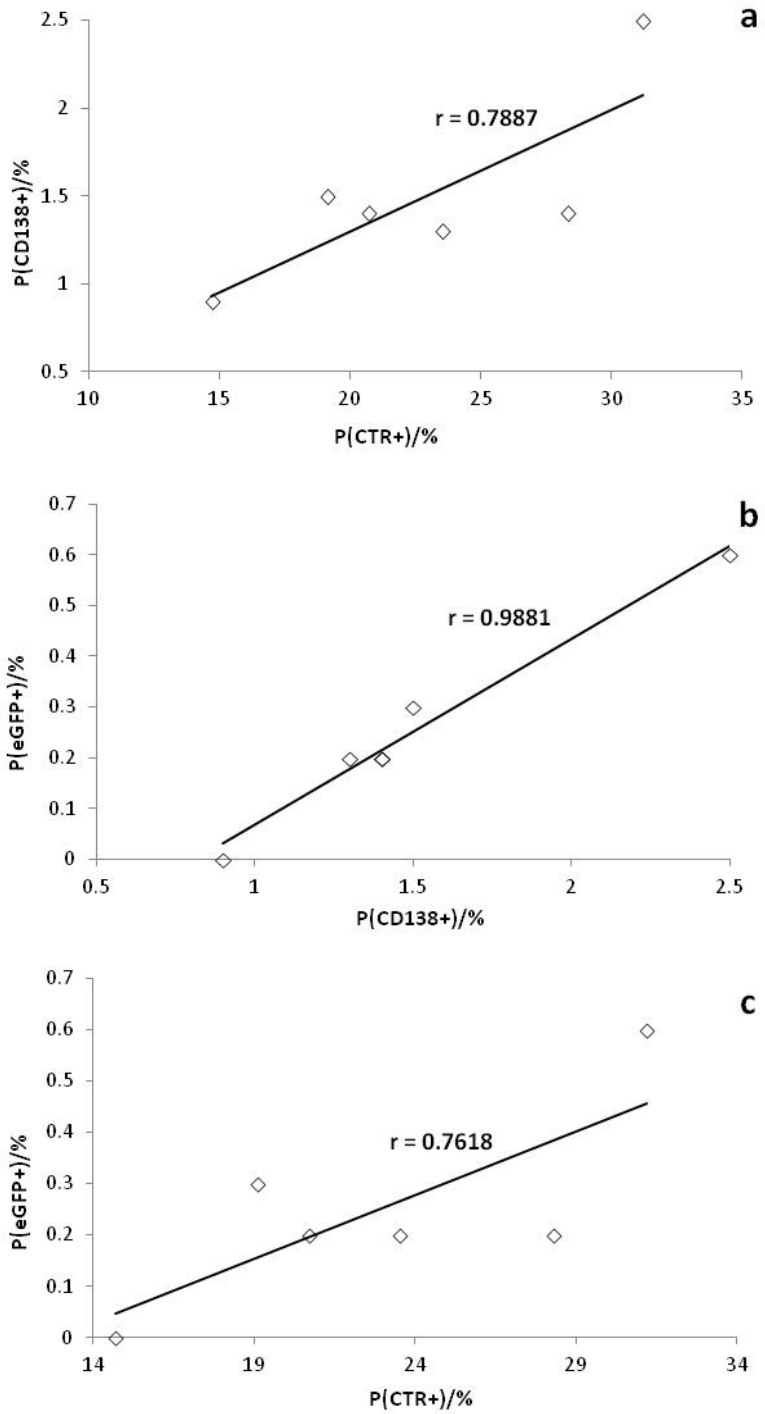

Figure 7.32: a: size of the CD138+ population as a function of the size of the CTR+ population; b: size of the eGFP+ population as a function of the size of the CD138+ population; c: size of the eGFP+ population as a function of the size of the CTR+ population in BM samples.

The P(CTR+, eGFP+) *vs.* P(eGFP+) function (Figure 7.33) is similar to the one obtained with the other set of mice (Figure 7.22) *i.e.* strong positive linear correlation with a slope close to 1; suggesting (confirming) that eGFP-5T33 MM cells become CTR+ when homing in the BM of C57Bl/KaLwRij mice. The P(CD138+, eGFP+) *vs.* P(CD138+) function (Figure 7.34) is similar to the one shown in Figure 7.23 in other words we confirmed the strong positive linear correlation between the two cell populations.

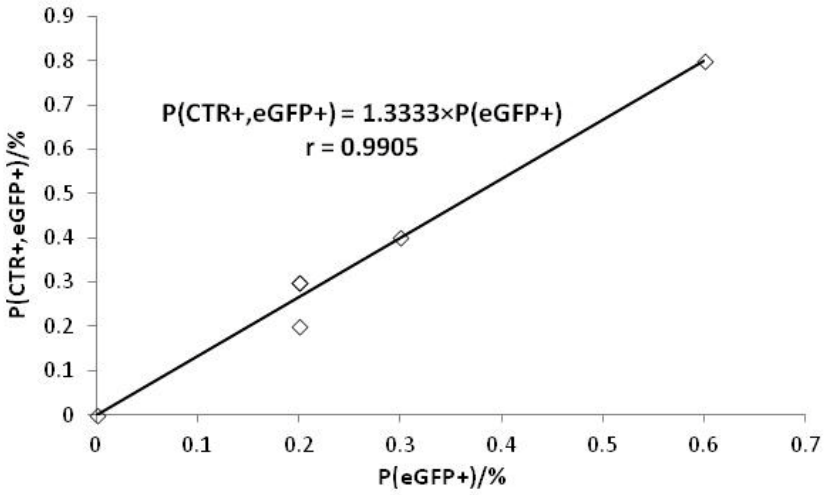

Figure 7.33: The size of the CTR+ and eGFP+ subpopulation as a function of the size of eGFP+ population in the BM.

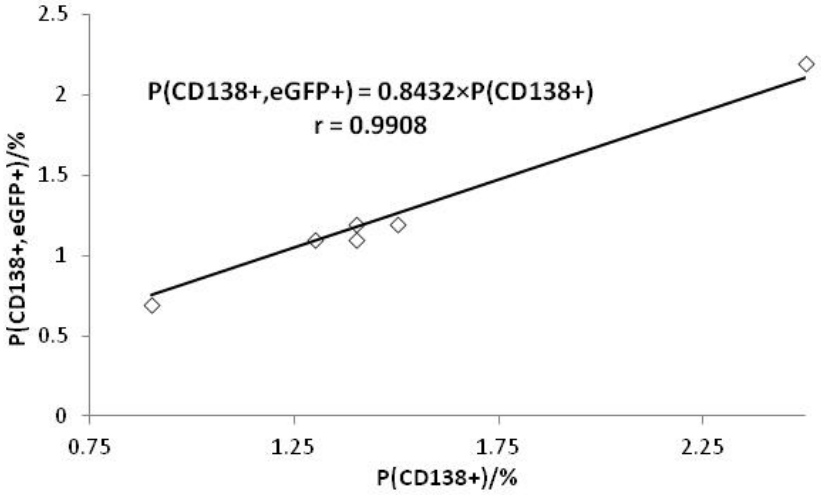

Figure 7.34: The size of the CD138+ and eGFP+ subpopulation as a function of the size of CD138+ population in the BM.

7.3.5 *In vivo* stability of Tc-99m labelled hynic-calcitonin derivatives

pH of the urine samples was slightly acidic, 6.9 (sample 1) and 6.0 (sample 2). HPLC chromatograms of the urine samples are shown in Figures 7.35-7.36. Mass spectrum of the compound(s) eluting at RT= 2.1 min is also shown (Figure 7.37) confirming the presence of tricine in the samples.

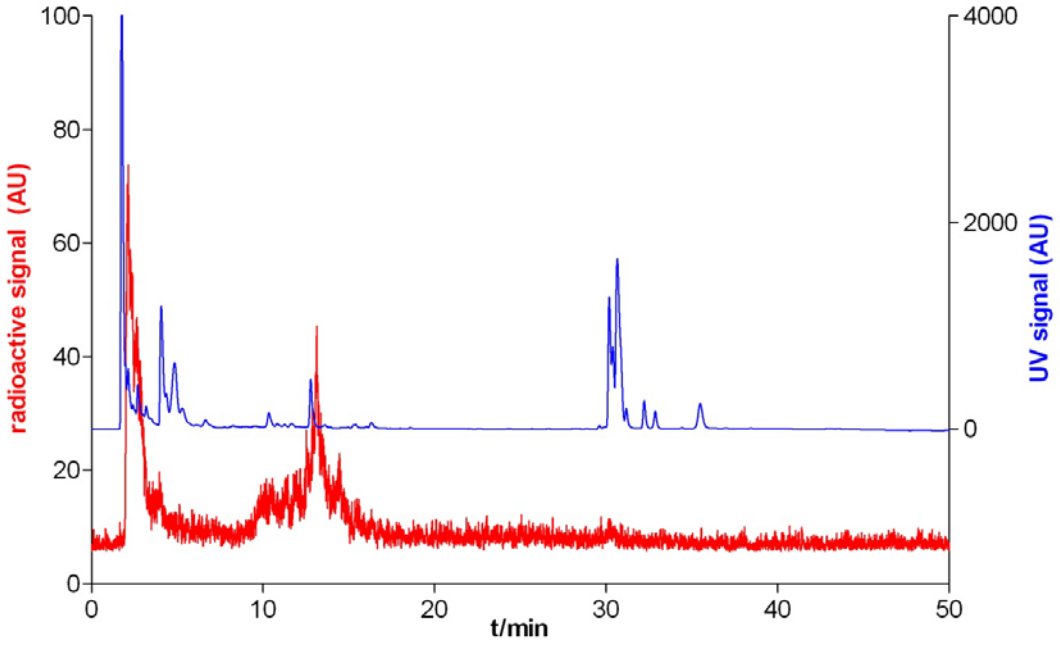

Figure 7.35: Radio (red) and UV (blue) chromatogram of a urine sample obtained 100 min post-injection from a mouse imaged with Tc-99m labelled sCTLys^{18}-hynic-TFA (sample 1).

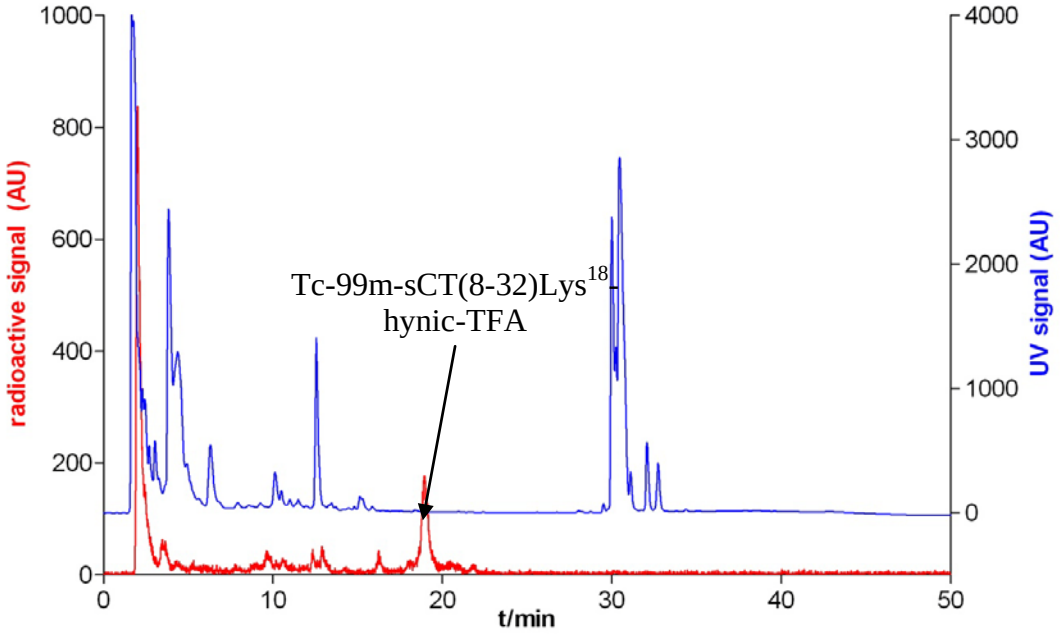

Figure 7.36: Radio (red) and UV (blue) chromatogram of a urine sample obtained 100 min post-injection from a mouse imaged with Tc-99m labelled sCT(8-32)Lys^{18}-hynic-TFA (sample 2).

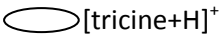

Figure 7.37: Mass spectrum of the RT=1.6-2.5 min region (sample 1)

Sample 1 only contained degradation intermediates eluting between 10-20 minutes and a small hydrophilic radioactive species (RT=2.1 min). Surprisingly 17% of the radioactivity recovered from sample 2 was still in the form of Tc-99m labelled sCT(8-32)Lys^{18}-hynic-TFA suggesting that the abbreviated radiopeptide is more stable *in vivo* than the full hynic-calcitonin sequence. In sample 2 only a minor fraction of activity was present in the form of degradation intermediates (RT=10-15 min) with the most intense peak being the one eluting at RT=2.1 min. These findings

confirm the results of *in vitro* assays *i.e.* the abbreviated radiopeptide is likely to be more resistant to degradation processes both *in vitro* and *in vivo*.

7.4 Discussion

Based on their biodistribution pattern both Tc-99m labelled hynic-calcitonin derivatives behave very similarly to the iodinated calcitonin sequence as assessed by Blower *et al.*: they found that 10 minutes post-injection >50% of the injected radiopeptide was in the kidneys with moderate uptake in the liver, lungs and gut [81]. Gut uptake is possibly related to the presence of pertechnetate (and released radioiodide in Blower's cited work).

When comparing the Tc-99m labelled sCTLys^{18}-hynic-TFA and sCT(8-32)Lys^{18}-hynic-TFA in the 5T33 MM model (15 days post-inoculation with 10^6 eGFP-5T33 cells) we find very similar liver SUVs (1.19 (0.04) and 1.26 (0.11) respectively). The average SUV in the spleen was higher with the full sequence than the abbreviated compound (6.57±0.80 *vs.* 4.00±0.49). However when comparing the spleen uptake of the two radiopeptide sequences to their baseline counterparts we found a higher relative increase in sCT(8-32)Lys^{18}-hynic-TFA uptake (baseline level 0.65±0.17 (control group) and baseline level for sCTLys^{18}-hynic-TFA 1.67±0.29). Taking into account every target organ we observed 2-6-fold increase in radiopeptide uptake depending on time-point and organ. This might seem moderate however still acceptable for a peptide radiopharmaceutical: *e.g.* when imaging osteolytic lesions with a Cu-64-labelled RGD peptide Wadas *et al.* achieved a 2-fold increase when comparing the uptake values to healthy controls [62]. The actual radiopeptide uptake they report on was around 1%ID/g. We use SUV instead of %ID/g; when converting the SUVs to %ID/g the average Tc-99m labelled sCT(8-32)Lys^{18}-hynic-TFA uptake in the spleen of the "15 days" group is 20.5±2 %ID/g.

It is likely that we would have detected higher and possibly imageable uptake in the BM if we had kept MM bearing mice for more than 15 days. It is known that at the onset of paraplegia the percentage of eGFP-5T33 cells suddenly increases from 2-3% to above 10% (Table 6.1 or [169]) in the BM thus at that point we could probably have imaged bone involvement. However we first wanted to test the possibility of detecting MM cells at low levels of presence in target organs to see if this could be an adequate method for detection of minimal residual disease as well as for micro-bone lesions. Bearing in mind that nanoSPECT/CT scanner, laboratory and Tc-99m-pertechnetate availabilities are limited (especially out of hours and over the weekend; on weekdays pertechnetate orders have to be submitted by 11am the day before) waiting for the onset of paraplegia would have been "risky" and possibly unethical as there was a chance of having to cull MM bearing mice without being able to perform an imaging or an *ex vivo* tissue counting experiment. Taking into account the very low tumour burden in organ homogenates strictly speaking mice bore MGUS and not MM at the time the experiments were carried out (*i.e.* myeloma cell counts were below 10%).

BM uptake of the abbreviated sequence in MM bearing mice was statistically the same as in healthy controls. *N.B.* BM uptake of the full sequence significantly decreased from day 14 to 15 but remained higher than in healthy controls, we could not find any explanation to this observation. We should note that these results should be interpreted with caution. Experiments reported in this chapter were not part of a "real" time course study: mice from different batches were inoculated with different batches of eGFP-5T33 cells and imaged on different days.

Liver, spleen and BM homogenates were stained for CTR and CD138 and analysed by flow cytometry. We did not find correlation between SUVs of Tc-99m-

sCTLys^{18}-hynic-TFA or Tc-99m-sCT(8-32)Lys^{18}-hynic-TFA and the size of the CTR+ population in any of the three organs. This observation was completely unexpected. It is possible that a CTR subtype is expressed that the antibody did not recognise. Staining the samples with another antibody could possibly help to answer this question. It is also possible that the cells analysed by FACS did not reflect the whole organ cell population because of sample preparation problems. For instance failure to wash out a representative sample from bone (only marrow was washed out, not cortical bone). Tracer uptake in the bone could be explained by osteoclast activity, and osteoclasts would not be washed out with the marrow.

All we know about the specificity of the primary antibody is that the immunogen was “synthetic peptide derived from a C-terminal sequence of rat calcitonin receptor” and the antibody “recognises an epitope within the cytoplasmic domain that is common to both C1a and C1b rat isoforms” [174] however it is unclear how these isoforms correspond to murine receptor isoforms. We should also take into account that targeting the receptor with the radiolabelled hynic-calcitonin derivatives is a ligand-receptor interaction that requires fully functional receptors. Staining with a CTR antibody on the other hand is an immunochemical method where the antibody recognises a part of the sequence. If that sequence is present the staining will be positive even if the receptor is non-functional. Since we were unable to find an anti mouse CTR antibody for FACS we had to test an anti rat CTR antibody designed for immunohistochemistry. We proved that the antibody stained mouse CTRs and could be used for FACS however based on the high concentration required for staining for FACS it is likely that the antibody has low affinity for the receptor under the reported conditions. The eGFP+ populations were minor even in the “15 days” group, imaging the animals at a latter time-point with greater bone

involvement and potentially more MM cells and osteoclasts could potentially have helped to have more known positive cells present (*N.B.* we did not have a strong positive control to study as osteoclasts cannot be analysed by FACS).

What we confirmed is that eGFP-5T33 cells undergo phenotypic change *in vivo*: cells obtained from *in vitro* cultures were CTR- however those present in organ homogenates were all CTR+. Similar observation (regarding other receptors and surface markers) were published by Vanderkerken *et al.* [171]. We also proved that in MM bearing mice there is a large population of CTR+ cells that are neither eGFP+ nor CD138+ suggesting that even a small population of MM cells can crucially influence their microenvironment and cause important phenotypic changes. *N.B.* we only stained the samples for one surface marker and one peptide receptor; it is quite likely that altered stromal cells start/stop expressing other surface markers and receptors too. These cells are likely to be other haemopoietic cells or progenitors homing in the target organs. *N.B.* CTRs have been identified in a number of lymphoid cells [67]. In future experiments samples could be stained for additional markers (*e.g.* CD3 or CD4) to characterise the CTR+ population.

We found that disease progress follows different pathways in different organs (*e.g.* no eGFP-5T33 clones were detected in all but three of the spleen samples) and our *ex vivo* studies could also confirm that eGFP-5T33 cells cultured *in vitro* are phenotypically different to those isolated from MM bearing mice (*i.e.* CTR expression). These findings may contribute to the better understanding of human MM and MGUS *i.e.* there may be important cytological parameters other than plasma cell count that could help to monitor disease progress and better predict the onset of clinical symptoms.

Based on the results reported in Chapter 6 we expected large eGFP+ populations in the liver and spleen however in most of the spleen samples that we analysed we did not find any eGFP+ cell. eGFP+ cell populations in liver samples were also very small. It is possible that eGFP expression was switched off in cells homing in these organs. Although we cannot exclude this possibility based on the literature and our experience this is not too likely to have happened. We only monitored the tissue distribution of In-111-oxine labelled eGFP-5T33 cells for up to 7 days. However MM bearing animals were imaged with the Tc-99m labelled hynic-sCT peptides at least 11 days post-inoculation. Cells initially homing in the liver and spleen might have migrated to the BM. Or after an initial lodging some of the cells were cleared by the immune system as part of a selection of MM cells and only those that best interacted with their microenvironment survived. It is also possible that cells that migrated to the spleen after injection were still present however they did not proliferate during the first 2 weeks or their proliferation was very slow in that microenvironment hence the size of the eGFP+ cell population was too small to detect. Alici and co-workers also found that proliferation of eGFP-5T33 cells was slow in the first 2 weeks after inoculation [169]. The small size of the eGFP+ cell population in the BM also conflicts with our data reported in Chapter 6 (*N.B.* we only detected radiolabelled MM cells in the BM in the second series of imaging studies for up to 6 hours). The controversy can be explained by factors mentioned in this paragraph. In addition, in their study Alici *et al.* found that the size of the eGFP+ cell population remained low for up to 4 weeks and there was a sudden (3-4-fold increase) in BM MM cell counts at the onset of paraplegia.

To summarise we can prove that the Tc-99m labelled hynic-conjugated calcitonin peptides target the liver, spleen and BM of 5T33 MM bearing mice.

However we could not correlate radiopeptide uptake to biological parameters and in some cases CTR+ populations were even smaller in MM bearing mice than in healthy controls however radiopeptide uptake was higher. Therefore it is unclear what do we exactly target. It would be beneficial to evaluate the radiopeptides at later stages of tumour progression in this model when there is a larger involvement and activation of osteoclasts resulting in more extensive bone disease (and also bearing in mind that mice will have to be culled well before the possible onset of paraplegia, refer to the paragraphs above).

In a set of *in vivo* stability studies we found that both hynic-calcitonin derivatives are metabolised to a small hydrophilic radioactive species via an intermediate, these results were similar to what we have seen in *in vitro* stability essays. We detected the intact Tc-99m-sCT(8-32)Lys^{18}-hynic-TFA the urine sample which suggests that the abbreviated sequence might be more stable than the full hynic-sCT radiopeptide; more samples should be analysed to prove this observation.

7.5 Conclusions and summary

We evaluated the Tc-99m labelled sCTLys^{18}-hynic-TFA and Tc-99m labelled sCT(8-32)Lys^{18}-hynic-TFA in the 5T33 murine MM model. We found that in most cases radiopeptide uptake was significantly higher in target organs of MM bearing mice than healthy controls. However we could not establish correlation between CTR levels and radiopeptide uptake or other parameters. Therefore the hynic-calcitonin derivatives need further evaluation, possibly in another disease model. We also need to find an anti mouse CTR antibody that is better characterised.

Chapter 8: Synthesis and characterisation of novel hynic derivatives as chelators for technetium and the synthesis of Fmoc-N-ε-(hynic-Boc)-Lysine

8.1 Aims

This chapter will report a review on hynic and a study on the structural aspects of hynic complexes. It will also report the synthesis of Fmoc-N-ε-(hynic-Boc)-Lysine, the hynic-conjugated lysine derivative used to synthesise sCTLys^{18}-hynic-TFA and sCT(8-32)Lys^{18}-hynic-TFA.

8.2 Introduction

Contents of this chapter virtually separate from the previous seven chapters that described the syntheses and evaluation of hynic-conjugated peptide radiopharmaceuticals to image MM. Chapter 8 is a purely chemistry and radiochemistry based chapter focussing on hynic and its technetium complexes. However this is important to this thesis as the hynic system is the one adopted for radiolabelling the calcitonin peptides.

From the radiolabelling and stability point of view the most important part of the radiopharmaceutical is what actually binds the radiolabel – in our case it is the hynic moiety in the peptide sequence. The role of the chelator is crucial: if a compound can only be radiolabelled in very low yields and/or the labelled compound is not stable enough it cannot be used for imaging. Moreover compared to the 1980's it is more of an expectation that the exact structure of a radiopharmaceutical (that of the labelled species) is known and the species is well characterised. For example Tc-99m labelled HEDP (1-hydroxyethane 1,1-diphosphonic acid) has been a clinically

used bone-seeking radiopharmaceutical for decades. However as pointed out by *e.g.* Torres *et al.* the labelled "compound" is in fact a mixture of several different species [175]. It is unlikely that such a drug would be licensed for use in humans nowadays.

When I started working on the project that led to this thesis I first reviewed the literature to understand the practical aspects of hynic-based radiopharmaceuticals. With the review I aimed to point out whether hynic was a sufficient chelator for our purposes and find out the possible difficulties that we may face when using hynic-conjugated compounds. Later with input from Anica Dose and Stefano C. G. Biagini (research collaborators at the University of Kent, Canterbury) the review was published in Inorganica Chimica Acta (*vide infra*). A statement on individual contributions to the published paper is shown in Appendix 11.

In the next step we designed a study that aimed to characterise the structure of hynic complexes and determine if novel hynic isomers and derivatives possessed improved chelating properties, the study was later published in Dalton Transactions (*vide infra*). The structure of the novel hynic derivatives used in the above study is depicted in Figure 8.1.

Figure 8.1: Structure of hynic (a), 2-hynic (b), 4-hynic (c), chloro-hynic (d) and dihynic (e).

Note that the synthesis of two new hynic derivatives (*i.e.* dihynic and chloro-hynic) was part of another thesis submitted to King's College London by Meszaros [176] and the synthesis of the 2-hynic and 4-hynic compounds was part of a doctoral thesis submitted to the University of Kent by Anica Dose [177]. *N.B.* ligand syntheses reported in the publication should not be considered as new results as far as this thesis is concerned. For a statement on individual contributions to the publication refer to Appendix 12.

8.3 Publications

8.3.1 Hydrazinonicotinic acid (HYNIC) – Coordination chemistry and applications in radiopharmaceutical chemistry

8.3.2 Synthesis and evaluation of analogues of HYNIC as bifunctional chelators for technetium (with electronic supplementary information)

8.4 Conclusions

After reviewing the literature we found that hynic is an efficient and versatile chelator for technetium. It can easily be conjugated to proteins and peptides and radiolabels rapidly under mild conditions. Since hynic is unable to saturate the coordination sphere of technetium co-ligands have to be used that can crucially affect the hydrophilicity and therefore the biodistribution of radiolabelled hynic conjugated compounds. Using certain co-ligands such as the most widely used tricine can lead to the formation of a high number of isomeric complexes. Although hynic has been quite widely used our knowledge on the exact structure of hynic complexes remains incomplete.

Our paper on the synthesis and structure of technetium-hynic complexes gave an insight of some structural aspects. We confirmed that hynic is a bidentate chelator rather than a monodentate ligand in technetium complexes by labelling and analysing hynic, 2-hynic and a non-chelating isomer 4-hynic. HPLC and LC-MS analyses also revealed the formation of isomeric complexes both in hynic-tricine and ternary hynic-tricine-EDDA complexes. A titration study confirmed that hynic was a very efficient chelator for technetium capable of binding the radiometal in as low as 6-fold excess. This means that very high specific activity is attainable which is especially important for this project in order to minimise the amount of peptide injected and therefore avoid physiological response. Labelling efficiency of the hynic derivative with two hydrazine groups (dihynic) was slightly worse than that of the hynic and 2-hynic compounds but it only formed complexes with one tricine co-ligand which reduced the number of isomeric complexes.

8.5 Synthesis of Fmoc-N-ε-(hynic-Boc)-Lysine

8.5.1 Introduction

The hynic-conjugated lysine derivative (**3**) was used to synthesise the hynic-conjugated calcitonin derivatives on solid phase. The reaction scheme for synthesising **3** is shown in Figure 8.2.

Figure 8.2: Synthesis of Fmoc-N-ε-(Hynic-Boc)-Lysine (3).

Fmoc-lysine-OH (**1**) is available commercially and NHS-hynic-Boc (**2**) can easily be synthesised based on the methods published by Abrams *et al.* [145]. We have synthesised **2** as part of another project, results of syntheses and characterisation of products are reported elsewhere [176]. Synthesis of the hynic-conjugated Fmoc-lysine derivative has been reported by several authors: Greenland *et al.* [115], Surfraz *et al.* [141] and Sladen [178] all reported high-yield syntheses (64%, 92% and 51% yield) of Fmoc-N-ε-(hynic-Boc)-Lysine. Their published methods suggested that the synthesis was relatively easy and straightforward as only required an overnight stirring of a mixture of **1** and **2** in dry DMF or dimethyl sulfoxide (DMSO) either at room temperature or 50°C and subsequent precipitation of the product by adding water to the reaction mixture. Greenland *et al*. purified the crude by normal phase chromatography; Sladen used solvent extraction while Surfraz *et al.* isolated the pure product. Originally the synthesis of this compound

was subject of another thesis of mine [176]. After numerous attempts to reproduce the results of Greenland *et al.* and Surfraz *et al.* the best result I could achieve was that I was able to detect traces of Fmoc-N-ε-(hynic-Boc)-Lysine in the "product" by LC-MS. Colleagues also encountered similar problems [179]. Finally Sladen's method led to moderate success on a small scale once (4% yield), I did not manage to reproduce this result any more, analysis of the reaction mixture of further syntheses suggested that only un-reacted starting materials were present. I speculated that hydrolysis of the NHS-group from **2** could be catalysed by adding a strong acid to the mixture (acid-catalysed ester hydrolysis). In an MPhil/PhD transfer report I reported the results of the first synthesis [180]. Although that synthesis was successful the yield was moderate (3.5%) due to the fact that only a precipitate containing the highly pure Fmoc-N-ε-(hynic-Boc)-Lysine was collected and a significant amount of precipitate containing the impure product was discarded. Later small scale test syntheses confirmed that the method was reproducible therefore the same method, followed by purification steps was applied to synthesise a larger batch; this work will be described below.

8.5.2 Materials and methods

8.5.2.1 Materials

Solvents (liquid chromatography grade) were purchased from Fisher. MS solvents were purchased from Sigma. Waters Sep-Pak C18 (6 cm^3, 1000 mg, 37-55 µm; part number 186004621) were purchased from Waters Corporation. Fmoc-Lys-OH hydrochloride (>98%) was purchased from Sigma-Aldrich (cat. number 17290) and used as received. D_6-DMSO was purchased from Sigma. **2** was synthesised as described earlier [176].

8.5.2.2 Analytical methods

The LC-MS instrument described in Chapter 2 was used. LC-MS method M3: “A”: water-0.1% formic acid (FA), “B”: MeOH-0.1% FA. 0-3 min: 5% B, 3-3.5 min: rising to 90% B, 3.5-10 min: 90% B, 10-10.5 min: falling to 5% B, 10.5-15 min: 5% B. Flow rate 0.4 ml/min, λ=254 nm. Column: Agilent Zorbax SB-C18, 2.1×30 mm, particle size 3.5 µm. Cone voltage 75V (positive mode ESI-MS).

NMR spectra were recorded on a Bruker Ultrashield 400 WB Plus NMR spectrometer at 400 MHz in 5 mm NMR sample tubes. Spectra were referenced to tetramethylsilane.

8.5.2.3 Synthesis of Fmoc-N-ε-(hynic-Boc)-Lysine

2 (840 mg, 2.4 mmol) was dissolved in 33 ml DMF and gave a brownish-orange solution. To this solution 4.5ml 10% TFA in water were added. After a couple of minutes of stirring at room temperature **1** (738 mg, 1.8 mmol) was added. The flask was connected to a condenser and the mixture was stirred under reflux at 70°C for 19 hours. After 19 hours the coffee-brown solution was transferred to a beaker then 150 ml distilled water were added resulting in prompt precipitation of an orangish solid. The precipitate floated on the surface of the solution. The mixture was stirred at room temperature for an hour. Upon stirring a significant amount of precipitate was formed. The solution was filtered on a sintered glass filter, washed with cold water and dried under vacuum. The collected crude weighed 304 mg. Before purification the crude was dissolved in 1% water in MeCN at a concentration of 13 mg/ml. The crude was then purified by solid phase extractions as follows:

1. The Sep-Pak column was washed with 6 ml MeOH
2. The column was washed with 6 ml 35% MeCN in water

3. 1 ml of the sample solution was pipetted directly onto the resin and left to elute
4. The column was eluted with 8 ml 35% MeCN in water and the eluate collected
5. After the first use each column was washed with 6 ml MeCN and re-used once

The crude and the pure product were analysed by LC-MS (method M3) and the purified product was analysed by NMR.

8.5.3 Results

The crude contained three major components (Regions 1-3, Figure 8.3). Region 1 was identified as the desired product **3** (observed m/z 604.2777 ($[M+H]^+$), calc. 604.2766). Region 2 contained unidentified by-products in the mass range of 200-400 Da. Region 3 was identified as Fmoc-N-ε-(hynic-Boc_2)-Lysine ($[M+H]^+$ observed m/z 704.3255, calc. 704.3290). Note that the above by-product would also be suitable for synthesising hynic peptides.

After solid phase extraction the product was 86% pure (Figure 8.4) based on its UV trace. Positive mode ESI mass spectrometry did not identify any major impurity. Due to the low amount of product it was used without further purification. Pure product fractions were unified and freeze-dried. 200 mg of the crude was purified yielding 120 mg pure compound (0.2 mmol, 15% overall yield).

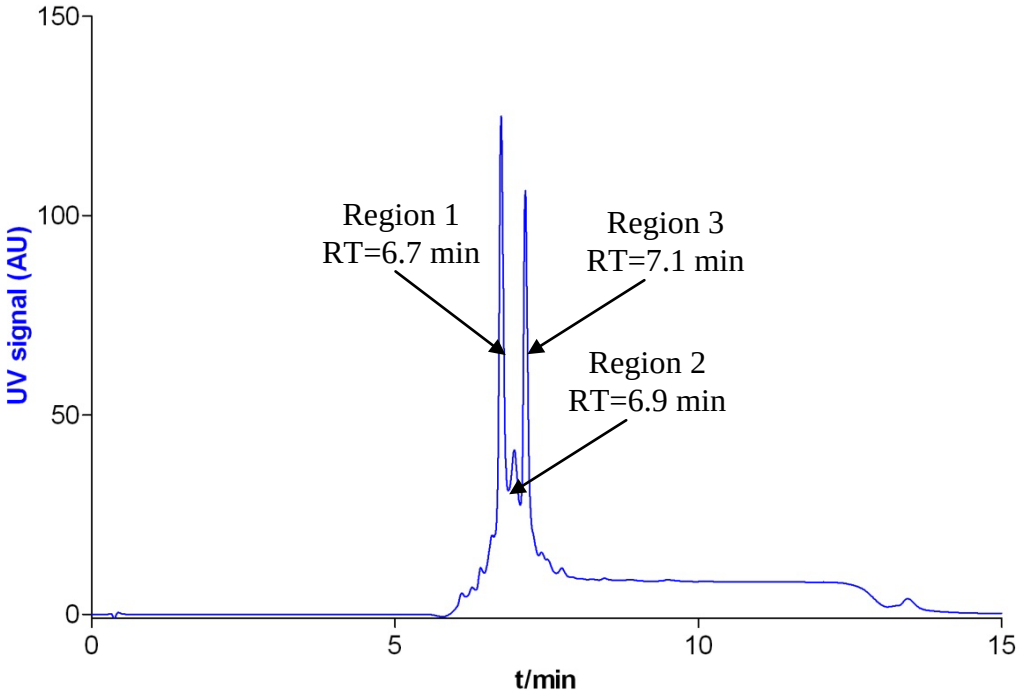

Figure 8.3: UV trace of the crude Fmoc-N-ε-(Hynic-Boc)-Lysine.

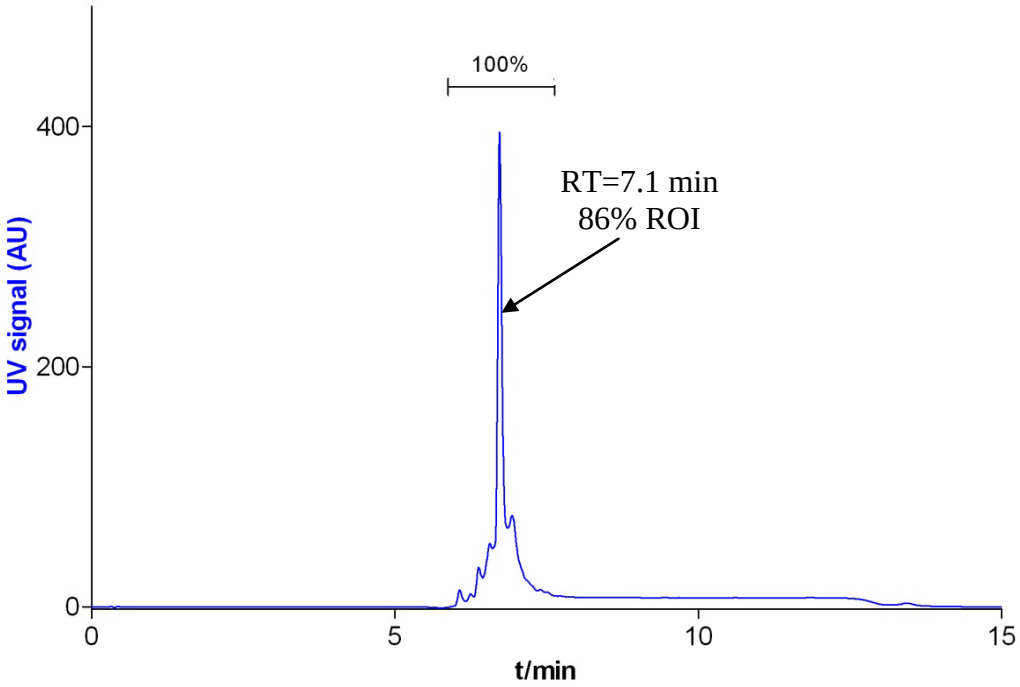

Figure 8.4: UV trace of the purified Fmoc-N-ε-(Hynic-Boc)-Lysine.

MS: observed m/z 604.2777 ($[M+H]^+$, 100%), calc. m/z for $[M+H]^+$ 604.2766. Mass spectrum is reported in Appendix 13.

NMR: NMR assignments are shown in Figure 8.5, the spectrum is reported in Appendix 13. δ_H (400 MHz; $(CD_3)_2SO$; Me_4Si): 1.10-1.28 (?H, m, **j**), 1.35 (12H, s, **a**), 1.42 (?H, m, **i**), 1.52-1.67 (?H, m, **k**), 3.15 (2H, m, **h**), 3.84 (1H, m, **l**), 4.15-4.21 (?H, m, **n**,**o**), 6.45 (1H, d, J=8.4, **d**), 7.26 (?H, t, J=6.9, **r**), 7.34 (?H, t, J=7.0, **q**), 7.56 (2H, d, J=7.5, **p**), 7.77 (2H, d, J=7.5, **s**), 7.88 (1H, d, J=7.0, **e**), 8.21 (?H, s, **g**), 8.47 (1H, s, **b**), 8.59 (1H, s, **c**), 8.85 (1H, s, **f**); **m** was not identified. Literature [115]: δ_H (270 MHz; $(CD_3)_2SO$; Me_4Si): 1.28 (2H, m, **j**), 1.41 (9H, s, **a**), 1.45 (2H, m, **i**), 1.58, 1.72 (2×1H, m, prochiral, **k**), 3.20 (2H, m, **h**), 3.73 (1H, m, **l**), 4.21-4.31 (?H, m, **n**,**o**), 6.50 (1H, d, J=8.0, **d**), 6.69 (1H, s, **m**), 7.31 (2H, t, J=7.4, **r**), 7.35 (2H, t, J=7.0, **q**), 7.68 (2H, d, J=6.9, **p**), 7.87 (2H, d, J=7.4, **s**), 7.96 (1H, d, J=8.0, **e**), 8.31 (1H, s, **g**), 8.55 (1H, d, J<2, **b**), 8.64 (1H, s, **c**), 8.92 (1H, s, **f**).

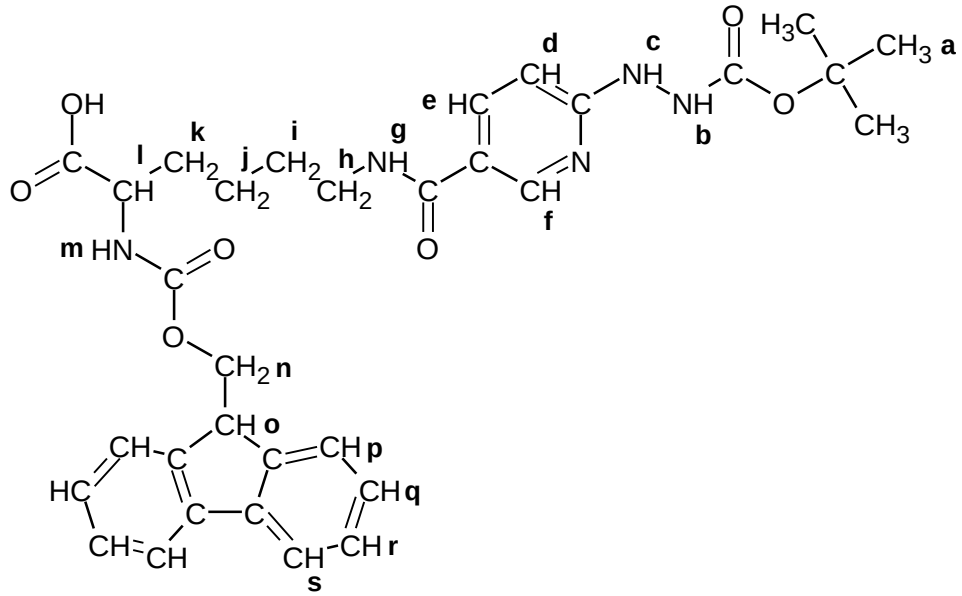

Figure 8.5: NMR assignments of Fmoc-N-ε-(hynic-Boc)-Lysine.

8.5.4 Discussion

After numerous attempts we managed to synthesise Fmoc-N-ε-(hynic-Boc)-Lysine. The yield was moderate especially when compared to the 50-90% yield reported by other authors. We found no explanation to this phenomenon. The cited

authors emphasised that they were using dry solvents; we on the other hand deliberately added water to the reaction mixture. O'neill achieved fairly high yields when reproducing the method reported by Surfraz *et al.*: after 3 weeks at room temperature he reported on ~40% yield [179]. Note that Surfraz *et al.* reported on a 92% yield after 15 h, we did not even detect traces of the product after an overnight reaction.

The product was 86% pure after purification hence the ^{1}H-NMR spectrum was very noisy which made peak assignments and quantification difficult, especially when peaks were overlapping (Appendix 13). Accurate mass of the product was determined and it matched the calculated value (1.82 ppm difference). When quantifying the proton spectrum we found twelve methyl protons (marked as **a** in Figure 8.5) instead of nine, this suggests that the Fmoc-N-ε-(hynic-Boc_2)-Lysine by-product was present in the sample. Due to the low amount of product and problems with peptide synthesis (refer to Chapter 2) we decided to use the Fmoc-N-ε-(Hynic-Boc)-Lysine without further characterisation or purification in order to save reagent. Synthesis of the hynic conjugated lysine derivative took 3 months longer than we had expected and any further delays could have jeopardised the completion of the whole project.

8.5.5 Conclusions

After numerous unsuccessful attempts we finally synthesised the Fmoc-N-ε-(Hynic-Boc)-Lysine at moderate yield. The literature does not report on difficulties regarding the synthesis but we and colleagues also encountered problems regarding low yields and reproducibility.

8.6 Summary

After reviewing the relevant literature we found that hynic was a versatile and efficient chelator for technetium. We confirmed that hynic binds the radiometal in very low excess therefore very high specific activities could be achieved in technetium-hynic complexes. We also confirmed that hynic was a bidentate chelator for technetium rather than a monodentate ligand.

We faced numerous problems whilst trying to synthesise the hynic-conjugated lysine derivative Fmoc-N-ε-(hynic-Boc)-Lysine for subsequent solid phase syntheses of the hynic-conjugated calcitonin derivatives. We were unable to reproduce any of the published syntheses hence we developed a modified synthesis method.

Chapter 9: Summary and future work

In this thesis we reported on the synthesis and evaluation of radiolabelled sCT derivatives as potential imaging agents for MM and other CTR+ malignancies. After reproducing the synthesis of sCTLys^{18}-hynic-TFA, first reported by Greenland [114, 115] we also synthesised an abbreviated hynic-sCT sequence sCT(8-32)Lys^{18}-hynic-TFA. The hynic-peptides were successfully radiolabelled with Tc-99m and Tc-99 in presence of tricine as co-ligand and the labelled species characterised by ITLC, HPLC and LC-MS. Both hynic-sCT derivatives formed technetium complexes with one tricine co-ligand suggesting that the histidine neighbouring to the hynic-derivatised lysine in the peptide sequence participated in binding the radiometal. We could achieve high specific activities with both radiopeptides. Around 6 µg of pure sCTLys^{18}-hynic-TFA or sCT(8-32)Lys^{18}-hynic-TFA could be labelled with 500 MBq of Tc-99m, that is enough for a human scan. *In vitro* stabilities were assessed on incubation in human serum and mouse kidney homogenate. Although incubating the radiopeptides in serum resulted in the formation of isomeric Tc-hynic peptide complexes significant amount of serum protein-associated radioactivity or pertechnetate was not detected. Incubation in mouse kidney homogenate resulted in rapid degradation to small hydrophilic radioactive species. *In vitro* uptake studies in CTR+ MCF-7 cells confirmed that the Tc-99m labelled sCTLys^{18}-hynic-TFA and sCT(8-32)Lys^{18}-hynic-TFA were both ligands for CTR with nanomolar affinity. These findings also confirm that the evolutionarily conserved disulfide loop in calcitonin peptides is not vital for receptor binding.

By using In-111-oxine labelled eGFP-5T33 cells we confirmed that 5T33 MM cells have a very high affinity to haemopoietic organs *i.e.* the liver, spleen and

BM. Even after 30 minutes post-inoculation when most of the cells were retained by the lungs we found an imageable amount of radiolabelled cells in the femora and tibiae. Lungs cleared with time and activity accumulated in the three haemopoietic organs. When imaging healthy control animals with the Tc-99m labelled sCTLys^{18}-hynic-TFA and sCT(8-32)Lys^{18}-hynic-TFA both radiopeptides accumulated rapidly in the cortex of the kidneys and were subsequently excreted to the bladder. Uptake in other organs was minor. When imaging eGFP-5T33 MM bearing mice with Tc-99m labelled sCTLys^{18}-hynic-TFA and sCT(8-32)Lys^{18}-hynic-TFA we found increased uptake in the liver, spleen and femora when compared to healthy controls. Liver, spleen and BM homogenates were stained for CTR and CD138 and analysed by FACS. CTR expression in haemopoietic tissues of MM bearing mice was usually higher than in controls however we could not establish correlation between radiopeptide uptake and the size of CTR+ population. eGFP+ and CD138+ populations were minor compared to CTR+ populations suggesting that MM cells evoked CTR expression in their microenvironment. Our results suggest that the Tc-99m labelled hynic-sCT peptides might not be efficient to directly detect microlesions of MM cells. However, they seem to be capable of detecting changes caused by a small population of MM cells in the biology of the liver, spleen and BM (upregulation of CTR levels in the eGFP- and CD138- population). Therefore imaging with radiolabelled sCT derivatives could be used to detect the presence of low levels of MM cells (such as in the case of minimal residual disease) due to changes in CTR levels in surrounding tissues in the liver, spleen and BM. The fact that a very small population of MM cells (*N.B.* the tumour burden was so low that strictly speaking mice bore MGUS) could be detected indirectly (*i.e.* via the changes they evoke in their microenvironment) suggests that the hynic-sCT radiopeptides are

sensitive imaging agents in this particular disease and their clinical evaluation is warranted.

Results of CTR staining should be treated with caution since the CTR antibody that we used was not very sensitive hence it had to be used in a high concentration. As part of future experiments staining the formalin fixed organ homogenates with another CTR antibody (one that is suitable for FACS analysis) could provide with comparative data to confirm or expand our FACS data. In addition using another technique such as immunohistochemistry could help to identify which cells or cell types become CTR+ in haemopoietic organs of MM bearing mice. Keeping mice inoculated with high activities of In-111-oxine labelled eGFP-5T33 cells for several weeks and imaging them regularly (*e.g.* in every 24 hours) would provide useful and possibly clinically relevant information regarding the progress of MM and the role of different haemopoietic tissues at different stages of the disease. Keeping a group of mice inoculated with In-111-oxine labelled eGFP-5T33 cells for 15 days (or longer) and imaging them with the Tc-99m labelled sCTLys^{18}-hynic-TFA or sCT(8-32)Lys^{18}-hynic-TFA (dual isotope imaging) would be a good way to correlate radiopeptide uptake to MM cell levels. Radiation damage might affect the proliferation of eGFP-5T33 cells, this should be investigated prior to a dual isotope imaging study. Another experiment that would be useful to carry out as continuation of this project is a study in which mice inoculated with 10^6 eGFP-5T33 cells are kept for longer than 15 days. This would probably result in higher radiopeptide uptake and larger eGFP+ and CTR+ cell populations hence imageable uptake in the bone. However such an experiment should be carried out with caution. Scanner and laboratory availabilities are limited and we do not have non-stop access to Tc-99m-pertechnetate, especially not on weekends. Therefore it is not guaranteed

that an imaging and/or biodistribution experiment could be carried out if mice became paraplegic. In a set of future experiments the Tc-99m labelled hynic-sCT peptides could be evaluated in another MM model or in general another CTR+ cancer model. Evaluating the radiopeptides in MM patients would also be very informative.

We also reported on the synthesis and evaluation of novel hynic analogues and derivatives and confirmed that hynic was most likely a bidentate chelator rather than a monodentate ligand in technetium complexes. After further characterisation and synthetic work two novel hynic derivatives, dihynic and chloro-hynic could be used as trifunctional chelators: the molecules can be conjugated to free amine groups in proteins or peptides via their carboxylic acid function, the hydrazine group or one of the hydrazine groups could chelate technetium whilst the chloro function or the second hydrazine group could be conjugated to another molecule *e.g.* a fluorescent tag and the resulting compound used for multimodality imaging.

Appendices

Appendix 1: Isotope peak distribution of sCTLys^{18}-hynic-TFA

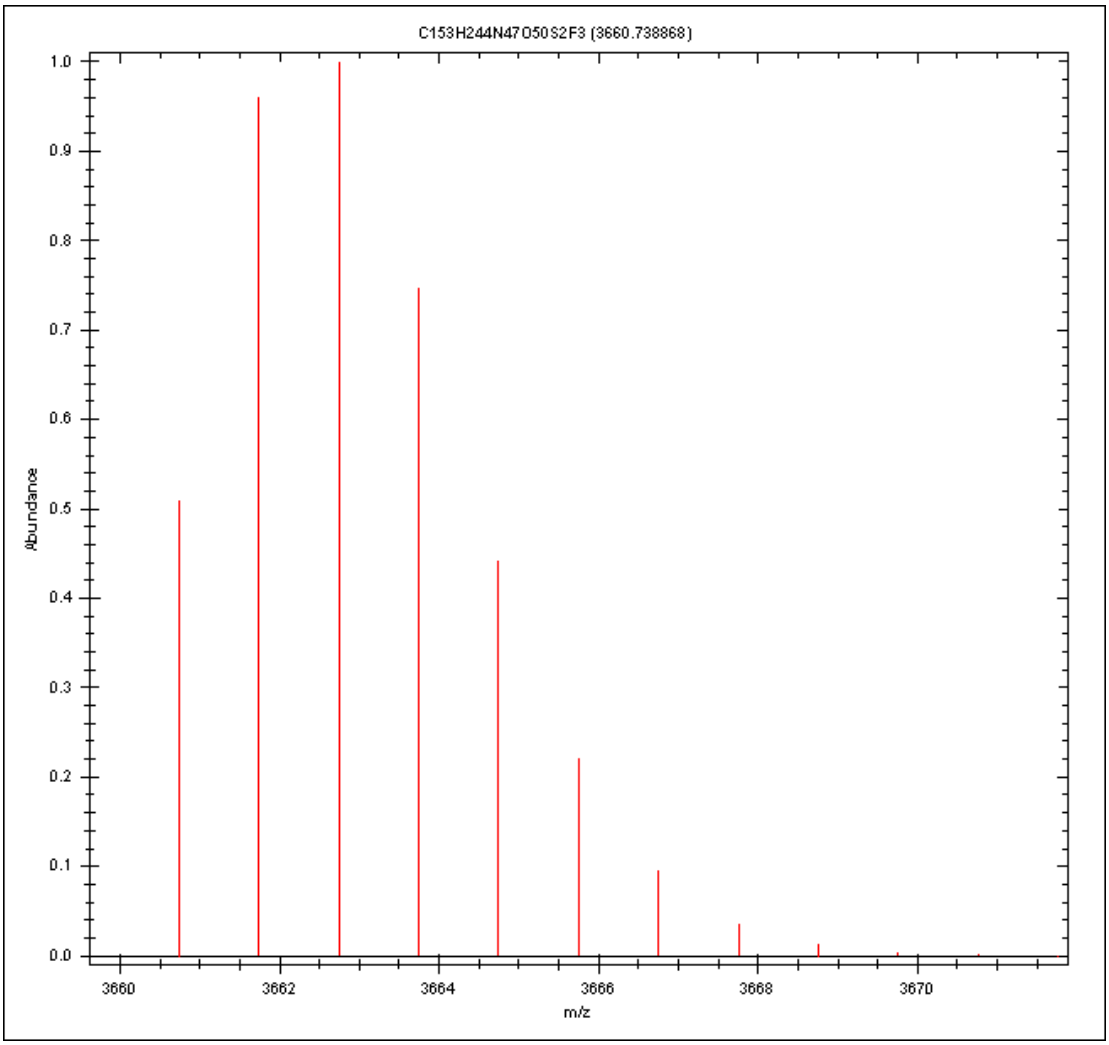

M/Da	Abundance (% largest)	Abundance (% sum)
3660.7389	50.82	12.62
3661.7417	96.01	23.85
3662.7439	100	24.84
3663.7460	74.65	18.54
3664.7478	44.26	10.99
3665.7496	22	5.46
3666.7513	9.48	2.35
3667.7531	3.62	0.9
3668.7548	1.25	0.31
3669.7565	0.39	0.1
3670.7583	0.11	0.03
3671.7601	0.03	0.01

Appendix 2: Isotope peak distribution of sCT(8-32)Lys^{18}-hynic-TFA

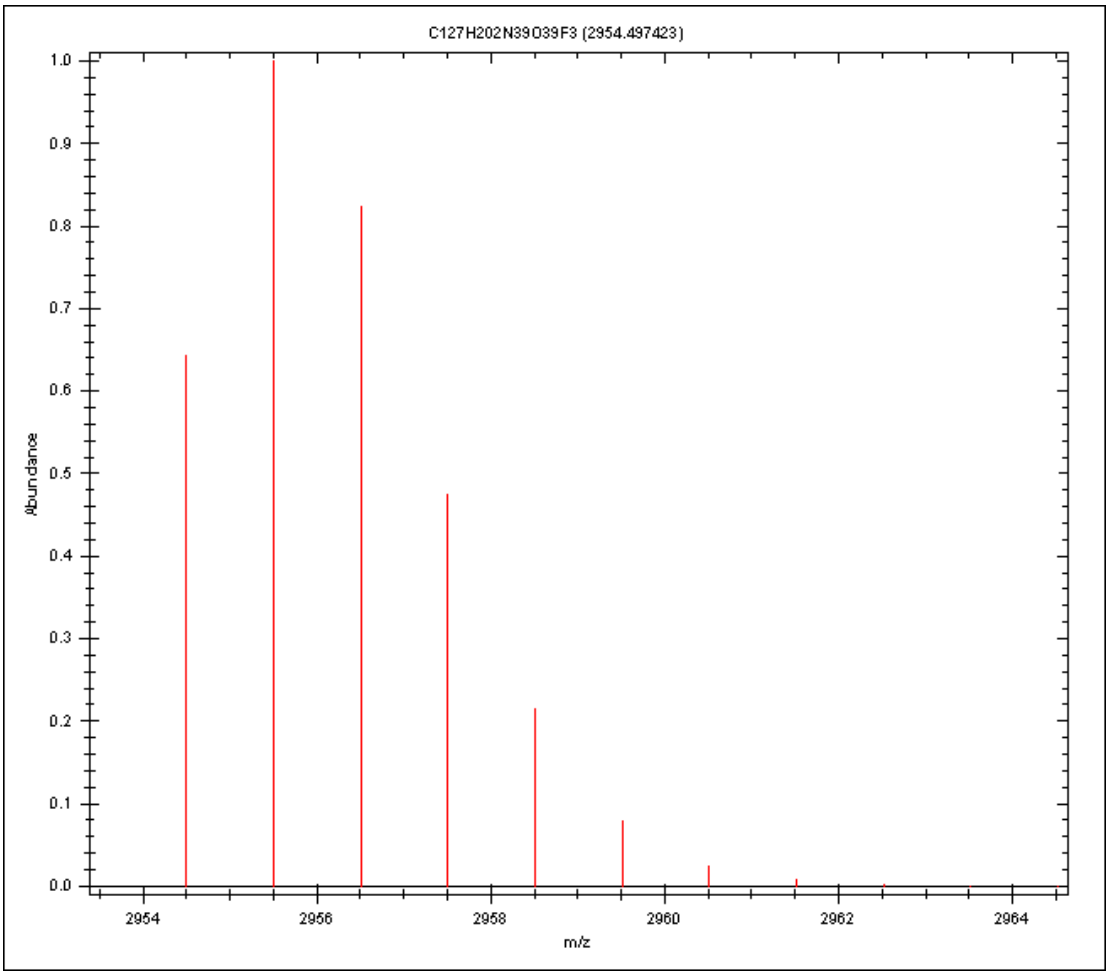

M/Da	Abundance (% largest)	Abundance (% sum)
2954.4974	64.34	19.66
2955.5002	100	30.56
2956.5030	82.37	25.17
2957.5057	47.5	14.52
2958.5083	21.44	6.55
2959.5109	8.03	2.46
2960.5134	2.59	0.79
2961.5160	0.74	0.23
2962.5185	0.19	0.06
2963.5210	0.04	0.01
2964.5234	0.01	0

Appendix 3: ITLC and HPLC chromatograms of pertechnetate and Tc-99m labelled tricine

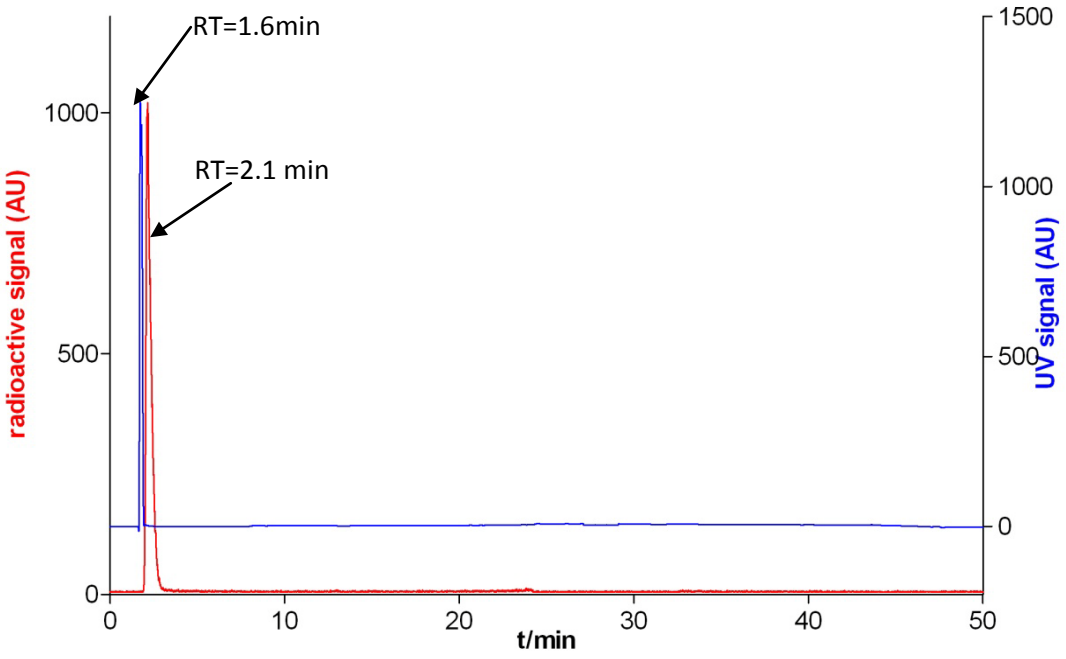

Figure A3-1: UV and radiochromatogram of Tc-99m labelled tricine (radiolabelled as sample C3 in Chapter 3, section 3.3.2).

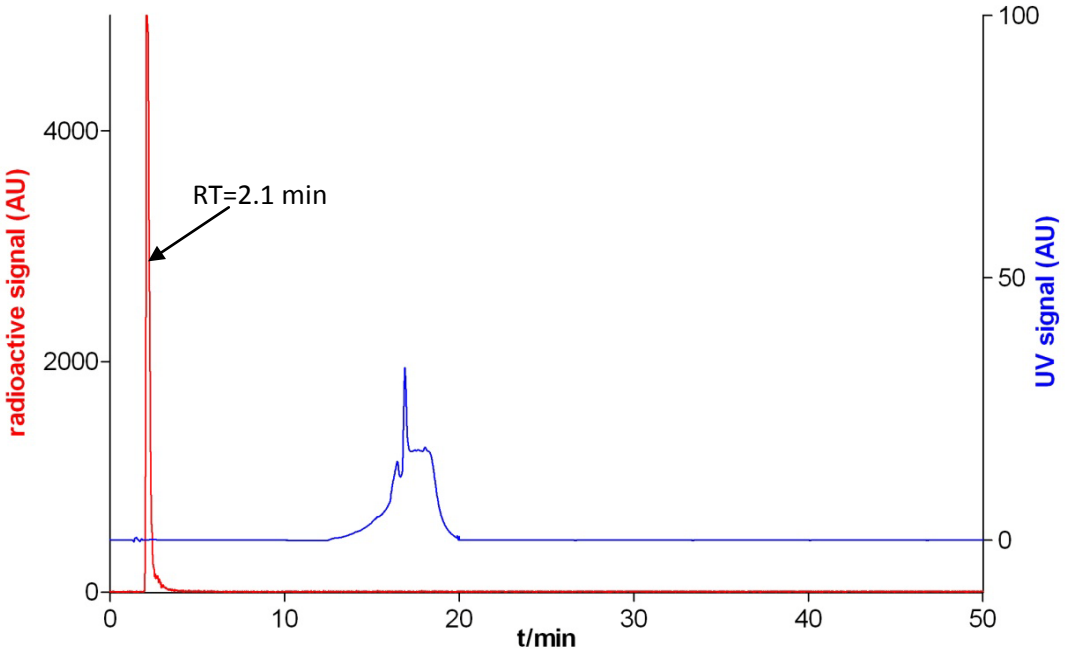

Figure A3-2: UV and radiochromatogram of ^{99m}Tc-TcO_4^- .

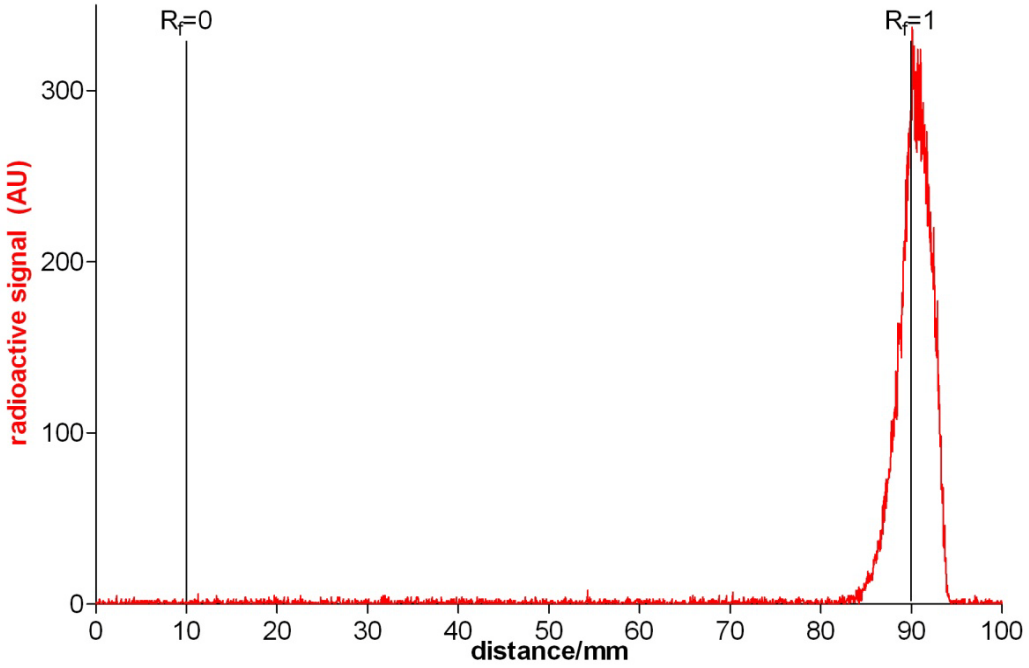

Figure A3-3: ITLC chromatogram of Tc-99m-TcO_4^- (ITLC-SA with saline mobile phase).

Appendix 4: Isotope peak distribution of [^{99}Tc+sCTLys^{18}-hynic+tricine+MeCN-5H]

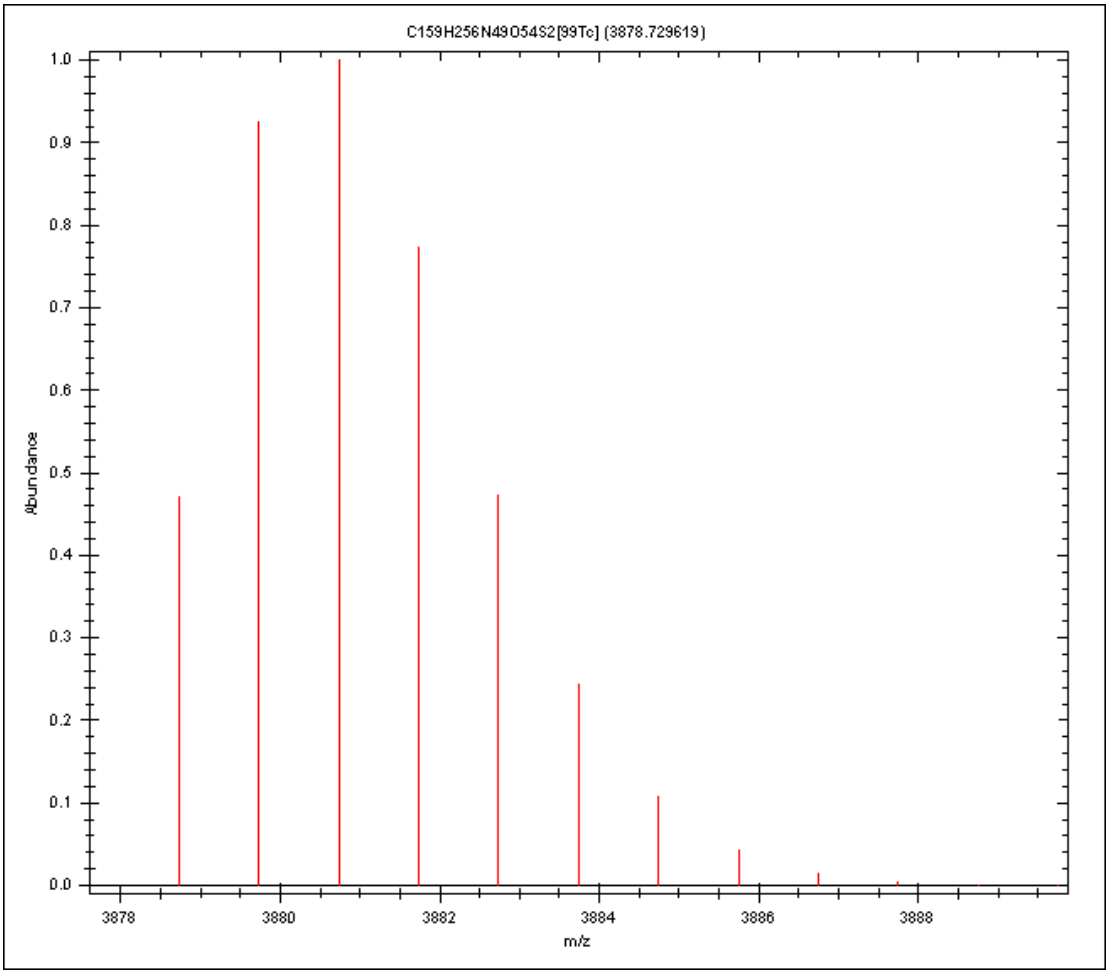

M/Da	Abundance (% largest)	Abundance (% sum)
3878.7296	47.16	11.62
3879.7324	92.65	22.82
3880.7347	100	24.63
3881.7368	77.23	19.02
3882.7387	47.33	11.66
3883.7405	24.31	5.99
3884.7423	10.82	2.67
3885.7440	4.27	1.05
3886.7458	1.52	0.37
3887.7476	0.49	0.12
3888.7493	0.15	0.04
3889.7511	0.04	0.01

Appendix 5: Isotope peak distribution of [^{99}Tc+sCT(8-32)Lys^{18}-hynic+tricine+MeCN-5H]

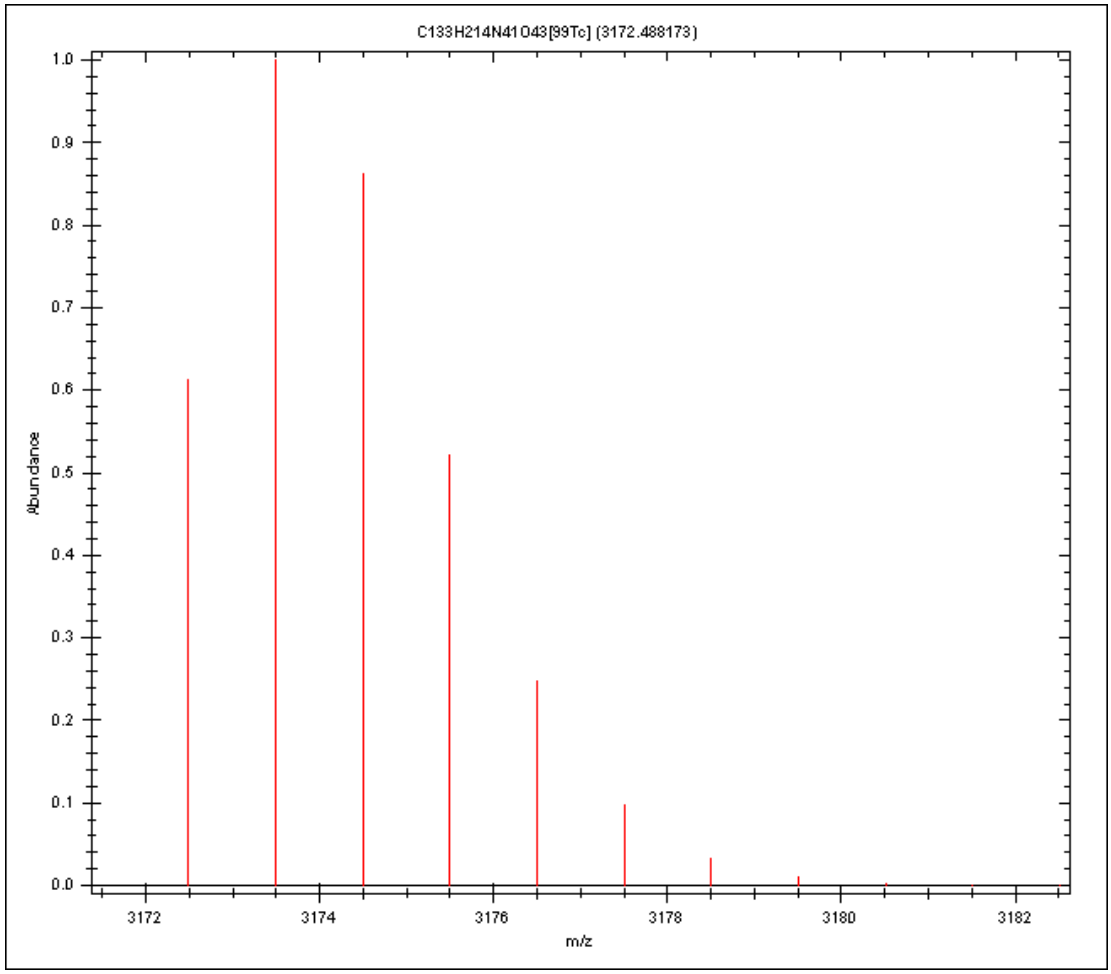

M/Da	Abundance (% largest)	Abundance (% sum)
3172.4882	61.38	18.1
3173.4910	100	29.48
3174.4937	86.39	25.47
3175.4964	52.27	15.41
3176.4990	24.76	7.3
3177.5016	9.74	2.87
3178.5042	3.3	0.97
3179.5067	0.99	0.29
3180.5092	0.27	0.08
3181.5117	0.07	0.02
3182.5142	0.01	0

Appendix 6: Cell culture media recipes

Culture medium 1: Dulbecco's Modified Eagle's Medium 4500 mg glucose/L (Sigma D5796); each 500 ml bottle supplemented with 50 ml Fetal Bovine Serum (Standard Quality, PAA A15-101) and 5 ml Penicillin/Streptomycin 100× (PAA 11-010)

Culture medium 2: RPMI-1640 Medium (Sigma R8758); each 500 ml bottle supplemented with 50 ml Fetal Bovine Serum (Standard Quality, PAA A15-101) and 5 ml Penicillin/Streptomycin 100× (PAA 11-010)

Appendix 7: Distress score sheet for daily monitoring of 5T33 MM bearing mice

General Distress Score Sheet				
~~Parameter~~	~~Animal ID~~	Score, Date/Time	Score, Date/Time	Comments
Appearance	Normal (0)			
	General lack of Grooming (1)			
	Coat Staring, Ocular and nasal Dischargess (2)			
	Piloerection, Hunched up (3)			
Food and Water intake	Normal (0)			
	Uncertain: Body Weight <5% (1)			
	Intake: Body Weight decreasing 10-15% (2)			
	No food or water intake (3)			
Natural Behaviour	Normal (0)			
	Minor changes (1)			
	Less mobile and alert, isolated (2)			
	Vocalisation, self mutilation, restless or still (3)			
Provoked Behaviour	Normal (0)			
	Minor Depression or exagerated response (1)			
	Moderate Change in expected behaviour (2)			
	Reacts violently, or very weak and precomatosed (3)			
Score	for each 3 (plus 2-5)			
	Total (0-20):			
	Total (0-20):			
	Total (0-20):			

Judgement

0-4 Normal

5-9 Monitor carefully, consider analgesics or other treatments

Suffering, provide relief, observe regularly. Seek second

10-14 opinion from NVS or NACWO. Consider termination

15-20 Severe distress, is this severity limit justified?

Wolfensohn, S & Lloyd, M. (2003) Handbook of Laboratory Animal. Management and Welfare. 3rd edition. Blackwell Publishing Ltd.

Appendix 8: Gamma counter calibration

A8.1 Introduction

Appendix 8 will discuss what problems we faced when we were calibrating the gamma counter on a wide range of activity. After taking into account several interpolation techniques we shall report the actual calibration curves too. These functions were used to calculate tissue uptake in *ex vivo* tissue counting studies reported in this thesis.

A8.2 Materials and methods

Standards were counted in a volume of 0.5 ml in the same type of scintillation vials as excised organs to minimise counting errors resulting from different sample geometries. The following standards were used (activities in kBq at reference time): 6088, 3044, 1522, 608.8, 304.4, 152.2, 60.9, 30.4, 15.2, 6.1, 3.0, 0. On the day of the imaging experiment standards were prepared as follows: six samples were prepared from the stock solution (with a known volume and activity of around 20 MBq (at time of measurement) as determined by the dose calibrator. *N.B.* the dose calibrator is designed to measure very high activities in a radiopharmacy setting. To my experience the instrument would lose accuracy below 10 MBq. All of the six samples were measured then the mean activity concentration and its coefficient of variation calculated. Standards would only be prepared if the coefficient of variation of the mean activity concentration was below 0.05, otherwise the measurement would be repeated with a new set of samples.

Once activity concentration of the stock solution had been calculated and decay-corrected to the reference time standards were prepared. Standards were gamma counted in the same worklist as excised organs and tissues with the same

settings (*i.e.* 10 sec/sample in the 110-155 keV window.) If detector dead time was above 10% for a sample or standard the standard (or sample) would be re-counted at a later time. The calibration curve (count rate *vs.* activity function) was determined by linear, piecewise linear (MS Excel) and inverse spline (SpCalc 2.12a) interpolation.

A8.3 Spline interpolation

Spline interpolation is probably the most sophisticated way of curve fitting. Its main advantage is the ability to adapt to non-linear tendencies. Non-linearity will always occur when calibrating an instrument on a very broad range *e.g.* when calibrating a gamma counter on a 0-6 MBq range. An inverse calibration curve on the 0-6088 kBq range is shown in Figure A8-1.

Being a piecewise function a single outlier will not alter the whole curve. On the other hand, since it is a polynomial function a spline will not necessarily be monotonic. In Figure A8-1 dotted lines represent points of inflection. In total we tested 3 independent sets of calibration data and all of them looked similar *i.e.* lots of points of inflections occurred on lower ranges. After validating the method on experimental data we found that points of inflection were present in the most "sensitive" pieces of the curve covering count rates belonging to some of the important organs such as spleen and femur. In one particular case we calculated slightly lower activity for a spleen sample which had 23% higher count rate in the gamma counter than for the sample with lower count rate. We therefore concluded that using spline interpolation would not be ideal for our purposes.

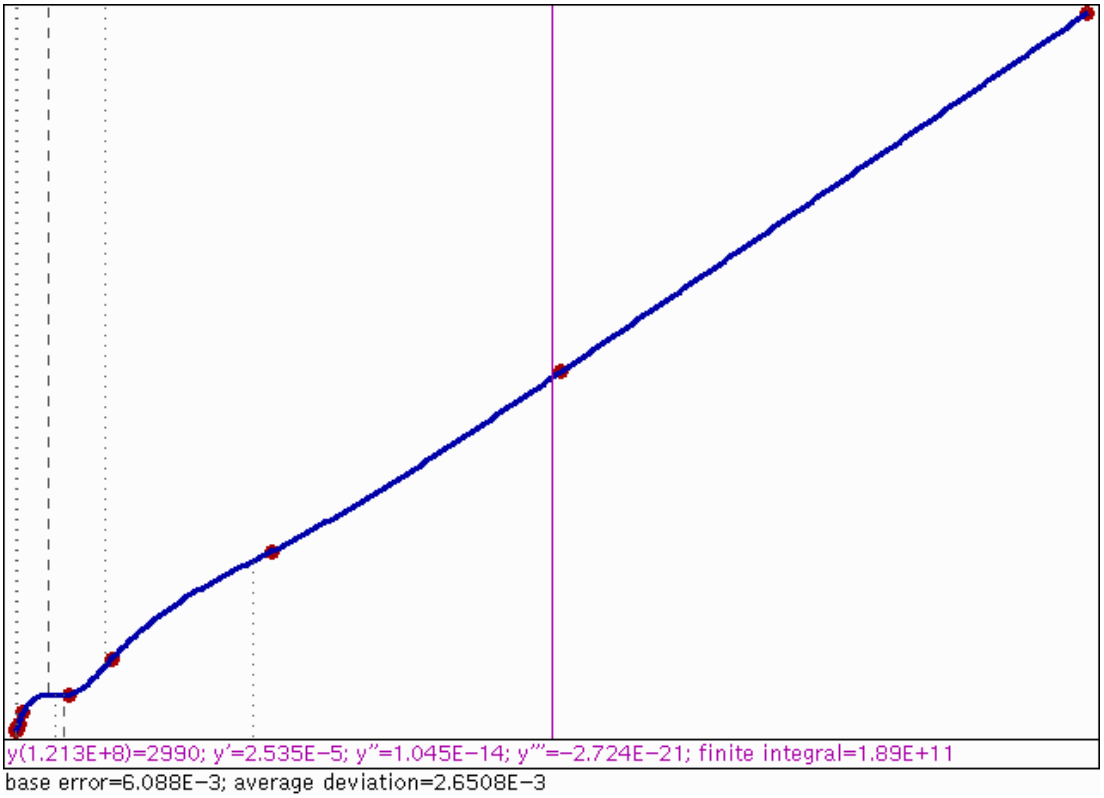

Figure A8-1: screenshot from Spcalc 2.12a. The y or activity axis ranges from 0-6088, the x or count rate (cpm) axis ranges from 2.63×10^2 to 2.43×10^8.

A8.4 Linear interpolation

Being able to fit a single line (or any other function) on the whole range would be beneficial as it could help to minimise or exclude some components of random error. Even without trying to fit a line on the calibration data set it seems highly unlikely that the calibration curve would be linear in such a broad range of activity. After fitting a line on the data set (Figure A8-2) one may think that the calibration curve is perfectly linear (R^2=0.9993). However if we highlight the first seven points (out of 12) on the very same graph (Figure A8-3) we will see that fitting a single line on our data set would completely be misleading.

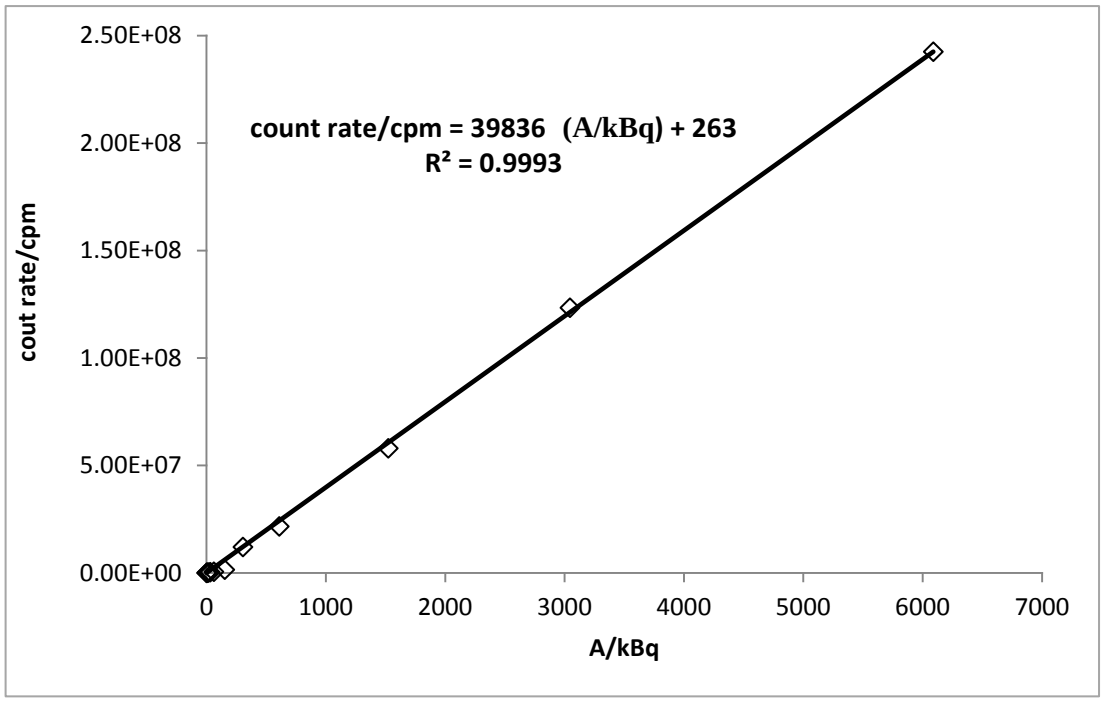

Figure A8-2: Results of linear interpolation.

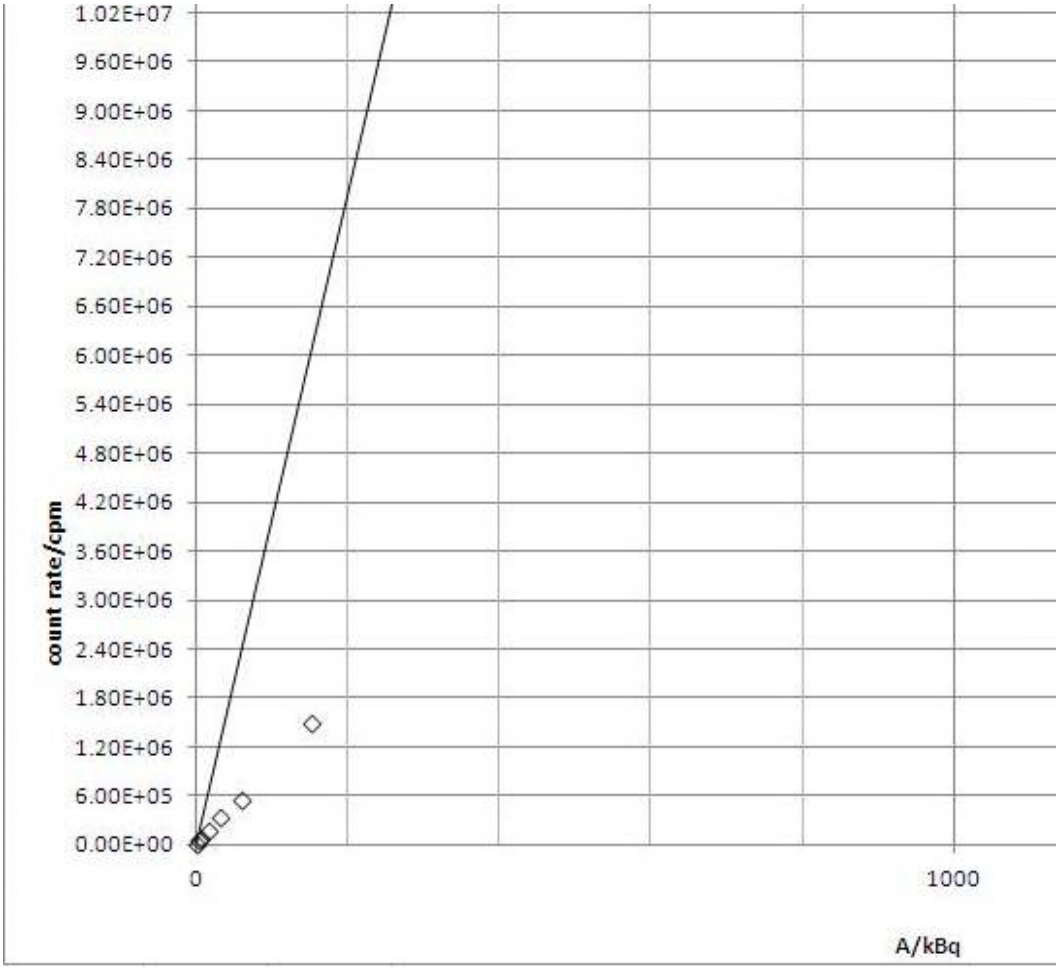

Figure A8-3: Results of linear interpolation (first seven points highlighted).

This observation can be explained easily: linear regression algorithms usually use the least squares method, so does MS Excel. Using the least squares method when there are 6 orders of magnitude differences in y values is “dangerous” as keeping the relative error of the last couple of points low (or close to zero) will result in nearly perfect fitting, even if points with lower values have 3-4 fold relative errors.

A8.5 Piecewise linear interpolation

Piecewise linear interpolation is likely to solve the problem that we encountered in section A8.4. If we use piecewise linear regression then the least squares method will become much more reliable; we only need to define subgroups of points with similar count rate values. Although the regression algorithm itself will become reliable defining subgroups of calibrants in a somehow arbitrary way will/can generate a significant (random) error that could jeopardise the reliability of our calculations. By using the same standards (same activities) and defining the same subgroup of calibrants the above error can be minimised and made systemic.

We formed the following subgroups of calibrants: 0-152.2 kBq (low range), 152.2-1522 kBq (mid range), 1522-6088 kBq (high range); results of piecewise linear calibration are shown in Figures A8-4–A8-6. Based on the results this calibration method was the most reliable therefore we decided to apply it when analysing *ex vivo* tissue counting data.

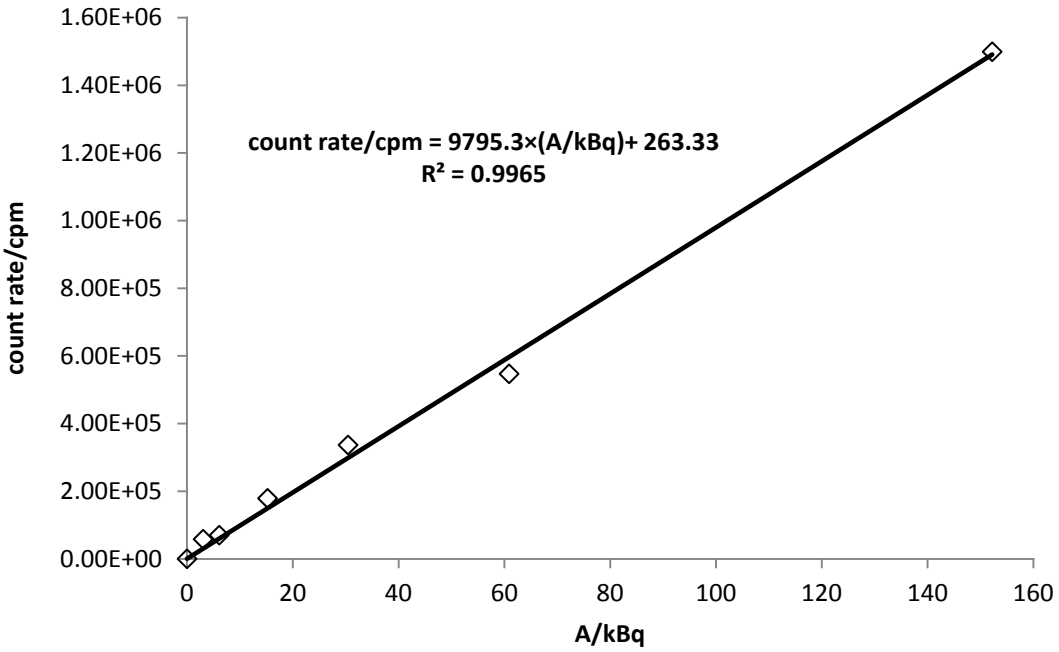

Figure A8-4: Results of piecewise linear calibration (low range).

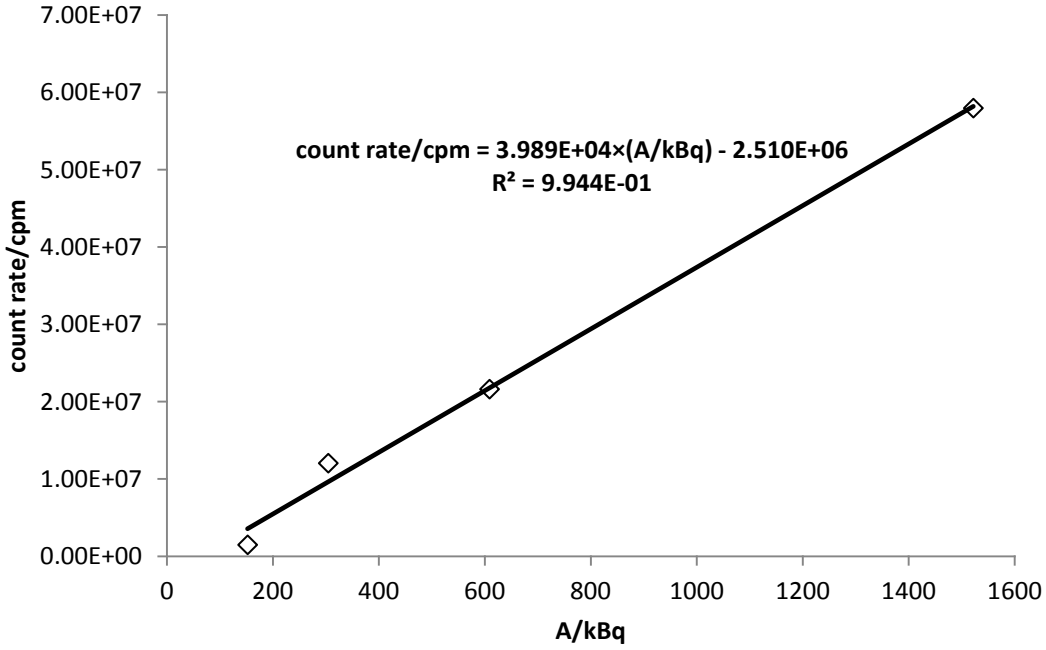

Figure A8-5: Results of piecewise linear calibration (mid range).

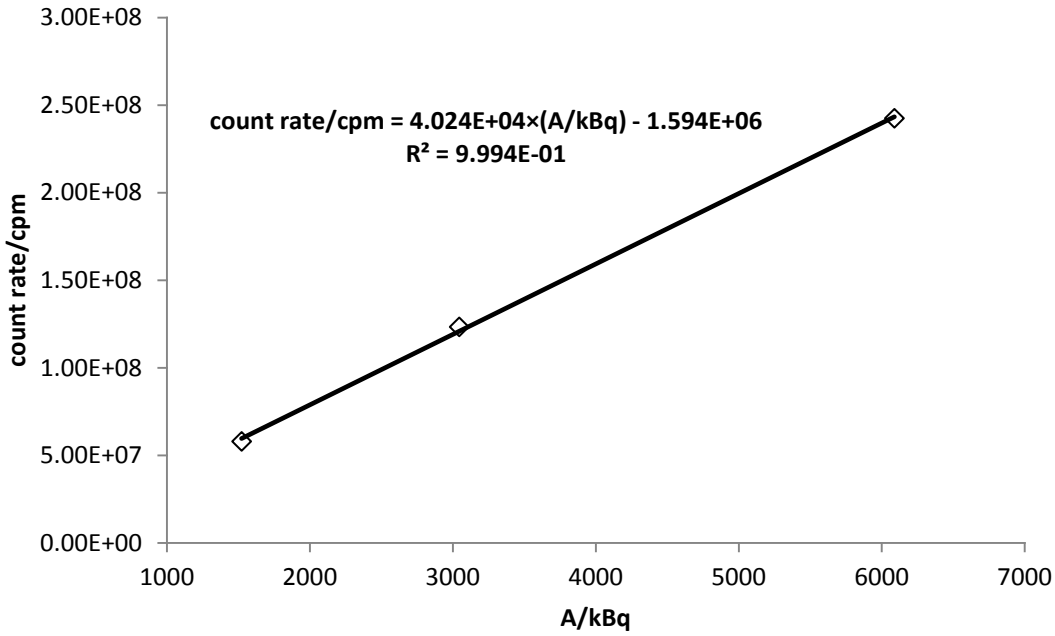

Figure A8-6: Results of piecewise linear calibration (high range).

The calibration functions above belong to a representative set of calibrants and only minor differences were found at later calibrations therefore these functions were used to calculate tissue uptake in biodistribution studies reported in this thesis.

A8.6 Conclusions

We demonstrated that using the appropriate calibration method is crucial when calibrating the gamma counter on a very broad range of activity otherwise the reliability of biodistribution calculations becomes questionable. After a short analysis of the three most widely used interpolation algorithms (*i.e.* linear, spline and linear piecewise interpolation) we found that piecewise linear interpolation was the most reliable even though its use required the arbitrary definition of three subsets of calibrants.

Appendix 9: Results of the FACS analysis of a rat kidney homogenate stained for CTR

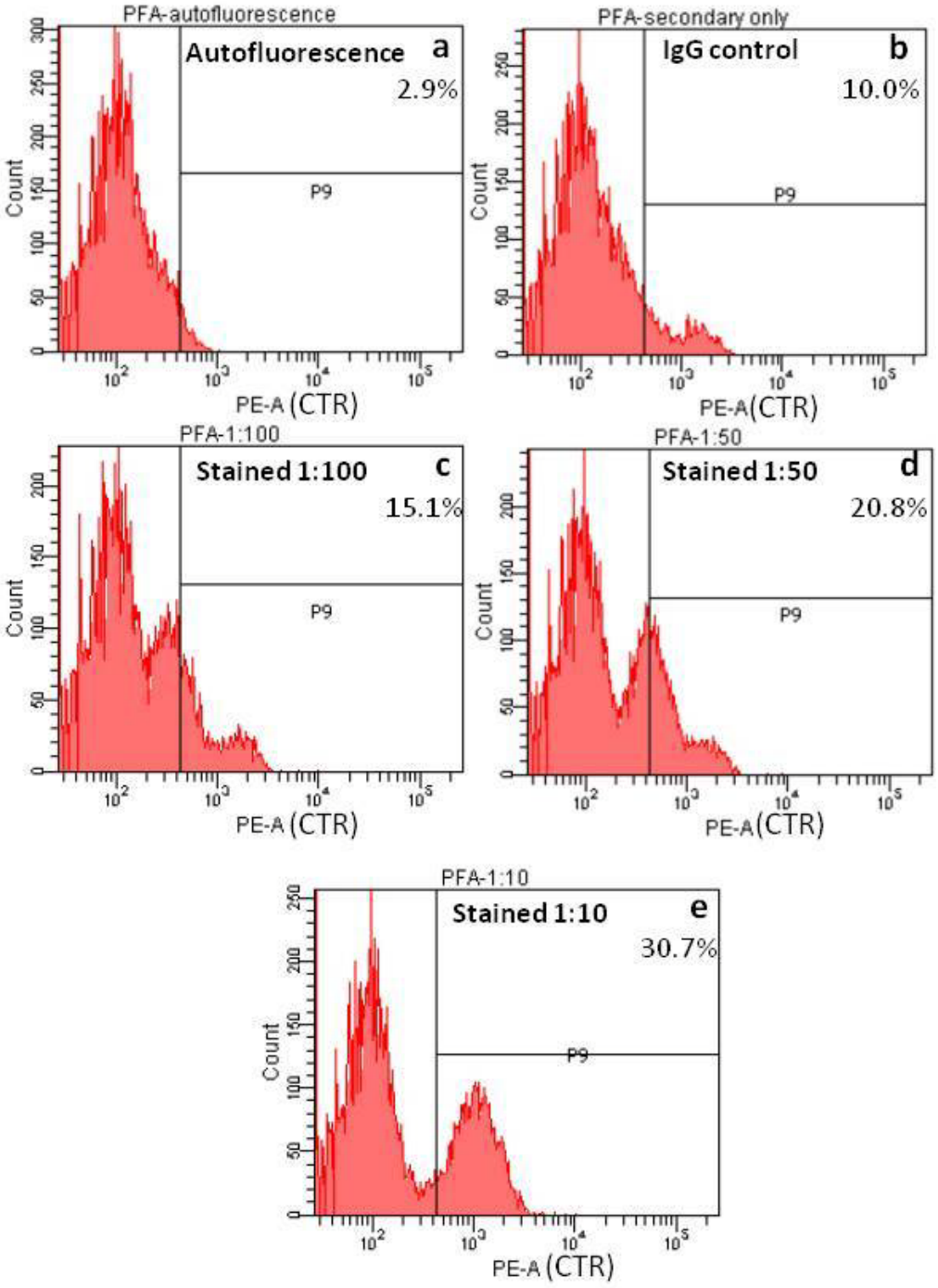

Figure A9-1: Results of the FACS analysis of a rat kidney homogenate stained for CTR: autofluorescence in the PE channel (a), non-specific binding of the secondary antibody (b), CTR staining in 1:100 (c), 1:50 (d) and 1:10 (e) dilution.

Appendix 10: Results of t-tests to establish the significance of difference in Tc-99m-sCTLys^{18}-hynic-TFA uptake among different groups of mice

Table A10-1 reports the results of two-sample, two-tailed heteroscedastic t-tests to establish the significance of difference in Tc-99m-sCTLys^{18}-hynic-TFA uptake among different groups of (control and MM bearing) mice. The null hypothesis was that mean SUVs in the two populations were equal and the alternative hypothesis was that mean SUVs in the two populations were different. The first row of the table contains the pair of datasets that we prove our hypotheses for. Target organs will be highlighted in bold, non-target organs with a difference significant at the level of at least p=0.05 will be highlighted in italics. Data regarding target organs and some non-target organs are also reported in Chapter 7, section 7.3.1.

	control gr. 2, "11 days" gr.	control gr. 2, "14 days" gr.	control gr. 2, "15 days" gr.	control gr. 2, "15 days (block)" gr.	"11 days" gr., "14 days" gr.	"11 days" gr., "15 days" gr.	"11 days" gr., "15 days (block)" gr.	"14 days" gr., "15 days" gr.	"14 days" gr., "15 days (block)" gr.	"15 days" gr., "15 days (block)" gr.
Heart	*0.0008*	*0.0008*	*0.0013*	*0.0021*	0.3440	*0.0445*	0.6389	0.2170	0.1910	*0.0286*
Lungs	*0.0453*	0.3930	*0.0263*	0.0904	*0.0073*	*0.0010*	*0.0029*	*0.0209*	0.2017	0.6160
Liver	**0.0034**	**0.0000**	**0.0012**	**0.0054**	**0.2421**	**0.0200**	**0.0138**	**0.0520**	**0.0287**	**0.2410**
Spleen	**0.4483**	**0.0005**	**0.0010**	**0.0431**	**0.0094**	**0.0013**	**0.0904**	**0.0445**	**0.4084**	**0.0201**
Stomach	*0.0002*	*0.0012*	0.8727	*0.0237*	*0.0218*	*0.0002*	0.6537	*0.0026*	0.1282	*0.0175*
Intestines	*0.0000*	*0.0068*	*0.0415*	0.1080	*0.0020*	*0.0128*	*0.0008*	0.8685	0.1048	0.3195
Kidneys	n/a	0.7002	0.0328	n/a	n/a	n/a	n/a	0.0604	n/a	n/a
Muscle	*0.0497*	*0.0074*	*0.0078*	*0.0377*	0.2874	0.0936	*0.0015*	0.4003	*0.0002*	*0.0022*
Femur	**0.0571**	**0.0033**	**0.0002**	**0.6764**	**0.0895**	**0.3260**	**0.0471**	**0.0151**	**0.0028**	**0.0158**
Blood	*0.0286*	*0.0087*	*0.0311*	*0.0003*	0.0837	0.0577	0.1736	0.1803	0.2031	0.0805

Table A10-1: Results of t-tests to establish difference of Tc-99m-sCTLys[18]-hynic-TFA uptake in different groups of mice

Appendix 11: Individual contributions to the review entitled "Hydrazinonicotinic acid (HYNIC) – Coordination chemistry and applications in radiopharmaceutical chemistry"

The review was published in Inorganica Chimica Acta as Meszaros, L.K., Dose, A., Biagini, S.C.G. and Blower, P.J., *Hydrazinonicotinic acid (HYNIC) - Coordination chemistry and applications in radiopharmaceutical chemistry.* Inorganica Chimica Acta, 2010. **363**(6): p. 1059-1069.

This statement is to certify that,

Levente Meszaros reviewed 51 references and drafted the manuscript.

Anica Dose reviewed 31 references and drafted the manuscript.

Stefano Biagini designed the review and wrote the paper.

Phil Blower was the principal investigator, designed the review and adapted the manuscript for final publication adding some critical analysis and interpretation, using data and references compiled and reviewed by Levente Meszaros.

Phil Blower
Principal investigator

Appendix 12: Individual contributions to the study entitled "Synthesis and evaluation of analogues of HYNIC as bifunctional chelators for technetium"

The study was published in Dalton Transactions as Meszaros, L.K., Dose, A., Biagini, S.C.G. and Blower, P.J., *Synthesis and evaluation of analogues of HYNIC as bifunctional chelators for technetium.* Dalton Transactions, 2011. **40**(23): p. 6260-6267.

This statement is to certify that,

Levente Meszaros synthesised 6-hynic, dihynic and chloro-hynic and characterised them by LC-MS and NMR, designed and performed radiolabelling experiments, characterised the radiolabelled species by HPLC and LC-MS and drafted the manuscript.

Anica Dose synthesised and fully characterised 2-hynic and 4-hynic and characterised 6-hynic, dihynic and chloro-hynic by elemental analysis and IR spectroscopy.

Stefano Biagini designed the study, interpreted NMR data on chloro-hynic and wrote the paper.

Phil Blower was the principal investigator, designed the study and adapted the manuscript for final submission.

Phil Blower
Principal investigator

Appendix 13: ^{1}H-NMR and mass spectra of Fmoc-N-ε-(hynic-Boc)-Lysine

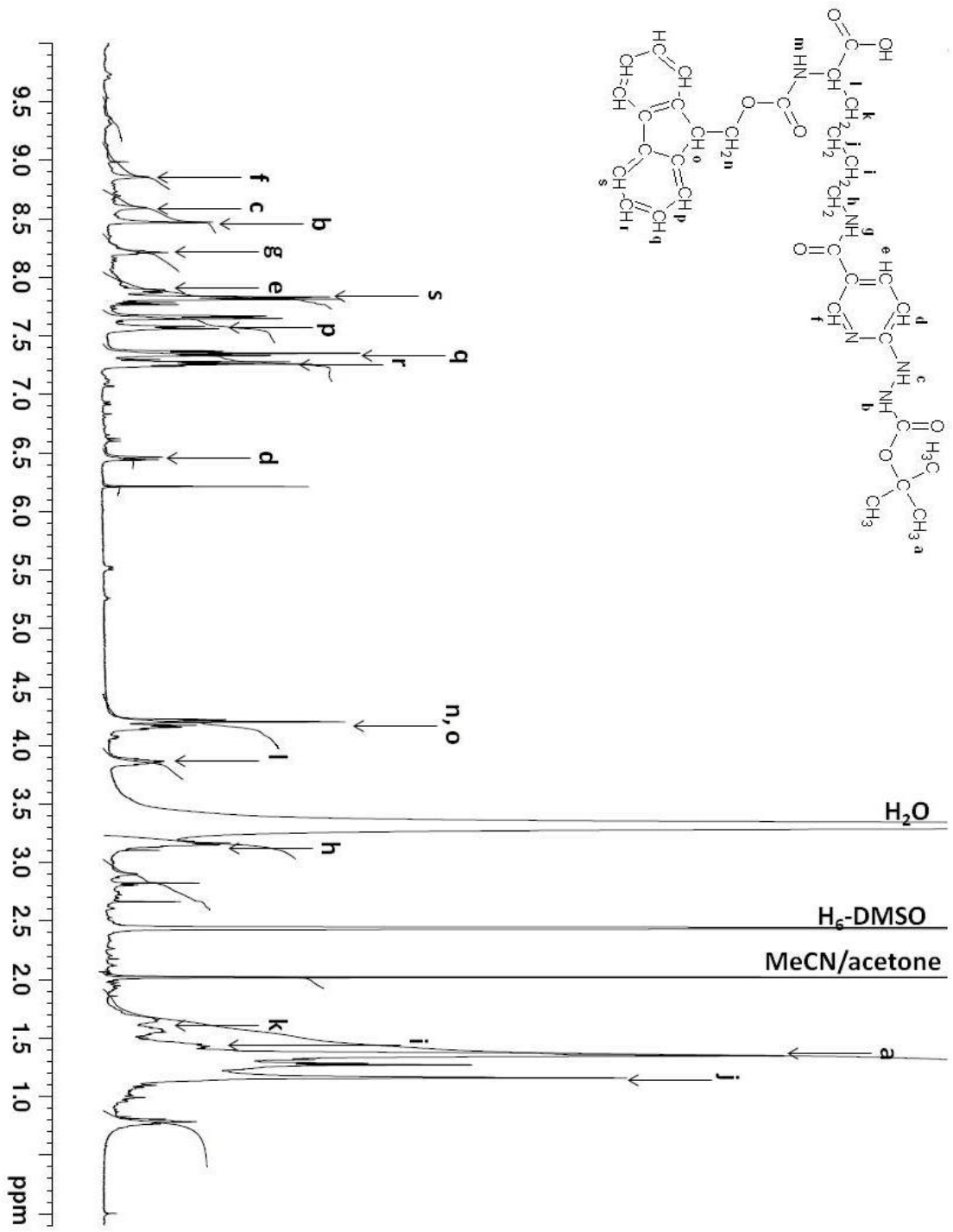

Figure A13-1: ^{1}H-NMR spectrum of the purified Fmoc-N-ε-(Hynic-Boc)-Lysine

Figure A13-2: Mass spectrum of the purified Fmoc-N-ε-(Hynic-Boc)-Lysine

References

1. Edwards, C.M., J.L. Zhuang, and G.R. Mundy, *The pathogenesis of the bone disease of multiple myeloma.* Bone, 2008. **42**(6): p. 1007-1013.

2. Van Camp, B. and P. Fenaux, *Multiple Myeloma - A model of nature - Introduction.* Pathologie Biologie, 1999. **47**(2): p. 87-88.

3. Kyle, R.A. and S.V. Rajkumar, *Multiple myeloma.* Blood, 2008. **111**(6): p. 2962-2972.

4. Westin, J., *Conventional chemotherapy in multiple myeloma.* Pathologie Biologie, 1999. **47**(2): p. 169-171.

5. Gahrton, G., *Allogeneic bone marrow transplantation in multiple myeloma.* Pathologie Biologie, 1999. **47**(2): p. 188-191.

6. Stevenson, F.K. and S.S. Sahota, *B cell maturation in relation to multiple myeloma.* Pathologie Biologie, 1999. **47**(2): p. 89-97.

7. Van Riet, I., *Homing mechanisms of myeloma cells.* Pathologie Biologie, 1999. **47**(2): p. 98-108.

8. Vanriet, I., et al., *Production of fibronectin and adherence to fibronectin by human myeloma cell-lines.* British Journal of Haematology, 1994. **87**(2): p. 258-265.

9. Hideshima, T., et al., *Advances in biology of multiple myeloma: clinical applications.* Blood, 2004. **104**(3): p. 607-618.

10. Raab, M.S., et al., *Multiple myeloma.* Lancet, 2009. **374**(9686): p. 324-339.

11. Lichtenstein, A., et al., *Interleukin-6 inhibits apoptosis of malignant plasma-cells.* Cellular Immunology, 1995. **162**(2): p. 248-255.

12. Oshima, K., et al., *Clinical and pathologic findings in 52 consecutively autopsied cases with multiple myeloma.* American Journal of Hematology, 2001. **67**(1): p. 1-5.

13. Rosenbaum, H., et al., *Multiple myeloma with pericardial involvement and cardiac tamponade: A report of three patients.* Leukemia & Lymphoma, 1996. **24**(1-2): p. 183-&.

14. Hall, M.N., et al., *Imaging of Extraosseous Myeloma: CT, PET/CT, and MRI Features.* American Journal of Roentgenology. **195**(5): p. 1057-1065.

15. Perezsoler, R., et al., *Liver involvement in multiple-myeloma.* American Journal of Hematology, 1985. **20**(1): p. 25-29.

16. Varettoni, M., et al., *Incidence, presenting features and outcome of extramedullary disease in multiple myeloma: a longitudinal study on 1003 consecutive patients.* Annals of Oncology. **21**(2): p. 325-330.

17. Short, K.D., et al., *Incidence of extramedullary disease in patients with multiple myeloma in the era of novel therapy, and the activity of pomalidomide on extramedullary myeloma.* Leukemia. **25**(6): p. 906-908.

18. Coffey, D., et al., *Liver failure as the only clinical manifestation of multiple myeloma.* Annals of Hematology, 2012. **91**(4): p. 625-627.

19. Moore, P.S., et al., *Molecular mimicry of human cytokine and cytokine response pathway genes by KSHV.* Science, 1996. **274**(5293): p. 1739-1744.

20. Burger, R., et al., *Human herpesvirus type 8 interleukin-6 homologue is functionally active on human myeloma cells.* Blood, 1998. **91**(6): p. 1858-1863.

21. Said, J.W., et al., *Localization of Kaposi's sarcoma-associated herpesvirus in bone marrow biopsy samples from patients with multiple myeloma.* Blood, 1997. **90**(11): p. 4278-4282.

22. Rettig, M.B., et al., *Kaposi's Sarcoma-Associated Herpesvirus Infection of Bone Marrow Dendritic Cells from Multiple Myeloma Patients.* Science, 1997. **276**(5320): p. 1851-1854.

23. Ismail, S.I., et al., *Frequent detection of Human Herpes Virus-8 in bone marrow of Jordanian patients of multiple myeloma.* Cancer Epidemiology. **35**(5): p. 471-474.

24. Sadeghian, M.H., et al., *Immunohistochemical study association between human herpesvirus 8 and multiple myeloma.* International Journal of Hematology, 2008. **88**(3): p. 283-286.

25. Berenson, J.R. and R.A. Vescio, *HHV-8 and multiple myeloma.* Pathologie Biologie, 1999. **47**(2): p. 115-118.

26. Martin, J.N., et al., *Sexual transmission and the natural history of human herpesvirus 8 infection.* New England Journal of Medicine, 1998. **338**(14): p. 948-954.

27. Kyle, R.A., *Clinical aspects of multiple myeloma and related disorders including amyloidosis.* Pathologie Biologie, 1999. **47**(2): p. 148-157.

28. Bartl, R. and B. Frisch, *Clinical significance of bone marrow biopsy and plasma cell morphology in MM and MGUS.* Pathologie Biologie, 1999. **47**(2): p. 158-168.

29. Kyle, R.A., et al., *Criteria for the classification of monoclonal gammopathies, multiple myeloma and related disorders: a report of the International Myeloma Working Group.* British Journal of Haematology, 2003. **121**(5): p. 749-757.

30. Bastard, C., *Cytogenetic abnormalities in malignant lymphoma and multiple myeloma.* Pathologie Biologie, 2003. **51**(6): p. 375-381.

31. Kyle, R.A., *Monoclonal gammopathy of undetermined significance.* Blood Reviews, 1994. **8**(3): p. 135-141.

32. Kyle, R.A. and S.V. Rajkumar, *Monoclonal gammopathy of undetermined significance.* British Journal of Haematology, 2006. **134**(6): p. 573-589.

33. Blade, J., *Therapeutic strategies and controversies in the treatment of multiple myeloma.* Pathologie Biologie, 1999. **47**(2): p. 192-198.

34. Sonneveld, P., *Drug resistance in multiple myeloma.* Pathologie Biologie, 1999. **47**(2): p. 182-187.

35. Laubach, J.P., et al., *The use of novel agents in the treatment of relapsed and refractory multiple myeloma.* Leukemia, 2009. **23**(12): p. 2222-2232.

36. Fermand, J.P. and S. Brechignac, *The role of autologous stem cell transplantation in the management of multiple myeloma.* Pathologie Biologie, 1999. **47**(2): p. 199-202.

37. Apperley, J.F. and P.I. Croucher, *Bisphosponates in multiple myeloma.* Pathologie Biologie, 1999. **47**(2): p. 178-181.

38. Vogel, M.N., et al., *Pathologic Fractures in Patients With Multiple Myeloma Undergoing Bisphosphonate Therapy: Incidence and Correlation With Course of Disease.* American Journal of Roentgenology, 2009. **193**(3): p. 656-661.

39. Berenson, J.R., et al., *Efficacy of pamidronate in reducing skeletal events in patients with advanced multiple myeloma.* New England Journal of Medicine, 1996. **334**(8): p. 488-493.

40. Winterbottom, A.P. and A.S. Shaw, *Imaging patients with myeloma.* Clinical Radiology, 2009. **64**(1): p. 1-11.

41. Dimopoulos, M., et al., *International myeloma working group consensus statement and guidelines regarding the current role of imaging techniques in the diagnosis and monitoring of multiple Myeloma.* Leukemia, 2009. **23**(9): p. 1545-1556.

42. Mulligan, M.E. and A.Z. Badros, *PET/CT and MR imaging in myeloma.* Skeletal Radiology, 2007. **36**(1): p. 5-16.

43. Adams, B.K., A. Fataar, and M.A. Nizami, *Technetium-99m-sestamibi uptake in myeloma.* Journal of Nuclear Medicine, 1996. **37**(6): p. 1001-1002.

44. Balleari, E., et al., *Technetium-99m-sestaMIBI scintigraphy in multiple myeloma and related gammopathies: a useful tool for the identification and follow-up of myeloma bone disease.* Haematologica, 2001. **86**(1): p. 78-84.

45. Giovanella, L., et al., *Tc-99m-sestamibi imaging and bone marrow karyotyping in the assessment of multiple myeloma and MGUS.* Nuclear Medicine Communications, 2008. **29**(6): p. 535-541.

46. Pace, L., et al., *Different patterns of technetium-99m sestamibi uptake in multiple myeloma.* European Journal of Nuclear Medicine, 1998. **25**(7): p. 714-720.

47. Fonti, R., et al., *Bone marrow uptake of (TC)-T-99m-MIBI in patients with multiple myeloma.* European Journal of Nuclear Medicine, 2001. **28**(2): p. 214-220.

48. Pace, L., et al., *Predictive value of technetium-99m sestamibi in patients with multiple myeloma and potential role in the follow-up.* European Journal of Nuclear Medicine, 2001. **28**(3): p. 304-312.

49. Koutsikos, J., et al., *Combined use of Tc-99m-sestamibi and Tc-99m-V-DMSA in the assessment of chemotherapy effectiveness in patients with multiple myeloma.* Journal of Nuclear Medicine, 2005. **46**(6): p. 978-982.

50. ElShirbiny, A.M., et al., *Technetium-99m-MIBI versus fluorine-18-FDG in diffuse multiple myeloma.* Journal of Nuclear Medicine, 1997. **38**(8): p. 1208-1210.

51. Goel, A., et al., *Radioiodide imaging and radiovirotherapy of multiple myeloma using VSV(Delta 51)-NIS, an attenuated vesicular stomatitis virus encoding the sodium iodide symporter gene.* Blood, 2007. **110**(7): p. 2342-2350.

52. Durie, B.G.M., et al., *Whole-body F-18-FDG PET identifies high-risk myeloma.* Journal of Nuclear Medicine, 2002. **43**(11): p. 1457-1463.

53. Schirrmeister, H., et al., *Initial results in the assessment of multiple myeloma using F-18-FDG PET.* European Journal of Nuclear Medicine and Molecular Imaging, 2002. **29**(3): p. 361-366.

54. Fonti, R., et al., *F-18-FDG PET/CT, Tc-99m-MIBI, and MRI in evaluation of patients with multiple myeloma.* Journal of Nuclear Medicine, 2008. **49**(2): p. 195-200.

55. Nanni, C., et al., *Role of F-18-FDG PET/CT in the assessment of bone involvement in newly diagnosed multiple myeloma: preliminary results.* European Journal of Nuclear Medicine and Molecular Imaging, 2006. **33**(5): p. 525-531.

56. Agool, A., et al., *18F-FLT PET in hematologic disorders: A novel technique to analyze the bone marrow compartment.* Journal of Nuclear Medicine, 2006. **47**(10): p. 1592-1598.

57. Agool, A., et al., *Radionuclide imaging of bone marrow disorders.* European Journal of Nuclear Medicine and Molecular Imaging. **38**(1): p. 166-178.

58. Nanni, C., et al., *11C-choline vs. 18F-FDG PET/CT in assessing bone involvement in patients with multiple myeloma.* World Journal of Surgical Oncology, 2007. **5**(1): p. 68.

59. Dankerl, A., et al., *Multiple myeloma: Molecular imaging with C-11-methionine PET/CT - Initial experience.* Radiology, 2007. **242**(2): p. 498-508.

60. Nishizawa, M., et al., *C-11-Methionine PET/CT for multiple myeloma.* International Journal of Hematology. **91**(5): p. 733-734.

61. Lee, S.M., et al., *Incidental finding of an C-11-acetate PET-positive multiple myeloma.* Annals of Nuclear Medicine. **24**(1): p. 41-44.

62. Wadas, T.J., et al., *Targeting the {alpha}v{beta}3 Integrin for Small-Animal PET/CT of Osteolytic Bone Metastases.* J Nucl Med, 2009. **50**(11): p. 1873-1880.

63. Watanabe, N., et al., *Multiple myeloma evaluated with Tl-201 scintigraphy compared with bone scintigraphy.* Journal of Nuclear Medicine, 1999. **40**(7): p. 1138-1142.

64. Ishibashi, M., et al., *Bone marrow uptake of thallium-201 before and after therapy in multiple myeloma.* Journal of Nuclear Medicine, 1998. **39**(3): p. 473-475.

65. Edwards, G.K., J. Santoro, and A. Taylor, *Use of bone-scintigraphy to select patients with multiple-myeloma for treatment with Sr-89.* Journal of Nuclear Medicine, 1994. **35**(12): p. 1992-1993.

66. Dispenzieri, A., et al., *A phase II study of Sm-153-EDTMP and high-dose melphalan as a peripheral blood stem cell conditioning regimen in patients with multiple myeloma.* American Journal of Hematology, 2010. **85**(6): p. 409-413.

67. Zaidi, M., et al., *The calcitonin gene peptides - biology and clinical relevance.* Critical Reviews in Clinical Laboratory Sciences, 1990. **28**(2): p. 109-174.

68. Copp, D.H. and B. Cheney, *Calcitonin - hormone from the parathyroid which lowers calcium-level of blood.* Nature, 1962. **193**(4813): p. 381-&.

69. Foster, G.V., et al., *Thyroid origin of calcitonin.* Nature, 1964. **202**(493): p. 1303-&.

70. Pearse, A.G.E. and Carvalhe.Af, *Cytochemical evidence for an ultimobranchial origin of rodent thyroid C cells.* Nature, 1967. **214**(5091): p. 929-&.

71. Pondel, M., *Calcitonin and calcitonin receptors: bone and beyond.* International Journal of Experimental Pathology, 2000. **81**(6): p. 405-422.

72. Wu, G.A., D.T. Burzon, and P.A. diSantAgnese, *Calcitonin receptor mRNA expression in the human prostate.* Urology, 1996. **47**(3): p. 376-381.

73. Wang, X.J., et al., *Calcitonin receptor gene and breast cancer: quantitative analysis with laser capture microdissection.* Breast Cancer Research and Treatment, 2004. **83**(2): p. 109-117.

74. Whitehead, M., et al., *Interrelations of calcium-regulating hormones during normal pregnancy.* British Medical Journal, 1981. **283**(6283): p. 10-12.

75. De Luise, M., et al., *Metabolism of porcine human and salmon calcitonin in the rat.* Journal of Endocrinology, 1972. **53**(3): p. 475-482.

76. Purdue, B.W., N. Tilakaratne, and P.M. Sexton, *Molecular pharmacology of the calcitonin receptor.* Receptors & Channels, 2002. **8**(3-4): p. 243-255.

77. Marx, S.J., et al., *Renal receptors for calcitonin - binding and degradation of the hormone.* Journal of Biological Chemistry, 1973. **248**(13): p. 4797-4802.

78. Huwyler, R., et al., *Plasma kinetics and urinary-excretion of exogenous human and salmon-calcitonin in man.* American Journal of Physiology, 1979. **236**(1): p. E15-E19.

79. Epand, R.M., et al., *Amphipathic helix and its relationship to the interaction of calcitonin with phospholipids.* Biochemistry, 1983. **22**(22): p. 5074-5084.

80. Epand, R.M., R.F. Epand, and R.C. Orlowski, *Biologically-active calcitonin analogs which have minimal interactions with phospholipids.* Biochemical and Biophysical Research Communications, 1988. **152**(1): p. 203-207.

81. Blower, P.J., et al., *Iodine-123 salmon calcitonin, an imaging agent for calcitonin receptors: synthesis, biodistribution, metabolism and dosimetry in humans.* European Journal of Nuclear Medicine, 1998. **25**(2): p. 101-108.

82. Hoff, A.O., et al., *Increased bone mass is an unexpected phenotype associated with deletion of the calcitonin gene.* Journal of Clinical Investigation, 2002. **110**(12): p. 1849-1857.

83. Dacquin, R., et al., *Amylin inhibits bone resorption while the calcitonin receptor controls bone formation in vivo.* Journal of Cell Biology, 2004. **164**(4): p. 509-514.

84. Chung, S.Y., et al., *Hypercalcemia and status epilepticus relates to salmon calcitonin administration in breast cancer.* Breast, 2005. **14**(5): p. 399-402.

85. Fouchereauperon, M., et al., *Calcitonin induces hypercalcemia in gray mullet and immature fresh-water and sea-water adapted rainbow-trout.* Comparative Biochemistry and Physiology a-Physiology, 1987. **87**(4): p. 1051-1053.

86. Srivastav, A.K. and L. Rani, *Influence of calcitonin administration on serum-calcium and inorganic-phosphate level of the frog, Rana-Tigrina.* General and Comparative Endocrinology, 1989. **74**(1): p. 14-17.

87. Chakraborty, M., et al., *Cell-cycle dependent coupling of the calcitonin receptor to different G-proteins.* Science, 1991. **251**(4997): p. 1078-1082.

88. Chakraborty, M., et al., *Cell cycle-dependent and kinase-specific regulation of the apical Na/H exchanger and the Na,K-ATPase in the kidney-cell line LLC-PK1 by calcitonin.* Proceedings of the National Academy of Sciences of the United States of America, 1994. **91**(6): p. 2115-2119.

89. Lerner, U.H., *Deletions of genes encoding calcitonin/alpha-CGRP, amylin and calcitonin receptor have given new and unexpected insights into the function of calcitonin receptors and calcitonin receptor-like receptors in bone.* Journal of Musculoskeletal & Neuronal Interactions, 2006. **6**(1): p. 87-95.

90. Delis, S., et al., *Asymptomatic calcitonin-secreting tumor of the pancreas. A case report.* Jop, 2006. **7**(1): p. 70-3.

91. Wuilmet, L., et al., *Digestive calcitonin-secreting tumors of the foregut: comparison with non-calcitonin-secreting tumors.* European Journal of Gastroenterology & Hepatology, 2006. **18**(9): p. 951-955.

92. Mullerpatan, P.M., et al., *Calcitonin-secreting tumor of the pancreas.* Digestive Surgery, 2004. **21**(4): p. 321-324.

93. Iacobone, M., *A calcitonin-secreting tumor of the pancreas.* Digestive Surgery, 2005. **22**(1-2): p. 114-114.

94. Fleury, A., et al., *Calcitonin-secreting tumors of the pancreas: About six cases.* Pancreas, 1998. **16**(4): p. 545-550.

95. Wimalawansa, S.J., *Amylin, calcitonin gene-related peptide, calcitonin, and adrenomedullin: A peptide superfamily.* Critical Reviews in Neurobiology, 1997. **11**(2-3): p. 167-239.

96. Zaidi, M., et al., *Osteoclast function and its control.* Experimental Physiology, 1993. **78**(6): p. 721-739.

97. Zaidi, M., et al., *Amylin-amide - a new bone conserving peptide from the pancreas.* Experimental Physiology, 1990. **75**(4): p. 529-536.

98. Wimalawansa, S.J., R.D. Gunasekera, and H.K. Datta, *Hypocalcemic actions of amylin amide in humans.* Journal of Bone and Mineral Research, 1992. **7**(9): p. 1113-1116.

99. Katafuchi, T., et al., *Calcitonin receptor-stimulating peptide, a new member of the calcitonin gene-related peptide family - Its isolation from porcine brain, structure, tissue distribution, and biological activity.* Journal of Biological Chemistry, 2003. **278**(14): p. 12046-12054.

100. Katafuchi, T., et al., *Identification of second and third calcitonin receptor-stimulating peptides in porcine brain.* Biochemical and Biophysical Research Communications, 2003. **308**(3): p. 445-451.

101. Katafuchi, T., K. Hamano, and N. Minamino, *Identification, structural determination, and biological activity of bovine and canine calcitonin receptor-stimulating peptides.* Biochemical and Biophysical Research Communications, 2004. **313**(1): p. 74-79.

102. Zaidi, M., et al., *Forty years of calcitonin - Where are we now? A tribute to the work of Iain Macintyre, FRS.* Bone, 2002. **30**(5): p. 655-663.

103. Cafforio, P., et al., *Functional expression of the calcitonin receptor by human T and B cells.* Human Immunology, 2009. **70**(9): p. 678-685.

104. Marx, S.J., et al., *Calcitonin receptors on cultured human lymphocytes.* Journal of Biological Chemistry, 1974. **249**(21): p. 6812-6816.

105. Tashjian, A.H., Jr., et al., *Calcitonin binding sites in bone: relationships to biological response and "escape".* Recent Prog Horm Res, 1978. **34**: p. 285-334.

106. Nakamura, M., et al., *Allelic variants of human calcitonin receptor in the Japanese population.* Human Genetics, 1997. **99**(1): p. 38-41.

107. Gorn, A.H., et al., *Expression of two human skeletal calcitonin receptor isoforms cloned from a giant cell tumor of bone. The first intracellular domain modulates ligand binding and signal transduction.* The Journal of Clinical Investigation, 1995. **95**(6): p. 2680-2691.

108. Albrandt, K., et al., *Molecular-cloning and functional expression of a 3rd isoform of the human calcitonin receptor and partial characterization of the calcitonin receptor gene.* Endocrinology, 1995. **136**(12): p. 5377-5384.

109. Beaudreuil, J., et al., *Molecular characterization of two novel isoforms of the human calcitonin receptor.* Gene, 2004. **343**(1): p. 143-151.

110. Nakamura, M., et al., *Calcitonin receptor gene polymorphism in Japanese women: Correlation with body mass and bone mineral density.* Calcified Tissue International, 2001. **68**(4): p. 211-215.

111. Nakamura, M., et al., *A new-type of human calcitonin receptor isoform generated by alternative splicing.* Biochemical and Biophysical Research Communications, 1995. **209**(2): p. 744-751.

112. Granholm, S., P. Lundberg, and U.H. Lerner, *Expression of the calcitonin receptor, calcitonin receptor-like receptor, and receptor activity modifying proteins during osteoclast differentiation.* Journal of Cellular Biochemistry, 2008. **104**(3): p. 920-933.

113. McLatchie, L.M., et al., *RAMPs regulate the transport and ligand specificity of the calcitonin-receptor-like receptor.* Nature, 1998. **393**(6683): p. 333-339.

114. Greenland, W.E.P., *PhD Thesis*, 2003, University of Kent, Canterbury.

115. Greenland, W.E.P., et al., *Solid-phase synthesis of peptide radiopharmaceuticals using Fmoc-N-epsilon-(Hynic-Boc)-Lysine, a technetium-binding amino acid: Application to Tc-99m-labeled salmon calcitonin.* Journal of Medicinal Chemistry, 2003. **46**(9): p. 1751-1757.

116. Gillespie, M.T., et al., *Calcitonin receptors, bone sialoprotein and osteopontin are expressed in primary breast cancers.* International Journal of Cancer, 1997. **73**(6): p. 812-815.

117. Nakamura, M., et al., *Genetic variants of calcitonin receptor and breast cancer in Japanese.* Breast, 1999. **8**(3): p. 104-106.

118. Sabbisetti, V.S., et al., *Calcitonin increases invasiveness of prostate cancer cells: Role for cyclic AMP-dependent protein kinase A in calcitonin action.* International Journal of Cancer, 2005. **117**(4): p. 551-560.

119. Thomas, S., et al., *Calcitonin increases tumorigenicity of prostate cancer cells: Evidence for the role of protein kinase A and urokinase-type plasminogen receptor.* Molecular Endocrinology, 2006. **20**(8): p. 1894-1911.

120. Thomas, S., A. Muralidharan, and G.V. Shah, *Knock-down of calcitonin receptor expression induces apoptosis and growth arrest of prostate cancer cells.* International Journal of Oncology, 2007. **31**(6): p. 1425-1437.

121. Bruzzaniti, A. and R. Baron, *Molecular regulation of osteoclast activity.* Reviews in Endocrine & Metabolic Disorders, 2006. **7**(1-2): p. 123-139.

122. Ishii, M. and Y. Saeki, *Osteoclast cell fusion: mechanisms and molecules.* Modern Rheumatology, 2008. **18**(3): p. 220-227.

123. Helfrich, M.H., *Osteoclast diseases.* Microscopy Research and Technique, 2003. **61**(6): p. 514-532.

124. Zaidi, M., et al., *Dimensional analysis of osteoclastic bone-resorption and the measurement of biologically-active calcitonin.* Experimental Physiology, 1994. **79**(3): p. 387-399.

125. Yumita, S., et al., *Biphasic effect of calcitonin on tartarate-resistant acid-phosphatase-activity in isolated rat osteoclasts.* Journal of Bone and Mineral Research, 1991. **6**(6): p. 591-597.

126. Selander, K.S., et al., *Calcitonin promotes osteoclast survival in vitro.* Molecular and Cellular Endocrinology, 1996. **122**(2): p. 119-129.

127. Selander, K.S., et al., *Characteristics of clodronate-induced apoptosis in osteoclasts and macrophages.* Molecular Pharmacology, 1996. **50**(5): p. 1127-1138.

128. Ikegame, M., et al., *Effects of continuous calcitonin treatment on osteoclast-like cell development and calcitonin receptor expression in mouse bone marrow cultures.* Journal of Bone and Mineral Research, 1996. **11**(4): p. 456-465.

129. Beaudreuil, J., et al., *Calcitonin receptor mRNA in mononuclear leucocytes from postmenopausal women: Decrease during osteoporosis and link to bone markers with specific isoform involvement.* Bone, 2000. **27**(1): p. 161-168.

130. Lee, S.-K. and J. Lorenzo, *Cytokines regulating osteoclast formation and function.* Current Opinion in Rheumatology, 2006. **18**(4): p. 411-418.

131. Bascal, Z.A., et al., *Effect of raised extracellular calcium on cell spread area in quail medullary bone osteoclasts.* Experimental Physiology, 1994. **79**(1): p. 15-24.

132. Bascal, Z.A., et al., *Osteoclasts from medullary bone of egg-laying japanese-quail do not express the putative calcium receptor.* Experimental Physiology, 1992. **77**(3): p. 501-504.

133. Shankar, V.S., et al., *Calcium influx and release in isolated rat osteoclasts.* Experimental Physiology, 1994. **79**(4): p. 537-545.

134. Bax, B.E., et al., *Functional consequences of the interaction of Ni2+ with the osteoclast Ca2+ receptor.* Experimental Physiology, 1993. **78**(4): p. 517-529.

135. Moonga, B.S., et al., *Correlates of osteoclast function in the presence of perchlorate ions in the rat.* Experimental Physiology, 1991. **76**(6): p. 923-933.

136. Rebel, A., et al., *Action of calcitonin on osteoclasts in Pagets bone-disease during long-term treatment.* Pathologie Biologie, 1977. **25**(9): p. 611-616.

137. Rennert, R., I. Neundorf, and A.G. Beck-Sickinger, *Calcitonin-derived peptide carriers: Mechanisms and application.* Advanced Drug Delivery Reviews, 2008. **60**(4-5): p. 485-498.

138. Silvestris, F., et al., *Expression and function of the calcitonin receptor by myeloma cells in their osteoclast-like activity in vitro.* Leukemia Research, 2008. **32**(4): p. 611-623.

139. Calvani, N., et al., *Functional osteoclast-like transformation of cultured human myeloma cell lines.* British Journal of Haematology, 2005. **130**(6): p. 926-938.

140. Terpos, E. and M.A. Dimopoulos, *Myeloma bone disease: pathophysiology and management.* Annals of Oncology, 2005. **16**(8): p. 1223-1231.

141. Surfraz, M.B.U., et al., *Trifluoroacetyl-HYNIC peptides: Synthesis and Tc-99m radiolabeling.* Journal of Medicinal Chemistry, 2007. **50**(6): p. 1418-1422.

142. Surfraz, M.B.U., S.C.G. Biagini, and P.J. Blower, *A technetium intermediate specifically promotes deprotection of trifluoroacetyl HYNIC during radiolabelling under mild conditions.* Dalton Transactions, 2008(22): p. 2920-2922.

143. Howland, K., *Personal communication*, 2010.

144. Harris, T.D., et al., *Synthesis of stable hydrazones of a hydrazinonicotinyl-modified peptide for the preparation of Tc-99m-labeled radiopharmaceuticals.* Bioconjugate Chemistry, 1999. **10**(5): p. 808-814.

145. Abrams, M.J., et al., *Technetium-99m-Human Polyclonal IgG Radiolabeled via the Hydrazino Nicotinamide Derivative for Imaging Focal Sites of Infection in Rats.* Journal of Nuclear Medicine, 1990. **31**(12): p. 2022-2028.

146. Babich, J.W., et al., *Technetium-99m-Labeled Hydrazino Nicotinamide Derivatized Chemotactic Peptide Analogs for Imaging Focal Sites of Bacterial Infection.* Journal of Nuclear Medicine, 1993. **34**(11): p. 1964-1974.

147. Ono, M., et al., *Intracellular metabolic fate of radioactivity after injection of technetium-99m-labeled hydrazino nicotinamide derivatized proteins.* Bioconjugate Chemistry, 1999. **10**(3): p. 386-394.

148. Meszaros, L.K., et al., *Hydrazinonicotinic acid (HYNIC) - Coordination chemistry and applications in radiopharmaceutical chemistry.* Inorganica Chimica Acta, 2010. **363**(6): p. 1059-1069.

149. Meszaros, L.K., et al., *Synthesis and evaluation of analogues of HYNIC as bifunctional chelators for technetium.* Dalton Transactions, 2011. **40**(23): p. 6260-6267.

150. Liu, S., et al., *Labeling a hydrazino nicotinamide-modified cyclic IIb/IIIa receptor antagonist with Tc-99m using aminocarboxylates as coligands.* Bioconjugate Chemistry, 1996. **7**(1): p. 63-71.

151. Babich, J.W. and A.J. Fischman, *Effect of "co-ligand" on the biodistribution of 99mTc-labeled hydrazino nicotinic acid derivatized chemotactic peptides.* Nuclear Medicine and Biology, 1995. **22**(1): p. 25-30.

152. King, R., et al., *Tc-99m-HYNIC-Gastrin Peptides: Assisted Coordination of Tc-99m by Amino Acid Side Chains Results in Improved Performance Both In Vitro and In Vivo.* Journal of Nuclear Medicine, 2009. **50**(4): p. 591-598.

153. Surfraz, M.B.U., et al., *Technetium-binding in labelled HYNIC-peptide conjugates: Role of coordinating amino acids.* Journal of Inorganic Biochemistry, 2009. **103**(7): p. 971-977.

154. Lambrecht, F.Y., K. Durkan, and E. Bayrak, *Labeling bombesin-like peptide with Tc-99m via hydrazinonicotinamide: description of optimized radiolabeling conditions.* Journal of Radioanalytical and Nuclear Chemistry. **284**(3): p. 539-545.

155. King, R.C., et al., *How do HYNIC-conjugated peptides bind technetium? Insights from LC-MS and stability studies.* Dalton Transactions, 2007(43): p. 4998-5007.

156. Greenland, W.E.P. and P.J. Blower, *Water-soluble phosphines for direct labeling of peptides with technetium and rhenium: Insights from electrospray mass spectrometry.* Bioconjugate Chemistry, 2005. **16**(4): p. 939-948.

157. Tsopelas, C., *The radiopharmaceutical chemistry of Tc-99m-tin fluoride colloid-labeled-leukocytes.* Quarterly Journal of Nuclear Medicine and Molecular Imaging, 2005. **49**(4): p. 319-324.

158. Tsopelas, C., et al., *Preparation and biological evaluation of Tc-99m-stannous fluoride colloid-labelled-leucocytes in rats Tc-99m-stannous fluoride-labelled-leucocytes in rats.* Journal of Labelled Compounds & Radiopharmaceuticals, 2003. **46**(8): p. 751-763.

159. Liu, S., D.S. Edwards, and A.R. Harris, *A novel ternary ligand system for Tc-99m-labeling of hydrazino nicotinamide-modified biologically active molecules using imine-N-containing heterocycles as coligands.* Bioconjugate Chemistry, 1998. **9**(5): p. 583-595.

160. Ballinger, J., *Personal Communication.* 2010.

161. Ono, M., et al., *Plasma protein binding of Tc-99m-labeled hydrazino nicotinamide derivatized polypeptides and peptides.* Nuclear Medicine and Biology, 2001. **28**(2): p. 155-164.

162. Graham, T., *Personal communication,* 2011.

163. Radl, J., et al., *Multiple-myeloma.* American Journal of Pathology, 1988. **132**(3): p. 593-597.

164. Manning, L.S., et al., *A model of multiple-myeloma - culture of 5T33 murine myeloma cells and evaluation of tumorigenicity in the C57Bl KaLwRij mouse.* British Journal of Cancer, 1992. **66**(6): p. 1088-1093.

165. Garrett, I.R., et al., *A murine model of human myeloma bone disease.* Bone, 1997. **20**(6): p. 515-520.

166. Manning, L.S., et al., *Assessment of the therapeutic potential of cytokines, cytotoxic drugs and effector cell-populations for the treatment of multiple-myeloma using the 5T33 murine myeloma model.* Immunology and Cell Biology, 1995. **73**(4): p. 326-332.

167. Turner, J.H., et al., *Radiopharmaceutical therapy of 5T33 murine myeloma by sequential treatment with Sm-153 ethylenediaminetetramethylene-phosphonate, melphalan, and bone-marrow transplantation.* Journal of the National Cancer Institute, 1993. **85**(18): p. 1508-1513.

168. Vanderkerken, K., et al., *Organ involvement and phenotypic adhesion profile of 5T2 and 5T33 myeloma cells in the C57BL/KaLwRij mouse.* British Journal of Cancer, 1997. **76**(4): p. 451-460.

169. Alici, E., et al., *Visualization of 5T33 myeloma cells in the C57BL/KaLwRij mouse: Establishment of a new syngeneic murine model of multiple myeloma.* Experimental Hematology, 2004. **32**(11): p. 1064-1072.

170. Vanderkerken, K., et al., *Selective initial in vivo homing pattern of 5T2 multiple myeloma cells in the C57BL/KalwRij mouse.* British Journal of Cancer, 2000. **82**(4): p. 953-959.

171. Vanderkerken, K., et al., *Multiple myeloma biology: lessons from the 5TMM models.* Immunological Reviews, 2003. **194**(1): p. 196-206.

172. Livieratos, L., *Personal communication,* 2012.

173. GEHealthcare, *Indium In 111 oxyquinoline for the radiolabeling of autologous leukocytes (protocol).*

174. AbDSerotec, *AHP635 datasheet*, 2012.

175. de Rosales, R.T.M., et al., *Re-188(CO)(3)-Dipicolylamine-Alendronate: A New Bisphosphonate Conjugate for the Radiotherapy of Bone Metastases.* Bioconjugate Chemistry, 2010. **21**(5): p. 811-815.

176. Meszaros, L.K., *Synthesis of hynic and novel derivatives for chelating Tc-99m*, in *Division of Imaging Sciences* 2009, King's College London.

177. Dose, A., *PhD thesis in preparation*, 2012, University of Kent, Canterbury.

178. Sladen, H., *PhD Thesis*, 2009, University of Kent.

179. O'neill, A., *Personal communication*, 2011.

180. Meszaros, L.K., *Osteoclast activity as a target for radionuclide imaging and therapy in multiple myeloma and other osseous tumours (transfer report)* in *Division of Imaging Sciences* 2010, King's College London.